TECHNISCHE UNIVERSITÄT WIEN

Plasma Probe Measurements for Electric Propulsion Device Ion Beam: Optimization and Standardization

Ausgführt zum Zwecke der Erlangung des akademischen Grades eines Doktor der technischen Wissenschaften unter der Leitung von

Dr. Stéphane Mazouffre

Centre National de la Recharche Scientifique (CNRS) - Institut de Combustion Aerothermique Réactivité Environment (ICARE) - Electric Propulsion.

Dr. Prof. Friedrich Aumayr

Institute of Applied Physics (E134)

eingereicht an der Technischen Universität Wien

Faculty of Physics

von

Valentin Hugonnaud

11843612

[redacted]

Wien, am eigenhändige Unterschrift

Acknowledgements

The journey which led to the realisation of the work presented in this thesis was an experience that I never thought lived. A few years ago, I assimilated a Ph. D degree to a long and intricate path where the candidate shall go through it on his own. Nowadays, as I must not tell lies, I think this was not so far from the truth. However, let's not confuse "on his own" and "lonely". Over the last four years I have gotten the chance to meet, know and exchange with many special persons who taught me more than what I have ever learnt in my life. I wish to use these few lines to thank all of them, hoping I am not forgetting anybody!

First, I would like to thank my supervisor Dr. Stéphane Mazouffre. I owe you so much. You introduced me to laboratory works and initiated me to the research profession which was a complete jump into a void. It was a chance of being your student. From my point of view, which might not be objective I admit it, you are one of the best experts in the electric propulsion community. You have also contributed to show me that life is not just about work. You have the rare capacity to put your trust into young unexperimented students and show them that they can make good things even though the path is hard. I hope, when time comes, I'll be able to provide the same feeling to the next generation.

I thank my advisor Prof. Aumayr which provided meaningful insights on several plasma physics aspects. Our talks and your expertise provided me the tools to properly understand measurement outcomes which allowed me to decide in which direction I should go next to see the full picture. You have also been a calm and patient support for guiding me through the administrative paperwork... in German... for that I have no words.

I fear to leave some names behind, but I take the risk. I thank my colleagues and friends at ICARE in the EP team. You guys were very helpful during my short stays in the lab. Thibault, aka "Thithi", I know you from a long time now, you are a great person, a dear friend, and a highly skilled engineer. Your inputs on Hall thrusters were crucial and prevented me to lose many hours on trying to figure out

"why in the heck this thruster doesn't want to ignite"! I will miss our late trainings near the Loire where we were trying to grow some muscles before running into a bar to join Ulysses, Thibault D and try to keep up with Etienne... I have a special thanks to give to Sedina, one of the most talented scientists I have ever met, for all our small talks early in the morning at the edge of her office. I finally thank Guillaume who made me laugh during lunch breaks and provided me help when I was struggling with set-up installations and facilities operation.

I have been lucky enough to spend most of my Ph. D time in Austria with the ENPULSION team. What an experience! Where can I start? First, I thank all members of the team who made me enjoy all the time spent in the office and the lab. Going to work was for me like spending time with friends while building thrusters rated for space, what more could I have asked for a 1st job? Of course, all days were not smooth, we had hard times. I have learnt that difficulties can be overcome with determination, mutual support, and the right leadership. Hence, thank you to all CXOs at ENPULSION, David, Alex, Thomas, and Felix. You took the risk to employ a young engineer who still needed to learn everything. Working at ENPULSION taught me so much on the industry and how to keep a team alive. David, thank you for all your advice, and fruitful comments for the last four years. I could have not dreamt better than learning with such a brilliant mind and a kind person. I thank Fabien for all the French talks on Friday afternoons about life. Celina, you know how to keep the company spirit alive, it would not be the same without you. Gerhard, your happiness is contagious and spread easily around, I did enjoy that. I also thank my Spanish colleagues Alvaro and Joan. Lou and Tony, I feel privileged of having been able to learn from you. Your advice about how to work a Ph. D out and still enjoying some free times were gold to me.

Besides ENPULSION and ICARE, I had the opportunity to collaborate with other institutions. First, I did appreciate the advice given by FOTEC's engineers Werner, Nina, Emre and Bernhard. Your expertise in electronics and plasma simulations were very helpful to build my set-ups and to better understand the outcomes. Secondly, I am grateful to the European Space Agency who let me work in their Electric Propulsion Lab at ESTEC, Netherlands. Eduard thank you for giving me the chance to extend my study on a third ion source, these test campaigns were very valuable to the content of this Ph. D dissertation. Siegfried, Martin, thank you guys for your support so I could have the experiments operational in due time. Finally, I warmly thank Dr. Carsten Scharlemann, who provided me the "need to be built" vacuum chamber where all experiments with the ENPULSION NANO laboratory unit were conducted. I have to say it was the first time I was

assembling a vacuum chamber and pretty sure it will be the last! (I hope...).

I have a special mention to Dr. Anica Lekic, my teacher in plasma physics during my Master, none of this would have been possible if you did not push me towards the right direction five years ago. I hope many students will have the chance to cross your path.

Unfortunately, we are living times where the society we inherited and participate to sustain rewards individualism and gives more credits to what it is said than what it is true. This pushes people to seek for fast knowledge instead of taking the time necessary to process information. Nowadays, fake news spread as fast as viruses. What happened in 2020 just made many people to understand that, as time flies, if you are not surrounded by the right persons then difficult times are even harder to come through. The next few lines are here to pause for a second and to show how grateful I am to have great people around me.

The first persons to come to my mind are my parents, my brother, and my family. I feel lucky of growing up with you guys. Dad, mum, you have always encouraged me for every project I wanted to undertake. You let me go and stay in the cold of Russia for months, you did not blink when you watched me skydiving for the first time and supported me when I started this Ph. D in a foreign country... Ok, writing these lines down make me feel like you should maybe ask yourself if that was reasonable! Never mind, you have never failed to guide me through life, thank you. Quentin, thank you for everything big brother. You showed me that it was possible to have a fresh new start and that it is just a matter of being bold to do it. Life happened to give me a second family "la rue des Semailles". I won't name all of you because I think this acknowledgement section is getting heavy, but you guys are the best! Spending time with you since I am five contributed to become who I am today.

My time in Vienna would have not been the same without my boys, Bryan, Tim, Quirin and Dima. I have unforgettable memories of German-based hikes (just a hike where you drink beers, those Germans...) and parties with Moscow mules!!! I know we won't see each other that often any more but I will do my best to keep what we built over these years.

Finally, Claire, *mon coeur*. If this adventure was made possible it is because of you. You let me throw myself in that project and kept supporting me even during hard times. You stood by me when thousands of kilometres were between us. You gave up everything and moved to a foreign speaking language country so I can complete this Ph. D work in the best conditions. For all of that thank you so much.

If I was stopping there, I would feel ungrateful to not mention the experi-

mental set-up which followed me in three different countries and never failed me (almost!). I want to give a high five to all vacuum chambers I used during my Ph. D work FH, GIGANT and NExET.

I am very thankful to all these protagonists who helped to shape the path to this specific moment and played a role in the engineering process to make who I am today.

Valentin Hugonnaud
Wien, Austria
February 2022

"It is our choices, [...], that show what we truly are, far more than our abilities."

A.Dumbledore, Harry Potter and The Chamber of Secrets
written by J.K.Rowling

"Anticipating problems and figuring out how to solve them is actually the opposite of worrying: it's productive."

Chris Hadfield, An Astronaut's Guide to Life on Earth

"Le talent, ça n'existe pas. Le talent, c'est d'avoir envie de faire quelque chose"

Jacques Brel

List of Symbols

α	Propellant utilisation	
α_{i_+}	Correction factor for multiple ionisation	
A_e	Area at nozzle exit plane	m^2
d	Distance	cm
d_a	Housing aperture diameter	mm
d_{cup}	Cup orifice diameter	mm
d_m	Mesh hole diameter	mm
d_{rep}	Repeller aperture diameter	mm
ΔV	Vorticity increment	km/s
η_b	Thruster current utilisation	
η_p	Probe efficiency	
η_t	Thruster efficiency	
e	Elementary charge	C
E_k	Kinetic energy	J
g_0	Acceleration of gravity	m/s^2
γ_{EE}	Ion-induced electron emission	
$\gamma_{L_{EE}}$	Ion-induced electron leaving the cup	
I_e	Electron current	mA
I_{EE}	Induced electron current	mA
I_{es}	Electron saturation current	mA
I_{em}	Emitter current	mA
I_d	Discharge current	A
I_i	Ion current	mA
$I_{i\&EE}$	Total ion and induced ion current	mA
$I_{i_{int}}$	Integrated ion current	mA
I_{i_m}	measured ion current	mA
Isp	Specific impulse	s
I_+	Ion current extracted from a RIT	mA

l	Jet length	μm
Λ	Indium surface tension	J/m^2
M	Mass ion	kg
$\dot{m}_p$	Propellant mass flow rate	kg/s
m_f	Spacecraft final (dry) mass	kg
m_i	Spacecraft initial (wet) mass	kg
m_p	Spacecraft propellant mass	kg
n_{nn}	number density	m^{-3}
n_e	electron density	m^{-3}
n_i	ion density	m^{-3}
N_0	Number of particles	
N_0	Number of ions	
λ	Effective plume divergence	$^\circ$
λ_m	Mean Free path	m
$\lambda_{m_{CEX}}$	Mean Free path for charge exchange	m
$\lambda_{m_{ionisation}}$	Mean Free path for ionisation	m
λ_D	Debye Length	cm
p_{atm}	Atmospheric pressure	Pa
P_b	Beam power	W
p_e	Static pressure	Pa
r_m	Distance between holes in a grid mesh	mm
s_{hv}	High voltage plasma sheath	m
σ	Standard deviation	
σ_{CEX}	Charge exchange cross section	
$\sigma_{ionisation}$	Ionisation cross section	
σ_{nn}	Collision cross section	m^{-2}
T	Thrust	mN
$\hat{T}$	Temperature	eV
θ_i	Incidence angle	$^\circ$
θ_{div}	Thruster beam semi-half angle	$^\circ$
θ_T	Taylor cone divergence	$^\circ$
u	Uncertainties	
U_d	Discharge voltage	V
Υ_s	Sputtering yield	atoms/ions
v_b	Bohm velocity	km/s
v_e	Particle exhaust velocity	km/s
V_{em}	Emitter voltage	V
V_{ex}	Extractor voltage	V
V_s	Plasma potential	V
V_p	Probe potential	V
ω_p	Plasma frequency	Hz
Z	Ionisation state	

List of Abbreviations

C	Collector
CNRS	Centre National de la Recherche Scientifique
CRP	Cathode Reference Potential
DMP	Dual-Mode Probe
EP	Electric Propulsion
FC	Faraday Cup
FEEP	Field-Emission Electric Propulsion
FOTEC	Forschungs- und Tehnologietransfer
GIE	Gridded Ion Engine
HT	Hall effect thruster
KEE	Kinetic energy emission
IS	Ion Screener
IIE	Ion-induced electrons
LP	Langmuir probe
PP	Planar Probe
PEE	Potential energy emission
PPGR	Planar Probe with a guard ring
R	Repeller
RIT	Radio-frequency Ion Thruster
RPA	Retarding Potential Analyser
EE	Electron emission

List of Figures

List of Tables

Contents

Abstract

Nowadays, electric propulsion technologies have taken an important part of the New Space industry market thanks to their ability to save mass and volume while providing a large total impulse. Space operators use electric propulsion to perform orbit transfer manoeuvres, attitude control, station keeping, atmospheric drag compensation and end-of-life disposal. This type of propulsion provides advantages for new GPS generation, life extension systems of satellites, interplanetary probes, and cargo vehicles. The miniaturization of space hardware as well as the reduction of the cost to access space paved the way for many private actors to get involve in the new space era. These new stakeholders need to have active control of their spacecraft or constellations and therefore, need electric propulsion systems. Electric thrusters, like Hall thrusters and Gridded Ion Engine, which can be operated at high power (kW range) have been dominating the electric propulsion market since the 90s. In less than 10 years the size and power downscaling trend of spacecraft brought a new need which was filled by low-power (< 200W) electric thrusters. This can be achieved if one realizes two types of measurements: i) on the one hand, direct measurements of the thrust and ii) on the other hand measurements of the ion beam properties. This PhD thesis focuses on the second category of measurements. The beam, or the plume, of an electric thruster is composed of ions, which are at the origin of the thrust, and electrons which enable a constant neutralization. Hence, the plasma is considered quasi-neutral. Information to collect regarding ions: flux, energy, and charge. It helps determining the total ion current, ionization efficiency of the thruster and the divergence angle of the beam. These parameters are important to assess the performances of the EP device and to investigate possible plasma-satellite interactions which could lead to anomalies or even to mission failure. However, the tools and techniques differ from one thruster manufacturer to another, making difficult to set standards. The thesis main objective is twofold, namely: i) to optimize the diagnostics which enable to measure the ion current (Faraday cup) and the ion energy (retarding po-

tential analyser) and ii) to provide information on the possibility to establish a universal probe design suited for different types of thrusters. It aims to improve the reliability for ions properties measurements and to standardize test campaign. This aims to ensure the accuracy of collected data and to enable relevant comparison between different thrusters, between different ground tests and with in-orbit acquired data. The main scope of this thesis includes two different propulsion technologies: a Hall thruster and a field-emission electric thruster. These propulsion systems were provided by the French national research centre (CNRS) and the private company ENPULSION. A third propulsion systems, a gridded ion engine provided by the European Space Agency (ESA) was less deeply studied. Due to delays and unexpected events throughout the thesis planning it was only possible to conduct experiments at the very end of the thesis agreement, hence only a small amount of data were collected with this technology. Still, combined, these three thrusters cover a wide range of plasma parameters and system performances. It was also made possible to access two different vacuum chambers to study the perturbation induced by facilities in the case of field-emission-electric propulsion system. Experiments outcomes show that it is possible to use a unique design to study these three electric thrusters. However, parts of the probe exposed to perturbations induced by interactions with the beam studied depend partly on the beam properties. This implies that the probe must be operated in a different way for each thruster. Indeed, we observed that in the case where we study the far-field plume of a low power all thruster the main factors inducing errors on the ion current density measurements are closely related to the material at the probe front aperture and also its diameter. Indeed, we showed that having a probe front equipped with molybdenum and located very close to the ion collector can decrease the an ion current collection by 15% compared to a design using graphite at the front. Moreover, we experimentally determined that decreasing the inlet diameter from 10 mm to 3 mm induce near 30% loss of ion signal on the collector cup near. We experimentally proved that the cause of such losses is mainly due to the xenon ion trajectory once they penetrate the Faraday cup. We found that ions rarely reach the bottom of the collector cup as they are mostly captured by the cup walls at the front. On the opposite, findings regarding FEEP thrusters show ion-induced electron emission are that the main effect to disturb ion current measurements by considerably increasing its value. Indeed, the measured signals are barely impacted by the change of material and dimension at the probe front but heavily influenced by the probe electric field lines, length and collector material. Results displayed in the thesis showed that if no active methods are used to redirect induced electrons back to the collector the length of the cup is the most

effective design parameter to optimize to mitigate the large current increase. For instance, the simple fact to reduce the Faraday cup length from 50 mm to 10 mm can artificially increase the ion current measured by 120% for ion energies of the order of 9 keV if no additional electrodes are used at the probe front to redirect the induced electrons back to the collector. We show that the emission rate of induced electrons can also be mitigated by the material use a sion collector. Indeed, molybdenum, tungsten and stainless steel showed relatively low induced electron yields compared to aluminium which was experimentally found to have yields 4 to 6 times larger than others. In addition we show that using a metallic foam with pore size larger than 0.4 mm, in our case aluminium foam, does help to decrease the induced electron yield by a factor 1.5. Finally, the feasibility of a dual mode probe was studied. The goal was to enable the measurement of ion currents and energies for similar plasma conditions. This two information would allow to indirectly deduce the thrust produced by the thruster. We managed to prove experimentally that such a device is working for the study of a FEEP thruster while for a Hall thruster more developments on the probe design are required.

Chapter 1

Space propulsion

Contents

1.1 Fundamentals

SIR Isaac Newton fundamental laws, published in the seventeenth century, provided the basis of propulsion. Despite the vivid imagination of few contemporary scientists and writers, one must have waited the down of the twentieth century to mathematically arrange the so-called "rocket equation", published by the famous Russian scientist Konstantin Tsiolkovsky. The equation links the amount of propellant needed by a spacecraft to change its velocity.

$$\Delta V = -v_e \, ln(\frac{m_f}{m_i}), \tag{1.1}$$

with m_i the wet mass of the spacecraft accounting for the propellant mass m_p, m_f its dry mass once all propellant is consumed, ΔV the velocity increment required to reach the mission objective and v_e the particle ejection velocity. Nevertheless, the latter is rarely used to compare propulsive systems and the specific impulse (Isp) is preferred. The Isp, expressed in seconds (s), can be defined as the impulsion delivered per unit of propellant consumed and reads:

$$Isp = \frac{v_e}{g_0}, \tag{1.2}$$

g_0 being the acceleration of gravity ($\sim 9.81\,m/s^2$) on Earth. Equation 1.1 is often expressed in terms of propellant to dry mass ratio as follow:

$$\frac{m_p}{m_f} = e^{\frac{\Delta V}{Isp\,g_0}} - 1. \tag{1.3}$$

The Tsiolkovsky equation stresses that propulsion systems with high ejection velocity, or Isp, require less propellant for a given velocity increment. Therefore, the propellant mass will only be a fraction of the spacecraft wet mass as illustrated by figure 1.1. The thrust of the propulsion system can be expressed as a function of the exhaust velocity and the propellant mass flow rate:

$$T = \dot{m}_p\, v_e, \tag{1.4}$$

The kinetic energy (E_k) released by the propulsion system is:

$$E_k = \frac{1}{2} m_p\, v_e^2, \tag{1.5}$$

The variation of this energy over time gives the beam power necessary to perform the manoeuvres:

$$P_b = \frac{1}{2} \dot{m}_p\, v_e^2, \tag{1.6}$$

Combining equations 1.2 and 1.4 and 1.6, one find the fundamental relationship between the input power (power given to the thruster unit to generate thrust), the thrust and the Isp:

$$T = \eta \frac{2\,P_{in}}{Isp\,g_0}, \tag{1.7}$$

where η is the thruster efficiency, see section 2.3.5, and P_{in} the input power. Previous formula shows that for a given power, either the thrust or the Isp is large.

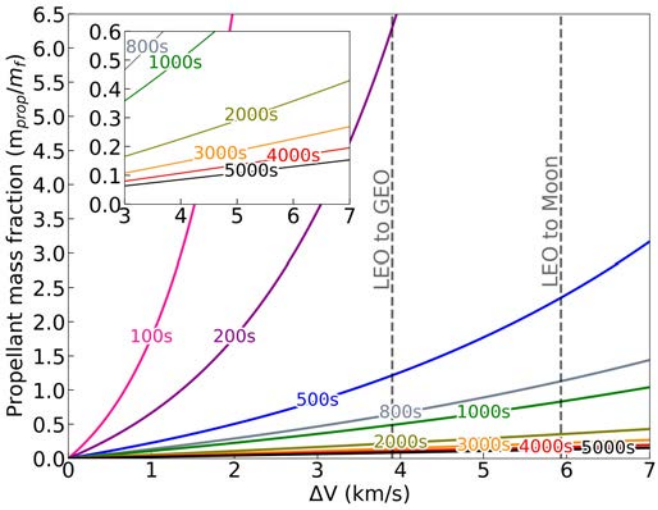

Figure 1.1: Evolution of the propellant mass to the spacecraft dry mass fraction against typical ΔV values given for different Isp. The dashed lines represents ΔV manoeuvres from low Earth orbit (LEO) to geostationary orbit (GEO) or to the Moon.

1.2 Electric propulsion

1.2.1 Limits and opportunities

A large thrust is necessary to get off the Earth gravity pull. Only chemical propulsion (CP) is safe and powerful enough to provide the required thrust to put into orbit a payload. The working principle of CP relies on converting the chemical energy stored inside the fuel into kinetic energy via a process of combustion. The latter is made possible while mixing a fuel and an oxidizer, both embedded on board of the rocket as opposed to classic jet engine principles. The resulting chemical thrust can be seen as the sum of momentum and pressure thrust as follow:

$$T_{CP} = \dot{m}_p v_e + A_e(p_e - p_{atm}), \tag{1.8}$$

with A_e the flow area at nozzle exit plane, p_e the static pressure at nozzle exit plane and p_{atm} the local atmospheric pressure. The so-called velocity thrust (e.g. momentum) and pressure thrust are related to the available energy. Typical nozzle design consist of a convergent and divergent section. The gas exhaust velocity is

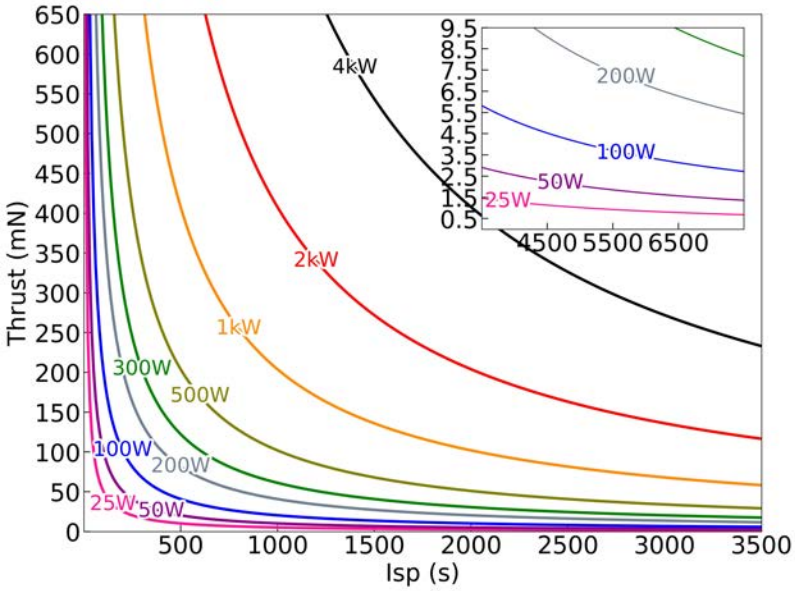

Figure 1.2: Deliverable thrust against Isp given for a set of input power.

higher in the diverging part of the nozzle. There, the particle density decreases, as does the temperature, due to the expansion process and therefore, the pressure p_e decreases. Consequently, to maximize thrust the pressure at the nozzle exit shall be as close as possible to the atmospheric pressure and meet $p_e = p_{atm}$. The momentum, via v_e, is limited by the law of physics. Indeed, the kinetic energy released by the thruster as expressed in equation 1.5 results from a potential energy conservation as stated by the first principle of thermodynamic. Any chemical propellant whether it is solid, liquid or gaseous stores energy within its covalent bonds therefore, the energy is limited. The maximum achievable velocity for a chemical propulsion system is around 5 km/s, which corresponds to 500 s of Isp. Consequently, as exemplified in figure 1.1 the propellant to spacecraft dry mass ratio is well above for chemical propulsion. This is where electric propulsion (EP) becomes a game changer for space mobility.

EP uncouples the energy source from the ejected propellant. Therefore high Isp values can be reached, close to several thousands seconds. Unfortunately, the power available on-board of a spacecraft is limited to tens of watts up to a few kilowatts. Indeed, except laser beam or nuclear reaction the only available source of energy in space is under the form of photon from the sun. Consequently, the

overall available power to deliver to an EP system relies on solar panel and battery efficiency. As a result of the limited useful power on-board of a spacecraft, an EP system can only provide very low (nN) to low thrust (mN). Figure 1.2 uses equation 1.7, with η equals 1, to illustrate the main limit. Despite its low thrust capacity EP is still advantageous to perform station keeping manoeuvres, spacecraft attitude control, slow but efficient orbit transfer or deep space exploration and de-orbiting manoeuvres [7].

1.2.2 EP technologies and applications

Electric propulsion systems work, in most cases, with partially ionized propellant. The method to create and accelerate the particles is categorised in three main groups: electro-thermal, electrostatic and electromagnetic.

Electro-thermal

Resistojets (figure 1.3a) and Arcjets (figure 1.3b) are the two predominant technologies amongst electro-thermal electric propulsion systems. The Resistojet working principle relies on heating a gas with a resistor and ejecting it through a solid nozzle. The propellant is stored under pressure as it is usually hydrogen, ammonia or decomposed hydrazine however alternative propellant, like water, has already passed flight demonstration. Generally, this type of thruster can deliver up to hundreds of mN of thrust at high power but the corresponding specific impulse stays as low as 100 s. They are advantageous in terms of size, reliability, cost compare with CP devices. In addition, they deliver a relatively large thrust level. They are amongst the simplest EP system but are limited by the temperature material can stand. Arcjet technologies get rid off the temperature limitation by heating up the propellant by means of an electric arc between an anode and a cathode. Consequently, the exhaust velocity can be up to 7 km/s and Isp between 500 and 700 s. However, the exhaust particle are in this case slightly ionized. Both technologies were mostly used by the United States in the eightieth and ninetieth on-board of communication satellite for station keeping in GEO necessary due to the lunar and solar gravitational perturbations of the orbit.

Electrostatic

The electrostatic thruster category encompasses the most used EP systems. Electrostatic devices use an electric field to accelerate ions. In contrast to electro-

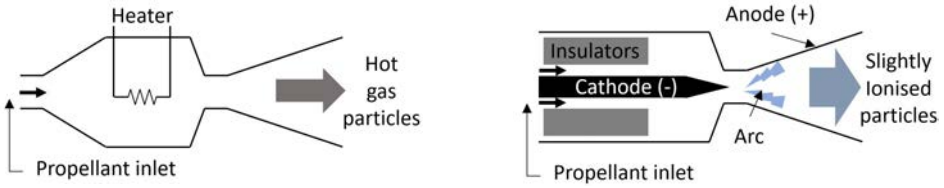

(a) Resistojet.

(b) Arcjet.

Figure 1.3: Schematic of the working principle of two electro-thermal electric propulsion systems.

thermal technologies, they can provide large Isp (1000 to 10000 s) at a cost of a reduced thrust (nN to mN). Therefore, they become appealing for long duration, high delta-V manoeuvres or for satellite constellation deployment (see section 1.2.3). In 1964 the first in orbit demonstration of an electrostatic thruster was completed with a mercury fuelled Gridded Ion Engine (GIE). More recently, in 2018, the scientific mission BepiColombo aiming to deepen our knowledge about the closest planet to the sun, Mercury, was launched. The spacecraft embedded four T6-type GIE (figure 1.4), powered by a 13 kW solar array. As the T6 are operated in pair, and each thruster requires between 4 and 5 kW, the maximum power demand approaches 10 kW. Each thruster can deliver $\sim$ 145 mN with 66% efficiency giving an Isp between 3700 s and 4600 s. Knowing the dry mass of the spacecraft, $\sim$2700 kg and the required ΔV $\sim$ 5.5 km/s we can use figure 1.1 to find that propellant mass reaches $\sim$15% of the total dry mass. With a low specific impulse chemical engine the propellant mass, for a given thrust, efficiency and power, would be close to 5 times the mass of the spacecraft. It is clear that EP makes feasible of such an important mission. The propellant is injected as a gas into a so-called discharge chamber. There, by different means, such as electron bombardment (Kaufman thruster[8, 9]), Radio Frequency waves (RF thruster[10, 11, 12]) or microwaves ([13, 14]), the propellant is ionized [15]. One singularity of GIE is that it uncouples the ionization process from the ion extraction and acceleration. Indeed, at the front of the thruster a grid assembly is used as an ion optic system to extract and accelerate ions outside the thruster core. This technique is highly efficient ($>$60%) and enables to reach large Isp values up to 10000 s with thrust values up to 200 mN[16] with a low beam divergence. Since only ions are ejected, the beam shall be neutralized with electrons to avoid spacecraft charging during in-space operation. The device, called cathode, dimensions

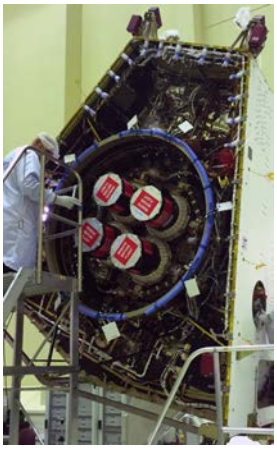

Figure 1.4: Integration of the four T6 gridded ion engine on the BepiColombo Mercury Transfer Module. © *European Space Agency*.

and power depend on the ion current density to be neutralized. Ion beams with large densities (i.e. $> \mathrm{mA/cm^2}$) need well designed hollow-type cathodes which require an important additional cost in power. On the other hand low densities can be neutralized by simple thermally emitted electron from a metal wire. Moreover, the ion optic system of GIE is constantly under study to minimise particle deposition and grid sputtering which decrease the thruster performances but also shorten its lifetime. Last but not least, GIEs can only work with limited current density, and therefore thrust, due to the Child-Langmuir law:

$$J_e = \frac{4}{9}\varepsilon_0 \left(\frac{2e}{M}\right)^{\frac{1}{2}} \frac{V^{\frac{3}{2}}}{d^2}, \tag{1.9}$$

with ε_0 the permittivity of free space, e/M the charge to mass ratio of particle, V and d the voltage difference and distance between the grids, respectively. To reach large current densities, V or d shall be increased. Both cases induces the formation of electric arc or shorting which degrade the thruster. Hence, to extract more current, the thruster needs to be bigger (i.e. wide grid diameter).

The second most studied electrostatic thruster is the so-called Hall effect thruster (HT). This technology uses the Hall effect discovered in 1879 by Edwin Herbert Hall, explaining that if a current goes trough a material immersed into a magnetic-field a voltage normal to the latter is induced. In the case of HT, electrons are injected, via a cathode, into the core of the thruster surrounded by permanent

magnets or coils to generate a magnetic-field. Electrons are trapped into an annular cavity and start to collide with the injected gaseous propellant creating a quasi-neutral plasma. The ions are then accelerated normal to the magnetic field, toward the thruster core exit. The same cathode is used to neutralize the beam in vacuum [17]. The absence of ion optic system allow to deal with high current densities providing high thrust to power ratio ($\sim$ 50 - 60 mN/kW). indeed, the use of magnetic field in a quasi-neutral plasma to create a strong electric field enable get rid off space charge limitation described by the Child-Langmuir law. However, the specific impulse is not going higher than 3000 s with typical values of 1500 s. This technology suffers as well from deterioration of the inner channel where the ionization and acceleration process occurs [18]. Nevertheless, it has been widely used for orbit transfer manoeuvres or station keeping in GEO of communication satellite. For instance, up to 40 % of mass is saved thanks to HT for the full electric Eutelsat platforms developed at Airbus Defence & Space. Despite a long transfer time from LEO to GEO, four to six months instead of a week, HTs are valuable due to the high total impulse required over the satellite lifetime, $\sim$ 15 years, necessary for station keeping ($\sim$ 25 m/s per year). Given their many advantages, modern HTs are developed to meet new power (<200 W) requirement of the New Space industry and therefore, are scaled down to a few centimetre in diameter. More details and knowledge enhancement on the technology working principle, limits and new challenges can be found in section 3.3.1.

Lately, interest for Electrospray and field-emission electric propulsion (FEEP) thrusters has grown mostly due to the New Space industry. These technologies rely on the formation of a strong electric field at the the tip of a sharp surface. For liquids, the field appears at the tip of the so-called Taylor cones [19]. The field, of which the magnitude is in the order of the atomic field, directly extract and accelerate the ions from the fluid [20]. These technologies cannot provide large thrust (μ N range) due to the very sharp area needed to form Taylor cones as well as cones instabilities preventing high current densities utilization. However, their size and Isp ($\geq$ 3000 s) make them ideal for thruster clustering or small- and nano-satellite deployment. Indeed array of electrospray injectors can be as small as a coin as depicted in figure 1.5 while flight proven FEEP thruster are not bigger than 1U (10$\times$10$\times$10 cm) and future thrusters will scale up to several Us. Their performances allow to provide the necessary ΔV to counteract atmospheric drag effect on satellite in the LEO to VLEO (Very Low Earth Orbit) region. Moreover, according to the Union of Concerned Scientists (UCS), by January 2021, close to 50% of operational satellites are considered inactive arising the main issue of this century space race: debris management. States are taking actions and set laws on

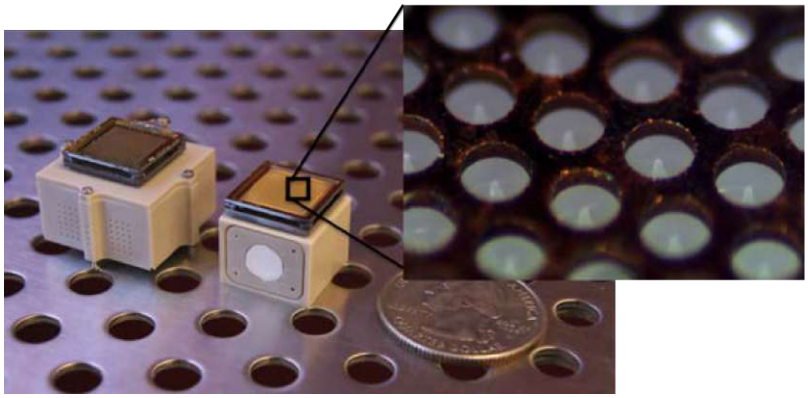

Figure 1.5: Integration of electrospray emitter arrays into a fully scalable tank [1].

de-orbiting manoeuvres for any satellite within the 25 years after it ceased to operate. The spacecraft must be slowly pushed towards the atmosphere for complete disintegration. If the ΔV is too large (e.g satellite in GEO) a so-called "graveyard orbit" is chosen with a perigee at least 300 km above GEO for a velocity increment of ~ 11 m/s. This requires around the same amount of fuel as three months of station keeping.However the main concern about electric thrusters fuelled with metal propellant is particle deposition. Layers of propellant deposition can affect the thruster operation over a long firing time but also the spacecraft performance (e.g. particle deposition on solar panels). FEEP thrusters beam will be thoroughly studied in section 3.3.2.

Electromagnetic

The very first electric thruster to be fired in space was a Pulsed Plasma Thruster (PPT) in 1964. Six units of PPT were equipping the soviet Zond-2 probe as a replacement of classic chemical thruster for attitude control. The probe was on its way to observe the planet Mars when one of the two solar panels broke down. The mission turned out to be a partial failure as the probe flew 1500 km away from the planet. It was a success to demonstrate the proper operation of PPT as they were fired for 70 minutes. A PPT working principle is straightforward. A dielectric (Teflon) is hit by a current arc induced by a discharge between an anode and a cathode as depicted by figure 1.6a. A very similar technology called Vacuum Arc Thruster (VAT) ablates directly the cathode instead of the dielectric, simplifying

the system. In both cases, the electromagnetic effects in the pulse accelerate the ion to high velocities. The thrust depends of the frequency of pulse the thruster can do. These two technologies can provide large as well as very precise thrust but technical challenges, such a material ablation location and impact homogeneity, impulsion duration, the use of magnetic nozzles or the magnitude of generated current, make them less attractive than other EP on the market. Nevertheless, thanks to their very small impulse bit they are often used, like in the case of Zond-2, for attitude control.

Finally, a technology currently studied for future application like deep-space travel and enabling very high thrust is the Magnetoplasmadynamic (MPD) thruster. The thrust is produced thanks to the Lorentz force ($J \times B$) induced by a strong radial current and an magnetic field as it is showed in figure 1.6b. Here, an additional electron source for neutralization is not necessary as the accelerated fluid stays quasi-neutral. In the 60s a Lithium-fed MPD thruster was developed in the soviet union and operated on ground at 100 kW, with a thrust efficiency of 45% and exhaust velocities close to 50 km/s, resulting in a thrust approaching 2 N. Nonetheless, the technology hasn't found yet a large interest for the current market.

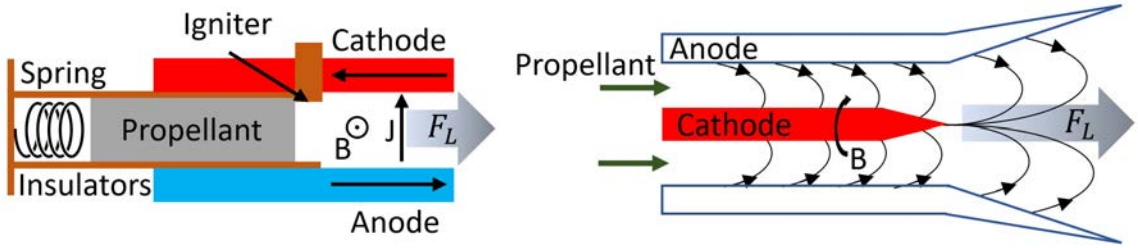

(a) PPT.

(b) MPD.

Figure 1.6: Schematic of two electromagnetic propulsion system.

1.2.3 Standardization

Since 1957 and Sputnik, the first satellite to be put in orbit ever, the space industry has drastically changed. For the first twenty to thirty years, space was one of the battle field of the cold war between the West and the East. At that time only economically and military powerful nations could afford to conquer space.

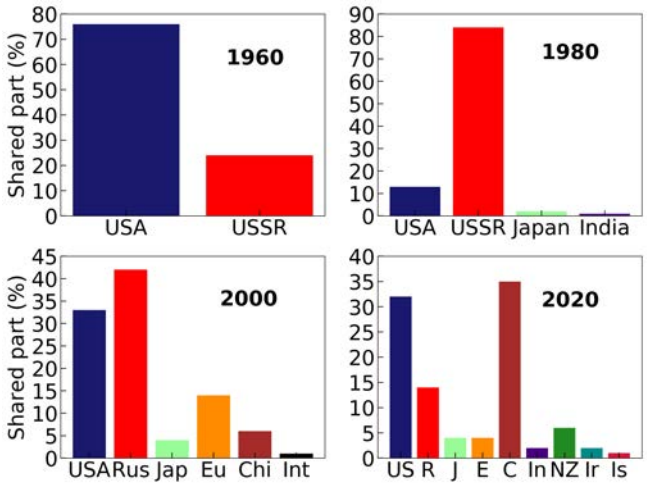

Figure 1.7: Market shares of launchers per country for 1960, 1980, 2000 and 2020. *Database source: Gunter's Space Page*

However, the cost in working force, raw material sources and technical challenges necessary to put one kilogram into orbit has completely changed in sixty years. To witness the evolution, launch capacities per country in 1960, 1980, 2000 and 2020 are plotted in figure 1.7. We see that during most of the second half of the twentieth century the rocketry technologies were in majority shared between the United States of America (USA) and the Soviet Union (USSR). In contrast, at the dawn of the twenty-first century until now, new states emerged and took their parts. In fact, in 20 years China succeeded to take close to 35% of rocket launch share market. Indeed, as the cold war ended in 1991, the economic domination of the USA and USSR weakened leaving room for others world powers to develop their space industry. The democratization of space is even more obvious when looking at figure 1.8. There, we see the repartition of number of satellite launched per world region and nation in 2020. Firstly, we observe that many nations have satellites in orbit despite the fact that they do not posses any launcher. The globalisation enhanced economic relation between states easing commercial agreement to put into orbit an object. Secondly, we observe that in contrast to observations made on figure 1.7, the USA held close to 80% of the total number of satellite launched in 2020, mostly due to the massive Starlink program deployment. Figure 1.9 to 1.10 help to understand the fast democratization of access to space and also the domination of the USA on the satellite market. In Figure 1.9 is plotted

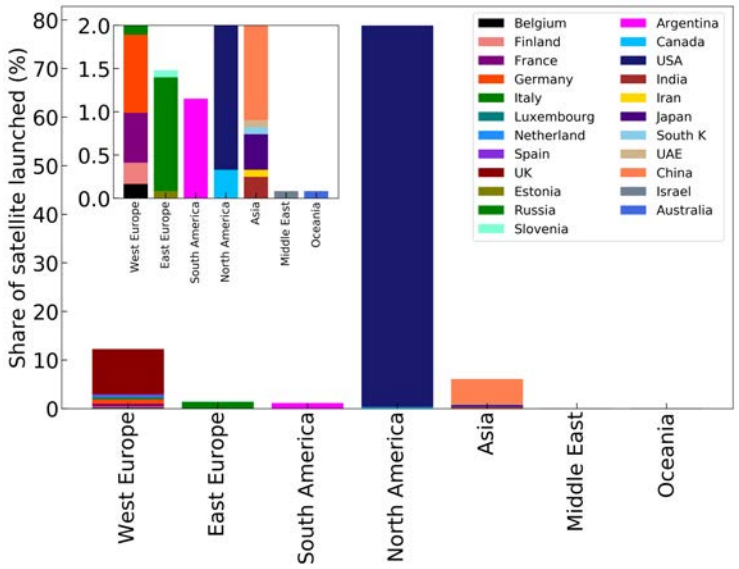

Figure 1.8: Market shares of satellites per region of the world in 2020. *Database source: Union of Concerned Scientists*

the evolution of number of launch from 1998 to 2020 as well as the orbit targeted. If looking at the total number of launch (black) we see that it has been increasing for the last twenty years. However, when looking at the orbit targeted we observe a decoupling around 2015. After that tipping point, the number of satellite sent to LEO (blue) increased drastically while those sent to other orbits (red) started to decrease. 2015 is the year where the company *SpaceX* proved the feasibility to recover the first stage of a rocket after its launch ,which was reused for the first time in 2017, decreasing drastically the cost of a ride. *SpaceX* is an American company who started to develop its own rocket in 2006 with a first success in 2008. Indeed, in the 2000s, space was not reserved to states any more and started to be widely used by private companies or for education purpose.

Such giant leap have been possible thanks to impressive technology achievements in electronics miniaturization and software programming. As a result, the space industry has completely changed its structure in trading large and costly satellites into several constellation-like small and cost-effective ones [21, 22]. This is referred as the New Space. Consequently, the use and type of satellite evolved as well as shown in figure 1.10 and 1.11. The first effect, as depicted by figure 1.10, of the New Space was to decrease the weight of satellite launched and

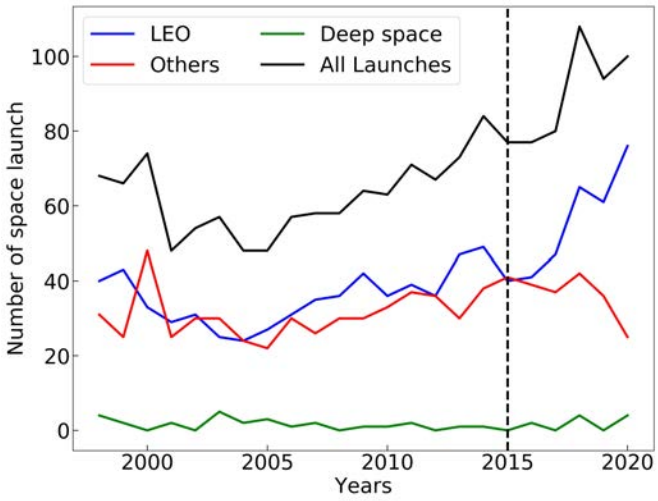

Figure 1.9: Evolution of the number of rocket launches and orbit targeted per year from 1998 to 2020.*Database source: Space Launch Report*

their life time [4]. The figure displays the averaged number of satellites launched, mass and expected lifetime per satellite from 2000 to the 1^{st} April 2021. In twenty years, with the largest change in the last ten years, the number of satellite launched increased by a factor 10 while their averaged mass and expected operation time dropped by 10 and 2 respectively. This allowed to increase the capacity for one rocket launch to put into orbit several satellites, and to set a record in 2021 with 143 satellite launched at once. Moreover, as they last less time in operation they must be replaced close to every 5 to 7 years assuring a constant production flow. This lead to the emergence of satellite constellations [7] with standards production criteria but also the multiplication of small launchers. For instance the London-based company *OneWeb* aims to send 650 hardware for its first generation and 7000 for the second. In the same way, *SpaceX* with its Starlink constellation plans on deploying 4425 satellites by 2024. Moreover, the use of orbits changed with the New Space as shown in figure 1.11. We observe that the satellite population launched in LEO soared since 2010s compared to MEO, elliptical and GEO orbit. We see that communication and Earth observation satellites are the main activities. In two years (2020 and 2021) more satellites were launched in LEO orbit than the sum of all launched from the last twenty years. LEO is cheaper to reach, space radiations are less harmful and data transmission is easier.

Therefore, due to the important yearly increase of satellites in constellation

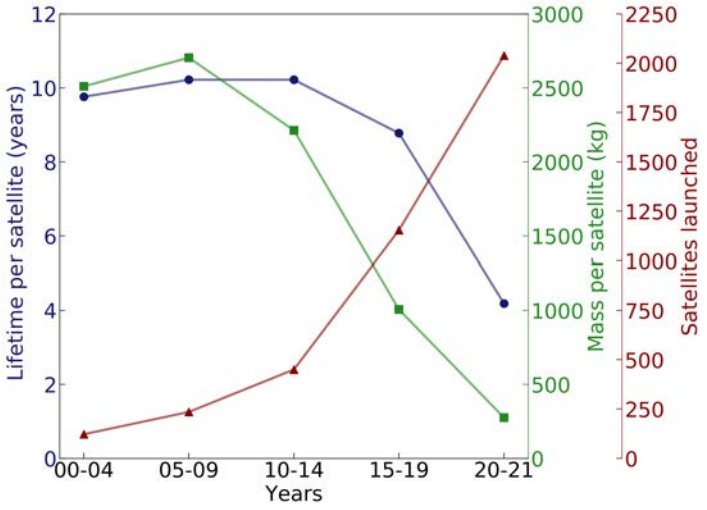

Figure 1.10: Evolution of the averaged mass at launch per satellite and their expected lifetime from 2000 to the 1st April 2021. *Database source: Union of Concerned Scientists*

and debris on this orbit coupled with strong atmospheric drag, the use of active manoeuvres control is a necessity. Electric propulsion systems are in this case the ideal candidates to fill the demand [23]. Nevertheless, most of the technologies developed were meant to be used on large and heavy satellite with power capacities of kW-range. The New Space with its NanoSats and SmallSats brings down the available power on-board down to few hundred watts. Therefore, the EP systems must be scaled down as well to meet satellite mass (100 - 300 kg) and power (< 200 W) requirements while keeping providing competitive total impulse.

The worldwide EP community spent a lot of effort in the last decade into R&D and fund-raising round to build start-up companies to commercialize their own product [26, 27, 28]. A list of companies working at providing EP systems with total system power below 200 W is given in table 1.1. We note that the majority were created in mid 2010s and, except some, most have been or are demonstrating their technology (IOD) in the 2020s. More importantly, we see that they cover a wide range of technologies (see section 1.2.2). Consequently, the propellant used and plasma properties like ion and electron densities, temperatures and energies differ as well as the thruster-spacecraft interaction. The European Space Agency with its European Cooperation for Space Standardization (ECSS) document has

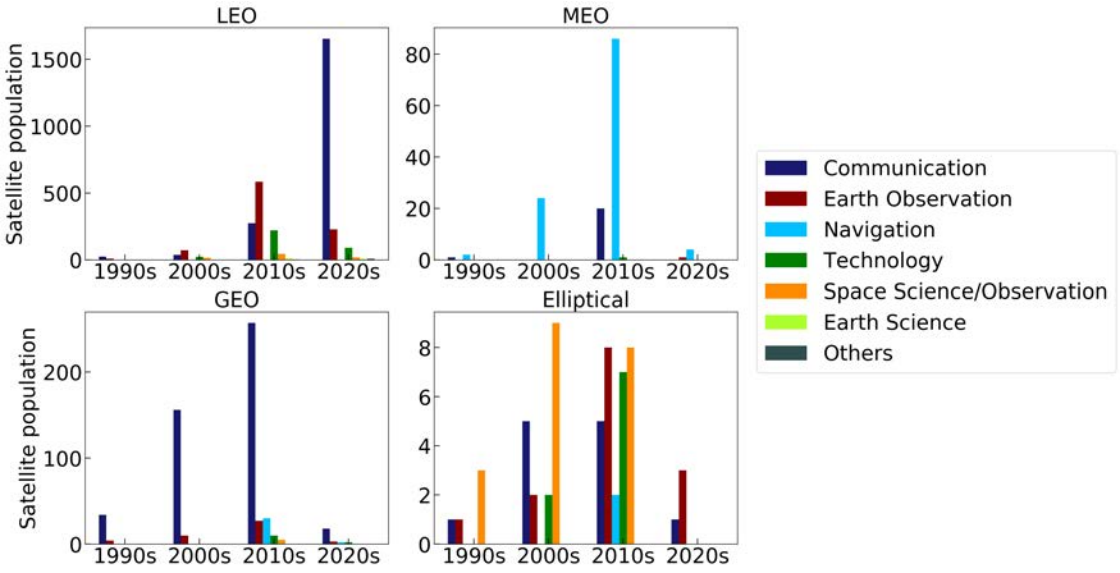

Figure 1.11: Evolution of the satellite population for LEO, MEO, GEO and Elliptical orbit and their use for the 1990s, 2000s, 2010s and 2020s. *Database source: Union of Concerned Scientists*

Table 1.1: List of low power (<200 W) EP systems available on the market

Company (date of creation)	Thruster name[1,2] / Technology	Technical maturity	System Power[1,2] (W)	Thrust[1,2] (mN)	Isp[1,2] (s)
	Europe				
Ariane Group (2015)	RIT µX / **RIT**	FM	50	0.05 - 0.5	300 - 3000
COMAT (1977)	PJP30 / **VAT**	DM	30	0.45	2500
ENPULSION (2016)	ENPULSION NANO[a],R3 & IR3 / **FEEP**	FM&QM&EM	8 - 40	0.001 - 0.350	2000 - 6000
	ENPULSION NANO AR3 / **FEEP**	EM	8 - 45	0.001 - 0.500	1500 - 4000
	ENPULSION MICRO[c] R3 / **FEEP**	FM	30 - 120	0.2 - 1.35	1500 - 6000
Exotrail (2017)	ExoMG-Nano-S[c] & L / **HT**	FM&EM	60	2.5	∼1300
	ExoMG-Micro-M+ & XL / **HT**	EM&EM	150	7	∼1100
Mars Space (2007)	PPTCUP / **PPT**	QM	2	0.040	600
	NanoPPT / **PPT**	EM	5	0.090	640
	Mini RF Ion Engine / **RF Thruster**	EM	19	0.850	2500
Morpheus (2018)	NanoFEEP / **FEEP**	DM	0.2 - 3	0.001 - 0.02	3000 - 8500
Space Electric Thruster System (2016)	ST-25 / **HT**	EM	100 - 180	5 - 11	1200
SITAEL (2010)	XR-50, XR-100 & XR-150 / **Resistojet**	FM	50 - 95	100 - 250	55 - 110
	HT 100 / **HT**	FM	120 - 350	6 - 18	1000 - 1600
Thrust Me (2014)	I2T5[b] / **Cold Gas**	FM	5-10	0.2	∼2600
	NPT30-I2[c] 1U & 1.5U / **GIE**	FM&EM	35 - 65	0.3 - 1.1	2400
	United State of America				
Accion System (2014)	TILE 2[c] / **Electrospray**	FM	4	0.04	1650
	TILE 3 / **Electrospray**	QM	20	0.45	1650
Applied Ion System (2019)	AIS-AHT1-PQ / **HT**	DM	10	0.02 - 0.05	500
	AIS-gPPT3-1C / **PPT**	EM	0.5	0.00022 - 0.0092	
Busek (1985)	BHT-100 / **HT**	EM	100	7	1000
	BHT-200 / **HT**	FM	200	13	1390
	BIT-1[c] / **RF Thruster**	EM	10	0.105	2250
	BIT-3[c] / **RF Thruster**	EM	56 - 75	1.1	2150
	BET-Max / **Electrospray**	NC	12 -14	0.0001 - 0.15	850 - 2300
	Micro Resistojet / **Resistojet**	NC	3 - 15	2 - 10	150
	BMP-220 / **PPT**	NC	3		
ExoTerra Ressource (2011)	Halo[b] / **HT**	QM	75 - 450	4 - 33	700 - 1500
L3Harris Technology (1890)	XIPS 8cm[d] / **GIE**	EM	100 - 300	10 -20	2500
Orbion Space Technology (2017)	Aurora / **HT**	DM	100 - 300	5.7 - 19	950 - 1370
T4i (2014)	Regulus[c] / **RF Thruster**	FM	20 - 60	0.25 - 0.65	650
	Russia				
Fakel[24] (1960s)	SPT-50 / **HT**	EM	225	14	860
	SPT-50M / **HT**	EM	225	14.8	930
	PlaS-34 / **HT**	EM	80 - 360	22	1300
	PlaS-40 / **HT**	QM	185 - 600	44	1880
	FG-34 / **HT**	DM	130 - 390	18	1360
	Japan				
Pale Blue (2020)	Water Resistojet[e] / **Resistojet**	FM	5 - 20	1 - 4	70 - 100
	Water Ion thruster[f] / **GIE**	QM	30 - 60	0.136 - 0.306	500 - 968
	South Africa				
Hypernova Space Technologies (2018)	Nano Thruster A[e] / **VAT**	QM	20	∼0.008 - 0.160	≥500
	Israel				
Rafael [25] (2002)	R-200EPS[f] / **HT**	DM	150 - 300	5 - 15	800 - 1200
	Australia				
Neumann Space (2015)	CT-PCAT[g] / **VAT**	EM	NA	NA	NA

[1] Source: https://satsearch.co/, [2] Source: https://www.satcatalog.com/
[a] IOD: 2018, [b] IOD: 2019, [c] IOD: 2021, [d] Flight heritage XIPS 25cm, [e] IOD: 2022, [f] IOD: 2021-2022, [g] In qualification

already started to implement guideline procedures for electric thruster testing. In theory, any thruster manufacturer must comply with test standards like vibration, thermal, radiation, shock or performance tests prior to commercialize its product.

1.3 Thesis scope and research content

1.3.1 Motivations

As a response to the need of low power systems enabling active and precise control of a spacecraft, electric propulsion emerged from laboratory to become a game changer in the New Space industry. The actual trend and previsions foresee a boom of EP demand for the next five to ten years. Few companies have already begun to provide their own solutions but most of the competitors will reach maturity in the coming years, and each will have their own system concept. Through the ECSS, rules start to be set to assure to satellite manufacturer and users that the selected propulsion system will comply with regulations. Nevertheless, some aspects are not yet considered for standardization and one of them is the thruster plasma, also termed plume or beam, characterization. The scope of this thesis is to start paving the way for plasma diagnostic standardization applicable to any type of EP systems. As presented in table 1.1 a wide range of electric thrusters from typical GIE and HT to FEEPs and electrosprays through PPTs or VATs are about to hit the market. As a result, most of the plume characterisation diagnostics proposed in the literature are either self-made or based on development made for a specific EP technology or/and in a given power range. However, decreasing the input power of the EP system impacts the plasma parameters. Indeed, ion densities can range from 10^{11} to 10^{18} m^{-3} with ion energies as low as a few electron-volts (eV) up to the keV-range. Moreover, the ionized propellant interactions with neutrals, electrons and material surfaces differ from one technology to another. Therefore, the development of tools which can be used universally to provide reliable information on plasma properties is necessary. Indeed, with accurate measurements key performance parameters of the EP system can be deduced such as thrust, specific impulse, beam deviation and divergence, total system efficiency and lifetime.

1.3.2 Content of the thesis

After defining how plasma physics is applied to diagnostic tools [29, 30] to characterize the plume of an EP system, chapter 2 describes the different techniques use by the EP community. There, detailed information is given on the electrostatic probe [31] family explaining their use, parameters that can be retrieved from measurements and pros and cons compared to other techniques and tools of the same category. To conclude, we present the probes selected in the frame of the thesis, namely the Faraday Cup and retarding potential analyser (RPA). Hence, this dissertation focuses on the measurements of ion current and energy.

Chapter 3 describes the three vacuum chambers used in this study as well as their corresponding acquisition system. Details about all Faraday cup designs are given afterwards. Finally, thorough descriptions of the electric thrusters included in this work are presented. The goal is to cover a wide range of ion current densities and energies as well as propellant and working principle. Therefore, a low power class Hall thruster, Radio Frequency Ion Thruster (RIT) and FEEP were chosen. The RIT will be discussed in appendix B. Preliminary studies already completed with the HT and FEEP are sum-up in section 3.3.1 and 3.3.2.

The effect of the probe geometry and dimensions on ion current measurements in the plume of the ENPULSION NANO FEEP [32, 33] laboratory unit are given in chapter 4. Moreover, ion induced electron emission yield for different current collector materials and geometries are presented. Eventually, the effect of the facilities used to conduct ion current measurements as well as the current emitter choice is discussed.

The plume of the ISCT200 [34] low power class HT is characterized in chapter 5. There, we study how the of the Faraday cup can influence the measured ion current. Moreover, we show which part of the ion collector cup (e.g. side walls, rear part) is the most exposed to ion impact and how this varies with the cup length. An alternative Faraday cup design is also introduced enabling the mitigation of particle deposition induced by the beam. Last but not least, the impact of the material and structure of the collector on the measured ion current is shown.

The last chapter of the thesis will gather all data presented to conclude whether or not an universal Faraday cup design is possible for completely different EP systems. Besides, operation of the probe for the various technologies is discussed. Finally, a preliminary study of a dual-mode probe concept is given enabling the measurement of the ion current density and energy for a fixed angular position and plasma conditions. The pros and cons as well as comparison with efficient Faraday cup and retarding potential analyser (RPA) are given based on experimental

results.

Due to delays and unexpected events in the thesis planning it was only possible to conduct partial analysis of the impact of the Faraday cup design when studying the ion beam from a low-power RIT, provided by the Europeans Space Agency (ESA). Nevertheless, the findings were judged relevant enough to be included in this Ph. D work, hence outcomes are described in Appendix B. There we detail the experiment apparatus and show ion current density measurements obtained different Faraday cup designs. First, we assess the impact of ion-induced electrons when using bulk aluminium versus a foam version. Then, we look at the impact of the probe length upon the recollection of ion-induced electrons. We compare ion current densities measure with a cup length of 50 mm versus 30 mm. Finally, we perform ion current density angular distribution measurement with probe aperture diameter of 7 mm and 3 mm to see if modifying the dimension of the probe entrance induces errors on the measured signal.

At the end of this dissertation several design recommendations and measurement method are proposed to operate a FC in the plume of a FEEP, a low power HT and RIT. Further studies shall be done to better characterize the effect of the distance of the probe from the thruster exit plan. Moreover, logically we would recommend to test our FC design upon other EP technologies with other different working principle (PPT, VAT, ECR) to expand the probe capacities.

Chapter 2

Plasma physics applied to electric propulsion diagnostics

Contents

2.1 Basic of plasma physics

On Earth the matter is mainly found in solid, liquid or gas state. However, at larger scale (e.g. Universe) these three states only account for 0.1% of the matter, the rest being made of plasma. This is known as the fourth state of the matter. It is reached when the latter is heated to high temperature. When heated up cold matter undergoes a vaporisation, then a dissociation and finally a so-called ionisation process. The latter results in a flow of free charged particles composed of ions and electrons. A plasma can also form when the neutral gas is subject to energetic electron bombardment or energetic photon absorption. Within a plasma coexist a trend to disorder, with thermal agitation, and a trend to order induced by the dynamic and collective aspect of the Coulomb interaction. The time scale is different for both phenomena and a trade-off is characterized by a plasma parameter equivalent to the ratio of the Coulomb interaction energy (e.g volume density of the electrostatic potential energy) to the measurement of the thermal agitation (e.g. volume density of the mean kinetic energy). It is used to distinguish ideal or kinetic plasma from highly correlated plasma, where disorder (≤ 1) or order ($\gg 1$) dominates, respectively. Plasmas studied in the scope of this thesis, and the majority of laboratory, industrial and natural ones, belong to the first category where the plasma parameter is well below 1. Nevertheless, these two trends allow the plasma to remain ionised creating the conditions preventing the separation of charges. This state of quasi-neutrality holds only for a given distance or volume L or L^3 and time scale T. For any dimensions below L or L^3 and motions faster than T charges can start to separate and an electric field can appear. The quasi-neutrality of a plasma can be written as:

$$\varepsilon \equiv \frac{n_e - Zn_i}{n_e + Zn_i}, \tag{2.1}$$

where n_e and n_i are the electron and ion density, respectively and Z the ionisation state. If $\varepsilon \ll 1$, the plasma is considered quasi-neutral and non neutral if $\varepsilon \leq 1$. If not specified, quasi-neutrality is implied for all plasma studied in this thesis work. The time and dimension scale are universal for all plasma and are defined as the Debye length λ_D and the plasma frequency ω_p.

2.1.1 Scale length

Mean free path

The mean free path is defined as the averaged distance travelled by a particle between two consecutive collisions. It reads:

$$\lambda_m = \frac{1}{n_{nn}\,\sigma_{nn}}, \tag{2.2}$$

where n_n is the number density of targets and σ_{nn} the collisions cross section for a given physical process (momentum exchange, ionization, dissociation...). The cross-section depends upon the kinetic energy of the particles involved in the process of interest. The number of collision per second f_c is the reciprocal of the mean time between two collisions:

$$f_c = \frac{v_n}{\lambda_m}, \tag{2.3}$$

where v_n is the mean velocity. In the case of electric propulsion studies, the mean free path is often a lot larger than the vacuum chamber sizes ($\sim$ 1 to 2 m).

Debye length

The Debye length λ_D characterizes the region where the quasi-neutral hypothesis is valid and the screening phenomenon holds. It reads:

$$\lambda_D = \sqrt{\frac{\varepsilon_0 k_b T_e}{n_e e^2}}, \tag{2.4}$$

where ε_0 is the vacuum permittivity, k_b the Boltzmann constant, T_e and n_e the electron temperature in Kelvin and density in m^{-3} and e the elementary charge. Let us consider a quasi-neutral plasma implying $n_e = n_i$. Ions are supposed to have a zero velocity as they are heavy since $m_i \gg m_e$ while electrons have a non-zero velocity. Therefore, electrons will tend to break neutrality as they move away from the ions. This creates an electric field which counters the electron flow pulling them back towards the plasma bulk. The distance over which electrons can move is the Debye length. In the case where $T_i > T_e$ equation 2.4 becomes:

$$\lambda_{D_{T_i>T_e}} = \sqrt{\frac{\varepsilon_0}{e n_e}\left(\frac{\hat{T}_e \hat{T}_i}{\hat{T}_e + \hat{T}_i}\right)}, \tag{2.5}$$

with $\hat{T}_e = k_b T_e / e$, the electron temperature in electron-volt. Also if T_i=T_e, it reads:

$$\lambda_{D_{T_i=T_e}} = \sqrt{\frac{\varepsilon_0 \hat{T}_e}{2 e n_e}}. \tag{2.6}$$

2.1.2 Plasma Frequency

The plasma frequency or plasma pulsation characterizes the rapid oscillations of the electron density, the so-called Langmuir wave. From another perspective it characterizes the time scale of the back and forth motion of the electrons around the ions governed by the Coulomb force as described above. Considering an electrically neutral plasma in equilibrium with cold ions, the plasma frequency ω_p reads in rad/s:

$$\omega_p = \sqrt{\frac{n e^2}{\varepsilon_0 m_e}}. \tag{2.7}$$

This time scale is also associated to the Coulomb burst of a non-neutral plasma such as a beam of charged particles. Without neutrality charged particles inside a beam tend to diverge due to the electrostatic repulsion effect. If the beam is slow, charge neutralization is needed to study them for a time scale larger than ω_p^{-1}. However, if the beam is fast enough the Laplace force, induced by the magnetic field generated by the beam itself, mitigate the Coulomb burst and induces a pinch effect which tend to gather particles which share the same current sign. In this thesis two EP systems, the FEEP (section 4) and RIT (B) will be operated as a simple ion beam without electron source or neutralizer.

2.1.3 Plasma sheath

A plasma sheath appears near a surface to preserve the quasi-neutrality inside the plasma by regulating the flux at its boundary. The transition from the plasma bulk to the sheath is smoothed by a pre-sheath region as exemplified in figure 2.1. The pre-sheath makes sure that the ions have a velocity near the Bohm velocity (v_B) when they enter the sheath [2]. Inside the sheath the potential drops to accelerate ions and electrons are at equilibrium between thermal agitation and electric deceleration. It is important to note that the dimension of a sheath depends on the plasma parameters and surface properties. It is usually of the order of λ_D. In the case of electric thruster plume studies the sheath can be either floating, no potential is applied to the surface, or at a high voltage (s_{hv}), when $|V_p|>V_f$ with

V_p the potential applied to the surface and V_f the floating potential for which the ion current I_i equals the electron current I_e. The work presented in this manuscript only deals with high voltage sheaths. For instance when the surface collection is biased negatively only ions are collected and electrons are screened. The sheath is therefore space charge limited and the Child-Langmuir law is needed to determine s_{hv} [29]:

$$s_{hv}^2 = \frac{4\varepsilon_0}{9}\sqrt{\frac{2e}{m_i}}\frac{|V_p|^{3/2}}{j_i}, \tag{2.8}$$

with j_i the ion current density at the entrance of the sheath and $j_i = j_B$ the Bohm current density. From the current conservation at the sheath entrance we have:

$$j_i = j_B = hen_e v_B = hen_e \left(\frac{kTe}{m_i}\right)^{1/2}, \tag{2.9}$$

with h the ratio between the density at the sheath entrance and the density in the bulk plasma. It equals $e^{-0.5}$ [35, 29]. Inserting equation 2.9 into 2.8 and using equation 2.4 for the Debye length one finally obtains:

$$s_{hv} = \frac{1}{3}\sqrt{\frac{2}{h}}\left(\frac{2|V_p|}{\hat{T}_e}\right)^{3/4}\lambda_D. \tag{2.10}$$

The sheath, and therefore the collection area, expands as we increase the absolute value of the voltage at the surface. Several models like, the Sheridan's or Johnson's one [29] are used when studying the plume of an EP system with electrostatic probe types to mitigate the effect of the collection area increase, see section 2.2.2. However, it has been shown that these model are not reliable in all circumstances [30]. Therefore, it is preferable to use different probe architecture to mitigate or completely suppress the sheath effect as it is explained in section 2.2 and 2.3.

2.1.4 Collisions

Within a plasma collisions between particles occur. They are of two types i) elastic and ii) inelastic where the internal state of particles are modified after the collisions. The latter is broached in this section.

Ionization

Ionisation of a gas can occur when there is a collision between an atom or a molecule with a neutral, energetic electrons or photons, during charge exchange

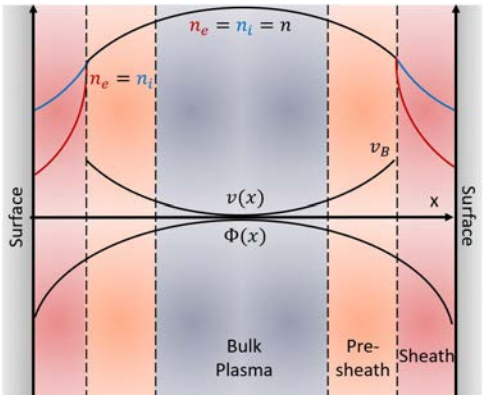

Figure 2.1: Schematic of pre-sheath and sheath formation at the edge of a plasma near a surface [2]. Due to the high electron velocity, the electron density decreases faster than the ion density, which creates an electric field to preserve quasi-neutrality.

collisions or by means of field effect. In electric thruster plasmas electron impact ionization is the most frequent mechanism. The electron energy must be higher than the first ionisation energy (E_I) of the gas. During the collision event, one electron is ripped off the neutral particle. The collision product results in one ion and two electrons. We use the particle ionization cross section to express the probability of ionization to happen. In the case of Hall thrusters operated with xenon this cross section is of the order of 3 to 4×10^{-20} m^2 [36] when considering electron energy between 20 and 40 eV. The neutral background pressure inside the vacuum system follows standard gas flow $P = n_0 kT$. The variable P is the pressure in Pascals, n_0 the neutral density in m^{-3} and k is the Boltzmann's constant ($1.38\times10^{-23}\, m^2.kg.s^{-2}.K^{-1}$). Considering the pressure during operation of the Hall thruster (10^{-5} mbar, see chapter 3) and the temperature in the vacuum chamber which is assumed to be near room temperature we obtain a background density in the range of 10^{18} m^{-3}. To compute the mean free path $\lambda_{m_{ionisation}}$ for ionization we use:

$$\lambda_{m_{ionisation}} = \frac{1}{n_0 \sigma_{ionisation}}. \tag{2.11}$$

Equation 2.11 gives a mean free path for ionisation close to 33 m, a value a lot larger than the facilities and probe dimensions used. However, note that locally the neutral background pressure can be 1 or 2 order of magnitude larger (e.g. in the thruster core) and electron energy higher. Finally, the first ionization energy

of xenon is 12.12 eV, the second is 21.21 eV and the third is 32.12 eV.

Charge exchange

In the case where a fast ion collides with a slow neutral a charge exchange (CEX) collision can happen when the neutral and the ion share the same core, e.g. Xe with Xe+. A CEX collision produce a fast neutral and a slow ion. This ion-neutral interaction is thoroughly studied in the case of plasma created by Hall thrusters or gridded ion engine. With GIE the neutral density at the exit of the ionization chamber is large. Hence, CEX collisions occur between grids. In this case, these fast neutrals are responsible for grid pulverization which reduces the thruster lifespan. In typical Hall thrusters a large amount of neutrals leave the channel which lead to numerous CEX collision events. Hence, slow ions move towards the plume edge, the so-called wings (>65°), as shown in figure 2.2. In this region of the plume the presence of slow ions is also due to diffusion process (e.g. momentum exchange). CEX collisions are highly dependent on the background pressure and on the particle density during the experiment [37, 38]. The equation that governs CEX collisions reads:

$$Xe^{+}(fast) + Xe(slow) \rightarrow Xe(fast) + Xe^{+}(slow). \tag{2.12}$$

We consider the averaged neutral density to be $10^{18}\,\mathrm{m}^{-3}$. To compute the mean free path $\lambda_{m_{CEX}}$ for the charge exchange collisions we use:

$$\lambda_{m_{CEX}} = \frac{1}{n_0 \sigma_{CEX}}, \tag{2.13}$$

with σ_{CEX} the charge exchange cross section for xenon. Based on data and formula given in [39] we find σ_{CEX} to be equal in average to $65\times10^{-20}\,\mathrm{m}^2$. As a result, equation 2.13 gives a mean free path between 150 cm, depending on the temperature and ion energy considered. However, we expect and assume to have local neutral densities 1 or 2 order of magnitudes higher in the probe (due to the closed geometry) and thruster core, respectively. As a result, we could have charge exchange mean free path between 15 cm and 1.5 cm.

2.1.5 Surface interaction

Last but not least, we have already mentioned how a plasma tries to keep its equilibrium state close to a surface (section 2.1) as the population of electrons and

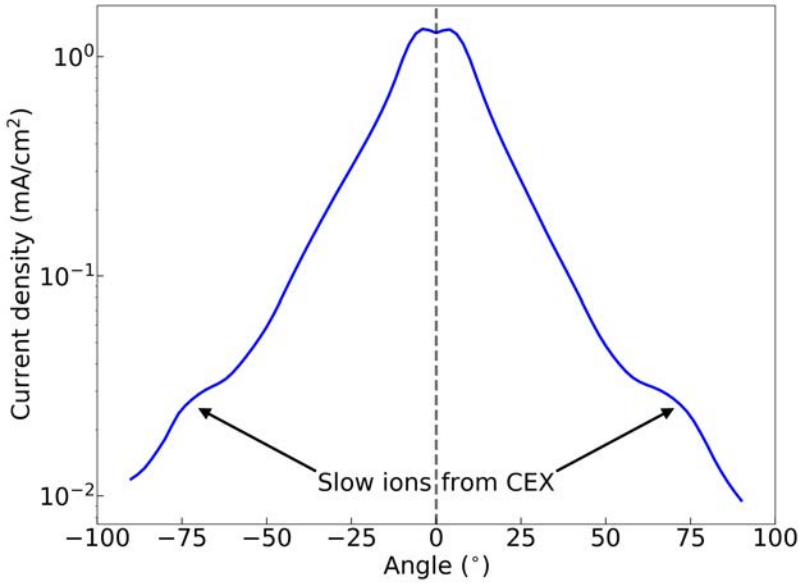

Figure 2.2: Ion current density angular distribution measured by a Faraday Cup in the plume of the ISCT200 Hall Thruster. The thruster is operated with xenon at 0.66 A, 250 V and 0.97 mg/s.

ions drops due to their collection. A charged particle can be either absorbed, scattered or neutralized when it hits a surface. It also can induce secondary electrons and degrade the surface material via sputtering. In like manners, neutral particles can be scattered or generate secondary electron as well. The particle-surface interaction is detailed in the following sections.

Introduction to SRIM software

Throughout this manuscript the software SRIM (Stopping and Range of Ions in Matter) is punctually used to better understand some experimental outcomes. SRIM includes a group of programs which calculate the stopping and range of ions into matter (e.g. ion implantation). A mechanical treatment is used for ion-atom collisions where projectile atoms are termed "ion" and target atoms are identified as "atoms" [6]. Plots displayed in chapter 5 are generated with the TRIM (Transport of Ions in Matter) program. TRIM allows to define the projectile and target species. The depth of the target as well as the number of particle to be included in computation iteration can also be defined by the user as showed in figure 2.3. We only used the "Monolayers Collision Steps / Surface Sputtering" type of calculation as sputtering yield is the information desired in our study case. This type of calculation gives also access to energy loss from the projectile to the target. This parameters gives information on the energy transferred by the projectile to the target materials which is subsequently converted into heat. The transfer can be direct from the projectile to the target electrons, hence it is labelled "IONS" in the program output. The energy can also be transferred after several collisions into the target body and therefore the loss will be labelled "RECOILS" in the program as it results from a recoiled target atom. More detailed information on interpretations are given in chapter 5.

Neutralization

When an ion reaches a surface it can be neutralized by recovering an electron from the surface. It results in a neutral which is either scattered until absorbed or directly absorbed, as illustrated in figure 2.4.

Scattering and sputtering

Ion-surface interaction can lead to scattering and sputtering effects, see figure 2.4. The former corresponds to the re-emission in random direction with a random

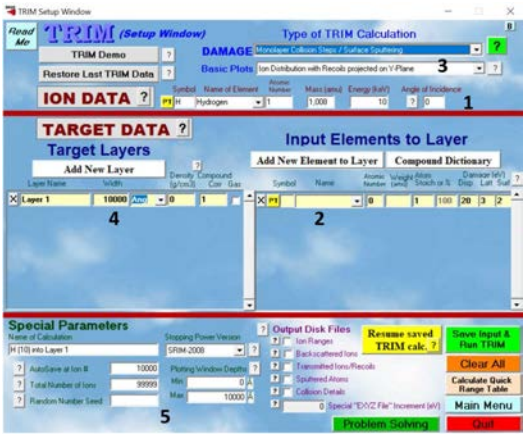

Figure 2.3: TRIM program interface. 1) projectile specie information, 2) target specie information, 3) type of calculation, 4) definition of the target layer width and 5) total number of projectile to be run.

velocity of the incoming ion. In contrast, sputtering occurs when the ion energy is greater than the binding energy of the surface material. A neutral particle is knocked out from the surface and emitted. This process tends to deteriorate and decrease the efficiency of plasma diagnostics physically inserted in the bulk plasma. The coefficient Υ_s is used to measure the sputtering yield of a material bombarded by a specific species, it reads:

$$\Upsilon_s = \frac{N_o}{N_i}, \tag{2.14}$$

where N_o is the number of particles ejected from the surface and N_i the number of incident ions. This phenomenon will be broached in section 4 and 5. In this work, the software *SRIM* [6] (Stopping and Range of Ions in Matter) is used to compute the sputtering yield of aluminium, steel, carbon, molybdenum and tungsten when bombarded by energetic xenon and indium ions. It is important to note that during the sputtering process the resulting neutrals emitted from the material have a certain probability to reach other surfaces. During this second collision the neutral can rip off an electron from the material surface leading to a current variation. The same phenomenon can happen with electron or ion-surface collisions. This process is known as secondary or ion-induced electron emission (SEE or IIEE) and can lead to very large perturbations in the acquisition of the ion current in the beam of an EP system as presented in section 4.1.

Ion induced electron emission

When a neutral or charged particle reaches a surface it can induce the emission of an electron by converting its kinetic or potential energy [40, 41, 42]. Potential electron emission (PEE) results from electron excitation due to conversion of internal energy while kinetic electron emission (KEE) occurs in the presence of kinetic energy transfer during collisions. The main difference is that PEE is independent of the incoming ion energy and is driven by the target material work function (ϕ), which is of the order of a few electron-volts for most materials, while KEE strongly depends on the ion energy. We use the secondary electron yield, also known as the second Townsend number [2], to quantify the number of electron emitted by incident ions, it reads:

$$\gamma_{EE} = \frac{Number\,of\,emitted\,electrons}{Number\,of\,incident\,ions}. \tag{2.15}$$

Translated in terms of current it becomes:

$$\gamma_{EE} = \frac{I_{EE}}{I_{i_m}}, \tag{2.16}$$

with I_{i_m} the ion current and I_{EE} the induced electron current. In practice when the ion is collected by a probe and an electron is ripped off of the collector surface the absolute value of the measured current is artificially increased. Therefore, we have $I_{EE} = I_{i\&EE}$ - I_{i_m} where $I_{i\&EE}$ is the ion measured current including the current rise induced by EE. Equation 2.16 gives:

$$\gamma_{EE} = \frac{I_{i\&EE} - I_{i_m}}{I_{i_m}}. \tag{2.17}$$

Note that the EE yield depends on the ion energy and incident angle and the material properties and structure. We will see in sections 4.1, 5.2 and annexe B that γ_{EE} can lead to large deviation from the real ion current when studying the plume of an EP system. All above mentioned plasma parameters can be measured, retrieved or calculated thanks to tools call plasma diagnostics presented in the next section.

2.2 Plasma diagnostics

Several techniques exist to retrieve plasma parameters in the plume of an electric thrusters. The two main category are laser-based techniques and electrostatic probes.

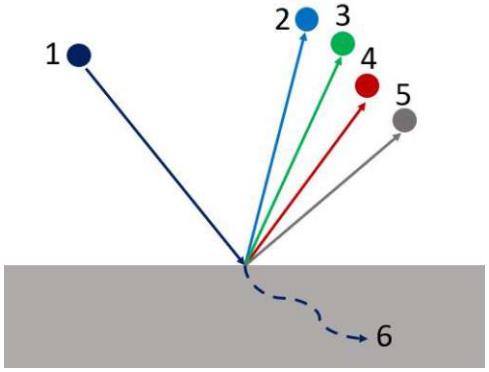

Figure 2.4: Schematic of possible output from ion-surface interaction. 1) incident ion, 2) Scattered ion, 3) Neutralization and neutral ejection, 4) induced electron emission, 5) Sputtered surface material and 6) absorption or displacement.

2.2.1 Laser-based plasma diagnostics

The most used laser-based plasma diagnostic is the so-called Laser-induced fluorescence spectroscopy (LIF). It is a non-intrusive technique which can measure particle temperature, detect species population and determine the velocity of particles along the laser beam direction [43]. The principle of LIF relies on the Doppler effect. A laser beam is tuned to excite an optical transition of a given atom, molecule or ion and the fluorescence light emitted during the relaxation process (de-excitation) is captured with a photoreceptor. It is extensively used to measure the ion velocity distribution function (IVDF) inside a Hall Thruster plume [44, 45]. It spotlighted that for ISCT200 thruster series the most probable ion group is accelerated up to 10 or 15 mm downstream of the thruster exit plane before the IVDF stabilizes. It showed the interaction between ion groups that originate from the opposite side of the thruster channel. Finally, it brought new evidence of the presence of CEX collision events in the near-field region of the thruster by measuring ions with a very low velocity. The electron temperature can also be retrieved indirectly from LIF measurements however, this approach lacks accuracy and it is complex and cumbersome compared to more classical tools like heated emissive, planar or Langmuir probes [46].

More recently, incoherent Thomson scattering, a diagnostic well-known in the field of plasma fusion [47, 48], has been implemented to measure electron properties in an electric thruster plume [49, 50]. In contrast to fusion plasmas, elec-

tric thrusters create a low temperature plasma resulting in a low plasma densities ($10^{10}\,\mathrm{cm}^{-3}$), which makes the acquisition of the scattered signal very challenging. However, when it is operated with success [51], the diagnostic is advantageous as it is non-intrusive preventing plasma perturbation during measurements. Other optical diagnostic tools,that do not rely on the use of lasers do exist like for instance optical emission spectroscopy and interferometry but these techniques are not much applied in the EP field to retrieve plasma parameters and ion properties. Overall, laser-based plasma diagnostics are advantageous because they do not disturb the plasma during data acquisition and enable to study plasma behaviour in the near-field region of an EP system , which remains infeasible with probe techniques such as electrostatic probes. However, they require expensive optical components, complicated setup and optical train and skills and experience to being properly used. Moreover, they are only efficient for a certain range of plasma density and therefore, cannot be used on very low density plasma as in the case of FEEP or electrosprays. Consequently, they are ideal for pure scientific work but unsuitable for plasma diagnostic standardization applicable to a large range of EP systems [46, 50].

2.2.2 Electrostatic probes

Electrostatic probes rely on the immersion of a conductive material, called electrode, into a plasma or a beam of charged particle. The ion and electron properties within the plasma or beam can be retrieved by simply applying a voltage on the electrode. The measured current, which can be either from ion or electron depending on the polarity of the applied voltage, is then processed to access plasma parameters as well as thruster performances. This category of plasma diagnostics is widely used in the EP community because it is simpler to build and implement than laser-based tools. Besides it is cost effective while still providing accurate outcomes and it can be used to study a wide group of electric thruster discharges and beams. The main drawback of this technique is that the current collector (the electrode) is directly in contact with the plasma. Therefore it induces perturbation caused by plasma-surface interactions [52], see section 2.1. Electrostatic probes are rarely operated in the near-field region of electric thrusters due to the high flux at stake there. Therefore, they are mostly used to study the far-field region.

Many different types of probe belong to the electrostatic category. Some provides more reliable information while others enable to access different plasma parameters. I propose to categorize the various designs in two distinct families i) those consisting in directly measuring a current and ii) those using a particle

selection process based on either their energy or the velocity before collecting the charged particles. Information about probe design is abundant in the scientific literature [53, 54, 55, 56, 57, 58, 59, 60, 61, 62, 31, 63, 64, 65] therefore, I will only describe probe designs relevant to the work presented in this dissertation.

Direct current measurement

Langmuir probes (LP) are the most common tool to measure basic but crucial plasma parameters (section 2.3.1). A voltage sweep is applied to the collecting part of the probe to measure the ion current and electron current. The current-voltage (I-V) curve is post-processed to retrieve plasma parameters such as the ion and electron density and temperature nn_i, T_i, n_e, T_e), the plasma potential (V_s) and floating potential (V_f) [66]. An ideal I-V curve is displayed in figure 2.5. Note that typical I-V curves available in the literature plot the ion and electron current as negative and positive values, respectively (see section 2.1.5). Nevertheless, to be consistent with the physical charge state of an ion and electron but also to ease comprehension and visualization, all ion and electron currents in this dissertation are displayed as positive and negative, respectively.

The first part of an I-V curve is called the ion saturation current. Theoretically, when the voltage applied to the probe (V_p) is negative all electrons are repelled and only ions are collected. However, in reality this signal is rarely constant and the ion current increases as V_p gets more negative. This is a consequence of the sheath effect artificially increasing the collecting area. Moreover, if not recollected, ion-induced electron emitted add another bias to the measured current (section 2.1.5). When V_p is getting close to positive values, an electron current starts to be collected. At I = 0, $I_i = I_e$ and the corresponding voltage bias is the floating potential V_f. The I-V part where only electrons are collected by the probe is the electron saturation current. There, in reality, the curve grows slowly as well due to the expansion of the sheath. The part measured between the ion and electron saturation current is the transition region. There, electrons are still being partially repelled as long as the probe voltage is lower than the plasma potential (V_p<V_s). Once V_s is overtaken the random thermal electron flux is entirely collected. V_s corresponds to the "knee" observed before entering into the electron saturation region. The method to obtain the plasma parameters is described in section 2.3.1. The ion current is of great interest for electric thruster plasma studies because thruster performance parameters, like thrust, depends mostly on it. Unfortunately, I_i is difficult to retrieve as the measured current can be affect by plasma-surface interactions.

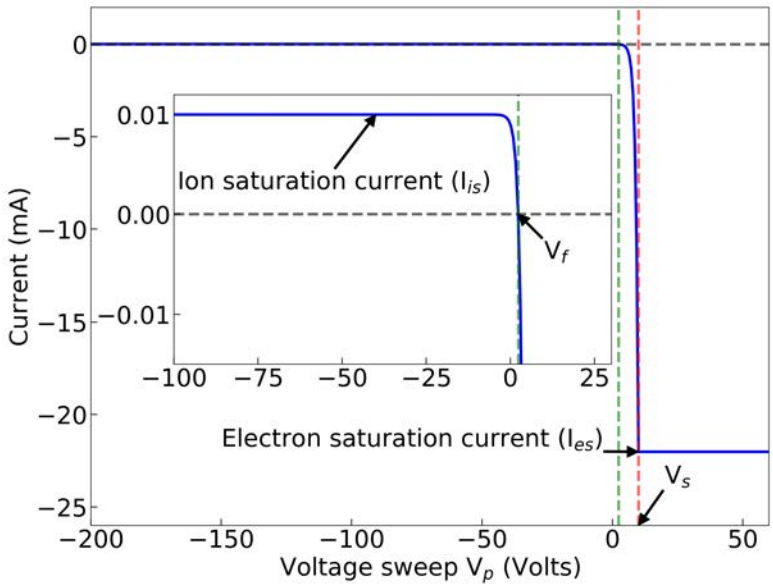

Figure 2.5: Ideal I-V curve measured with an electrostatic probe (Langmuir, planar probe or Faraday cup).

A first approach to mitigate the perturbation is to use mathematical models and implement them during I-V curve post-processing. The most used models are the orbital-motion-limited theory [67], Bernstein-Rabinowitz-Laframboise (BRL) theory [68, 69] and the Allen-Boyd-Reynlds (ABR) theory [70, 71]. Each models set their own initial conditions and hypothesis making their application difficult for a general case study. A second approach consists in improving the probe geometry to minimize the sheath expansion during ion collection. Therefore, classic cylindrical Langmuir probes with a simple wire as collector evolved to a planar probe design. Using a planar surface ease the current acquisition and post processing. Nevertheless, pure planar probes still need mathematical models to deal with the sheath effect, although minimized compared to a cylindrical probe. A technique is to install a conductive ring, called guard ring, around the collector surface separated by a very thin insulator to minimize the sheath expansion. The diameter of the insulator depends on the plasma conditions. When the collector and the guard ring are biased to the same potential the sheath is supposed to be flat on the top of the collector. Consequently, the plasma sheath is uniform and does not expand as $|V_p|$ increases. This requires to have a guard ring much larger

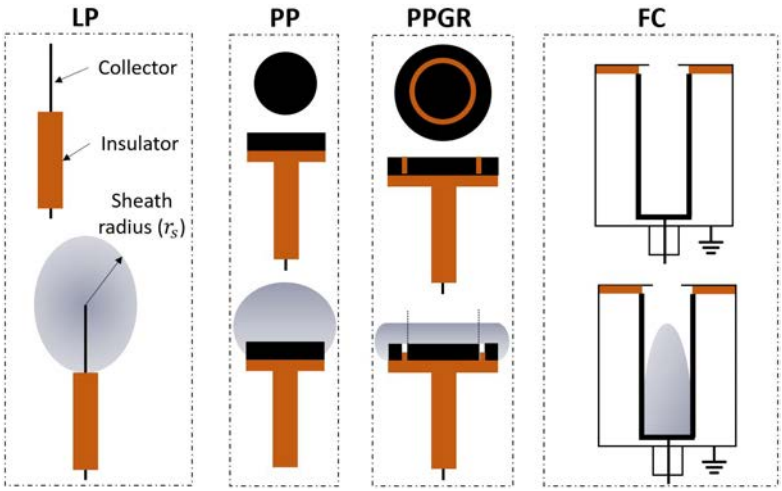

Figure 2.6: Drawing of a cylindrical Langmuir probe (LP), planar probe (PP), planar probe with guard ring (PPGR) and Faraday cup (FC). An illustration of the sheath expansion is displayed as well for each probe.

than the plasma sheath to prevent edge effect to perturb ion trajectory [72, 30]. One side effect is the increase in plasma-surface interaction (section 2.1). Moreover, the gap between the guard ring and the collector is directly exposed to the ambient plasma and therefore, is sensitive to particle deposition. Even with ingenious design, after a long operation time the formed layer reaches a threshold thickness short-circuiting both electrodes. The optimal way to minimize or even suppress change in size of the collecting area is to trap the ions in a close system so the sheath cannot expand, as illustrated by figure 2.6. This is how a Faraday cup works. The collector is a cup with the open side directed towards the plasma. The cup is encapsulated into a grounded housing to avoid interaction with ambient plasma. The collecting area is defined by the housing orifice diameter (d_a) which must be the smallest size of the system ($d_a < d_{cup}$). When properly designed a FC can accurately measure an ion current providing meaningful insight on the thruster performance envelop. Therefore, this probe type was chosen to be optimized and standardized in order to converge toward an universal tool to be used for different plasma thruster beams. More details about the tested FC design are available in section 3.2.

Energy selection

A retarding potential analyser (RPA) working principle is similar to those mentioned in the previous section except that ions go first through an energy filter before being collected. In this manner the ion energy distribution inside the electric thruster beam can be retrieved. A classic retarding potential analyser is made of four successive grids perfectly aligned and a collector encapsulated into a grounded housing. The first grid or gate electrode (GE) is here to protect the incoming particles to be disturbed by the ambient plasma. Therefore, it is either left floating or connected to ground. The second grid or electron repeller electrode (ERE) is biased negatively. It is used to repel primary electrons of the plasma. The third grid or ion repeller electrode (IRE) is here to select ions according to their kinetic energy. A positive voltage is applied and only ions with energy (E_i) greater than eV_{IRE} can go through. The grid standing in front of the collector also called electron suppressor electrode (ESE) is negatively biased. It redirects the ion-induced electron from the collector so they can be recollected. The collector is usually set to ground potential or slightly biased negatively to repel induced electrons emitted the grids. To build a RPA, thoroughly theoretical study must be conducted beforehand as the overall design depends on the plasma parameters. A vast documentation exists giving guidelines to determine the grid mesh size, the distance between the grids, the number of grids, the type of material to use [73, 53, 74, 75]. I will give here a summary of the based formula for designing an efficient RPA. This theoretical approach has been followed for the RPA used in section 6 with a FEEP and Hall effect thruster.

The distance between grids, especially with ERE and IRE is of great importance. Indeed, once primary electrons are screened only ions remain in the region between ERE and IRE giving rise to space charge effects (SCE). The maximum distance (x) between these two grids can be found as a relation with the most probable ion energy E_{max} [74]:

$$x \leq \left(\frac{4\varepsilon_0 E_{max}}{9e^2 n_i} \right)^{1/2}, \tag{2.18}$$

Moreover, if x is too large electrostatic lens effect can occurs deviating ions from their trajectory and preventing them from reaching the collector. To avoid this, x should be small compared to the mesh size. Another equation gives the upper limit between these two grids as a function of λ_D, $\hat{T}_e$ and the potential difference

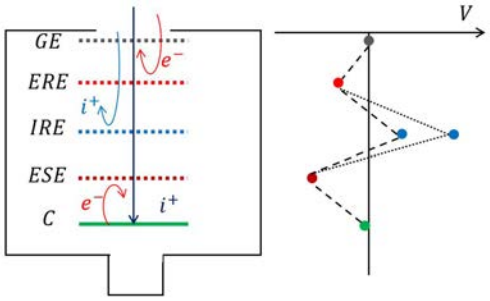

Figure 2.7: Schematic of typical RPA design with four grids. GE shield the probe from the ambient plasma, ERE repeal primary electrons, IRE select ions based on their energy and ESE pushes IIEE back to the collector.

between ERE and IRE ($V_{ERE-IRE}$) [75]:

$$x \leq 1.02\lambda_D \left(\frac{V_{ERE-IRE}}{\hat{T}_e} \right)^{3/4}. \tag{2.19}$$

Moreover, the energy resolution of the RPA depends on the grid distance as follow:

$$\frac{\Delta E}{E} = \frac{1}{x} < 10\% \tag{2.20}$$

If x is too large a build-up of positively charged ions can form caused by ion-neutral interaction leading to a potential hill. If it becomes larger than the voltage applied to the grid itself some ions can be pushed back which would decrease the value of the most probable energy.

Regarding the inlet aperture, d_a should be smaller than λ_D. To set the grid dimensions equation 2.21 can be used to find the balance between the mesh hole diameter d_m and the distance between them r_m [76, 77]:

$$0.1 < \frac{r_m}{d_m} < 1. \tag{2.21}$$

A typical I-V curve is displayed in figure 2.8. The measured ion current (red, left) is displayed along with its first derivative dI/dV (blue, right). Once the retarding potential applied to IRE overtake the ion energies the measured ion current drops until all ions are completely screened. The corresponding peak of the ion energy distribution function is referred to as the most probable energy (E_{max}). In this particular case the thruster is set to a discharge voltage U_d of 350 V, the peak,

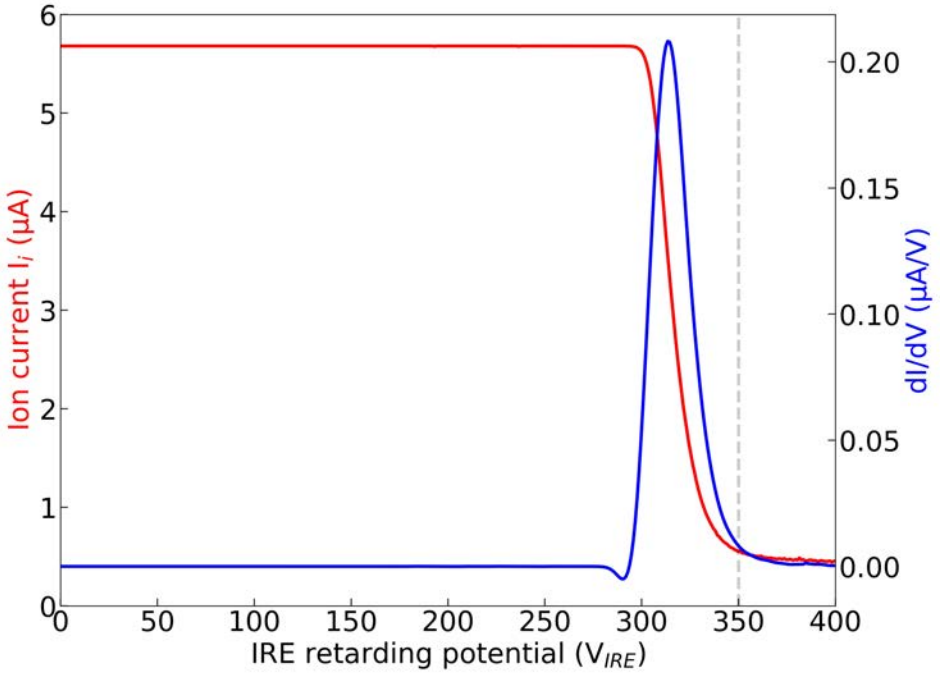

Figure 2.8: I-V curve and first derivative of the ion current acquired with a RPA on the ISCT200 Hall thruster axis at 26.6 cm. The thruster fires at $I_d = 0.66$ A, $U_d = 350$ V (dashed line), 10.4 mg/s and a Cathode Reference Potential (CRP) at -6.75 V. The maximum peak corresponds to the most probable energy E_{max}.

so E_{max}, is observed at 314 V. The shift towards lower energy, in the case of HT, is well-known and can be attributed to ionization, plasma-wall interaction, beam divergence and cathode potential.

Introdcution to SIMION software

The software SIMION is used in chapter 4 - 6 to support or bring new insight into findings obtained experimentally. SIMION is an ion optics simulation program that models ion optics problems with 2D symmetrical and/or 3D asymmetrical electrostatic and/or magnetic potential arrays. It allows to define the charge of a particle and its energy. It is also possible to define the origin of the particle and the form of the source (e.g. single point, circle, disk distribution). The software allows the user to input the particles velocity or kinetic energy then run them

through a given geometry. SIMION only simulate singly-charged (in contrast to multi-charge) particles. Space charge effects computations within an ion beam are complex and the software struggle to properly model them. Nevertheless, it is possible to simulate those effects by using "Coulomb", "Factor" and "beam repulsion" mode prior to run a simulation. Overall these modes are closer to reality when the space charge distribution is time independent as the computation is simpler. In our study we haven't used any of these mode for the following reason: 1) Studies in chapter 4 focuses on a pure ion beam operated at low current range and we do not expect space charge to be a major perturbation factor. 2) In chapter 5, the study focuses on a complex plasma (i.e. plume of a Hall thruster) and therefore the few times SIMION is used it was more to assess the behaviour of a single particle immersed in different electric fields than the behaviour of a group of particles.

2.3 Computation of parameters

2.3.1 Plasma parameters

Plasma parameters can be retrieved from I-V curves acquired with an electrostatic probe. Several quantities are relevant:

- The floating potential (V_f) is found at $I = 0$.
- The plasma potential V_s is the maximum of the first derivative of the current measured $V_s = V_{p_{max(dI/dV)}}$ or using the second derivative as $V_s = V_{p_{(d^2I/dV^2)=0}}$.
- When V_p<0 the ion current is measured. If the slope of the I-V is too large then some mathematical model shall be used to account for the sheath expansion [67, 68, 69, 70, 71]. The ion current density reads $j_i = I_i/A$, A being the physical area of the collector.
- The electron current I_e reads:

$$I_e = I_{es}(V_p - V_s)e\hat{T}_e, \tag{2.22}$$

  With I_{es} the electron saturation current at $V_p = V_s$, since at this voltage there is no sheath around the probe and the area is equal to the collector area A:

$$I_{es} = en_eA\left(\frac{e\hat{T}_e}{2\pi m_e}\right)^{1/2}, \tag{2.23}$$

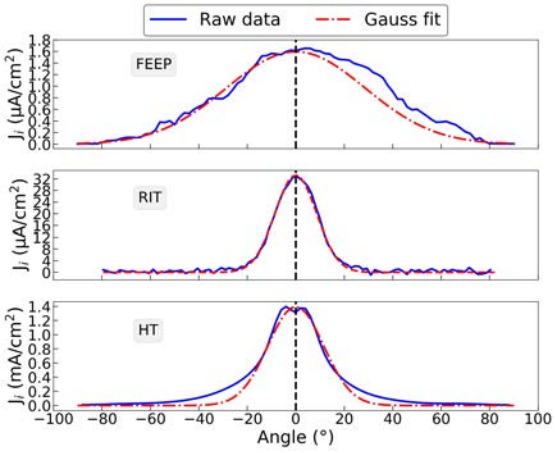

Figure 2.9: Top: Ion current density angular distribution acquired at 25 cm from a FEEP thruster with 16 well distributed injectors firing at 2 mA and 6 kV. Middle: The beam profile belongs to a low power RIT firing at 12.11 mA and U_+ = 1150 V. The probe is 43 cm away from the thruster exit plane. Bottom: The current distribution of the plume of the ISCT200 Hall Thruster firing at 0.66 A, 250 V and 9.61 mg/s. The dashed red lines are Gaussian fits.

- Assuming a Maxwellian distribution of the energy of electrons T_e can be retrieved. We used the slope of the $ln(I_e)$ curve once the ion current is subtracted from the raw I-V curve. It reads:

$$\hat{T}_e = \frac{1}{slope(\log(I_e))}. \tag{2.24}$$

- To determine the electron density n_e, equation 2.23 can be used as there is no sheath.

- Finally the ion current density is found using the Bohm current formula, valid inside the sheath :

$$I_i = Aen_i v_B \rightarrow n_i = j_i \left(\frac{e^3 \hat{T}_e}{m_i} \right)^{-1/2}, \tag{2.25}$$

2.3.2 Integrated total ion current

The integrated total ion current $I_{i_{int}}$ can be retrieved from the ion current density angular distribution acquired in the horizontal plane that contains the thruster axis.

Figure 2.9 displays the beam profiles acquired with a Faraday cup for a FEEP (top), RIT (middle) and HT (bottom). It is clear that beams have a different current angular distribution shape. While the RIT beam profile can be assumed to be a Gaussian, the two others are not. The FEEP current profile can be asymmetric if the firing needles are badly distributed over the crown and the HT profile shows large current at large angles. Therefore, to calculate $I_{i_{int}}$, the integration method shall be compatible for all three thrusters profiles. We use cylindrical coordinates and assume symmetry of the beam around the thruster axis. We find $I_{i_{int}}$ as [78]:

$$I_{i_{int}} = \pi d^2 \int_{\frac{-\pi}{2}}^{\frac{\pi}{2}} j_i(\theta) \mid \sin(\theta) \mid d\theta, \tag{2.26}$$

with d the distance from the thruster to the probe, θ the angle between the probe and the thruster axis on the horizontal plane. The integration is done numerically and uses Simpson's rule. A full demonstration to obtain equation 2.26 is given in appendix A.

2.3.3 Ion energy

The ion energy can be retrieved with the first derivative of an I-V curve measured with a RPA (2.8). Two values can be found i) the most probable ion energy E_{max} and ii) the mean ion energy E_{mean}. The latter is calculated from the integration of the whole area covered by dI/dV.

$$\begin{cases} E_{max} = max(\frac{dI}{dV}) \\ E_{mean} = \int_{V_i}^{V_f} \frac{dI}{dV} dV, \end{cases} \tag{2.27}$$

where V_i is the voltage when the current starts to drops. V_f is the potential once all ions are screened by IRE and there is no more ion current on the collector.

2.3.4 Probe efficiency and accuracy

When the ion current is known and directly controlled, like in the case of a FEEP and a RIT, one can determine the probe ion collection efficiency (η_p). If there are no ion losses during measurements then $\eta_p = 1$. It corresponds to the ratio between the integrated total ion current and the known ion current I_{em} (for FEEPs) or I_+ (for RITs).

$$\eta_p = \frac{I_{i_{int}}}{I_{em}}, \, or \, \eta_p = \frac{I_{i_{int}}}{I_+}. \tag{2.28}$$

This parameter is used in section 4 to compare probe design outputs. There, I_{em} is averaged over 800 data points acquired during 25 minutes to mitigate small current oscillation during plume scans.

The uncertainty accounted to calculate η_p read:

$$u = \frac{\sigma}{\sqrt{n}} or u = \frac{\sigma}{\sqrt{3}}, \tag{2.29}$$

where σ is a standard deviation and n the number of acquisitions. The first equation applies if the data set has a normal distribution. If it has a rectangular or uniform distribution the second equation is preferred. All uncertainties considered are then summed up following a linear error propagation with 99% confidence level:

$$u = \sqrt{\sum_{i=1}^{n} u_i^2}, \; u_{99\%} = ku(k=3). \tag{2.30}$$

The factor k, called coverage factor, is used here to give greater confidence that measurements are including in our tolerances. In this study only the probe pointing and positions, the acquisition system accuracy, the probe cleanness, the vacuum conditions and the telemetry (current control) are included in our uncertainty budget. All values, expect the telemetry and acquisition system, are extrapolated from the internal document released by the European Space Agency [79]. Based on this document the long exposure of the probe to the beam would induce $\pm 0.28\%$ uncertainty. The vacuum conditions (e.g. Pressure, Vacuum gauge) would account for 0.63%. The probe pointing and positioning increase uncertainties by $\pm 1.15\%$. The local heating effect, vacuum fluctuation, reading uncertainties are not considered here either because it is not possible to define it or the uncertainty are very small compare to parameter mentioned above. Using 2.30 gives $u = 4\%$ with a coverage factor of 3. Further details regarding uncertainties for measurements with the FEEP and HT are given in section 3.

2.3.5 Thruster performance parameter

Important thruster performance parameters can be derived from the ion current ($I_{i_{int}}$) and energy (E_{max}, E_{mean}).

Current and propellant utilization

The current utilization (η_b) is of importance for Hall thrusters as those devices are not operated with direct ion current control [17]. A Hall thruster provides thrust

when delivering a discharge current (I_d) that incorporates both ion and electron contribution (see section 3.3.1). The current utilization is the ratio between $I_{i_{int}}$ and I_d.

$$\eta_b = \frac{I_{i_{int}}}{I_d}. \tag{2.31}$$

This ratio is around 0.8 for high-power HTs [80, 81]. That means about 20% of the current is provided by the electrons which do not contribute to the thrust. The propellant mass utilization α is the ratio of the ion mass flow rate to the propellant mass flow rate. It corresponds to the fraction of the propellant mass flow rate injected into the discharge channel that is ionized. This quantity directly characterizes the ionization efficiency, hence it has to be maximized. The propellant utilization reads [82, 83]

$$\alpha = \frac{\dot{m}_i}{\dot{m}} = \frac{1}{\dot{m}} m \sum_{n=1} \frac{I_{n+}}{ne}, \tag{2.32}$$

where $\dot{m}_i$ and $\dot{m}$ are the ion mass flow rate and the atom mass flow rate, respectively, m is the atomic mass, e is the elementary charge and I_{n+} the current associated with ions having a $n+$ electric charge. Note that multiply-charged xenon ions with charges up to 3+ have been detected in the plume of a 200 W Hall thruster [84]. As the multiply-charged ion fraction is often unknown, the ion beam is assumed to be solely composed of singly-charged ions. This hypothesis induces small overestimation of α since only 90% of the ion population is singly-charged for the thruster operation points used in our study [84]. The propellant utilization α is then given by the following formula:

$$\alpha = \frac{1}{\dot{m}} \frac{I_{i_{int}}}{e} m. \tag{2.33}$$

For high-power HTs this ratio lies between 85% and 95%. For low-power HTs the current utilization is much lower with values around 70%.

Beam divergence

The beam divergence refers to the width of the beam. The latter can be estimated using the half-angle θ_{div} computed from $I_{i_{int}}$. It is common to assume that $I_{i_{\theta_{div}}}$, the current corresponding to θ_{div}, is 95% of the measured ion current [85, 63, 31]. Therefore it reads:

$$I_{i_{\theta_{div}}} = \pi r^2 \int_0^{\theta_{div}} j_i(\theta) \cdot \sin(\theta) \cdot d\theta = 0.95 \cdot I_{i_{int}}. \tag{2.34}$$

However, an effective plume divergence angle (λ) is often used [85, 86] to consider momentum losses associated to plume divergence when one wants to compute thrust. λ accounts for calculation of losses, and not torque, due to the fact that some ions are not travelling parallel to the thruster axis and the radial component from both sides cancel each other out. It corresponds to the ratio of the axial ion current and the total ion current $I_{i_{int}}$. λ reads:

$$\lambda = \arccos\left(\frac{I_{axial}}{I_{i_{int}}}\right) \tag{2.35}$$

$$\lambda = \arccos\left(\frac{\pi R^2\left[\int_0^{\frac{\pi}{2}} j_i(\theta)\cos(\theta)\sin(\theta)d\theta\right]}{\pi R^2\left[\int_0^{\frac{\pi}{2}} j_i(\theta)\sin(\theta)d\theta\right]}\right) \tag{2.36}$$

Thrust and losses

The thrust reads :

$$T = I_{i_{int}}\cos(\lambda)\,\alpha_{i_+}\sqrt{2E_i\frac{m}{q}}, \tag{2.37}$$

with $\cos(\lambda)$ corresponding to the divergence losses and α_{i+} a correction factor for multiple ionization [85, 87, 88, 89, 90, 91]. The factor $\sqrt{\frac{2m}{q}}$ equals 1.65×10^{-3} for xenon (Xe) propellant and 1.53×10^{-3} for indium (In). In this study, indium ions are considered singly-charged [92].

Thruster efficiency

Finally, knowing the total system power, the overall thruster efficiency can be computed as follow:

$$\eta_t = \alpha\frac{T v_e}{2P_{tot}}. \tag{2.38}$$

Often, we find in the literature that $\alpha = 1$ which means that the whole propellant is completely ionised. However, this is rarely, hence the thruster efficiency can easily be overestimated as α can be lower than 1. Nonetheless, in the event where the propellant mass flow rate can be measured precisely (e.g. Hall thrusters, gridded ion engines), equation 2.38 can be used under the following form:

$$\eta_t = \frac{T^2}{2\dot{m}P_{tot}}. \tag{2.39}$$

Chapter 3

Experimental apparatus and preliminary studies

Contents

3.1 Vacuum chambers, acquisition systems and measurement procedure

3.1.1 Experiments with a FEEP thruster

Two vacuum chambers, with different dimensions, were used to test the FEEP thruster. Most of the experiments were conducted inside a cylindrical stainless-steel vessel of 0.91 m in diameter and 1.75 m in length located at the aerospace engineering's department laboratory of Wiener Neustadt University of Applied Sciences (FH Wiener Neustadt). Without gas injection, the pumping system allows the residual pressure in the tank to go down to 10^{-7} mbar. During operation of the FEEP thruster the pressure level is typically 4×10^{-6} mbar. Since the chamber is meant to host FEEP thrusters, additional care must be taken regarding materials inside the chamber. Therefore, a 1.32 m long cylindrical aluminium shield is installed inside the chamber to minimize the back flow of indium atoms during operations. It reduces the nominal diameter of the chamber down to 0.67 m. Deflectors with a sawtooth shape are installed at the back of the chamber to minimize the probability to have ions being directly back scattered towards the thruster during operation. This facility was built during the first months of the PhD thesis. A larger vacuum chamber was used to assess facility effects on the plume of a FEEP thruster. The research subsidiary Forschungs- und Technologietransfer GmbH (FOTEC) made available the LIFET 4 vacuum chamber designed to host liquid metal ion sources where a beam diagnostic system was developed in 2018 [93, 77] (see right side of figure 3.1). The chamber is 2.2 m in diameter and 3 m long. The pressure during the thruster operation is of the order of 2×10^{-6} mbar. The probe is mounted on at the centre of a remotely controlled semi-circle rotating arm. The arm can host 23 probes arranged at different intervals in the latitude direction. The arm can be rotated stepwise from -80° to +80° at a distance of 95 cm from the thruster. The probe is located on the left side of the extension allowing scan from -90° to +70°, and measurements were done 83.7 cm away from the thruster emitter crown.

In the FH chamber the holding structure lies on an aluminium plate that is electrically connected to the inner cylindrical shield. The two parts are grounded. The FEEP thruster is mounted onto a 3D printed aluminium plate with heat pipes in order to efficiently control the thruster temperature during operation. The plate

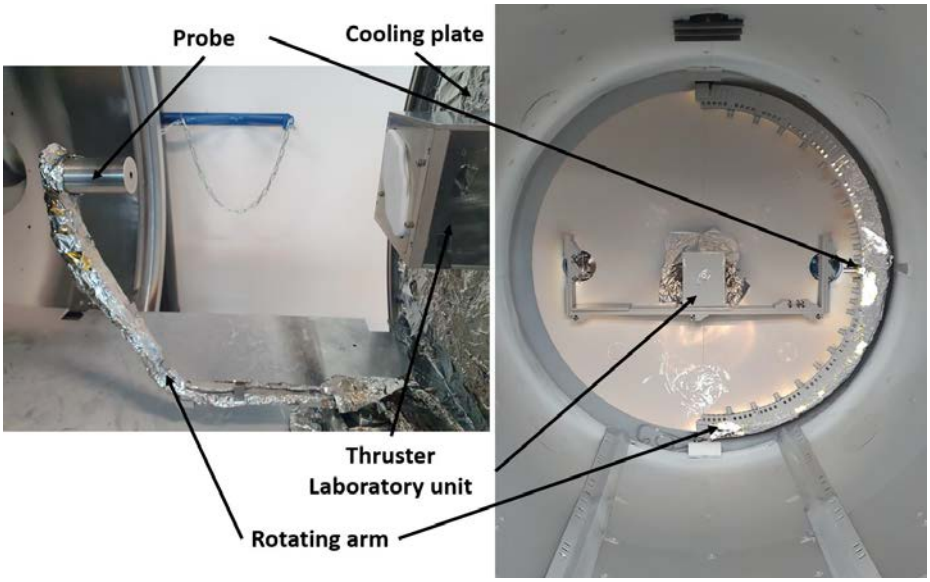

Figure 3.1: FH (left) and Lifet 4 (right) vacuum chambers.

is connected to a recirculating cooler (JULABO chiller) to keep the temperature of the interface down to 15°C. The chamber frame is connected to the ground. The probe is installed on an aluminum rotating arm, see left side of figure 3.1. The structure allows automatic alignment of the probe with the thruster equatorial plane. The probe holder is mounted on a URS1000BCC motorized rotation stage from Newport controlled from the atmospheric side. The thruster centreline is referred to as the 0° angular position. The pivot point of the rotating structure is aligned with the thruster exit plane. The system enables a scan from -90° to +90° on the horizontal plane that includes the thruster axis. The alignment of the system is done thanks to a laser cross (*TOOLCRAFT CL12*). The distance d between the probe aperture and the thruster exit plane is 26.1 cm. As $d \gg d_{emitter}$ the point source hypothesis is valid [72, 37, 80]. The entire mechanical structured is grounded. The whole experimental set-up is displayed in figure 3.2.

A calibrated Keithley 2050 sourcemeter is used to measure the ion current collected by the probe. The device can be operated from 20 mV to 200 V in voltage source and measures 10 nA to 1 A with 0.012% basic measure accuracy. For simultaneous direct current measurement on different probe parts a Keithley 2410 is coupled to the previously mentioned sourcemeter. It offers a broad range of currents [1 A – 10 pA] and voltages [$\pm$1100 V - $\pm$1 V] with a high degree of stability and accuracy. We use a high voltage power supply from Heinzinger (*Heinzinger*®

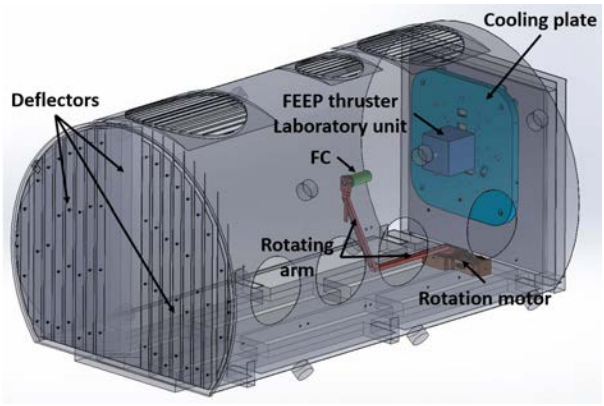

Figure 3.2: 3-D model of the FEEP experimental apparatus in the FH chamber.

PNC 20000 - 10 pos [94]) to operate the RPA (see section 6) and to allow the IRE grid to reach voltages larger than the applied emission voltage. It enables voltage output up to $\pm 20\,\mathrm{kV}$ for a maximum total power of 200 W.

A home-made program is used to synchronize all devices, to enable position control and to record and save measured data. Note that all current density angular distributions cover a circular arc from -90° to + 90 with a 2° step (see section 3.3.1). The current is averaged from 10 consecutive measurements acquired over 15 seconds at each angular position.

Due to the numerous probe designs investigated in the frame of this work in various vacuum chamber and with different emitter heating cycles, a clear test procedure was followed as explained in table 3.1. The procedure starts the day after the chamber is pumped down once the pressure reaches about 10^{-6} mbar and the thermal outgassing is completed. Note that step 3 and 4 follow text scripts. The thruster V-I characterization is used to monitor possible variation of the thruster electrical impedance caused by a large number of vacuum cycles. This parameter impacts the total discharge voltage needed to reach identical firing conditions.

3.1.2 Experiments with a low-power Hall thruster

Experiments on the Hall thruster have been performed in the cryogenically pumped New Experiments on Electric Thrusters (NExET) grounded vacuum chamber [46, 18]. A photograph of the NExET chamber is shown in figure figure 3.3a. It is a 1.8 m in length and 0.8 m in diameter stainless steel vessel. The overall pump stack warrants a background pressure as low as 2×10^{-5} mbar-Xe during opera-

Table 3.1: Heat-up, ignition, measurements and shut down procedure of the FEEP.

Step	**Action**	**Duration**
#	#	min
1	Thruster heat-up at 6 W	90
2	Thruster temperaure stabilization	10
3	Thruster ignition script	15
4	Thruster V-I characterization	8
	Hot stand-by	
5	Measurements	xx
6	Next thruster operation point and stabilization	10
	Repeat step 5 and 6 if needed	
8	Thruster shut-down	
9	Chamber evacuation the next day	

tion of a 200 W input power plasma source. A schematic of the chamber and the experimental set-up is drawn in figure 3.3b. The arrangement is nearly identical to the one used with the FEEP. The probe is mounted on a rotating arm controlled by a Newport rotation stage. The distance between the FC entrance and the thruster exit plane (d) is here limited by the vacuum chamber diameter. Consequently, d is fixed at 27.4 cm ($\sim$8 thruster outer channel diameters). The far field plume is usually defined as the region where d is greater than four thruster diameters [63]. Here the Hall thruster fired in NExET is therefore assumed to be a point source for the probes. [72, 37, 80].

RPA measurements were conducted with the SEMION system commercialized by Impedans Ltd [95]. The instrument allow ion current acquisition at the collector while biasing the other grids.

The test procedure used with the Hall Thruster is given in Table 3.2.

3.2 Probe designs

3.2.1 Planar probe

A 14 mm diameter planar probe was used to measure plasma parameters from the ISCT200 Hall thruster and the ENPULSION NANO laboratory unit FEEP

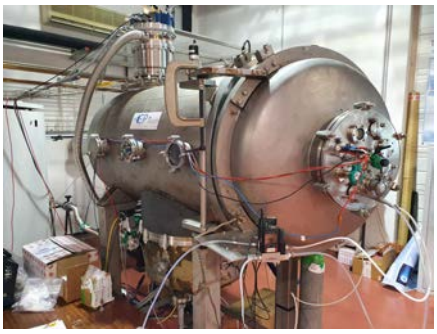

(a) Picture of the NExET vacuum chamber.

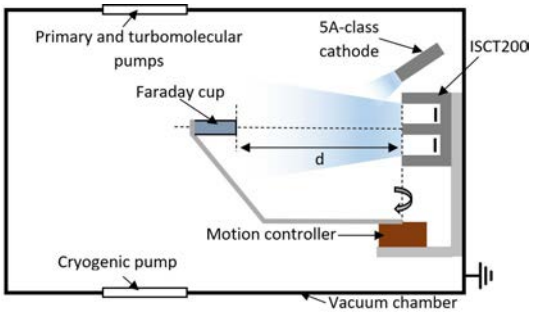

(b) Layout of the apparatus used with the ISCT200 Hall Thruster.

Figure 3.3: NExET vacuum chamber.

Table 3.2: Heat-up, ignition, measurements and shut down procedure of the ISCT200.

Step #	**Action** #	**Duration** min
1	Cathode heating	20
2	Thruster ignition	
3	Hall thruster stabilization	30
4	Setting of the operation point and stabilization	5
5	Measurements	
6	Next operation point and stabilization	5
	Repeat step 5 and 6 if needed	
7	Thruster shut-down	
8	Cathode shut-down	

thruster. The collector material is made of graphite.

3.2.2 Faraday cup

In section 2.2.2 we discussed about the most suitable electrostatic probe to be used to measure the ion beam properties for different electric thruster technologies. A Faraday cup seems to be an ideal candidate has it greatly mitigates the sheath effect during ion current acquisitions, it can be cost-effective, easy to implement and its working principle provides some degree of freedom to modify the design baseline [63, 31]. A FC is composed of three main components as shown in figure 3.4. The pod or housing (A) is grounded and shields electrons from the ambient plasma. The collector (C) is used to collect the ion flux penetrating inside the probe. The collector is subject to heavy ion bombardment and sensitive to subsequent ion induced electron emission as discussed in sections 4.1 and 5.2. The collector diameter is 12 mm for all Faraday cup designs studied in this work. Between the housing front and the collector top an electrode is inserted (B). In the literature it is designated as a "collimator", however to avoid confusion with the word "collector" the term "repeller" is used instead. Historically, the repeller is used to define the ion flux entering the probe. Therefore, it needs to have the smallest orifice diameter of the system. It screens thermal electrons and acts as a filter for ion velocity vectors. In this manner, it avoids saturation of the measurement chain when the FC is placed in the centre of the ion beam. It needs to support high level of stress such as heating, pulverization, deposition. Its role as well as its position is discussed in sections 4.1, 4.3 and 5.4. Polyetheretherketone (PEEK) is used for electrical insulation. It is a thermoplastic compatible with ultra-high vacuum application which can withstand high temperatures (melting temperature is 343°C).

Numerous probe designs were tested and results are presented and discussed all over this manuscript. Therefore, a nomenclature (ID) has been implemented to identify the FC design parameters under investigation. Each ID includes two groups in the form of A.B.C.D-X.Y.Z. The first group accounts for the probe length, inlet diameter size, and the location of the repeller as shown in figure 3.5 and described in the property list 1 . The second group informs on the collector shape, the material used and whether it has a foam structure or not as displayed by figure 3.6 and detailed in the property list 2 .

1. 1^{st} ID group

   A Represents the length of the cup. It can be 50 mm, 30 mm or 10 mm.

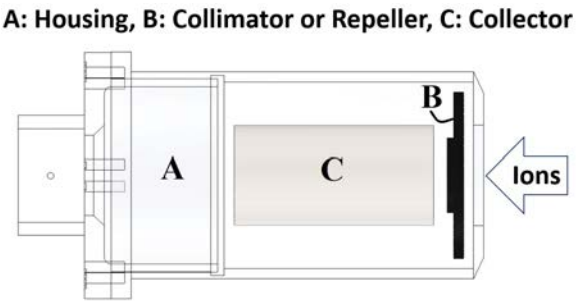

Figure 3.4: Main parts of a Faraday cup.

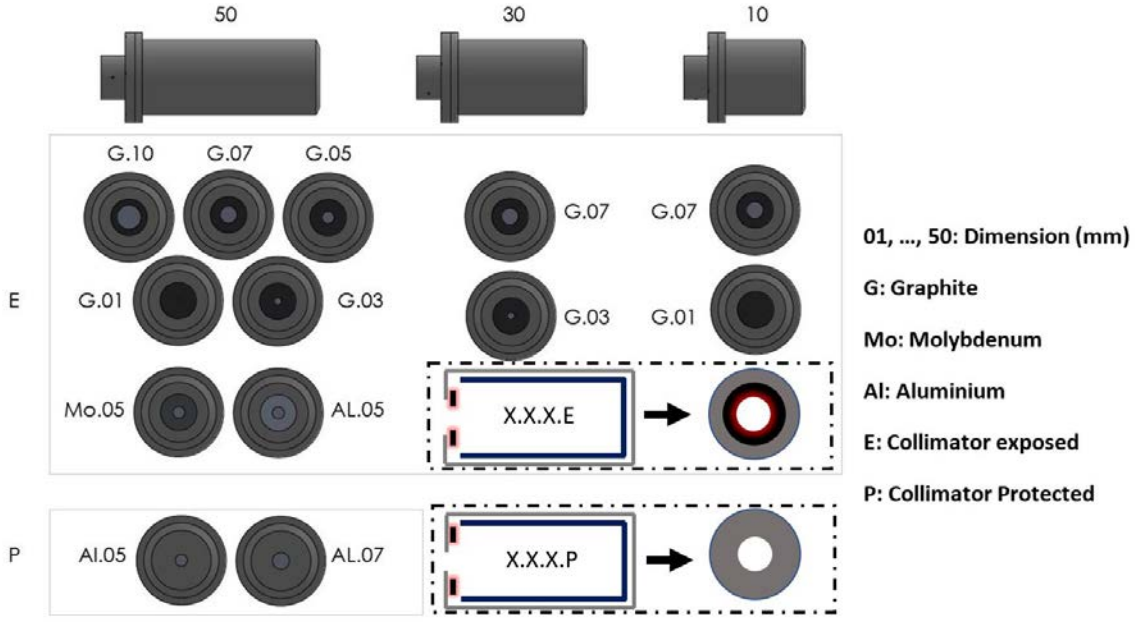

Figure 3.5: 1st ID group. The probe length, the inlet aperture d_a, the probe front material and the position of the repeller are represented in this group.

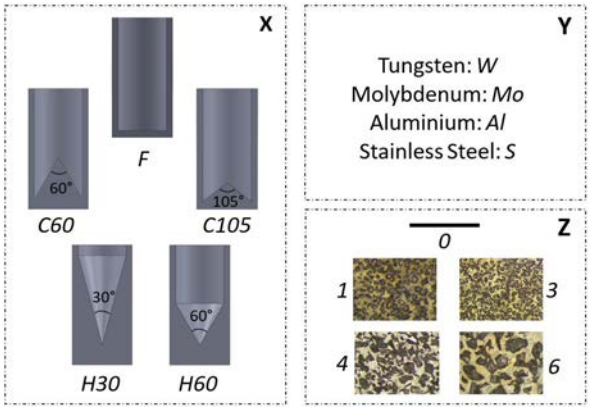

Figure 3.6: 2^{nd} ID group. The collector geometry and material are identified in this group.

B Refers to the probe front material. It can be either graphite (G), molybdenum (Mo) or aluminium (Al).

C Informs on the inlet aperture diameter d_a. It can be 10, 07, 05, 03 or 01 mm

D Gives information on the position of the repeller. If the repeller is exposed to the ion beam and collimates the ion flux ($d_a = d_r$), then the letter E is used. On the contrary, when the repeller is placed behind the housing and the housing front aperture d_{pod} is smaller than the collimator aperture diameter d_r, the collimator is considered protected from the ion beam and the letter P is used ($d_a = d_{pod}$).

2. 2^{nd} ID group

X Informs on the shape of the collector. It can be flat (F), conical towards the probe front (C) or directed to the back of the probe (H), with the opening angle value equals to 30, 60 or 105, for 30°, 60° and 105°, respectively.

Y Refers to the material used on the rear side of the collector cup. It can be made of tungsten (W), molybdenum (Mo), aluminium (Al) or stainless steel (S).

Z The material can be either solid (0) or has a foam structure with different pore sizes 1, 3, 4, 6 (see table 3.3).

Table 3.3: Description of the foam materials commercialized by Exxentis [5].

Parameters	F1	F3	F4	F6
D_{max} (mm)	0.2 - 0.35	0.4 - 0.63	0.4 - 1.0	0.63 - 1.6
D_{min}, (μm)	40 - 50	70 - 90	150 - 200	500 - 600
Volume porosity (%)	55-65			
Density (g/cm^3)	1 to 1.2			
Operating temperature (°C)	from -200 to +250...550			
Aluminium alloy	AlSi7Mg			

For example, the FC identified as 30.G.07.E - F.Al.4 refers to a Faraday cup with a 30 mm long cup where the front part of the probe is in graphite, the opening diameter is 7 mm and the collimator is in the configuration where it is exposed to the plasma. The collector is flat, made of aluminium foam #4. A FC called 50.Al.05.P - C105.Mo.0 has a cup of 50 mm, its front material is aluminium, its aperture is 5 mm and the collimator is protected from the ion beam. The collector has a conical shape with an opening angle of 105°, it is made of regular molybdenum (no foam structure). Few studies pointed out the capacity of complex surface to reduce γ_{EE} [96, 97, 98, 99]. Materials like velvet carbon seems to be the most efficient as their body is composed of multiple nano-fibres which can ease trapping ion-induced electrons [100, 99]. Unfortunately, this type of material are exceptionally difficult to get and a foam structure was used instead, as listed in table 3.3.

3.2.3 Retarding Potential Analyser

Two different RPA designs were used to retrieve the ion energy distribution of the ISCT200 Hall thruster and the ENPULSION NANO laboratory unit FEEP thruster.

Hall Thruster

Based on the requirements stated in section 2.2.2 the RPA is composed of four grids with a molybdenum ion collector and an inlet aperture diameter of 7 mm. Molybdenum is known for having a low ion-induced electron emission yield [63] when bombarded by xenon ions. The grid mesh is 0.7 mm giving $0.1<\frac{r_m}{d_m}<1$. Using equation from section 2.2.2 the grids are spaced by 4 mm. However we have ΔE = 50 V/mm to 87.5 V/mm for discharge voltages between 200 V and 350 V.

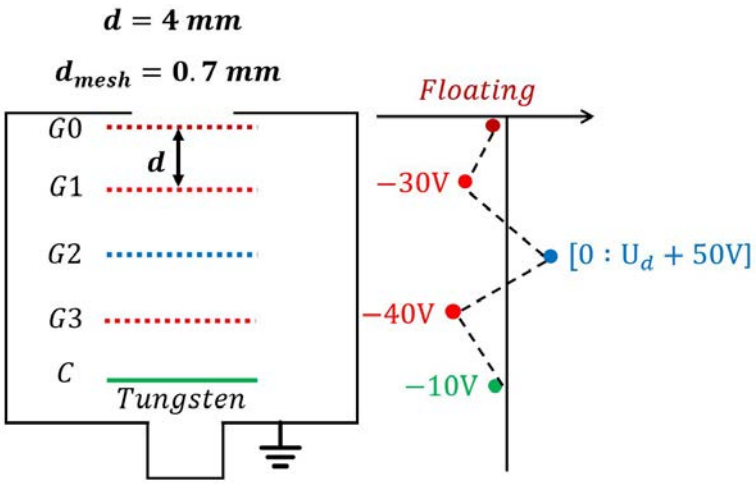

Figure 3.7: Schematic of the RPA design used to measure the ion energy with a low power class Hall thruster. Grids are spaced by 4 mm and the mesh is 0.7 mm. The collector is made of Molybdenum.

Considering that the grid holes are 0.7 mm large the energy resolution ranges between ± 17.5 V and ± 30.6 V. Here, the energy resolution is larger than 10% to meet limitations imposed to avoid electrostatic lens effects. The RPA architecture is showed in figure 3.7.

FEEP Thruster

The RPA was designed based on previous work done at FOTEC [77, 101] and considering the dimension limitations broached in section 2.2.2. RPA dimensions in the case of FEEP thrusters are less restrictive due to the low ion densities at stakes, see section 3.3.2. Mühlich et al. [77] provide all information for the design of a RPA to study the ion beam of a FEEP. They showed that due to the keV range ion energy of a FEEP thruster shorting can appear between grids. Therefore, we reduced the number of grids from four to three, the last grid being the IRE. The ion collector is made of tungsten as the material presents a low ion induced electron emission yield for indium ions, as shown in section 4.1. The collector is placed 8 mm downstream. The two other grids upstream the IRE are spaced 4 mm from each other. The grid mesh is 1.1 mm for a total transparency of $\sim$50%. ΔE ranges from 0.250 kV/mm to 1.250 kV/mm for emission voltage from 2 keV to 10 keV. Therefore, the RPA energy resolution is comprised between ± 0.1375 kV

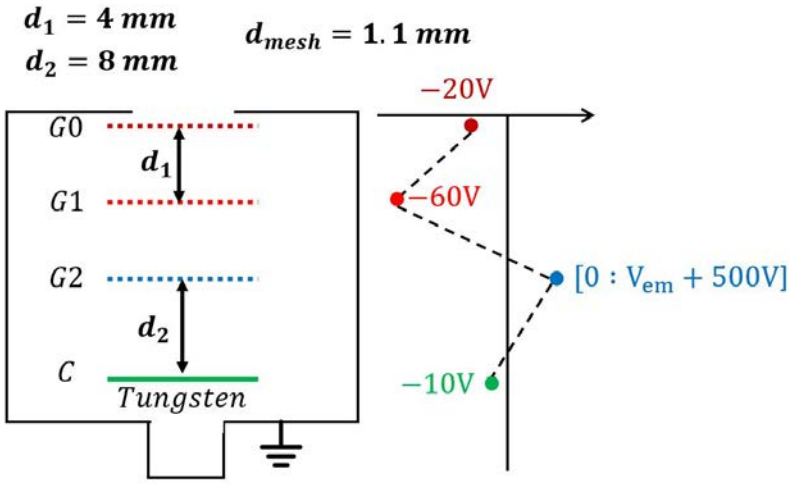

Figure 3.8: Schematic of the RPA design used to measure the ion energy with a low power class Hall thruster. Grids are spaced by 4 mm and the mesh is 1.1 mm. The collector is made of Tungsten and sits 8 mm below the last grid (IRE).

and ±0.6875 kV. The GE and ERE grids are biased to -30 V and -60 V. Since the ion acceleration voltage V_{em} is largely greater than the voltage applied to GE, there will be no consequences on the measured energy. The RPA architecture is showed in figure 3.8.

3.3 Electric propulsion systems

3.3.1 ISCT200 Hall Thruster

Working principle

A Hall thruster is an electrical propulsion device that uses a plasma discharge with magnetized electrons to ionize and accelerate a propellant gas [80, 102, 89, 103] as schemed in figure 3.9. The principle relies upon a magnetic barrier and a low-pressure dc discharge generated between an external cathode and an anode. The latter is located at the upstream end of a coaxial annular dielectric channel that confines the discharge. A fraction of the electrons emitted by the thermionic cathode flows downstream to neutralize the ion beam. The remaining part travels toward the anode to maintain the plasma discharge. The propellant gas, typically xenon, is introduced at the back of the channel. Magnetizing coils or permanent

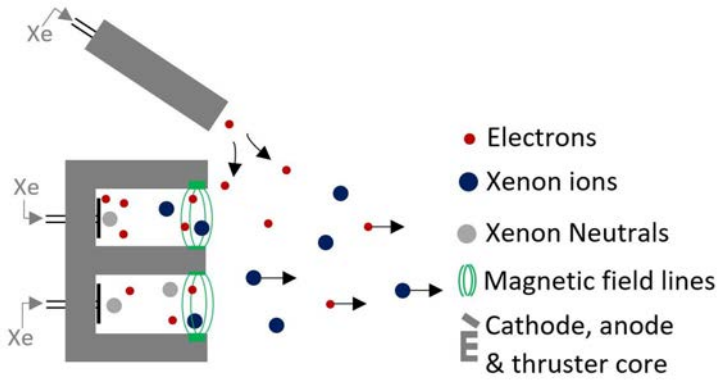

Figure 3.9: Hall effect thruster working principle.

magnets, incorporated into a magnetic circuit, provide a radially directed magnetic field of which the strength is maximum in the vicinity of the channel exhaust. The magnetic field is chosen to be strong enough to make the electron Larmor radius much smaller than the discharge chamber characteristic dimensions, but weak enough not to affect ion trajectories. The electric potential drop is mostly concentrated in the final section of the channel owing to the low axial mobility of electrons in this restricted area. The electric field governs the propellant atoms ionization and the ion acceleration. The combination of the radial magnetic field with the axial electric field generates an $E \times B$ electron drift in the azimuthal direction, the so-called Hall current. The latter is responsible for the very efficient ionization of neutral atoms inside the channel.

The MIREA 5 A cathode

A cathode is a critical component to operate a Hall thruster. As opposed to gridded ion thrusters or FEEP, with Hall thrusters the ionisation is made possible only because of the primary electrons coming from the cathode. In our study we use a so-called hollow cathode. Such category of cathode is a complex and sensitive instrument. It is heavily study since long and optimal operation is difficult due to plasma instabilities at the cathode orifice and insert, thermal management issues inside the core of the cathode and material deterioration due high pulverization and sputtering rate. The cathode is made of a LaB_6 pellet pressed supported by a molybdenum pellet holder. The LaB_6 insert emits electrons by thermionic emission thanks to the heating circuit as showed in figure 3.10. The heat power for operation is around 200-300 W. A mass flow rate of 0.3 mg/s of xenons is injected

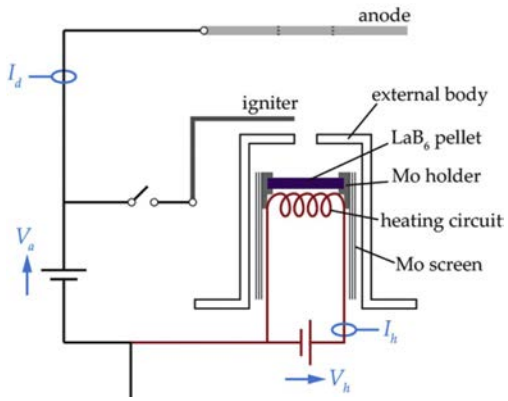

Figure 3.10: Schematic of the electric set-up of a MIREA 5A cathode ©[3].

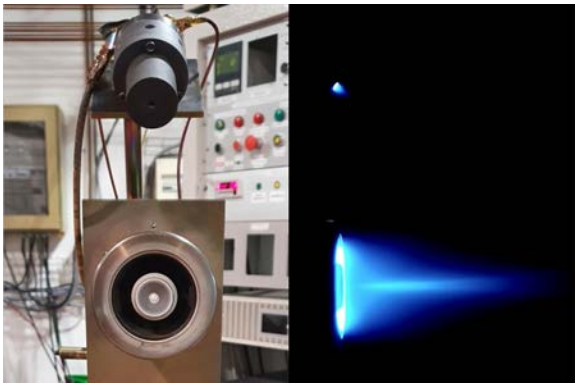

Figure 3.11: Photograph of the ISCT200 assembly (left) and during firing with xenon in the NExET chamber (right).

into the cathode body to create a plasma at the cathode orifice before extracting electrons and accelerating them towards the anode (i.e. core of the thruster). The ignition procedure is as follow: 1) to heat the insert until it reaches the threshold temperature for thermionic emissions to occur 2) open the valve to flow xenon through the cathode core 3) Apply a voltage between the heater and the "igniter" to create a plasma 4) then switch the igniter off so the voltage drops occurs between the anode and the cathode. Once xenon is injected into the core of the thruster then the thruster ignition occurs.

Thruster characteristics

The ISCT200 Hall thruster is a 200 W-class HT with a classical magnetic field topology. Details about the ISCT200 series and thruster architecture can be found in [34, 18, 104]. The annular channel walls of the ISCT200 are made of BN-SiO2 ceramic. The channel geometry is in the so-called $2S_0$ configurations, which means the channel cross-sectional area is twice the one of the well-known Russian SPT100 [105, 106]. The $2S_0$ configuration ensures a high ionization degree. The magnetic field is generated by way of small samarium–cobalt magnets either cylindrical or with a ring segment shape for most recent versions. The latter enable a more optimize use of the volume. The xenon propellant gas is injected homogeneously inside the channel using a high porosity mullite ring ceramic placed behind the channel back plate. The anode is a wide stainless steel ring placed at the back of the channel against the outer wall. During operation, the thruster body is floating. A heated 5 A-class hollow cathode with a disk-shaped LaB_6 emitter was used to generate the electron current [3, 107]. The cathode is located outside the channel with its orifice in the vertical plane that contains the channel outlet, tilted towards the thruster as can be seen in figure 3.11. The cathode exit plane is 10 cm away from the anode centre. The cathode, which is operated with a constant xenon mass flow rate ($\dot{m}_c$) of 0.3 mg/s, is electrically connected to the thruster anode and floating. Two different thruster units were used. HT1 was operated at 0.66 A for U_d = 200 V and 250 V. HT2 was fired at different current discharge 0.66 A, 0.8 A and 1 A for a fixed voltage. Similarly, the thruster was fired at 200 V, 250 V, 300 V and 350 V for a fixed current discharge. As many experiments have been performed during various time periods with opening of the tank in between, the xenon flow through the thruster anode had to be adjusted and may slightly differ from one test to another for same thruster current discharge and voltage. Therefore, the thruster mass flow rate will be specified individually.

Current oscillations

Figure 3.12 displays the AC part of discharge current oscillations, i.e. the mean value has been subtracted, during HT1 and HT2 operation. The top of the figure displays the current traces of HT1 when firing at 0.66 A and 200 V and 250 V. We note that at 250 V current oscillations are stronger. The standard deviation of the discharge current is 0.039 A at 200 V and 0.37 A at 250 V. HT2 firing points for 0.66 A, 0.8 A and 1 A with a discharge voltage fixed at 250 V (middle), show that oscillations magnitude increases with I_d. Nevertheless, the standard deviation of

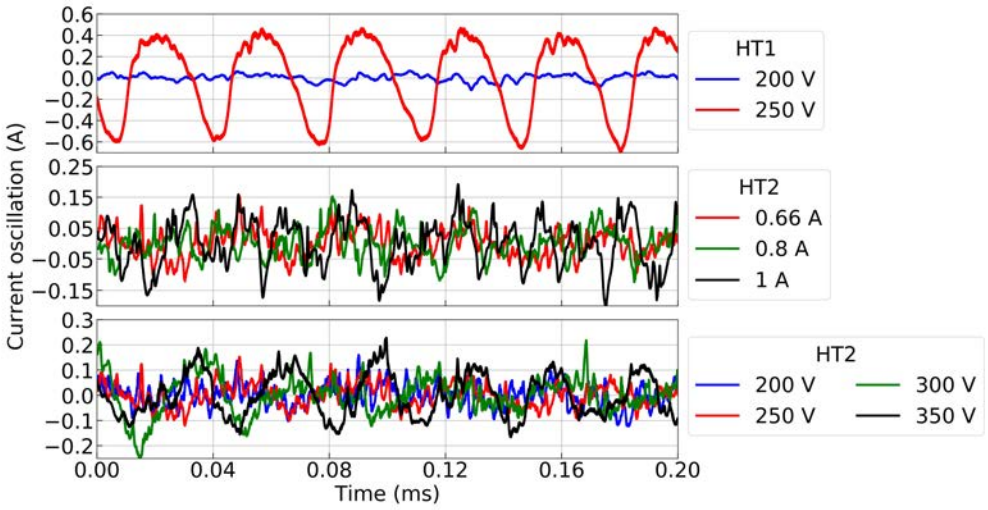

Figure 3.12: Discharge current oscillations for HT1 and HT2. Top: HT1 firing at 0.66 A, 200 V and 250 V. Middle: HT2 in operation at 0.66 A, 0.8 and 1 A with U_d fixed at 250 V (middle). Bottom: The thruster fires at 0.66 A with discharge voltages of 200 V, 250 V, 300 V and 350 V.

the oscillations ranges from 0.046 A for 0.66 A to 0.078 A for 1 A. The plot at the bottom of figure 3.12 shows the current oscillations at 0.66 A and discharge voltages of 200 V, 250 V 300 V and 350 V. At 200 V and 250 V the standard deviation is close to 0.045 A whilst at 300 V and 350 V, the standard deviation increases to 0.075 A and 0.08 A. In the case of HT2, the increase of instabilities observed at higher I_d are due to the thruster performance limits. Indeed, the ISCT200 series was developed to be operated at 200 W and therefore, when operated above this power limit, its operation becomes less optimum as the magnetic field is not changed. However, this PhD work is not focus on improving thruster performance, hence these suboptimal operation conditions are not a problem as current oscillations are stable over time. Nonetheless, current oscillations shall be included in our uncertainty budget, hence the larger error bars in the case of the Hall thruster for all plots in this dissertation.

Plasma parameters

Figure 3.13 plots typical I-V and first derivative measurements of the current acquired with a planar probe (see section 3.2) in the far-field region (≈27 cm) of the ISCT200 Hall thruster. We clearly identify the ion saturation branch when the

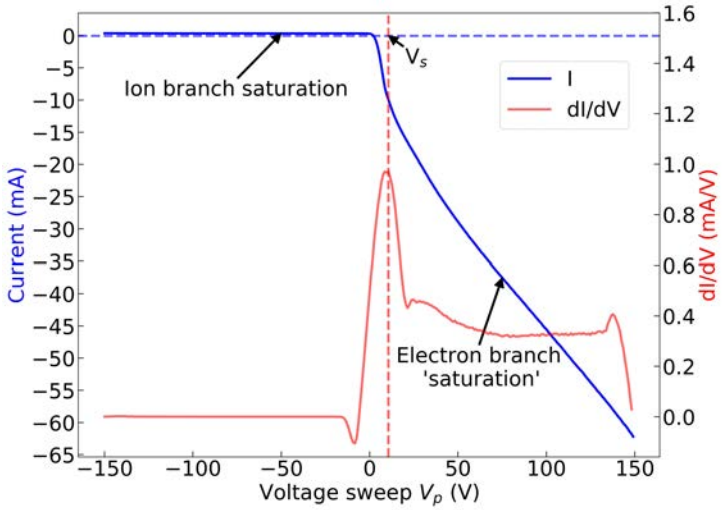

Figure 3.13: Typical I-V curves acquired with a 14 mm wide planar probe in the far-field region (≈27 cm) of the ISCT200 Hall thruster. The probe is located at -30° from the thruster centre axis. The thruster fires at 0.66 A, 200 V and 0.8 mg/s. The ion and electron saturation branch are identified as well as the plasma potential deduced.

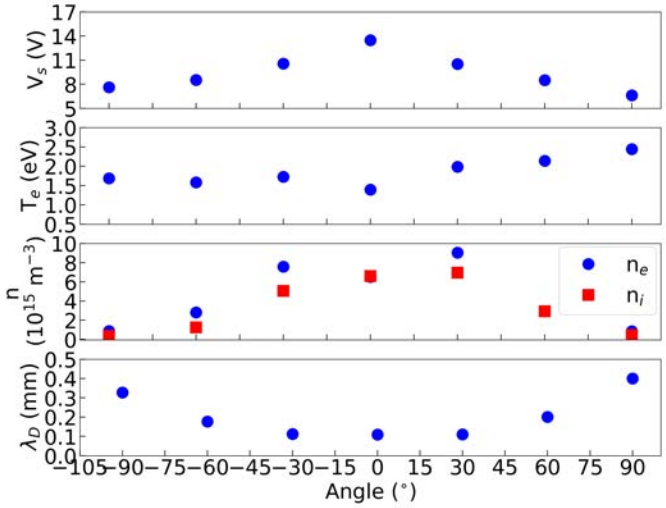

Figure 3.14: Plasma potential, electron temperature, electron density and electron Debye length retrieved from the plume data of the ISCT200 Hall thruster firing at 0.66 A, 200 V and 0.8 mg/s at a distance $d \approx 27$ cm. Current is acquired with a 14 mm wide planar probe.

probe collector is negatively biased. Then, as explained in chapter 2 the floating potential is found to be near 2 V and the plasma potential close to 10 V. The latter is found as being the abscissa of the maximum value on the y-axis of the first derivative curve. However, unlike the theory presented in the previous chapter the electron saturation branch does not truly saturate. Indeed, we observe a constant increase mostly cause by sheath expansion and secondary as well as ion-induced electron emissions. Still, the 'knee' characteristic of the change from the transition region to the electron saturation region is clearly visible. Figure 3.14 displays an estimation of plasma parameters retrieved from I-V curves similar to the one display in figure 3.13 at several angular positions. The thruster is firing at 0.66A, 200 V and 0.8 mg/s. Note that values are not far from plasma parameters measured in the beam of high power HTs [30]. As expected we observe that λ_D increases as the probe goes away from the thruster axis. Indeed, the plasma potential as well as the electron density decreases whilst the electron temperature remains quasi constant around $2.0 \sim 2.5$ eV. We note that the quasi-neutrality hypothesis holds since the ion (red square) and electrons (blue circle) densities are of the same order.

Table 3.4: I_{int} computed for different angular steps. The probe design is 50.G.10.E - F.Al.4

$d\theta$ (°)	I_{int} (A)
1	0.481
2	0.4803
3	0.481
5	0.4808

Angular step

To optimize the measurement time and also to find the optimal minimum angular increment step during ion current density angular distribution measurements, the total ion current $I_{i_{int}}$ was computed for several values of $d\theta$ namely 1°, 2°, 3° and 5°. Note that $d\theta$ shall be at least greater than d_a/d [46]. We can see in table 3.4 that there is almost no influence of the angular step on the computation of $I_{i_{int}}$. Therefore, a 2° angular step is used to optimize the time period of a full angular scan through the plume (∼22 minutes). This step still provides enough data point to plot realistic beam envelops. The same analysis was conducted with the ENPULSION NANO thruster and no major variation was noticed. Therefore, the same step size is applied.

Probe voltage

The I-V curve acquired at different angular positions with the ISCT200 thruster are displayed in figure 3.15. They show that a collector bias fixed at any potential lower than -40 V is sufficient to mitigate perturbation induced by primary electrons whatever the angle, as the collected ion current stay unchanged.

3.3.2 The ENPULSION NANO thruster

The ENPULSION NANO thruster is produced by the Austrian company *Enpulsion*. It is built from the heritage of 20 years of development done at *FOTEC* [108, 109, 110, 77, 93]. The thruster is a high specific impulse, liquid indium, field-emission electric propulsion (FEEP) system. It enables precise orbit and attitude manoeuvres [111, 32, 91]. It has a $10 \times 10 \times 10$ cm envelope which makes easy its implement into satellite structure. It is controlled via a power process-

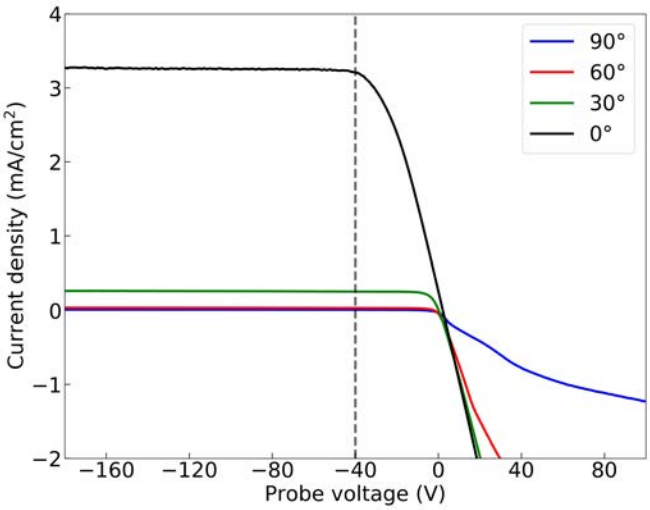

Figure 3.15: I-V curves acquired with FC 50.Al.7.P - F.Al.3 at different angular positions. The dashed line indicates -40 V. The ISCT200 fires at 1 A, 250 V and 1.395 mg/s.

ing unit (PPU) [91]. The ENPULSION NANO is delivered with two cathodes to neutralize the ion beam during operation. The maximum system input power is 40 W which makes the thruster ideal for formation flight and constellations of small satellites. The core of the ENPULSION NANO is a passively fed, porous ion emitter consisting of 28 sharp needle tips, also called injectors. The thruster operates with indium as propellant when the molten metal is in liquid state. At time of writing, the thruster has achieved significant space heritage with over 65 units in space. Thrust is generated based on FEEP physics [112, 87, 113].

Working principle

The ENPULSION NANO working principle rely on the field evaporation emission of a liquid metal. When a strong electrostatic field (10^9 V/m) is applied at the apex of a sharp needle-like structure wetted with a liquid metal, it adopts a conical shape [114, 115]. This cone was described for the first time by Gilbert in 1600 and mathematically theorised by Taylor in 1964, hence its name Taylor or Taylor-Gilbert cone [116]. It is at equilibrium, not necessary stable though, when the surface tension is balanced by the electrostatic force. Taylor mathematical model gave the semi-half angle θ_T to be approximately equals to 49.3° [116]. The evolution of the Taylor angle θ_T is proportional to the emission current I_{em} as

(a) (b)

Figure 3.16: The ENPULSION NANO units © *ENPULSION* (left) and a crown firing with 28 needles [4].

follow:

$$\theta_T = \theta_{T_0} - \frac{d\theta}{dI_{em}} I_{em}. \tag{3.1}$$

Niedrig determined experimentally $\theta_{T_0} = 51.1°$ and $\frac{d\theta}{dI_{em}} = 0.3\,°/\text{mA}$ [117]. Nevertheless, these values were obtained for a single needle facing an extractor plate. This set-up is far from the configuration of the emitter (multi-needles, circle distribution) used by the ENPULSION NANO. Hence, these values cannot be used in our cases. At emission current greater than $10\,\mu$A per needle, which is often the case with the ENPULSION NANO, a jet forms at the tip of the Taylor cone as exemplified in figure 3.17. The jet length is directly related to the onset voltage (V_0), the threshold potential to overcome to start ion emission, and the emitted current [117]:

$$l = \frac{2}{3\pi\Lambda}\sqrt{\frac{mV_0}{2e}} I_{em}, \tag{3.2}$$

where Λ is the surface tension of indium (560 J/m^2 at the melting point temperature). Note that above $20\,\mu$A it is not possible to determine the exact length of the jet since the Taylor cone and the jet concave shape is not valid any more [116].

On its way through the needle tip the liquid flow can undergo perturbation induced by the strong electrostatic field and droplets formation then emission occur, as shown in figure 3.17. They are neutrals and therefore impact the mass efficiency of the thruster since they do not contribute to thrust. The fraction of

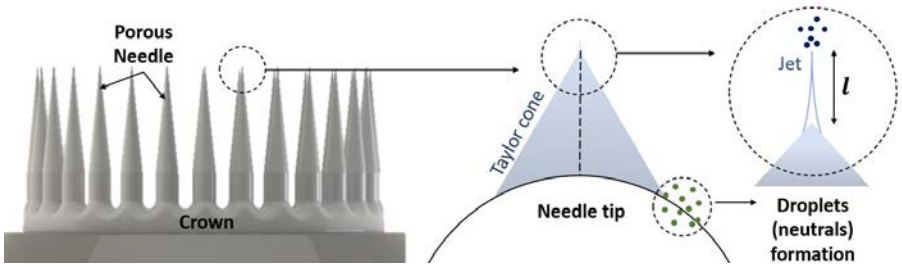

Figure 3.17: Drawing of the Taylor cone and droplet formation when a liquid metal a the tip of a needle undergoes large electrostatic forces.

emitted droplets increases with the current emission. Overall, the ion beam produced by the ENPULSION NANO is assumed to be composed of ions and neutrals (e.g droplets) with some thermal electrons. The latter find their origin from the secondary electrons effects known from a long time in LMIS [118]. The emitter temperature varies with the ion current due to ion-induced electron emission. Still, they have little influence on the LMIS mechanism [119]. Field evaporation is the dominant mechanism in LMIS which contribute to ion and induced electrons formation.

To provide E fields exceeding the emission threshold, called onset voltage, a counter electrode termed extractor (V_{ex}) is used. It aids in both ionization and acceleration process. It enables to reach potentials difference exceeding 10 kV. The extractor is placed around the crown of needles to obtain homogeneous fields.

Laboratory units

For all measurements, the thruster holding structure is grounded to the vacuum chamber wall. Moreover, to ease the acquisition of the ion signal, direct neutralisation of the low current density ion beam produced by the thruster is not necessary, so neutralizers were turned off. Results described in this thesis rely on measurements and analysis of the ion beam produced by four laboratory versions of the ENPULSION NANO. Each laboratory unit (LU) crown displayed in figure 3.18 have different needles distribution. LU-A (top left) had only 9 injectors not well distributed in the azimuthal direction whilst LU-B (top right) had also a reduced amount of total injectors firing (16) but well distributed. The reduced amount of firing emitter tips is due to the production process used for these laboratory units [33]. More than 85% of the injectors are firing for LU-C and LU-D allowing comparisons between these two units. Thruster parameters during firing

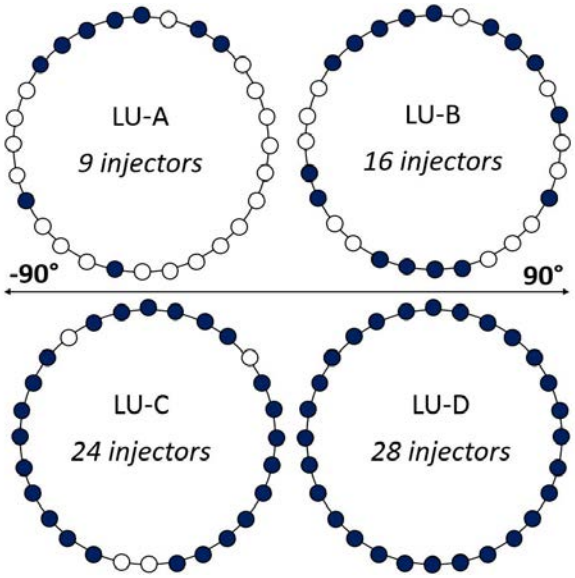

Figure 3.18: Ion emitter distribution on the crown of the four laboratory units used in the thesis. The ion beamlet distribution of LU-A, B and C was determined in FH chamber whilst LU-D was firing in LIFET 4.

conditions are recorded by the PPU with 1% of uncertainty enabling high stability and accuracy during measurements.

Through the test campaign the emission voltage was set between 2 kV and 10 kV. The thruster was fired at 1 mA, 2 mA, 3 mA and 4 mA of current emission. The extractor voltage is adjusted to keep one of these two parameter constant when the other varies. The stability of the controlled emitted ion current for different thruster operations is plotted for LU-A, LU-B and LU-C in figure 3.19. The signal is centred to 0 for better oscillation visualizations. Here, signals are stable as the standard deviation is never larger than 3% of the commanded current. Hence, considering an uniform distribution and a coverage factor of 3 for a level of confidence of 99%, values given for η_p are displayed with uncertainties of $\pm 4.5\%$.

Plasma parameters

An I-V curve acquired with a PP in the plume of LU-B is displayed in figure 3.20. An estimation of the plasma parameters retrieved from measured I-V are shown in figures 3.21 and 3.22. We observe that λ_D is of the order of few centime-

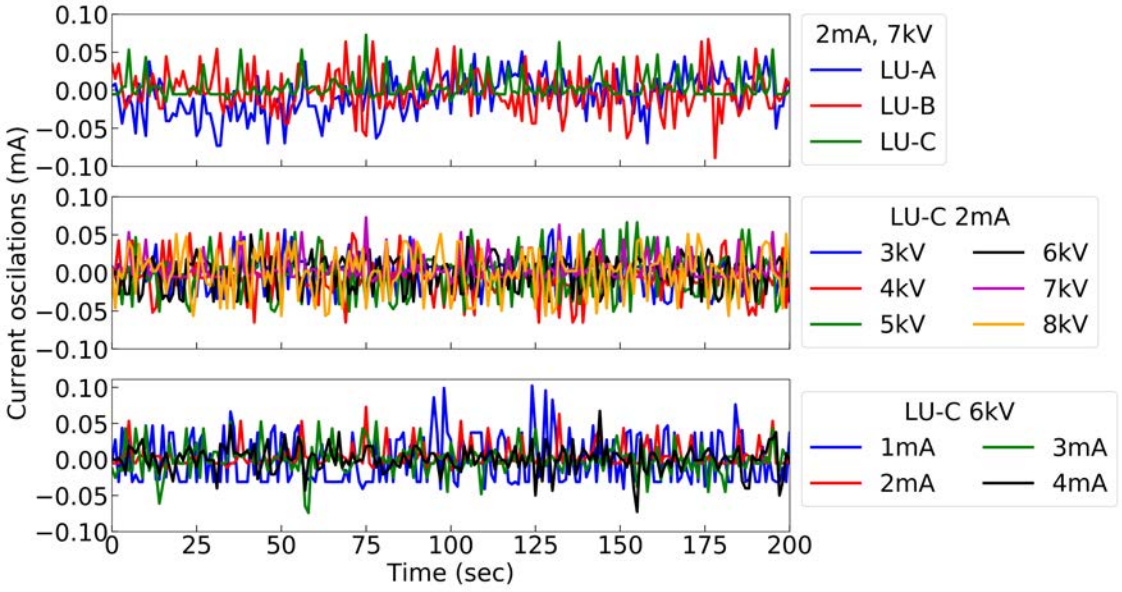

Figure 3.19: Ion current reading stability of LU-A, LU-B and LU-C for different thruster operating points.

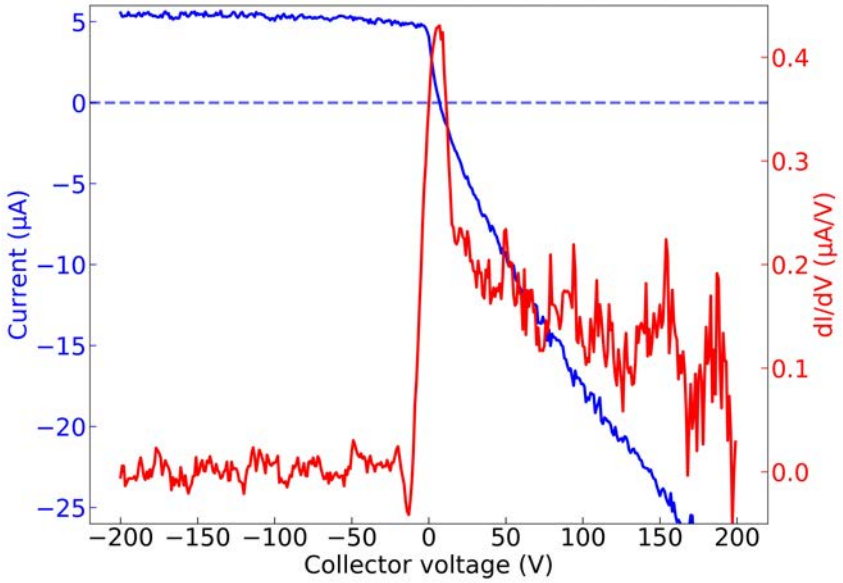

Figure 3.20: I-V curve (blue) and first derivative (red) acquired with LU-B at 0° when firing at 2 mA and 8 kV.

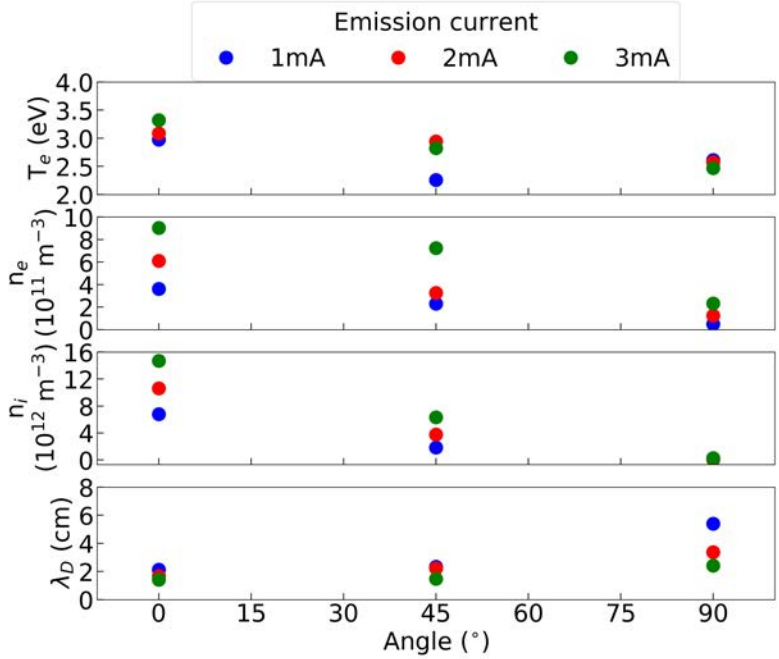

Figure 3.21: Plasma parameters for different angular positions and emission current (I_{em}) at constant acceleration potential (V_{em}) of 8 kV. The thruster is LU-B.

.

tres and slightly increases at angular positions away from the thruster axis. The electron temperature and density decreases at large angles. Note that the plasma potential is low and stable around 8 V for all thruster operations. The electrons inside a FEEP ion beam originates from thermal emission and interaction with the chamber walls. We note that the ion density can be up to 18 times higher than the electron one. This is mainly due to the absence of electron source to neutralize the beam. This value decreases as the probe moves towards larger angles. Nevertheless, it stays constant even when the emission current increases. Indeed, both electron and ion densities increase with I_{em}. T_e is quasi constant around 2.5 $\sim$ 3 eV. When fixing the emission current and applying different voltages to the emitter electrode we observe that both the electron and ion densities increase with the potential applied. Nevertheless, the electron to ion density is constant with the elctron population accounting for 5.7$\pm$0.7% of the ions. As a result λ_D is the lowest when the applied voltage is the highest. The average electron temperature is stable at $\sim$3 eV.

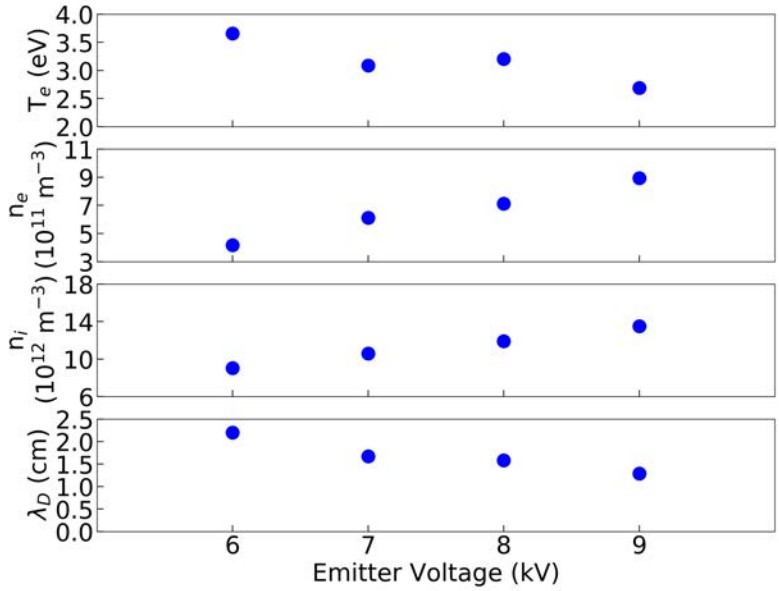

Figure 3.22: Plasma parameters for different emission voltage (V_{em}) at constant current emission (I_{em}) of 2 mA. The thruster is LU-B.

.

We note that the densities for a FEEP thruster are 3 to 4 orders of magnitude lower than in the case of Hall thrusters. The main consequence is that the Debye length is 100 times higher for FEEPs than for HTs. Figure 3.23 confirms that to implement a diagnostic providing accurate information on the ion parameters of a electric thruster plume, a planar probe is not a reliable option. Instead, one shall use a tool mitigating at maximum the sheath expansion during measurements. Indeed the figure displays I-V curves (top) acquired on the axis of LU-B and the ion current density angular distribution measured for LU-C with a PP and FC. Both laboratory units fire at 2 mA and 7 kV. In both cases the ion current is $\sim$1.87 times higher with the PP than with a FC. Moreover, the I-V shows that with a FC measurements are less disturbed by the electron population as the probe manages to screen most of them. When the voltage applied to the probe overtakes 0 V the PP drops towards negative values whilst the FC current barely changes. Moreover, the ion current traces displayed on the top plot of figure 3.23 have a slope near $\sim$1.53 nA cm^{-2} V^{-1} for the PP and 0.55 nA cm^{-2} V^{-1} for the FC. The factor three between the two slope values is caused by the sheath expansion and ion-induced electron perturbations undergone by the PP as it will be shown in section

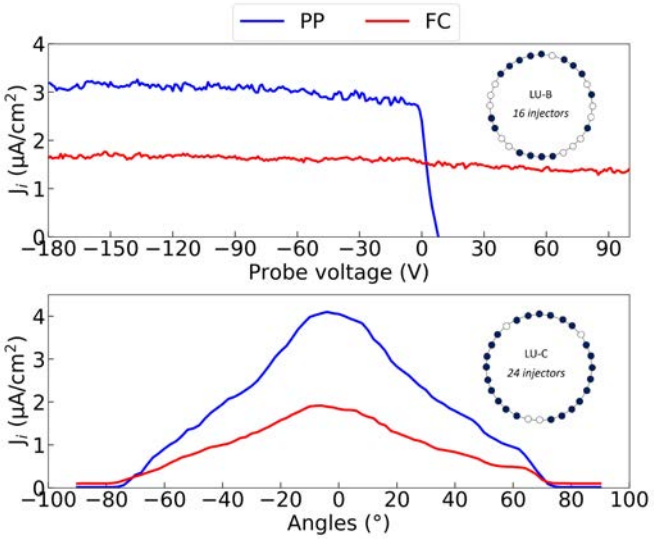

Figure 3.23: Probe type impact on the acquisition of the ion current. LU-B (top) and LU-C (bottom) are firing at 2 mA and 7 kV. The curves represent current acquired with a planar probe (blue) and a Faraday cup (red).

4.

Current-voltage characterization

When using a Faraday cup, the I-V characterization of the ion beam from the ENPULSION NANO differs from the one measured with a Hall thruster can be observed when comparing figures 3.15 and 3.24. Indeed, if thermal electrons are properly screened the measured current is mainly an ion current even when the collector voltage is larger than 0 V. Figure 3.24 displays an I-V curve acquired on the FEEP thruster axis (0°) with the FC 50.Al.05.P - F.Al.4. The collector (V_{coll} or V_c) potential is swept while the repeller ($V_{repeller}$ or V_r) is biased to -100 V. The top plot represents the collector current while the bottom one shows the current on the repeller acquired simultaneously. The dashed lines delimit three distinct zones:

1. In the case of $V_c < V_r < 0$, both electrodes measure an ion current. However, the current measured by the repeller only accounts for 1% of the total current entering the probe.

2. At $V_r < V_c < 0$, a current drop occurs on the collector while the current mea-

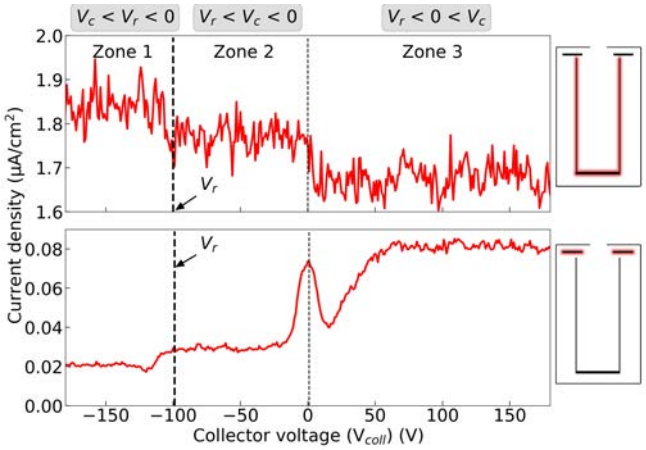

Figure 3.24: I-V characterization acquired with FC 50.Al.05.P - F.Al.4 at 0° displaying three different regions. V_r is fixed at -100 V. Current measured on the collector (top) and repeller electrode (bottom) are acquired simultaneously. LU-B fires at 2 mA, 7 kV and -7.4 kV

sured by the repeller increases. It corresponds to a change of direction of ion-induced electron (see section 2.1.5 and 4.1) produced by the collector. The ion current measured by the repeller now approaches $\sim 1.5\%$.

3. When $V_r < 0 < V_c$ the collector current drops again while the repeller current rises to reach magnitudes three times higher than in zone 2, and close to 4.5% of the total current going through the propbe is measured. This current variation is caused by thermal and induced electrons produced by the probe front as well as by a fraction of primary ion or scattered ions from the cup. Once the collector potential is above 0 V, electrons that were shielded by the repeller in zone 1 and 2 can now go through the potential barrier and reach the collector.

Therefore, zone 2 gives the most accurate value, undisturbed, of the ion current. Note that the slope measured in zone 2 between -100 V and 0 is small enough ($\approx$ -42 pA . V$-$1) to consider any voltage point to provide the correct ion current. Therefore, current density angular distribution measurement of the ENPULSION NANO shall be done with the FC following the condition : $V_r < V_c < 0$.

Table 3.5: Evolution of the probe efficiency for different extractor voltages.

I_{em} mA	V_{em} kV	V_{ex} kV	η_p #
3	12.9	-3	0.941
3	11.3	-5	0.948
3	9.8	-7	0.951

Impact of the needle distribution

Before assessing different Faraday cup designs, let us study the influence of needle number and distribution on the ion beam profile and probe output. LU-A (red) and LU-C (blue) ion current density angular distributions are plotted in figure 3.25. Due to the lower number of needle firing, to reach the same emission conditions the extractor voltage had to be adjusted. Therefore, LU-A had V_{ex} = -9.85 kV and LU-C had V_{ex} = -3.95 kV to reach 2 mA and 7 kV of current and voltage emission, respectively. We observe that the beam profile for LU-A is more deformed with a lower current between [-20:20]°. When we compute η_p, the ion collection efficiency of the probe (see section 2.3.4), we obtain 80.9±4.5% for LU-A and 97.2±4.5% for LU-C. In the case of LU-A most of the firing needles are grouped on the top of the crown. Then, when the extractor voltage is set to high value, like in this case, the ion beam deviates from the thruster axis and moves upward. Therefore, an important fraction of ions fly above the probe. The impact on the beam divergence is also non negligible although weaker. Indeed, θ_{div} is 66 ° for LU-A and 69 ° for LU-C. So, LU-A divergence angle is only 4.5 % lower than LU-B whilst the crown fires with only 32% of its capacity. Similarly, up to 80% of the ion current is captured by the probe in the case of LU-A despite measurements made on a single plane with the hypothesis of symmetry around the thruster axis. Nevertheless, figure 3.25 shows that probe design parameters cannot be compared from one laboratory unit to another except if there is enough needles firing with a relatively uniformed distribution in the azimuthal direction..

Impact of the total applied voltage

To compare probe design while using the same laboratory unit one must set constant firing parameters. As explained earlier, due to numerous vacuum cycles and other parameters such as temperature, the emitter crown impedance can vary between each cycle. Therefore, the extractor voltage needs to be adjusted to reach

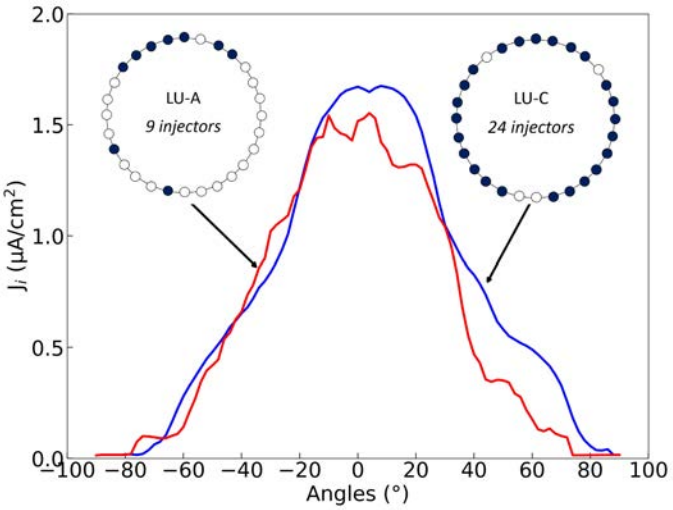

Figure 3.25: Impact of the needle number and distribution on the ion beam shape. LU-A and LU-C are firing at 2 mA and 7 kV. The extractor voltage is fixed at -9.85 kV for LU-A and -3.95 kV for LU-C.

similar firing conditions. We used LU-D in FOTEC's LIFET 4 chamber to measure the applied voltage influence on the probe outputs. In contrast to the set-up used with LU-A, LU-B and LU-C with the FH chamber, at FOTEC we were able to use two external high voltage power supplies enabling higher total discharge voltage between the emitter and the extractor. Figure 3.26 displays the evolution of the beam divergence against emitter or extractor voltages. The dashed lines are linear fits. The blue line fits the data where the extractor and emitter voltage change but the emitter current is fixed at 3 mA. The red line fits data with a fixed extractor voltage but different emission parameters. In all cases, the emitter fires with 28 needles. We observe that the beam divergence is not, or very little, impacted (red) even though the thruster current and voltage output increase. On the opposite, the beam divergence increases with the extractor voltage (blue). Interestingly, the total ion current measured by the probe is almost not impacted by the change in parameters. Table 3.5 displays the total ion current I_{iint} and probe efficiency computed from the ion current density angular distribution of the LU-D. We note that despite the change of extractor settings inducing a slight enlargement of the beam as displayed in figure 3.26 the probe efficiency is not impacted and measures close to 95% of the ion emitted current.

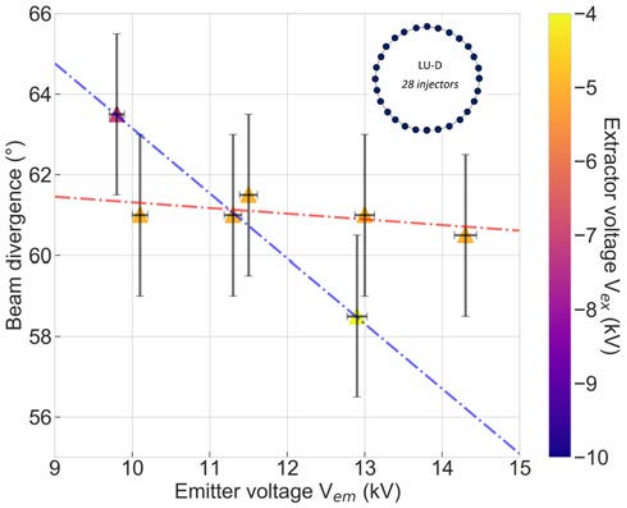

Figure 3.26: Beam divergence computed from the LU-D ion beam firing with 28 needles. The emitter current was 2, 3, 4 and 5 mA for extractor voltages at -5 kV and 3 mA for V_{ex} = -3 kV and -7 kV.

Current losses to the extractor

During ion current density angular distribution scan, the extractor voltage and current is constantly monitored with the same accuracy than the emitter section. The current measured on the extractor electrode originates from ions accelerating from the needle tip with a velocity vector directed towards the extractor. This can happen when the extractor voltage is set to very high values. For instance, in the spirit to asses a worst case scenario, we measured the ion current losses to the extractor of LU-A when it fires at 2 mA, 7 kV and with V_{ex} set to -9.85 kV. The extractor collects in average 3.1±0.65% of the emitted ion current in such circumstances. This value goes down to 0.085±0.025% for LU-C where the firing needles are well distributed and the extractor voltage is reduced. Moreover, at firing conditions where the emitted current allowed by the PPU is maximum (e.g 4 mA) and V_{ex} is set to -9.25 kV, LU-C extractor only intercepts in average 0.38±0.04% of the emitted ion current, which is negligible. Nevertheless, for consistency the current use to compute the ion collection efficiency η_p corresponds to I_{em} - I_{ex}.

Chapter 4

Ion beam study: The ENPULSION Nano FEEP

Contents

In this section, our study focuses on the optimization of a Faraday cup architecture to accurately measure the ion current in the plume of a FEEP thruster. We first characterize the impact of ion-induced electrons on the probe measurement outcomes. Then, we evaluate several passive methods (e.g. cup length, shape and material) to mitigate this effect before actively (FC field lines modifications) changing the ion-induced electrons direction towards the cup. We investigate the

influence of the aperture diameter and material. Based on these results we show how the distance between the probe entrance and the cup is a critical design parameter. Finally, we discuss the effect of the facilities and probe distance to the thruster exit plan on the thruster beam divergence.

4.1 Ion-induced electron emission

4.1.1 Measurement method

In section 2.1.5, we broached the impact of ion-induced electron emission (IIE) on the measured current. In the case of indium-based FEEP thrusters data is scarce on how important is this phenomenon upon the ion current. One shall remember that the yield of ion-induced electron emission, γ_{EE}, depends on projectile ion energy, incidence angle and collector material properties. Commonly, γ_{EE} is determined by applying a voltage sweep on the ion collector V_{coll} placed downstream an electrode V_{ele} with a fixed negative voltage [120, 65]. When $V_{coll} < V_{ele}$, the current measured on the collector is $I_c = I_{i\&EE}$, with $I_{i\&EE}$ the ion current including the contribution from IIE. Then, when $V_{coll} > V_{ele}$, the current measured on the collector corresponds to the true, i.e. unperturbed, ion current, $I_c = I_i$. Therefore, as showed in section 2.1.5, γ_{EE} reads [42]:

$$\gamma_{EE} = \frac{I_{i\&EE} - I_i}{I_i}. \tag{4.1}$$

However, if one only uses the above mentioned measurement method two problems arise when $V_{coll} > V_{ele}$: 1) the collector will start to collect ion-induced electrons emitted by the electrode placed upstream, 2) a fraction of the ion current can be collected by the electrode and not the target. In both cases the yield for the target will be impacted. These issues are only valid if the beam studied is mainly collected by the probe rear part. In the case of the ENPULSION NANO we assume it is the case based on visual inspection of the probe once it has been used as pictured in figure 4.1. To mitigate the artificial rise of γ_{EE} the architecture of a FC was modified, see figure 4.2. This way, the FC can be configured with a cup (A) or a disk (B) as ion collector. The repeller placed upstream is biased negatively to screen thermal and ion-induced electrons emitted by plasma-probe interaction. Two I-V curves, for an ion collector made of aluminium (FC 50.Al.7.P - F.Al.0), are displayed in figure 4.3 illustrating the problem stated above. The ion current without IIE contribution should correspond to the current measured in zone 2 (see

Figure 4.1: Photograph of the rear part of a Faraday cup exposed to the ion beam. The circle distribution is defined by the probe aperture diameter.

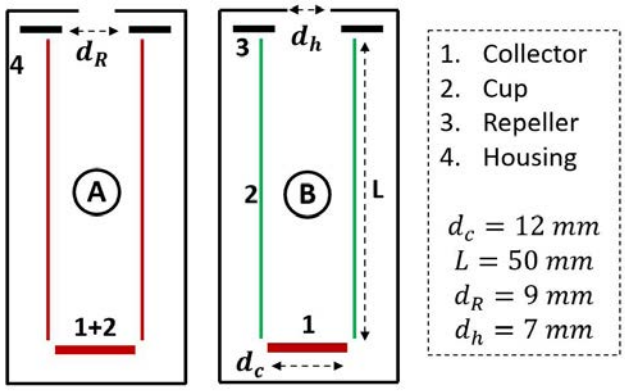

Figure 4.2: Schematic of probe configuration used to measure γ_{EE}

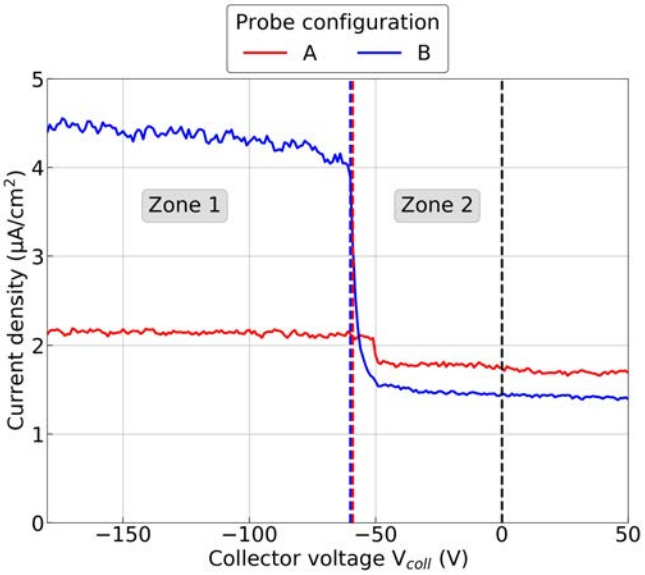

Figure 4.3: I-V curves measured with different probe configurations. Probe *A* uses the collector and the cup as one electrode while with configuration *B* these two elements are electrically uncoupled. The two coloured dashed lines corresponds to V_{ele} at -60 V. The black dashed line ease the visualisation for the transition from negative to positive voltages. The thruster is LU-C.

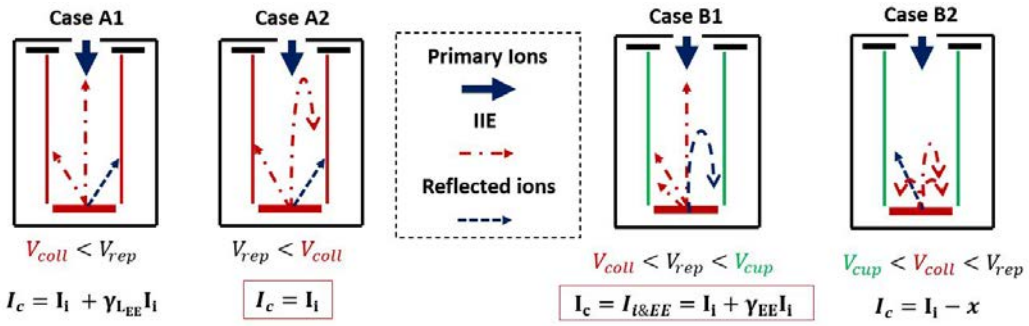

Figure 4.4: Explanation of the measurement method to obtain γ_{EE}

section 3.3.2). However, in this zone the two configurations A and B give different values with $I_B < I_A$. Figure 4.4 provides explanations for current measured in zone 1 and 2 for configuration A and B. In zone 1, IIE are not recollected with both configurations, since V_{ele} is higher, hence an overestimated measured current. The current measured by B is increased due to IIE from the ion collector located at the rear of the probe. The current measured by A is solely perturbs by ion-induced electrons that escape the cup (see section 4.2.2). Therefore, in both cases the current is artificially increased but not with the same factor. A manages to recollect an important part of ion-induced electrons in zone 1. In zone 2, all ion-induced electrons are recollected as $V_{coll} > V_{ele}$, V_{ele} being V_{rep} and V_{cup} with configuration A and B, respectively. The current difference seen between the two configurations is because a fraction of the ion signal is now collected by the cup in the case of B.

Figure 4.5 and 4.6 show the current change with the voltage inside probes A and B with FC 50.Al.7.P - C60.Al.0. In configuration A (figure 4.5), the repeller is biased to -60 V and IIE are recollected when V_{coll} is higher than V_{rep}. The shift observed is caused by a potential dip at the repeller aperture centre. While a current drop is observed on the collector (top), no specific change is seen on the repeller (bottom) at the same voltage. This seems to indicate that in zone 1 induced electrons from the cup are not collected by the repeller but leave the probe instead. Moreover the ion current measured in zone 2 by the repeller is 100 times lower than the collector current and therefore, can be neglected. In configuration B, a different behaviour is observed. Figure 4.6 is divided in three plots. The first one (top) show currents measured by the collector. The second plot (middle) displays currents acquired by the cup. The third one (bottom) compares the current measured with configuration A against the sum of currents acquired by the

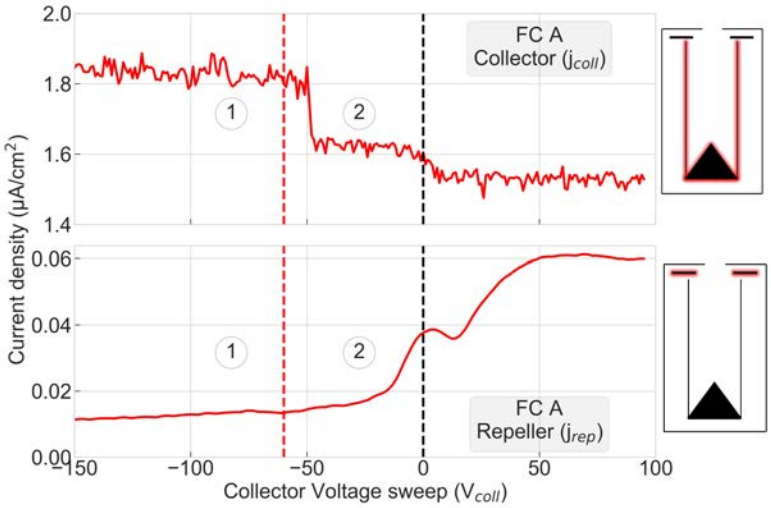

Figure 4.5: Current measured on the collector (top) and repeller (bottom) simultaneously during a voltage sweep on the collector. The probe is FC 50.Al.7.P - C60.Al.0 in configuration *A*. The thruster LU-C fires at 2 mA and 6 kV.

collector and cup with *B*. On the top and middle plot, three different voltages are applied to the cup: −60 V, 0 V and 20 V. In each cases the current value is the same on the collector and cup before and after IIE recollection. Indeed in zone 1, the current measured on the cup is mainly from electrons, hence negative, corresponding to IIE emitted by the collector. When V_{coll} overtakes V_{cup} the cup current becomes positive and goes higher than the current observed on the collector which decreases. When the voltage applied to the collector reaches 100 V near 90% of the ion current inside the probe is measured by the cup with only 10% remaining on the collector. In this configuration, IIE from the collector are properly recollected by the latter but an additional electron current is collected as well and a large ion loss towards the cup sides is observed. On the third plot (bottom) we clearly see that the sum of currents measured on the cup and collector matches the current measured by FC *A*, and overall no losses are observed. The current peak observed corresponds to the IIE recollection at 60 V (i.e. V_{ele}). In the same manner, the ion current behaviour is measured for a flat stainless steel collector (FC 50.Al.7.P - F.S.0) and the corresponding I-V curves are plotted in figure 4.7. LU-C fires at 1 mA with V_{em} sets to 3 kV (bottom) and 5 kV (top). Currents acquired simultaneously on the collector (blue) and cup (green) with FC *B* as well as their sum (black) are plotted along with current measured with FC *A* (red). At

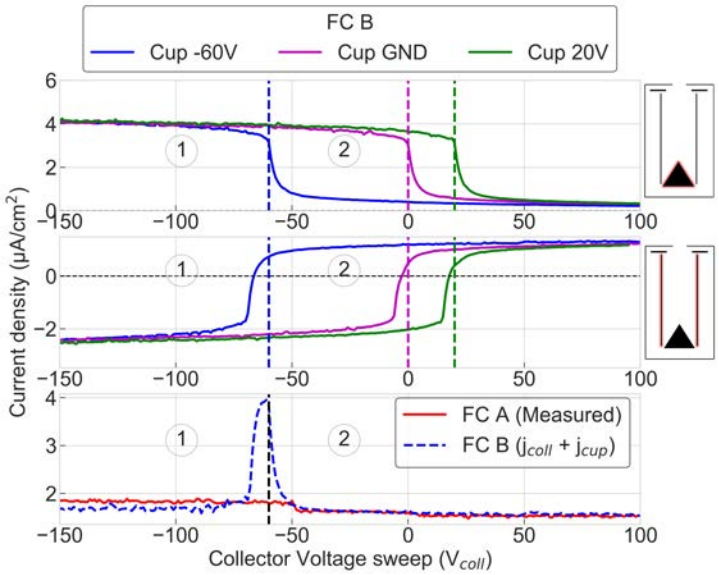

Figure 4.6: Current acquired simultaneously on the collector (top) and cup (middle) during a voltage sweep on the collector. The probe is FC 50.Al.7.P - C60.Al.0 in configuration *B*. The thruster LU-C fires at 2 mA and 6 kV. The bottom plot compares current acquired with FC *A* and FC *B*.

Table 4.1: List of materials used as ion collector.

Material	Geometry	Properties	Name
Aluminum	conical	Plain, $\alpha_1 = 105°$	Alc
Aluminum	conical	Plain, $\alpha_2 = 60°$	Alc2
Aluminum	flat	Plain	Al
Aluminum	flat	Foam #1[5]	F1
Aluminum	flat	Foam #3[5]	F3
Aluminum	flat	Foam #6[5]	F6
Molybdenum	flat	Plain	Mo
Tungsten	flat	Plain	W
Stainless steel	flat	Plain	S

5 kV we notice the same trend than observations made on figure 4.6 for the sum of FC *B* currents and FC *A*. Nonetheless, the current peak is less pronounced due to lower ion energy and ion-induced electron yields at stake (see section 4.1.2). However, at 3 kV no particular current peak is observed. When looking at the current distribution inside the probe we see that at 3 kV, near 98% of the ion flux inside the cup reaches the collector. Moreover, no electron current is measured on the cup due to the extremely low yield of stainless steel in this firing condition. However, when $V_{coll} < V_{cup}$ a non negligible amount of the ion flux starts to be collected by the cup ($\sim 13\%$). Through experiments it was observed that for every flat materials studied, 10 to 20% of the ion flux is measured by the cup once electrons emitted by the collector are recollected (i.e. $V_{cup}<V_{coll}<0$). Moreover, compared to I-V showed in figure 4.6 with a conical collector, it can be argued that the fraction of ion flux measured on the cup varies with the collector shape. These observations confirm the starting assumption regarding the collection of the whole ion flux by the collector and the need to implement our segmented Faraday cup to properly determine γ_{EE}. Therefore, currents obtained with the FC $B1$ and FC $A2$ will be used in equation 4.1 to accurately determine γ_{EE}. To measure I_i FCA voltages follow $V_{coll} = -30$ V and $V_{rep} = -60$ V. To acquire $I_{i\&EE}$ FCB voltages are $V_{coll} = -30$ V and $V_{rep} = 20$ V. It was possible to measure γ_{EE} for flat and conical aluminium collector, flat tungsten collector, stainless steel as well as molybdenum and aluminium foam with different pore sizes as described in table 4.1.

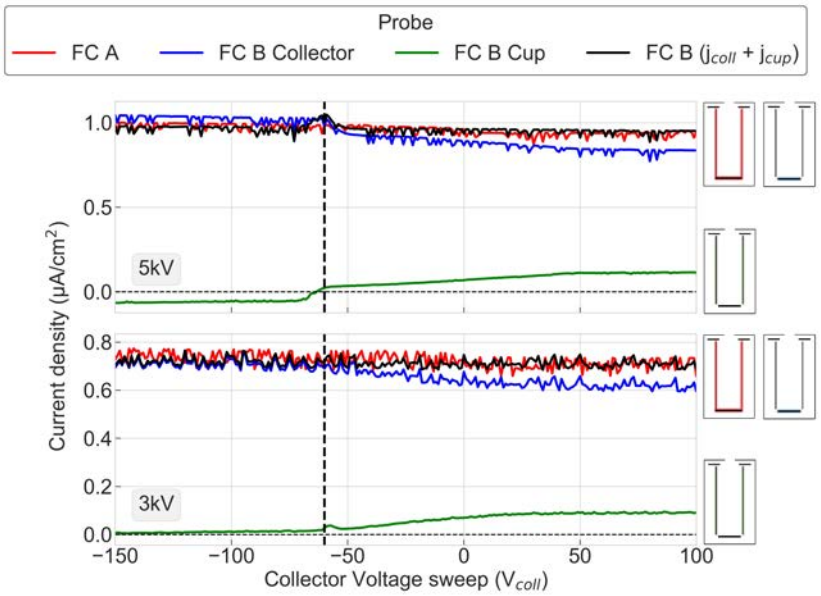

Figure 4.7: IV curves for a flat stainless steel collector (FC 50.Al.7.P - F.S.0) with firing condition of 1 mA 3 kV (top) and 5 kV (middle). The two first plots compare current acquired between with FC *A* (red) and FC *B* collector (blue) and cup (green) during a voltage sweep on the collector. The bottom plot compares current acquired with FC *A* (red) and FC *B* (blue) at 1 mA and 5 kV. The thruster is LU-C.

4.1.2 Ion collector material property

Figure 4.8 displays ion-induced electron yields measured following the method detailed in section 4.1. Material studied are aluminium (a), tungsten (b), molybdenum (c) and stainless steel (d) flat discs, which are widely used amongst the EP community. The plots display the evolution of their respective γ_{EE} against the mean ion energy for different emission current. Note that in this case study $E_{mean_i} \gg \phi$, as ϕ is of the order of a few eV [42] for studied materials. Therefore, PEE mechanism are neglected and only KEE are considered. Figure 4.8 shows that the yield increases monotonically for all materials. However, while the yield is of the same order for molybdenum, tungsten and steel, γ_{EE} obtained with aluminium is 3.5 to 4.5 times larger. Moreover, between the lowest and highest mean ion energy the growth rate differs for the four materials. Indeed, the rise is around 57% for molybdenum, 67% for tungsten, 72% for aluminium and approaches 95% for steel. It is noteworthy to mention that these yields are up to 2 or 3 orders of magnitude larger than data available in the literature for xenon, krypton and iodine [63, 65]. In addition, in the case of an aluminium collector we note that at 2 mA the yield is getting larger than the other measured yield above 5 keV. After several measurements we saw that the behaviour keep occurring. The reason for such decoupling of the yield is still unknown as the yield should only depend on the ion energy and not on the current.

Figure 4.9 shows γ_{EE} obtained with different ion collector aluminium properties and geometry. Figure 4.9a shows the evolution of the yield for aluminium foams *AlSi7Mg* F1 and F6 as described in section 3.2.2 with LU-A firing at 1 mA. In both cases the yield increases with the ion energy. However, the yield is smaller for F6. In average γ_{EE} drops by 26%±8.4% between F1 and F6. Nevertheless, the yield variation between low and high ion energy impact approaches 40%±3% for both collectors. The observed yield reduction can be caused by different IIE emission sites. When increasing the pore size, IIE originates from deeper locations inside the collector. Hence the probability to recollect IIE before they escape the foam structure increases.

Figure 4.9b shows the evolution of the yield for a flat bulk aluminium collector (Alf) and a flat foam aluminium collector (F6) measured with LU-C. First, γ_{EE} is in average 60%±8.5% lower with F6. Second, the difference between both yields slightly increases with the ion energy indicating that a foam structure is less impacted by the increase of ions energy.

It is observed that γ_{EE} for F6 measured with LU-A and LU-C is not the same. Figure 4.10 shows the variation of γ_{EE} for Mo (bottom) and F6 (top) obtained

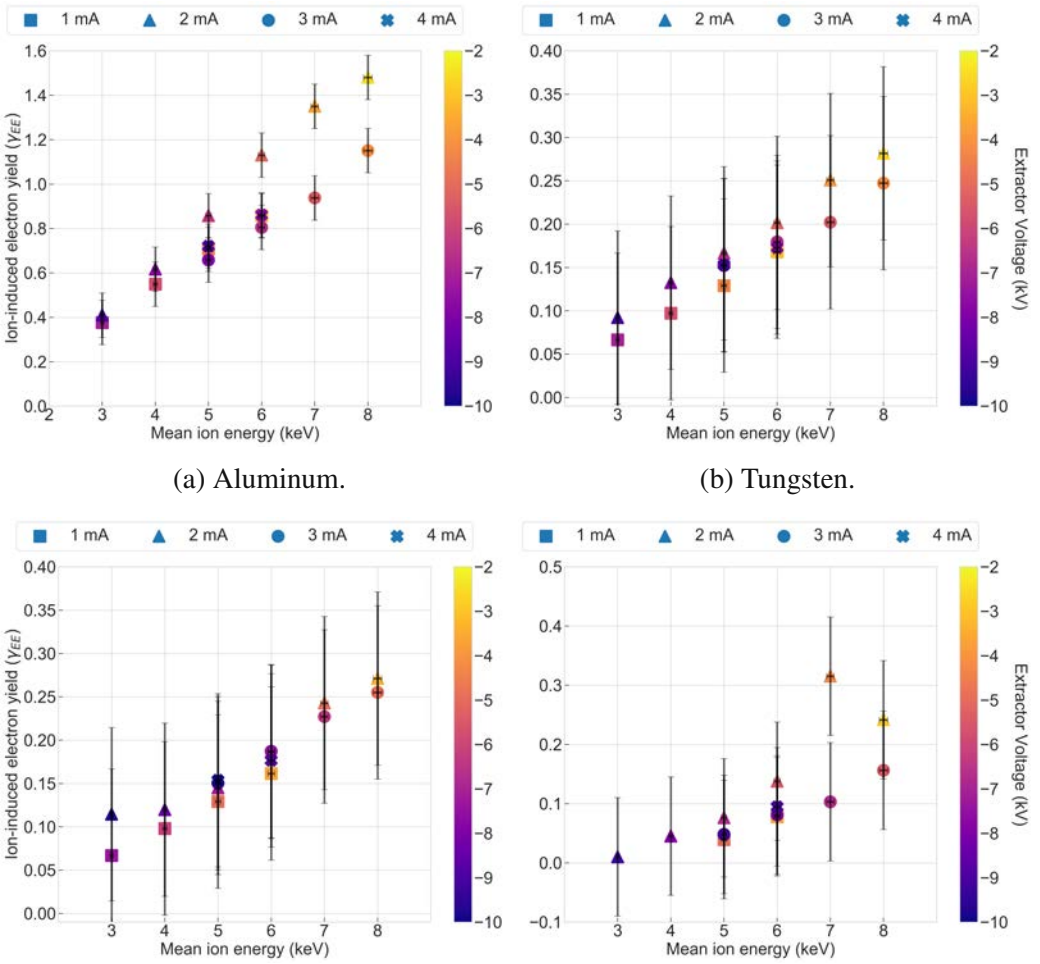

(a) Aluminum.

(b) Tungsten.

(c) Molybdenum.

(d) Stainless Steel.

Figure 4.8: Ion-induced electron yield (γ_{EE}) from different flat ion collector obtained with the thruster LU-C firing at 1, 2, 3 and 4 mA. The ion bombardment is normal to the target.

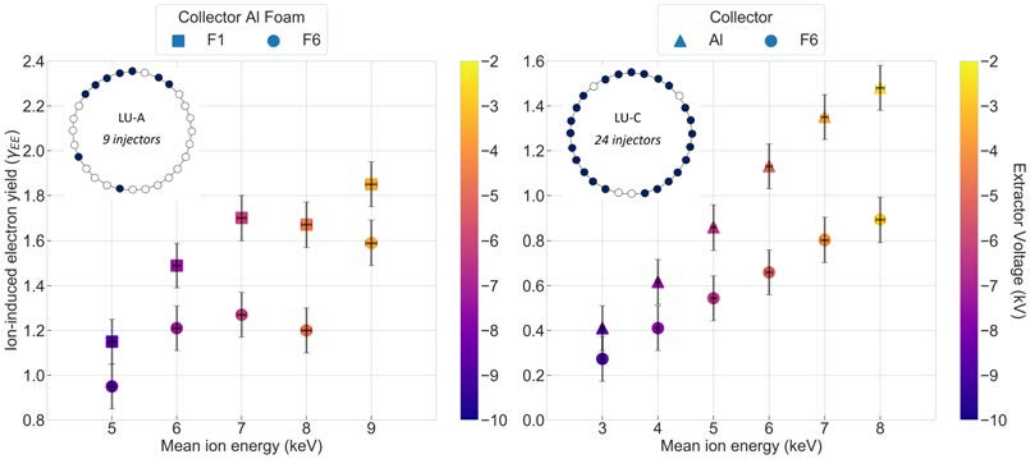

(a) γ_{EE} obtained with LU-A at 1 mA for different aluminium foams.

(b) γ_{EE} obtained with LU-C at 2 mA for aluminium and foam#6 .

Figure 4.9: Dependency of γ_{EE} with collector material property and geometry

with different thruster units. Note that it was not possible to reproduce the exact same operation points as LU-A needed more extraction voltage to provide similar emission parameters. The PPU limits prevented to reach emission voltage below 5 kV for LU-A and above 6 kV for LU-C at 1 mA. γ_{EE} obtained for F6 with LU-A increased by 84% and 98% for 5 kV and 6 kV, respectively. On the contrary, there are no major change for the molybdenum collector as the variations are within the uncertainties of the measurement method. Note that for both materials the rate of change between the minimum and maximum yield is identical +40% and +58% for LU-A and LU-C, respectively. The increase of the measured yield for F6 could be caused by higher dependency to the ion incidence angle than Mo. Indeed, due to the needle distribution and the large extractor voltage used with LU-A the ions going through the probe might not hit the collector with a velocity vector identical to those from LU-C. Owing to its foam structure, the probability to have ions hitting its surface with an incidence angle different than 0° increases. The next section brings insights into the effect of the incidence angle upon γ_{EE}.

4.1.3 Ion collector shape

Figure 4.11 shows the evolution of γ_{EE} for different aluminium collector geometries. Once more the yield increases monotonically with the bombarding mean

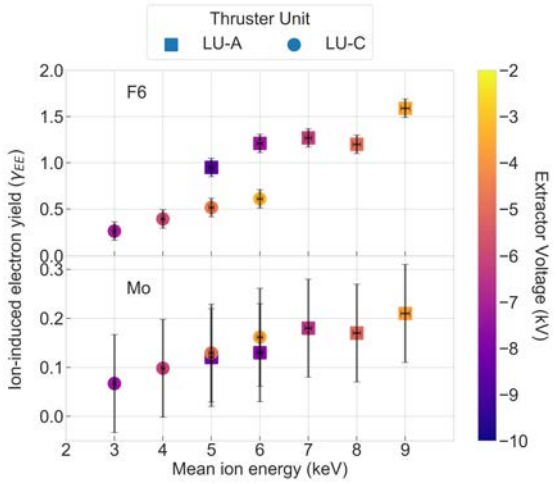

Figure 4.10: γ_{EE} variation for F6 and Mo when measured with LU-A (squares) and LU-C (circles).

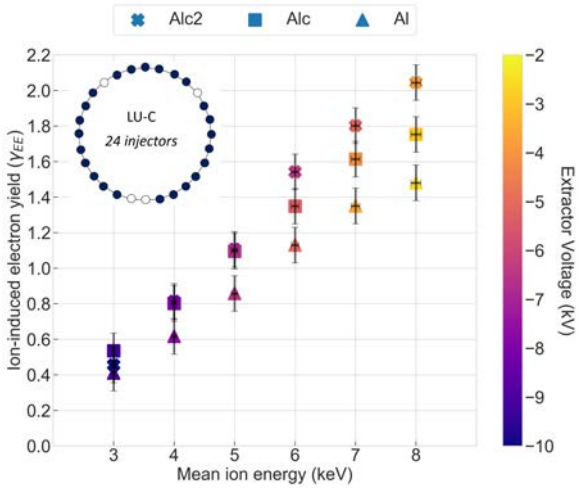

Figure 4.11: Ion-induced electron yield obtained with the ion source LU-C for different collector geometries. The thruster fires in mode 2.

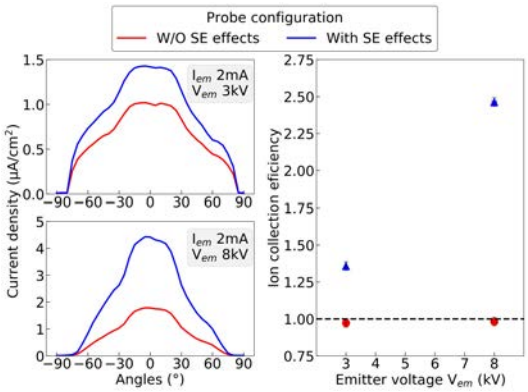

Figure 4.12: Beam profiles (left) and related ion collection efficiency (right) acquired with a flat aluminium ion collector showing the effect of IIE on ion current assessment. The thruster LU-C fires at 2 mA with emitter potential set at 3 kV and 8 kV.

ion energy. Here, we assume that ions entering the probe have a velocity vector purely perpendicular to the probe entrance plane. Therefore, when the angle which defines the conical shape of the collector decreases, the incidence angle (θ_i) increases. In this case, ions hit Alc with $\theta_i = 37.5°$ and Alc2 with $\theta_i = 60°$. We observe that increasing the incidence angle increases the yield of IIE. For higher θ_i it is easier for an ion to rip off electrons from the surface. In average, between Al (flat) and Alc the yield increases by 19.5%±3.4%. From Alc to Alc2 the yield increases by 14.3%±3% at the highest mean ion energy.

4.1.4 Ion-induced electron mitigation.

Despite large ion-induced electron yields at stake when measuring ion properties from indium-based FEEP thruster, the perturbation can be mitigated with the right probe architecture and voltage configuration. Figure 4.12 shows the ion current density distribution acquired with a flat aluminium collector disturbed or not by ion-induced electron emission. The right plot of figure 4.12 displays the corresponding probe ion collection efficiency (η_p). When the IIE are completely suppressed, the probe efficiency is the same no matter the thruster firing condition. Similarly, figure 4.13 shows that without IIE effects the ion current density distribution is independent from the collector material.

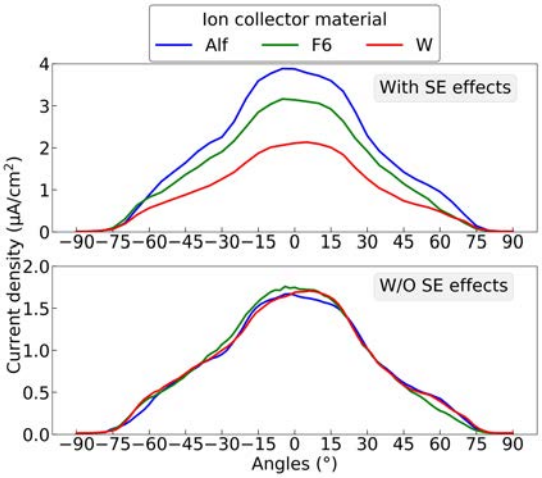

Figure 4.13: Beam profile acquired with (top) and without (bottom) IIE effects for different collector materials. Data was acquired for the ion source LU-C operating at 2 mA and 7 kV.

4.2 FC dimension impact

4.2.1 Measurement method

It was showed that ion-induced electrons have a strong impact on the measured ion current. One solution to mitigate the induced perturbations is to adjust the field lines inside the probe to actively recollect all IIE. Nonetheless, this method can lead to current losses to the electrode used to push IIE back to the collector. In this section, the impact of the probe length is studied to evaluate a passive method to mitigate the fraction of IIE leaving the probe. $\gamma_{L_{EE}}$, the corresponding yield, is used as an indicator of the amount of IIE leaving the probe. It reads:

$$\gamma_{L_{EE}} = \frac{I_{i\&L_{EE}} - I_i}{I_i}, \tag{4.2}$$

with $I_{i\&L_{EE}}$ the current measured by the cup when $V_{coll} < V_{rep}$ and IIE leave the probe.

4.2.2 Length of the cup

In this section three different cup lengths are examined, 50 mm (**50**.G.07.E-F.Al.4), 30 mm (**30**.G.07.E-F.Al.4) and 10 mm (**10**.G.07.E-F.Al.4). Figure 4.15 displays

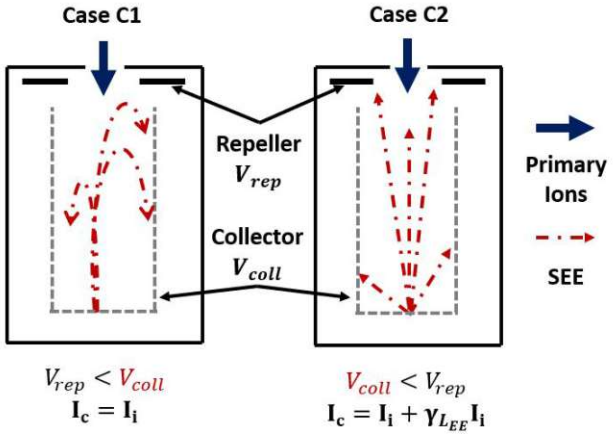

Figure 4.14: Measurement method to obtain $\gamma_{L_{EE}}$

I-V curves acquired with LU-B at 0°. The dashed line represents the repeller potential $V_{rep} = -20$ V. For $V_{coll} < V_{rep}$, the measured current increases when the cup length decreases. Once V_{coll} overtakes V_{rep}, the measured current density drops and the signal is more stable. Nonetheless, while the 50 mm cup measures slightly higher current densities than the 30 mm one, a major difference is noticed between these two cups and the 10 mm one. The previously reported current differences is believed to be due to changes in the thruster extractor voltage. Due to small impedance variations the total discharge voltage had to be adapted to reach similar current and voltage emission conditions. In this case the extractor was at -6.8 kV, -7.1 kV and -7.4 kV for 50 mm, 30 mm and 10 mm respectively. When the extractor voltage increases, the ion current angular distribution enlarges which decreases the ion current on the thruster axis. However, the gap between the 10 mm FC and the two other cups is too large to be only caused by extractor voltage variations. In order to remove the extractor effect upon our measurements, full scans of the ion beam are performed. Results are displayed in figure 4.16 at the top and middle plots. For the top plot, the beam profiles are acquired while no active techniques (i.e. $V_{rep} = 0$) are used to push the IIE back to the collector. On the contrary, for the middle plot all IIE are actively recollected (i.e. $V_{rep} < V_{coll} < 0$). At the bottom is displayed the angular dependency of $\gamma_{L_{EE}}$ for a given cup length. The yield remains constant over the whole beam profile. At large angles ($> 60°$) facilities effect are predominant and signal is too weak to properly compute yields. Once more, we notice that $\gamma_{L_{EE}}$ is larger for the 10 mm cup. Moreover, the beam profile acquired with the 10 mm cup seems to measure less current than the other

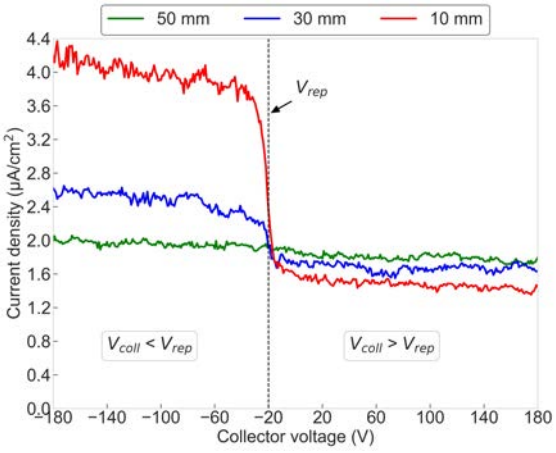

Figure 4.15: I-V curves obtained with a cup 50 mm (circle), 30 mm (square) and 10 mm (triangle) in length. The collector voltage is varied while the repeller is biased to −20 V.

two once all IIE are properly recollected by the collector.

Table 4.2, shows the ion collection efficiency for each probe obtained from the profiles plotted in figure 4.16. When the geometry and potential of the probes are tuned (i.e. second part of the table), the closer to 1 the figures the better (i.e. no artificial current rise is measured). Indeed, as expected the 50 mm and 30 mm have a collection efficiency close to 100% when IIE effects are suppressed. Moreover, without active recollection of the IIE the 30 mm cup is sensitive to the ion energy, the higher the energy the larger the overestimation of the ion current. On the opposite, the 50 mm cup is little or not impacted by the ion energy and only overestimate the ion current by 5% when only passively recollecting IIEs. Regarding the 10 mm cup, it is the most sensitive to ion energy changes and only provides ion collection efficiencies close to 85% once all IIE are actively recollected. It confirms that the current densities difference observed in figure 4.15 and 4.16 are not caused by an extractor voltage variation. The ion losses observed with the 10 mm cup is likely to be caused by reflected ions not properly recollected. Indeed, if an ion is not properly neutralized when hitting the cup rear part, it can be reflected with an unknown direction. The ion trajectory simulation software SIMION was used to bring some insight into the ions behaviour inside the cups (see section 2.2.2). The reflected ion originates from a circle distribution located at the cup rear part with a diameter equal to the probe aperture, as showed in figure 4.17. The collector voltage is to -50 V ans is considered negligible before the ion

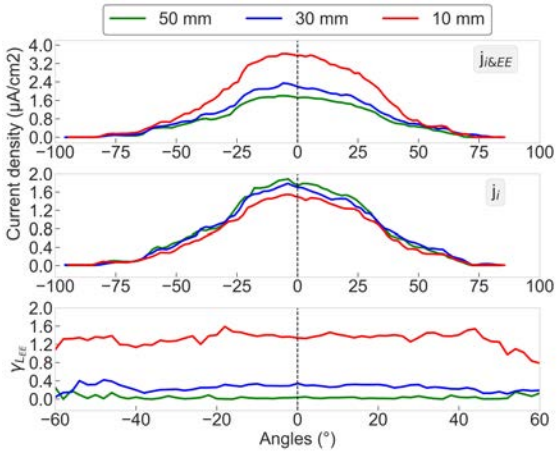

Figure 4.16: Ion current densities profile of the laboratory thruster measured with a 10 mm, 30 mm and 50 mm long cup. Case of loss (top) and recollection (middle) of IIE. The angular distribution of the respective $\gamma_{L_{EE}}$ is plotted at the bottom. LU-B fires at 2 mA and 7 kV.

energy of the reflected particles. Therefore, only the reflected angle is modified in the simulation with a distribution going from 0° to 90° with 1° increment. The simulations show that in the case of a 50 mm and 30 mm long cup, reflected ion are still collected by the side of the cup for reflection angles lower than 81° and 77°, respectively. However, in the case of a 10 mm long cup, ions start to escape the probe for reflection angles larger than 46°. Hence, we see that it is more probable to have ions being reflected outside the cup for a 10 mm long cup.

Figure 4.18 plots the dependency of $\gamma_{L_{EE}}$ against mean ion energy. Yields are the largest for the 10 mm cup and highly dependent on the mean ion energy. This difference could be linked to 1) the IIE energy, the more energetic the IIE the higher the probability to reach the top and 2) the IIE emission angular distribution. The IIE are expected to have energies of a few eV and would be accelerated by the electric field inside the cup. However, modifying the voltage applied to the collector and the repeller does not modify the yield, therefore it can be assumed that the emission angular distribution is the predominant process. Once more the SIMION software was used to simulate IIE emission for each cup length. The emission site is centred on the probe axis with a circle distribution as large as the probe aperture. 200 electrons are flown with emission divergence angle from 0° (straight line) to 90° as pictured in figure 4.19. All electrons reaching the probe aperture are counted as lost and contribute to the ion current bulk. Note that we

Table 4.2: FC $\gamma_{L_{EE}}$ measured for different cup lengths (50 mm, 30 mm and 10 mm) and mean ion energies with 10% error margin. The collector is a flat aluminium foam disk #4.

IIE leaving the probe			
Ion energy	η_p **10 mm**	η_p **30 mm**	η_p **50 mm**
keV	#	#	#
6±0.06	1.82±0.08	1.19±0.05	1.06±0.05
7±0.07	1.95±0.09	1.24±0.06	1.06±0.05
8±0.08	2.06±0.09	1.23±0.06	1.05±0.05
9±0.09	2.26±0.11	1.32±0.06	1.05±0.05
IIE trapped by the cup			
Ion energy	η_p **10 mm**	η_p **30 mm**	η_p **50 mm**
keV	#	#	#
6±0.06	0.85±0.04	1.00±0.05	0.97±0.05
7±0.07	0.86±0.04	0.99±0.05	0.99±0.05
8±0.08	0.84±0.04	0.98±0.05	0.98±0.05
9±0.09	0.85±0.04	0.99±0.05	0.99±0.05

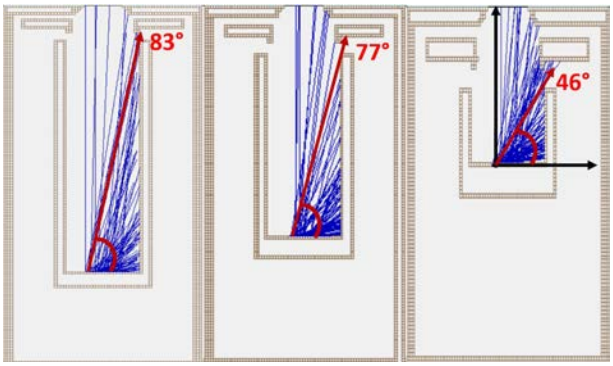

Figure 4.17: Ion trajectory simulation of reflected ions for cup length of 50 mm (left), 30 mm (middle) and 10 mm (right). The angle of reflection varies between 0° and 90° and ions originate from a centred circle distribution with a radius equals to the probe aperture. The collector voltage is set to -50 V and the repeller is grounded.

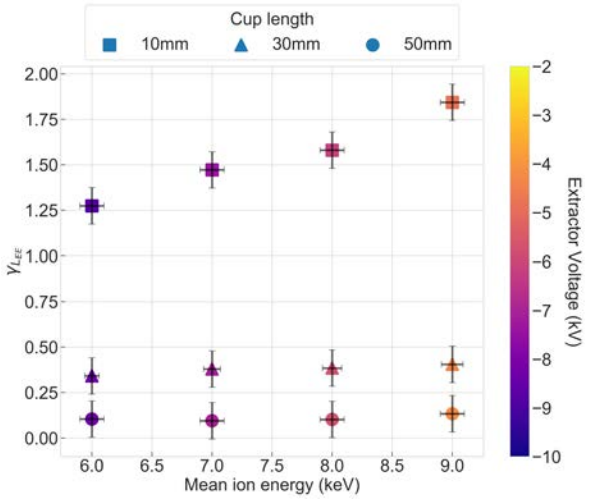

Figure 4.18: Evolution of γ_{LEE} with the mean ion energy. LU-B fires at 2 mA.

only count electrons reaching the aperture and not those being collected by an other electrode than the cup. Considering that $E_i \gg E_{IIE}$ we assume that if IIE manage to go beyond the cup top, they will be attracted by the energetic ion beam coming from the probe aperture. Figure 4.20 displays the evolution of the fraction of IIE leaving the probe as a function of the divergence angle. The dashed lines represents experimental values of the fraction of electrons leaving (κ_{IIE}) the probe obtained as follow:

$$\kappa_{IIE} = 1 - \frac{I_i}{I_{i\&LEE}}, \tag{4.3}$$

This value equals to 9.8±0.05%, 23.9±5% and 59±4% for 50 mm, 30 mm and 10 mm, respectively. They are averaged figures computed for cases with ion energy from 6 kV to 9 kV. Simulations show that the fraction of IIE leaving the probe drops faster as the probe is longer. 20% of the simulated IIE always manage to reach the probe aperture with the 10 mm long cup. The intersection points between experimental and simulation values indicate an estimation of the most probable divergence angle of the emitted IIE. It lies between 33° and 43°.

From our results it is clear that the cup length of a FC is a critical parameter to passively mitigate the effect of IIE upon the measured ion current. Moreover, it shows that even with active mitigation techniques small cup lose ion collection efficiency as they fail to properly trap all ions.

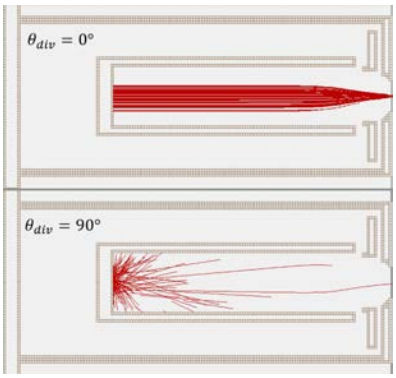

Figure 4.19: IIE trajectory simulated with the software SIMION for a 50 mm cup long. The electrons originate from the cup bottom centred on the probe axis with a diameter equals to the probe front. IIE are emitted with a divergence angle of 0° (top) and 90° (bottom).

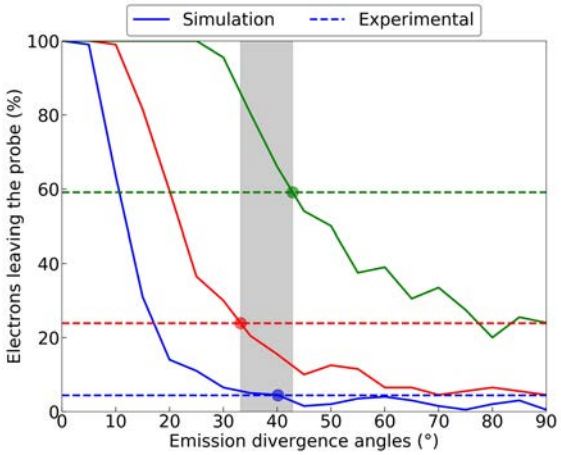

Figure 4.20: Simulated evolution of the fraction of IIE leaving the probe as a function of the emission divergence angle. The dashed lines are averaged values obtained with experimental measurements with cup length of 50 mm, 30 mm and 10 mm.

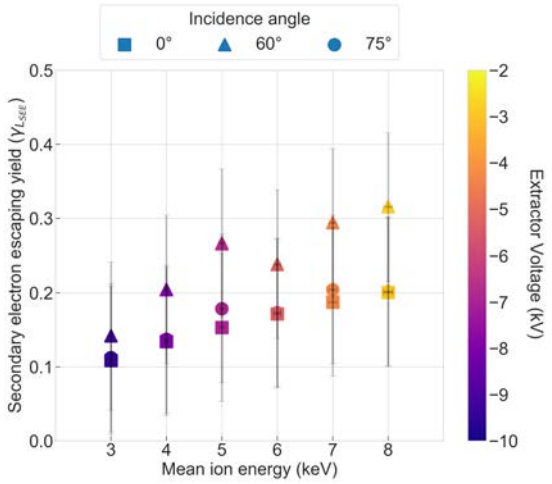

Figure 4.21: Ion-induced electron escaping yield obtained with the ion source LU-C for different collector geometries. The thruster fires in at 2 mA.

4.2.3 Shape of the cup

Another method to passively mitigate the effect of IIE on current outputs is to modify the cup rear part. It was showed in section 4.1.3 that modifying the ion collector increases the fraction of IIE emitted. Nonetheless, section 4.2.2 brought evidence that IIE could have an emission divergence angle ranging between 33° and 43°. Moreover, IIE are emitted normal to the surface where they originate from. Consequently, modifying the direction of emission towards cup inner surface might improve the IIE mitigation. Once more $\gamma_{L_{EE}}$ is used to compare the probe designs. Here, the tested probes are 30.Al.07.P - F.Al.3, 30.Al.07.P - H30.Al.3 and 30.Al.07.P - H60.Al.3, giving θ_i of 0° (square), 75°(circle) and 60°(triangle), respectively. They are 30 mm long cup enabling few IIE to leave the probe without losing ions as detailed in section 4.2.2. Figure 4.21 shows $\gamma_{L_{EE}}$ acquired for LU-C firing with ion energy from 3 kV to 8 kV. As expected $\gamma_{L_{EE}}$ increases between 0° and 60°. In average $\gamma_{L_{EE}}$ is 33.5%±6.2% larger at 60°. However, at the largest incidence angle, $\gamma_{L_{EE}}$ falls back to values measured at $\theta = 0°$.

Figure 4.22 provides a qualitative explanation for the observed behaviour when increasing θ. In the middle, the ion beam hits the material with $\theta_i = 0°$. We know from figure 4.11 that at 0° the yield of IIE is the lowest and increases with the incidence angle. The red dashed arrow is a visual illustration of the magnitude of IIE being emitted: the thicker the arrow the larger the electron emission. To the

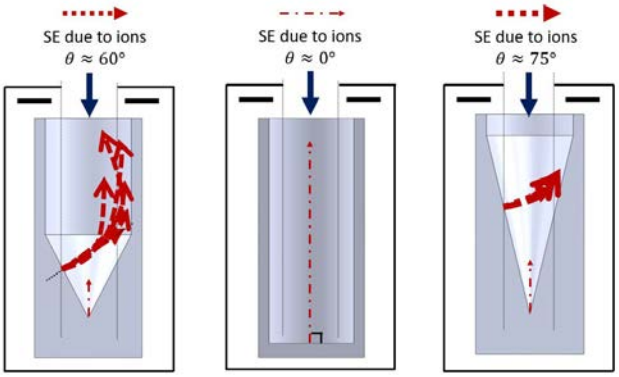

Figure 4.22: Schematic explaining the ion-induced electron emission behaviour when modifying the collector rear section shape.

left and right cups geometries give $\theta_i = 60°$ and 75°, respectively. In both cases the ion-induced electrons are emitted normal to the surface with a divergence angle between 33° and 43° (see section 4.2.2). Owing to the opening angle of the collector for the configuration (60°) IIE have more probabilities to be emitted in directions closer to the probe aperture and leave the cup, hence increase $\gamma_{L_{EE}}$.

Consequently, IIE impact on current outputs can be further mitigate if the normal to the impacted surface points towards the inner parts of the collector cup. Overall, the IIE can be passively suppressed without ion information losses if the cup geometry and dimensions are adequately designed.

4.3 Particle deposition mitigation

When probing an ion beam with a FC the front of the probe is the most exposed part as it is directly in contact with the primary ion flux, thermal electrons and neutrals. Usually, with standard designs the repeller (also called collimator in the literature) is used to define the ion flux. Figure 4.23 shows the ion collection efficiency of FCs with different repeller materials exposed to the ion beam (top): Graphite (50.**G**.05.E - F.Al.4), molybdenum (50.**Mo**.05.E - F.Al.4) and aluminium (50.**Al**.05.E - F.Al.4). All three materials are often used by the EP community for electrostatic probes. The plot at the bottom of figure 4.23 shows the ion collection efficiency for front aluminum with configuration 50.Al.05.**E** - F.Al.4 (i.e. exposed) and 50.Al.05.**P** - F.Al.4 (i.e. protected) as introduced in section 3.2.2. Data acquisition is done with the Faraday cups measuring in zone 1 (section 3.3.2).

Table 4.3: Variation of ion collection efficiencies when electrons induced by the probe front are repelled ($V_{col} = -30$V and $V_r = 0$ V) or attracted ($V_{col} = +20$V and $V_r = -20$ V). Values are obtained with a FC configuration X.X.X.E and X.X.X.P.

Ion energy	X.X.X.E	X.X.X.P
keV	%	%
6±0.06	0.072	0.064
7±0.07	0.045	0.071
8±0.08	0.058	0.088
9±0.09	0.063	0.107

For the top plot, where the probes are in configuration X.X.X.E, we observe a trend towards lower values of efficiency from front made of graphite to molybdenum and to aluminum. Nonetheless, the variation is small and lie in our measurements uncertainties which makes difficult any interpretation. The second plot shows values of η_p for a probe front made of aluminum for configuration X.X.X.E (repeller defines the ion flux) and X.X.X.P (repeller behind the point of collimation). In both cases the repeller, either exposed or protected, is left grounded. We observe that the X.X.X.P configuration always has the highest η_p. Moreover, when both configurations are operated to measure in zone 3 (section 3.3.2), the efficiency drop induced by the collection of electrons emitted by the probe front is minimized with configuration X.X.X.P, as displayed in table 4.3. In average X.X.X.P efficiency decreases by 5.9±0.9% while X.X.X.E gives 8.3±1.7%. The variation of η_p tends to increase with the ion energy and the trend is stronger for the X.X.X.E configuration. Using the housing front as collimator instead of the repeller it self provides extra shielding for the collector. In configuration X.X.X.P the cup top is positioned further away from the probe entrance which reduces the probability to collect electrons and IIE produced at the front inlet. Owing to the small variation observed, it is harsh to clearly identify the process leading to the drop of ion collection efficiency. Nevertheless, this phenomenon is observed in the case of Hall thrusters with a larger impact, further explanations can then be found in section 5.4.

Indium is a liquid metal which tends to deposit easily on material surfaces. Figure 4.24 shows different part of a Faraday cup after being exposed for a long time to the beam of LU-B. Parts which are constantly exposed to the thruster plume, e.g. repeller and housing front in the case of X.X.X.E configuration, show no trace of propellant deposition. Coating on these surfaces are directly removed

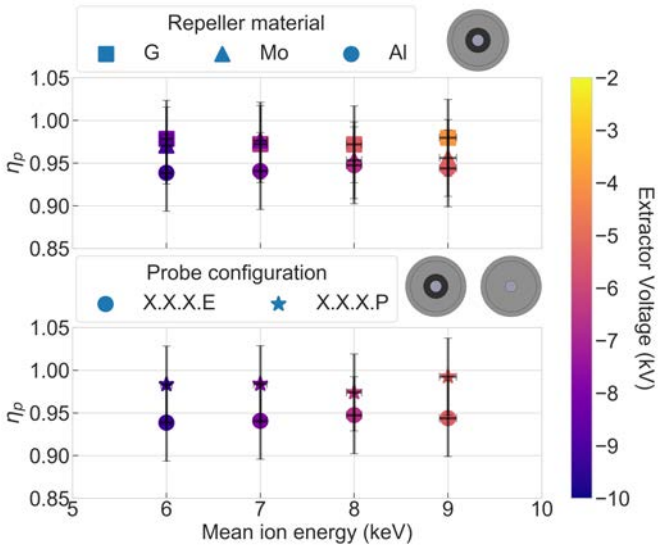

Figure 4.23: Top: ion collection efficiency for probe front made of graphite (square), molybdenum (triangle) and aluminum (circle). Bottom: η_p for X.X.X.E (circle) and X.X.X.P (star) FC configurations with the probe front in aluminum. LU-B fires at 2 mA.

by the energetic ion beam. However, hidden parts of the FC (e.g. insulators) located between the repeller and housing front present a thin layer of metal. In the course of time particle accumulation on insulators will lead to failure of the probe either due to current leak to ground or because of short circuit. With configuration X.X.X.P only the housing front is exposed and conductive coating formation cannot occur on critical parts of the FC as the ion beam goes directly through the collector.

4.4 FC aperture sizing

The collection area used to compute I_{iint} is given by the smallest diameter of the probe assembly. The aperture diameter d_a of a FC is of great importance since it defines the ion flux flowing through the probe. To assess possible effect of the probe aperture upon the outputs five different probe designs are tested: FC 50.G.10.E - F.Al.4, 50.G.07.E - F.Al.4, 50.G.05.E - F.Al.4, 50.G.03.E - F.Al.4 and 50.G.01.E - F.Al.4. They all share the same characteristics (e.g. cup length, repeller exposed to the main beam, collector material) except for the probe aperture

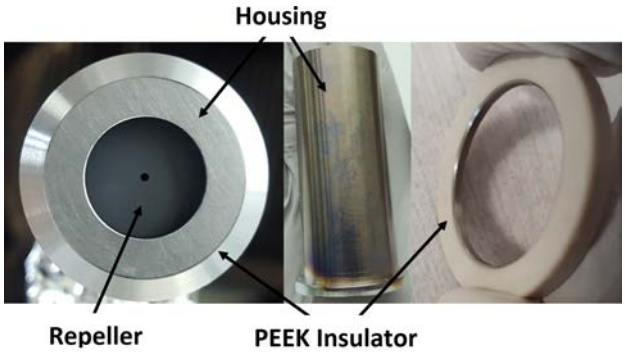

Figure 4.24: Indium propellant deposition on insulator.

dimension which goes from 10 mm to 1 mm.

The top plot of Figure 4.25 displays the ion current density angular distribution measured with a 10 mm and 1 mm aperture. Here, the thruster is LU-B firing at 2 mA, 6 kV (blue) and 9 kV (red). It shows that the 1 mm aperture FC measures less ion current density in both cases over the whole beam profile. Indeed, the 10 mm wide aperture measures 10±5% to 12±%4.5 more ion current density between −60° and +60°, for 6 kV and 9 kV, respectively. The impact of the aperture dimension upon the computed beam divergence θ_{div} is given in figure 4.25 (bottom). Here, LU-B fires at 2 mA and 8 kV and data is normalized to the value obtained with the 5 mm wide aperture. Interestingly, despite the ion signal difference observed between the largest and the smallest d_a on the top plot, the corresponding θ_{div} remains constant whatever the aperture size. Owing to the fact that the method to compute θ_{div} relies on considering 95% of the whole current distribution (section 2.3.5), θ_{div} does not change as the ion current density losses are relatively identical over the whole beam profile.

Figure 4.26 plots the ion collection efficiency evolution for each aperture diameter with and without active trapping of IIE. We observe a light trend towards lower collection efficiencies as the aperture diameter decreases from 10 mm to 3 mm. However, the 1 mm aperture shows different behaviour whether IIE are actively trapped or not by the cup. Here, the aperture diameter is small enough that the circle distribution of the IIE emission increases the probability of IIE to reach the probe top for a constant emission divergence angle. Then, when the fraction of IIE capable to escape are actively trapped by the cup the efficiency drops further down. As a result a difference in d_a of a factor 10 can lead to an efficiency drops of 10%. Identical measurements were done with 30 mm (square) and 10 mm (triangle) cup length as shown in figure 4.27. There, we only plotted

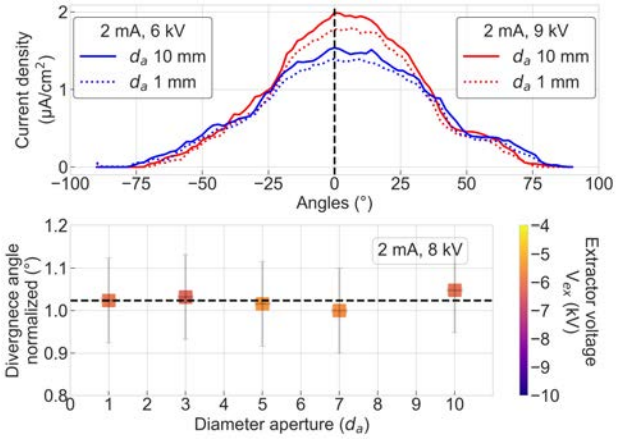

Figure 4.25: Top: current density angular distribution (J_i) with $d_a = 10$ mm and 1 mm with thruster operated at 2 mA, 6 kV (blue) and 9 kV (red). Bottom: evolution of θ_{div} computed with different FC diameter with the thruster firing at 2 mA and 8 kV.

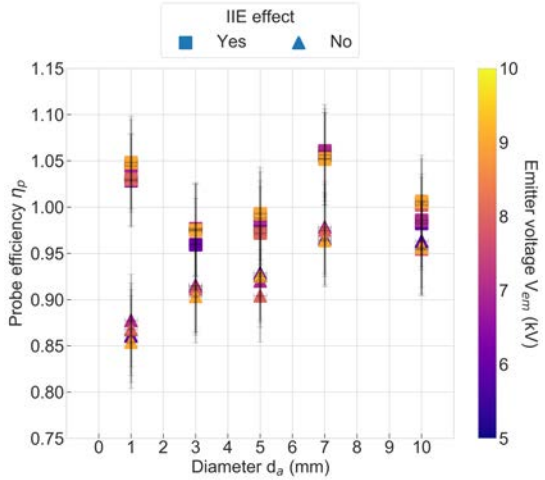

Figure 4.26: Probe collection efficiency for different inlet aperture diameters. LU-B fires at 2 mA. Values are given when IIE are actively trapped (square) or not (triangles).

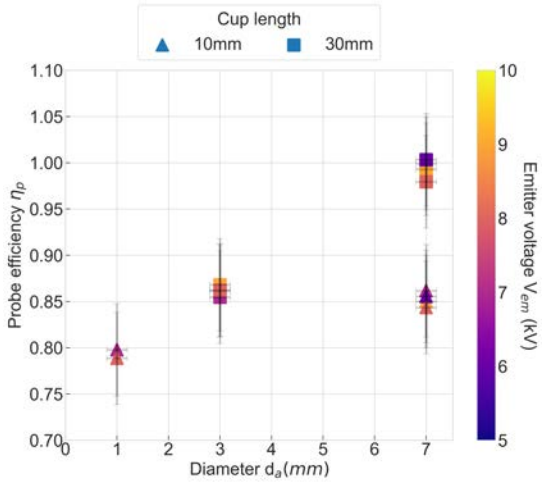

Figure 4.27: Probe collection efficiency for different aperture diameters with cups 10 mm (triangle) and 30 mm (square) long. LU-B fires at 2 mA and IIE are actively trapped.

probe efficiencies when IIE are actively captured. The same behaviour is observed as the probe aperture decreases. Also we remark from figure 4.26 and 4.27 that for the ratio $\frac{d_a}{l_{cup}} = 0.1$ the probe efficiency constantly decreases by 7% between a 50 mm and 30 mm or 30 mm and 10 mm long cup.

Nonetheless, in the case of the 50 mm long cup η_p variation between inlet diameter of 10 mm and 3 mm are small and could also be caused by experimental uncertainties. For instance, reducing the probe inlet diameter can induce a misalignment between the probe and the thruster firing axis. Therefore, a part of the ion beam would not be collected and η_p would be less. Up to now, we have only tested different aperture diameter for FC configured as X.X.X.E (section 4.3). Table 4.4 shows the ion collection efficiency variation obtained with LU-B and LU-C when the probes are in X.X.X.P mode. Surprisingly, the 7 mm inlet shows η_p values 4% lower than the 3 mm one. Even though the trend is reversed, variations are still within measurements uncertainties. Further explanation are given in section 5.4.2 when assessing the impact of the inlet aperture for a Hall thruster. There, variations observed are non negligible and can be safely interpreted.

Table 4.4: Ion collection efficiency variation between a 7 mm and 3 mm aperture diameter. The parameter is obtain for LU-B and LU-C firing at 2 mA and 7 kV. Values are given with a confidence level of 99% (k=3)

Configuration X.X.X.P (section 4.3)	
LU-B	**LU-C**
%	%
-4.2 ± 4.5	-4.9 ± 4.5

Table 4.5: Experimental differences between test campaign into the FH and LIFET 4 vacuum chamber.

Parameter	**FH**	**LIFET 4**
LU	LU-C (24 needles)	LU-D (28 needles)
Probe to thruster distance	$\sim$84 cm	$\sim$25 cm
Probe holding structure	see section 3.1.1	see section 3.1.1
Power supplies	Power processing unit	Laboratory power supplies

4.5 Facility and set-up induced perturbations

Up to this section all experiments have been carried out in the 0.67×1.32 m FH chamber. It was possible to conduct one test campaign inside the LIFET 4 vacuum chamber at FOTEC (2.2×3 m) to assess any facility or set-up effect on our results. Based on previous study outcomes we selected to use the probe 50.07.Al.P - F.Al.3 for this experiment. The latter has been used for several thruster operation points in the FH chamber. Nevertheless, owing to LIFET 4 availability and experiment restriction, it was not possible to duplicate the exact same experimental set-up. Differences are listed in table 4.5. Note, that the LUs are not the same but more than 85% of the crown is firing in both cases. Therefore, the ion beam produced by LU-C could be slightly off-centre and would need to be corrected during post processing.

Figure 4.28 shows the beam profiles acquired with LU-D (top) and LU-C (bottom). Both units fire at 3 mA with extractor voltage ranging from -3.9 kV to -7.7 kV for LU-C and -3 kV to -7 kV for LU-D. As expected, with lower V_{ex} values the ion beam profile is slightly more focused. Current acquisition is near zero when the probe is located at $\theta<-70°$ in the case of LU-D profiles. Note that due to set-up constraint in LIFET 4 it was not possible to go higher than 70°, but as we shall see it does not impact our results. For LU-C the probe still mea-

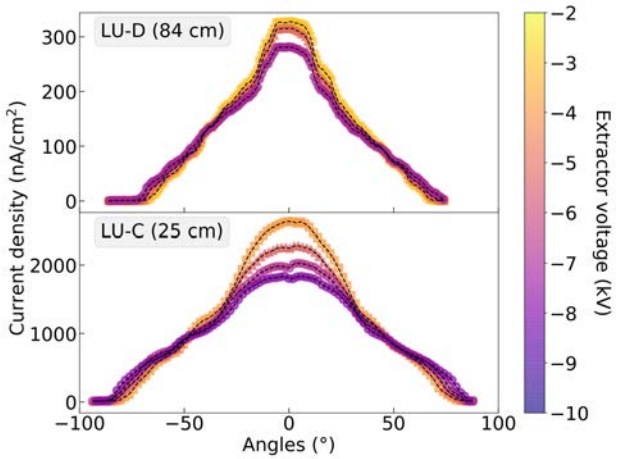

Figure 4.28: Beam profiles acquired with FC 50.07.Al.P - F.Al.3 for LU-C in the FH chamber (bottom) and LU-D in the LIFET 4 chamber (top). The laboratory units fire at 3 mA. LU-D ion current distribution is measured 84 cm away from the thruster exit plan. LU-C profiles are obtained at 25 cm. IIE effects are actively suppressed.

sures current until ±85°. Moreover, when measuring closer to the emitter crown the current density is 10 times larger. Nonetheless, both profiles shows the same trend. Below ± 45° beam profiles with the lower extractor voltage reads the larger current density. Beyond this point the density drops and becomes the lowest to be measured. For both LUs we can distinguish three zones. The first, between ±4° and ±6° for LU-C and LU-D, respectively shows constant current density. The second zone goes up to 15° for LU-D and 35° for LU-C. There, the current density decreases sharply. Then, for both LUs the signal drops slowly until no more current is measured. Note that the profile shapes are similar to those presented by Mühlich et al. [101] when they numerically modelled the ion beam of the ENPULSION NANO thruster. Overall, the profiles acquired with LU-C at 25 cm from the thruster in a smaller chamber present the same trend but with flatter pattern. We believe this could be induced by the distance probe-thruster and details are given in next paragraph. The divergence angles θ_{div} are extracted from the beam profiles and plotted in figure 4.29. As expected θ_{div} increases as the extractor voltage is further decreased (see section 3.3.2). However, we remark that the beam divergence for LU-C reads in average 16% more than for LU-D. Here, firing needle distribution cannot be the reason for such a difference as LU-C fires with 4 less needles than LU-D and therefore, the opposite behaviour should be

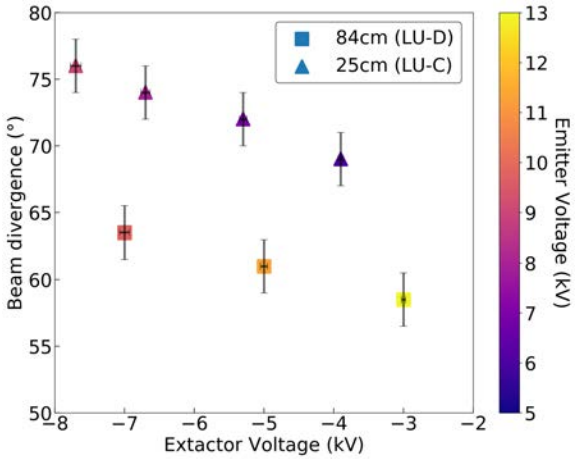

Figure 4.29: Evolution of LU-C and LU-D beam divergences as a function of the extractor and emitter voltage. θ_{div} is computed from beam profiles displayed in figure 4.28. The probe to thruster distance is 84 cm and 25 cm for LU-D and LU-C, respectively.

observed, as showed in section 3.1.1.

The ion collection efficiency is therefore retrieved from several profile acquisitions as plotted in figure 4.30 (bottom). At the figure top, θ_{div} is given for both LUs as a function of the total voltage between the emitter and extractor for different ion current emission. θ_{div} retrieved for LU-C are grouped around $72\pm3.4°$ while $61\pm1.4°$ for LU-D. On the opposite, η_p remains stable whatever the distance between the thruster and the probe. Values oscillate between 0.95 and 1.05 which indicates that close to 100% of the known emitted ion current is properly collected. Two factors could be involved in the beam divergence discrepancy: 1) the distance between the thruster and the probe and 2) facility effects. The second should not influence much our results as the pressure during testing was of the same order (e.g. 10^{-6} mbar) and electric field lines induced by the thruster operation are contained below the dimension of the smaller chamber as showed in figure 4.31. There, the SIMION software computes the field lines distribution around the thruster when its extractor is biased to -10 kV, the maximum value allowed by the PPU used to operate LU-C. The chamber walls as well as the probe housing and the thruster casing are grounded. The emitter voltage is set to $+10$ kV and the probe repeller and cup are set to -60 V and -30 V respectively. The figure points out that at 25 cm (left) from the thruster exit plane the probe is immersed into the low magnitude electric field lines, implying the set-up might be the cause

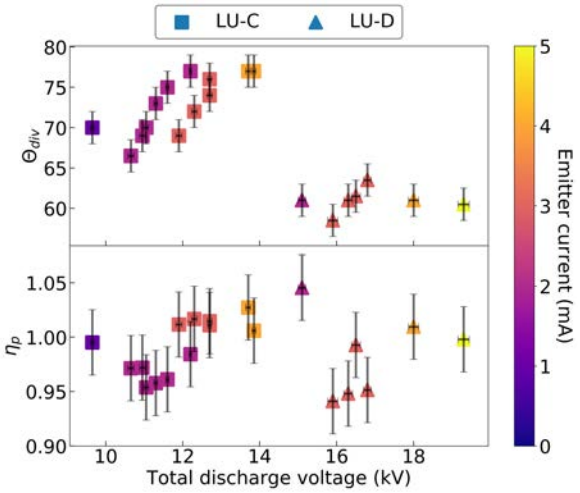

Figure 4.30: Evolution of the measured beam divergences and probe efficiency as a function of the total discharge voltage. θ_{div} and η_p are given a wide range of thruster operation. The probe to thruster distance is 25 cm and 84 cm for LU-C and LU-D, respectively.

of the beam enlargement. The fact that the probe is in the region where ions are still influenced by the extractor voltage is an issue. There, when extracted from the crown ions are further accelerated by extractor voltage. Once ejected they are instantly decelerated by the very same voltage and their energy goes down to the emitter voltage value. At 25 cm the probe seems to be at the edge of this region. Therefore, the ions would have almost completely slowed down to the emitter potential. However, their velocity vector (e.g.trajectory) might still be influenced by the extractor field lines. We observe that the field lines have a "mushroom" like shape describing a sharp deviation of the lines from the thruster axis close to the crown, followed by a slow refocusing effect. Moreover, the multiple ignition sites of the crown induced by the circular distribution could also lead to space charge effects close to the thruster exit plan. This would contribute to push ions away from their original direction.

In the end, further tests shall be done to properly identify this phenomenon. For instance, performing a firing test in LIFET 4 with a FC placed 25 cm away from the thruster would help to confirm or to refute this analysis. Eventually, if this is confirmed it would imply that below a supposedly distance of $\sim$30 cm the region would be qualified as near-field region (as used in the case of Hall thruster) since thruster operation effects are still predominant. Moreover, this

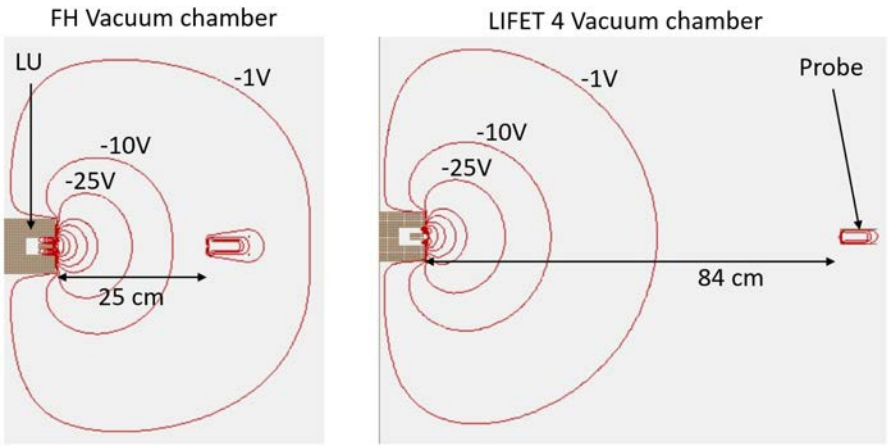

Figure 4.31: Electric field line distribution computed with the SIMION software for the probe located at 25 cm (left) and 84 cm(right). The extractor voltage is set to -10 kV and the emitter to $+10$ kV.

would imply that at a close distance from the thruster exit plane ions might initially be accelerated at large angles before being redirected on the thruster axis.

Chapter 5

Ion beam study : The ISCT200 Hall thruster

Contents

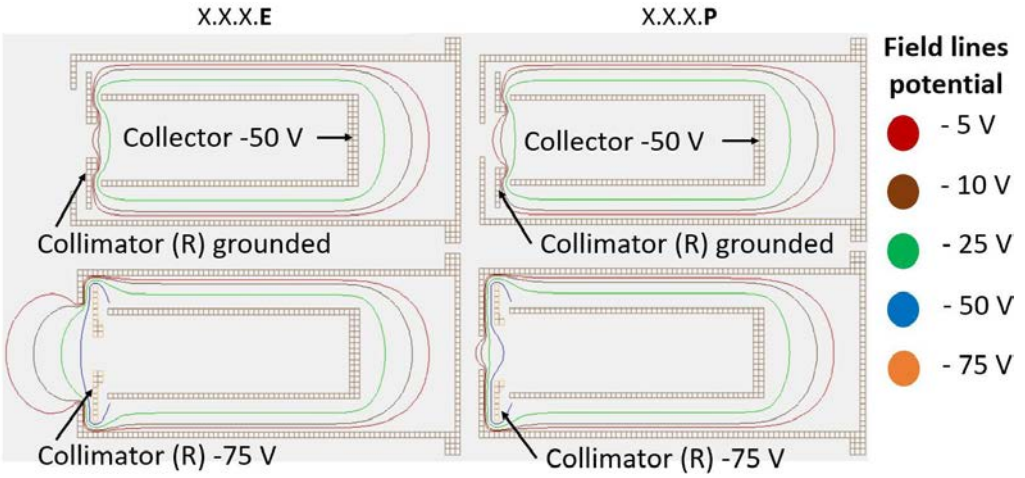

Figure 5.1: Field lines computed with SIMION. Configurations X.X.X.E (left) and X.X.X.P (right) with the repeller grounded (top) and at −75 V (bottom).

5.1 Field lines

Contrary to FEEP thrusters, low power HT are usually operated at a relatively low discharge voltage (100 V to 400 V). As a result, ion energy inside the beam in the far-field region has a magnitude quite similar to the voltage applied to the FC. Therefore, current measurements are easily influenced by the probe settings. Figure 5.1 displays the field lines distribution, computed with the SIMION software, inside a FC in configuration X.X.X.E (left) and X.X.X.P (right). The collector voltage is always kept to −50 V and the repeller is either left grounded (top) or set to −75 V (bottom). The latter configuration is used to actively recollect IIE as thoroughly detailed in section 4. Field lines from −5 V to −75 V are displayed. It is clear that the X.X.X.P configuration mitigate the probe field lines intrusion into the bulk plasma. With X.X.X.E configuration, field lines expand more easily which could lead to interactions with low-energy particles. It is well known that HT plumes have a wide ion energy distribution going from the discharge voltage down to a few electron-volts at large angles. Therefore, small variations induced by the FC operation distorts outputs as shown in figure 5.2. Plots display the ion current density angular distribution of HT1 acquired with FC 50.Al.05.P - F.Al.4. HT1 fires at 200 V (left) and 250 V (right) and 0.66 A. Profiles are also presented in a logarithmic scale to ease visualization of current behaviour at large angles. The repeller is either grounded (blue) or biased to −75 V (red). The latter config-

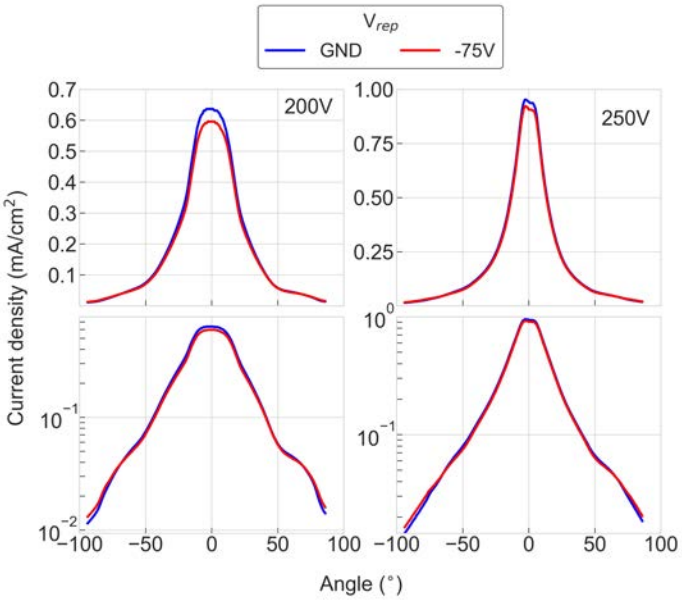

Figure 5.2: Current density angular profile acquired with FC 50.Al.05.**P** - F.Al.4 with the repeller grounded or biased to −75 V. HT1 fires at 0.66 A, 200 V (left) and 250 V (right). Profiles are displayed with a linear (top) and logarithmic (bottom) scale.

uration measures lower current density on the thruster axis and slightly higher at large angles (>75°). In this region, the probe is close to the chamber walls where the plasma-facility interaction is non-negligible. Moreover, slow ions from CEX collisions inside the plume are also present. As a result a potential drop, as produced by the repeller potential, easily attracts background charged particles [121]. In the vicinity of the thruster centre axis ions are expected to have the highest energy ($\sim U_d$, see section 6) with their velocity vector collinear to the thruster axis. Therefore, ions should be the least disturbed by the repeller voltage. Surprisingly, the current drop appears to be the highest in this region.

Figure 5.3 shows the influence of the repeller voltage on the measured ion current. The I-V curves displayed are acquired on axis for different V_{rep}. We observe that as V_{rep} is more negative, the current measured by the collector decreases. Overall, the slope of the curves are sensibly equal and of the order of 5×10^{-5} mA.V^{-1}.cm^{-2}. Moreover, a current drop is not seen once $V_{rep} < V_{coll}$ as experienced with the FEEP thruster (section 4). Due to the low energy at stake γ_{EE} is expected to be small and therefore γ_{LEE} is negligible with a 50 mm long

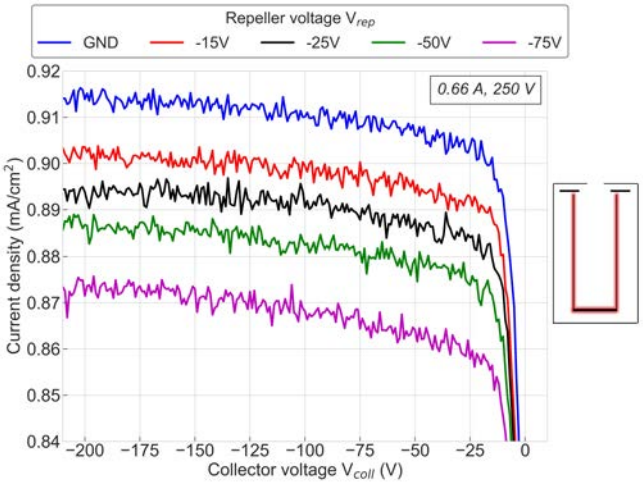

Figure 5.3: I-V curves acquired for different repeller voltages at 0° with configuration 50.Al.05.**P** - F.Al.4. HT1 fires at 250 V and 0.66 A.

cup.

Figure 5.4 shows I-V curve with a voltage sweep applied to the repeller while the collector is grounded, the current density measured on the repeller increases when the voltage applied is more negative. Here, the slope is large as the current measured is greatly influenced by sheath expansion [31] and IIE emissions. However, the current intercepted by the repeller remains low compare to the signal measured by the collector (<3%). The increase observed on the repeller in figure 5.4 is also less than the current drop seen in figure 5.3. Therefore, a part of the current seems to be lost to other parts of the probe or does not enter the probe. To better understand changes observed in the measured ion current density, simulations have been carried out with the SIMION software [122].

In our study, singly-charged Xe ions with different kinetic energies flow through a 2-D FC. As a first analysis we simulated the behaviour of different monoenergetic ion beams through the X.X.05.**P** - F.X.X. Results are displayed in figures 5.5 and 5.6. Two scenarios are considered. In the first case, the simulation displayed in Figure 5.5 includes 200 singly-charged xenon ions with energy of 5 eV (red), 10 eV (black), 100 eV (green) and 250 eV (blue). Ions have a velocity vector collinear to the Faraday cup axis. In the simulation a 10° divergence angle was applied to maximize the number of ions entering the cup. The collector, represented by the central cup, is biased to −50 V. Twice the potential of the collector is applied to the repeller. Figure 5.2 to 5.4 showed that with such a FC configura-

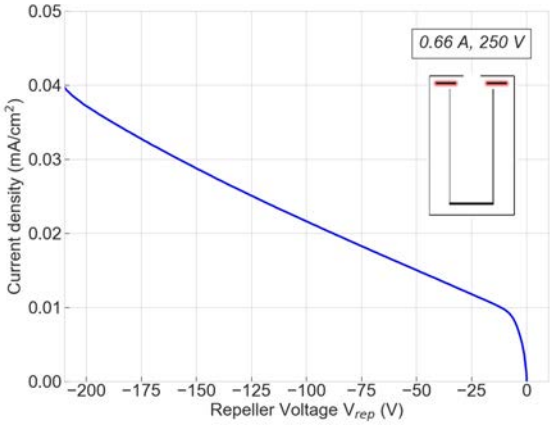

Figure 5.4: I-V curves acquired with 50.Al.05.**P** - F.Al.4. Here, a voltage sweep is applied to the repeller (V_{rep}) while the collector is grounded. HT1 fires at 0.66 A and 250 V.

tion a fraction of the ion current is either lost to the repeller, to other parts or does not penetrate the probe. Figure 5.5 shows that ions tend to not be captured by the repeller when entering the probe. On the contrary, when the ions energy is low the particles are focused into the cup. Also, a part of the beam is collected by the cup side walls. Figure 5.6 shows outputs for the second scenario where it is assumed that the ion beam enters the probe with an incidence angle larger than 0°. Two groups of ion energy are used: 10 eV (top) and 250 V (bottom). The ion energy range was chosen based on the large ion energy distribution within the plume of a Hall thruster. For experimental purposes, the incident angles were chosen randomly, and the slope was accentuated to maximize the chance for an ion to be directly collected by the repeller. The goal here was to assess the probability of an incoming ion to reach the repeller placed behind the housing front. We observe that low energy ions are focused and directed towards the cup. However, energetic ones get closer to the repeller and only a small fraction reach it while the rest is still collected by the cup side wall. Consequently, two additional simulations have been ran as shown in figures 5.7 and 5.8. Here, we consider ion reflection from the primary ion beam to the cup side and rear walls. The semi-half-angle of the possible reflected ions was maximized to 90° to examine the worst case scenario. Figure 5.7 displays simulation outcomes when it is assumed that the ion collision with the cup induces 95% loss of energy at best and only 50% at worst. Therefore,

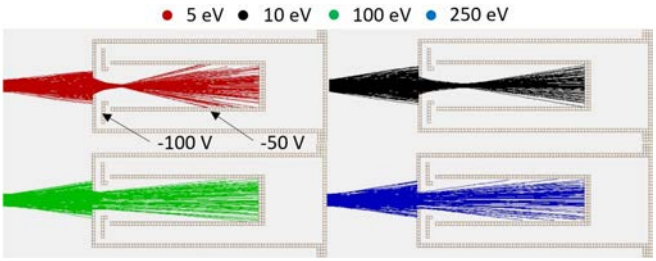

Figure 5.5: Ion simulations performed with the software SIMION. Each configuration displays the ion trajectory going through the FC. Potential is fixed at −50 V and −100 V for the collector and repeller, respectively. Ion energies are 5 eV (red), 10 eV (black), 100 eV (green) and 250 eV (blue). The probe aperture diameter is 5 mm.

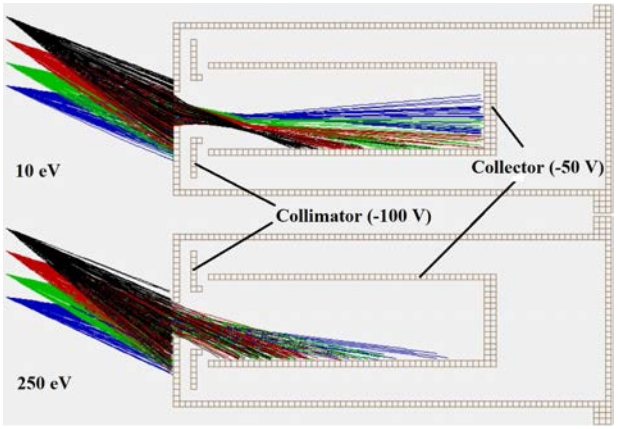

Figure 5.6: Ion simulations performed with the software SIMION. Each configuration displays the ion trajectory through the FC. The colour code refers to different incident angles. Potential is fixed at −50 V and −100 V for the collector and repeller, respectively. Ion energies are 10 eV (top) and 250 eV (bottom).

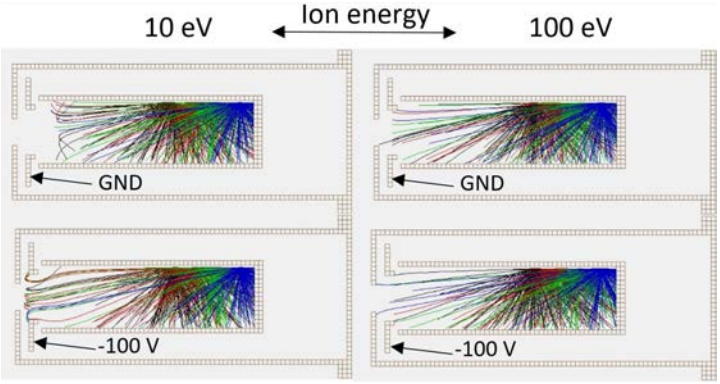

Figure 5.7: Ion simulations performed with the software SIMION. Each configuration displays the possible trajectory of ion rebounds from the lateral side of the FC. The colour refers to different rebound location. The collector is at −50 V. The repeller is either grounded (top) or biased to −100 V (bottom). Ion energies are 10 eV (left) and 100 eV (right).

ions with 10 eV and 100 eV are flown with random velocity vectors. In this scenario ions are scattered 35 mm (black), 40 mm (red), 45 mm (green) and 50 mm (blue) from the cup top. For each case, the FC has a collector biased to −50 V and the repeller is either grounded (top) or set to −100 V (bottom). When the repeller is grounded, around 5% of the most energetic ions escape the cup while all low energy ones are completely redirected back to the collector. However, once the repeller is at −100 V close to 10% of low energy ions escape the cup or are collected by the repeller. Ions with 100 eV are barely affected by the change of voltage inside the cup. Likewise, figure 5.8 displays behaviour of scattered ions from the cup rear part. The energies used are 10 eV (black), 50 eV (red), 75 eV (green) and 100 eV (blue). The collector is set to −50 V while the repeller is either grounded (top) or −100 V (bottom). In the same manner than ion reflection from side walls, applying a potential to the repeller does attract a small fraction of low energy reflected ions from the cup bottom.

Numerical simulations show the probability to collect primary ions from the primary beam with the repeller protected behind the FC housing is negligible. Using a more negative potential on the repeller than on the collector moves the ion trajectory towards the cup. This, however, leads to a larger ion spread, hence a larger ion collection on the side walls of the cup. Furthermore, a fraction of ions reflected from the bottom and the cup side walls can be directed towards the repeller if the latter is biased more negatively than the collector. As a result, a

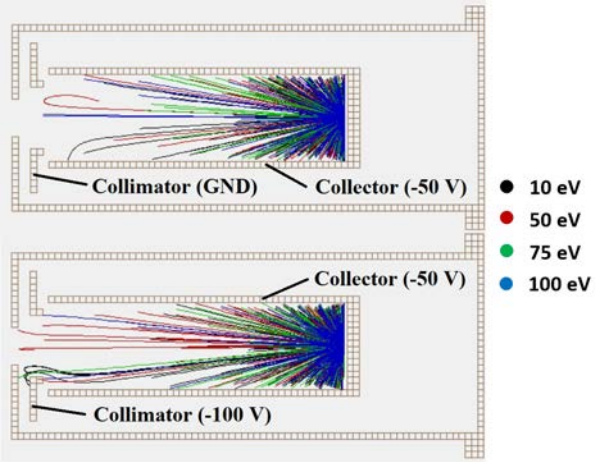

Figure 5.8: Ion simulations performed with the software SIMION. Each configuration displays the possible trajectory of ion rebounds from the bottom of the FC. The collector is at −50 V. The repeller is either grounded (top) or biased to −100 V (bottom). Ion energies are 10 eV (black), 50 eV (red), 75 eV (green) and 100 eV (blue).

small fraction of the primary ions is not collected and the measured ion current is lower as seen in figure 5.2 and 5.3. Finally, a Hall thruster plume is more complex than a simple ion beam. Consequently, these simulations must be seen as a first, yet valuable, step to better grasp the ion behaviour inside a FC. For instance, the influence of the plasma at the probe entrance is not incorporated in the simulations. Moreover, the sheath expansion at the probe inlet and its possible influence on particles found near the top of the cup is also not considered in this numerical study.

5.2 Ion collector optimization

5.2.1 Material impact

The performance of different material as ion collector are displayed in figure 5.9. There, I-V curves are acquired at different angular positions when HT2 fires at 0.66 A and 300 V with xenon as propellant. For all studied materials the collector is a disk 12 mm in diameter and 3 mm thick. An aluminium grid is placed 4 mm upstream with hole sizes of 0.7 mm (see RPA design in section 6). The

Table 5.1: Xenon ion-induced electron emission yields at 0° retrieved from I-V curved for molybdenum, stainless steel and aluminium. Values are given with a confidence level of 99% (k=3).

Discharge voltage (U_d) V	**Molybdenum ([63] and [84])**	**Molybdenum (experiment)**	**Stainless steel**	**Aluminium**
250	0.03401	0.0287±0.0053	0.1174±0.0216	0.107±0.0198
300	0.0349	0.036±0.0103	0.0758±0.0218	0.069±0.0199

latter is biased to -100 V during the voltage sweep applied to the disk. Materials studied are molybdenum (blue), stainless steel (red) and aluminium (green). They are often used in the EP community when working with electrostatic probes. As these curves were acquired at different days and since we are looking at a specific angular position, shifts in current density between each material are attributed to the thruster operation. However, the behaviour of the I-V curves is analysed to determine how much IIE effect can perturb the ion current measured in the case of a Hall thruster. All materials experienced a current drop once the voltage applied to the disk V_{col} overtakes the one on the grid V_{grid}. This is characteristic of IIE recollection as explained in section 2. The I-V curves are not stables as they slightly drift towards lower values as V_{col} approaches 0 V. Nonetheless, after a thorough data post-processing it was possible to obtain γ_{EE} for these three materials. To compare our results we used the values given by Brown et al. [63] in their recommended practice for use of Faraday probe in electric propulsion testing. There, they provide values of γ_{EE} of molybdenum when bombarded by xenon ions singly-charged, doubly-charged and triply-charged xenon ions. In our study we cannot discriminate between multi-charged and singly charged xenon ions. Therefore, we used the data provided by Ekholm et al. [84] indicating the fraction of singly and multi-charged xenon ions inside the plume of a 200 W Hall thruster. The overall yield for molybdenum is given in table 5.1. Experimental values obtained for molybdenum are of the same order than those used as reference with better fitting at 300 V. Therefore, we can assume the values obtained for stainless steel and aluminium give a correct order of magnitude for γ_{EE}. As expected, molybdenum is the less impacted by IIE effects. Yields given for aluminium and stainless steel are close to each other and uncertainties are quite large to conclude on which one is the largest. Nonetheless, for all materials IIE effects never increase the measured ion current by more than 12% at 250 V and 8% at

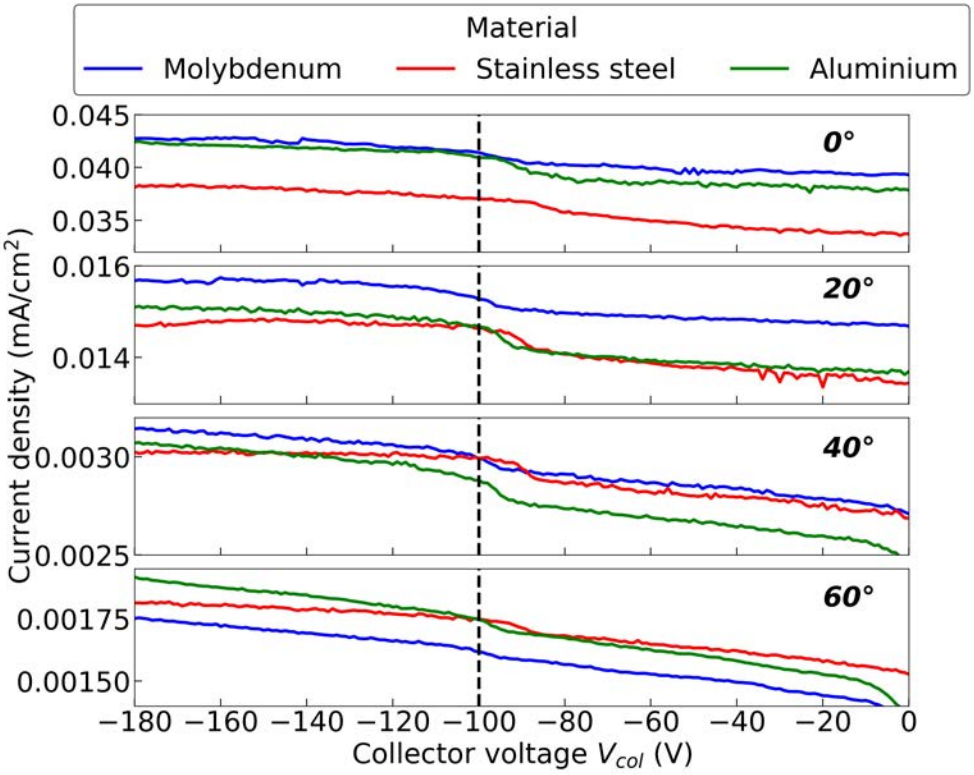

Figure 5.9: I-V curves acquired with 12 mm disks made of molybdenum (blue), stainless steel (red) and aluminium (green). The grid placed upstream the disk is biased to -100 V. HT2 fires at 0.66 A and 300 V.

300 V due to the low ion energy at stake.

5.2.2 Structure impact

The current densities measured with 12 mm diameter disks made of foam #1 and #6 (see section 3) are compared to those acquired with a bulk aluminium disk. I-V curves for different angular positions are displayed in figure 5.10. V_{grid} is set to -100 V during the applied voltage sweep. Here, the curves measured with both foams when V_{coll} is lower than V_{grid} show a large ion current increase and unstable behaviour. While the bulk aluminium measures current densities of the order of 4 μA/cm^2 on the thruster axis, foams reach values as high as 150 μA/cm^2, close to 40 times larger. Even at 60° off the centre axis, Foams #6 collects 5 times more than the regular aluminium disk. However, when all IIE are recollected (i.e. $V_{coll} > V_{grid}$) all three materials measure almost the same ion current as shown in the insert with enlarged I-V curves between -120 V and 0 V. The signal is stable and decreases slowly as the collector voltage approaches zero. As a result of the I-V curves, it is clear that foams do not help to mitigate ion-induced electron emission, on the contrary it worsen the process. The fluctuations monitored below -100 V could indicate that IIE originates from several spots inside the foam cavities. It is observed that the larger the cavity the higher the ion current increase. Moreover, the IIE process could also be worsen by background neutrals trapped into the pores of the foams. These neutrals would generate secondary electrons whilst not being measured by the disk. Finally, the presence of ions with a velocity vector not collinear to the probe axis will hit the foams with a random incidence angle. The resulting electron emission would be therefore larger. Moreover, ions being scattered inside a cavity will hit easily another surface of the pore increasing IIE process as exemplified in figure 5.11.

5.2.3 Results Recap

In this section we have shown that the ion-induced electron emission yield measured for molybdenum, stainless steel and aluminium when bombarded by 200 - 300 eV xenon ions has a relatively low influence on the measured ion current. However, the yield measured for molybdenum is near 60% lower than the one obtained with two other material studied.

We also tried to assess the impact of a foam structure as ion collector and its capacity to lower down γ_{EE} compared to its bulk version. In our study we chose to compare aluminium with aluminum foam. Two foam configurations were used

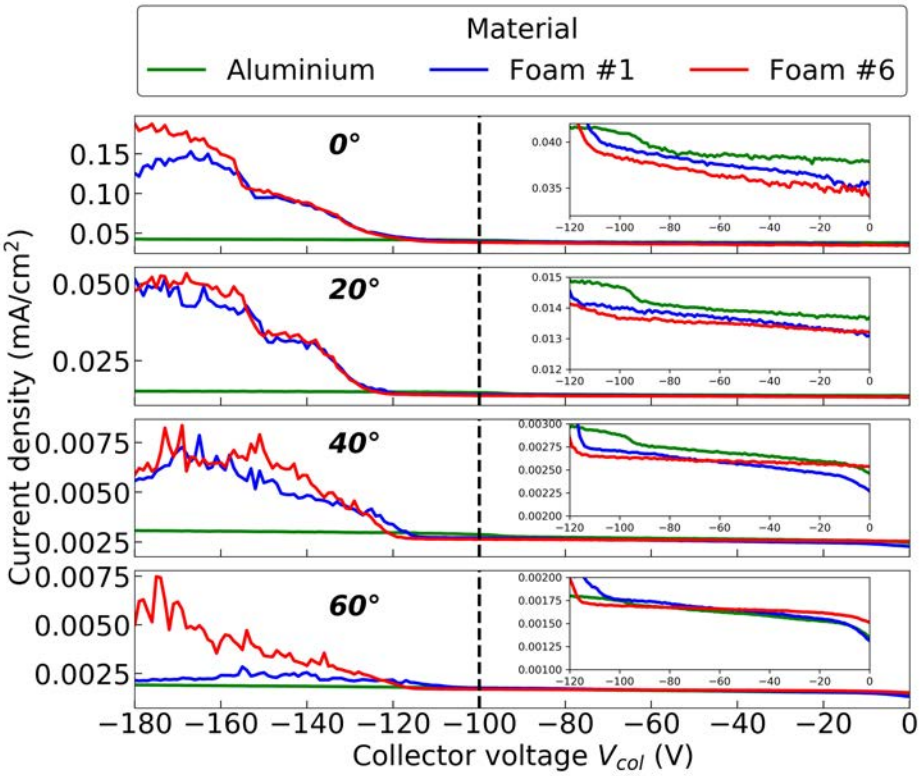

Figure 5.10: I-V curves acquired with a 12 mm disk made of bulked aluminium (green), foam #1 (blue) and foam#6 (red). The grid placed upstream the disk is biased to -100 V. HT2 fires at 0.66 A and 300 V. A detail range from -120 V to 0 V is given in the insert of each plots to better visualize curves behaviours once IIE do not affect the measured signal.

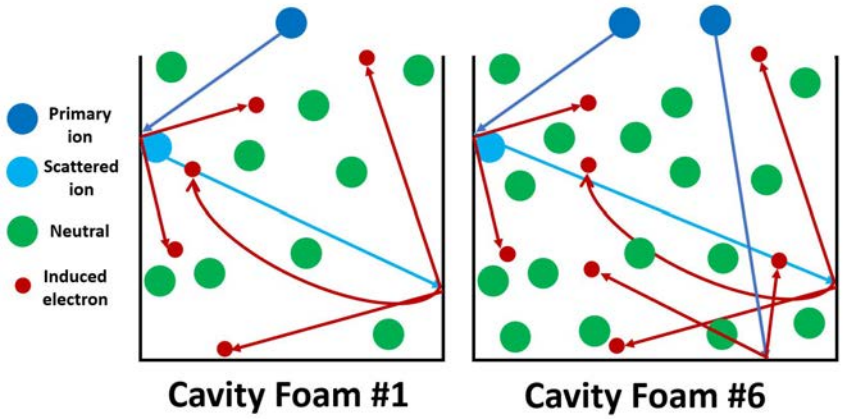

Figure 5.11: Illustration of probable effect causing the ion current to increase when using the a simple disk as ion collector. Primary and scattered ions are represented in dark and light blue, neutrals in green and ion-induced electrons in red.

with different pore sizes. experiment outcomes were surprising as we observed that a the foam version induce a higher ion-induced electron yield as opposed to observation made in chapter 4 and work published in the literature [97, 98, 99]. We believe that the issue is coming from the material used (i.e. aluminium) and the experiment conditions (background pressure not low enough).

To conclude we would recommend to use as ion collector a material which presents a low γ_{EE} (i.e. molybdenum, tungsten, graphite). The use of a complex structure (e.g. foam) for better trapping induced electrons shall be also made of low γ_{EE} material.

5.3 Ion current distribution inside a Faraday cup

Section 5.1 demonstrated that in the case of Hall thrusters the probe signal is extremely sensitive to potential differences within the device. Therefore, passive methods to mitigate ion-induced perturbations are necessary. It was showed in section 4 that increasing the length or modifying the shape of the cup helps to reduce perturbations.

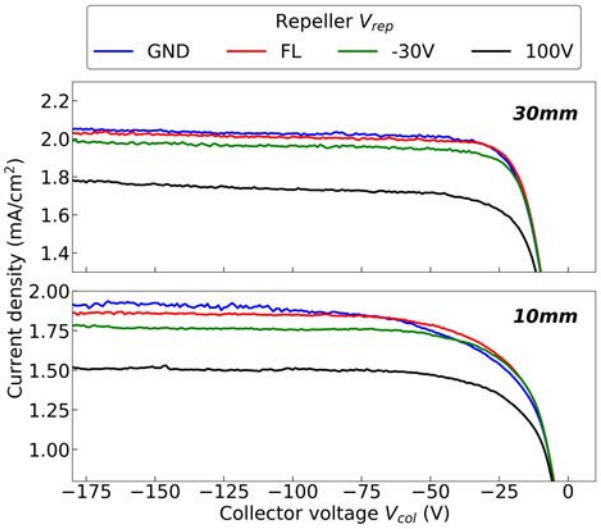

Figure 5.12: I-V curves acquired at 0° with different cup length: 30 mm (top) and 10 mm (bottom). HT2 fires at 0.66 A and 300 V.

5.3.1 Cup length

To investigate the impact of the cup length on the measured ion current we used Faraday cup configurations **X**.G.7.P - F.Al.3 with different length (50 mm, 30 mm and 10 mm). Figure 5.12 displays I-V curves acquired at 0° with a 30 mm and 10 mm long cup while HT2 fires at 0.66 A and 300 V. The current density is plotted against the voltage applied to the collector while the repeller is either left grounded, floating or biased to -30 V or -100 V. It is seen that increasing V_{rep} towards negative values induces ion current losses from the collector, as detailed in section 5.1. Moreover, no sharp current drop is seen when V_{coll} overtakes V_{rep} implying the IIE does not manage to reach the probe inlet even though the cup length is small. The main difference observed is the shift of the beginning of primary electrons influence towards negative voltage values when the cup is 10 mm long.

Figure 5.13 shows the ion current density angular distributions acquired with each design when HT2 fires at 0.66 A and 200 V (1st row), 250 V (2nd row), 300 V (3rd row) and 350 V (4th row). Mass flow rate of xenon set during each profile acquisition is also given. The flow rate is not always the same but variations are small enough to assume that they do not greatly impact the shape of the beam. The figure shows each plots in a linear (left) and logarithmic (right) scale. In

each cases, the main observed differences are located either in the region between -10° and +10° or in the thruster wings after ±55°. There is no immediate specific behaviour that can be spotted from all profiles. Nonetheless, beam profiles acquired with a 50 mm and 10 mm show two different behaviours. First, at 200 V and 250 V the 10 mm long cup always measures more ion current. The difference is accentuated for the lowest voltage. For discharge voltages above 300 V both measure around the same current in the region comprises between -10° and +10°. However, in the thruster wings (i.e. >55°) the 10 mm long cup measures more. Morevoer, it is noted that with a 30 mm cup beam profiles are narrower. It measures more on the thruster axis and less in the wings region. This can be induced by a diminution of CEX collisions inside the thruster beam. We believe it is caused by an experimental bias. Indeed, these beam profiles were acquired after more than 60 hours of out-gassing with the primary pumping system while others only had 15 hours. Therefore, we assume the experimental conditions were better, reducing CEX phenomenon within the beam. Overall, the 10 mm cup tend to measure more ion current than the two other lengths.

Figure 5.14 displays the integrated ion current retrieved from the beam profiles. Values are given when HT2 fires at 0.66 A with different discharge voltages as well as when it fires at 250 V with $I_d = 0.8$ A. The results confirm the experimental bias which occurred during the 30 mm experiment. Indeed, the diminution of CEX did change the shape of the beam but the ionization efficiency of the thruster is independent from it. Therefore, the ion current retrieved is equal to the one computed with a 50 mm long cup whatever the thruster operation, hence no change induced by the cup length. However, ion currents obtained with a 10 mm long cup are always larger. The ratio is ∼30% at 200 V, then ∼9% at 250 V and it stabilises at ∼3% for 300 V and more. The excess of ion current is probably due to the expansion of the plasma sheath from the cup rear part. As the probe is smaller, the benefice of an ion collector with a cup-like shape is not optimal any more, hence the ion collection area is larger than the physical and known area defined by the probe inlet.

5.3.2 Cup shape

The shape of the cup could be optimized to enhance ion collection by better trapping them inside. Figure 5.15 displays the I-V curves obtained at 0° with FC configurations 30.G.7.P - **X**.Al.3. The cup rear part is either flat (top), 60° conical (middle) or 30° conical (bottom). The plots represent the evolution of the current density measured during a voltage sweep applied to the cup for different

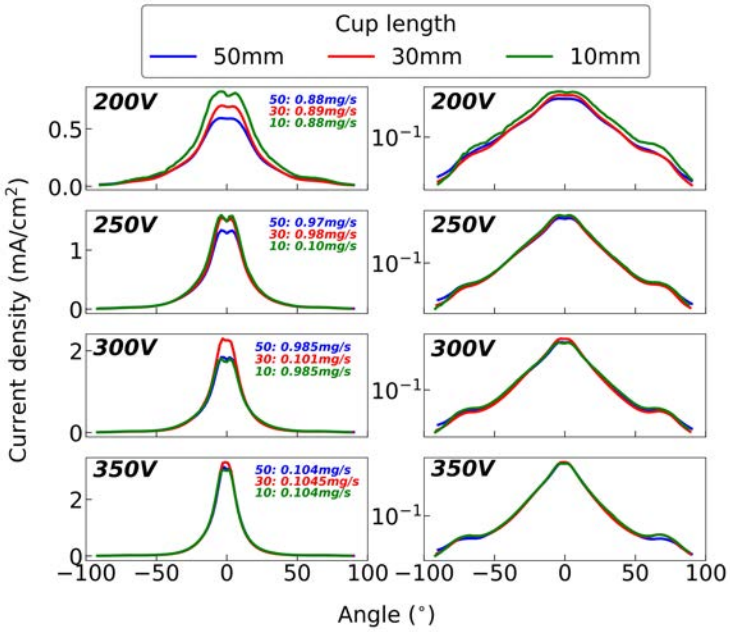

Figure 5.13: Ion current density angular distributions acquired with different cup length: 50 mm (blue), 30 mm (red) and 10 mm (green). HT2 fires at 0.66 A for different discharge voltages. Profiles are given with a linear (left) and logarithmic (right) scale.

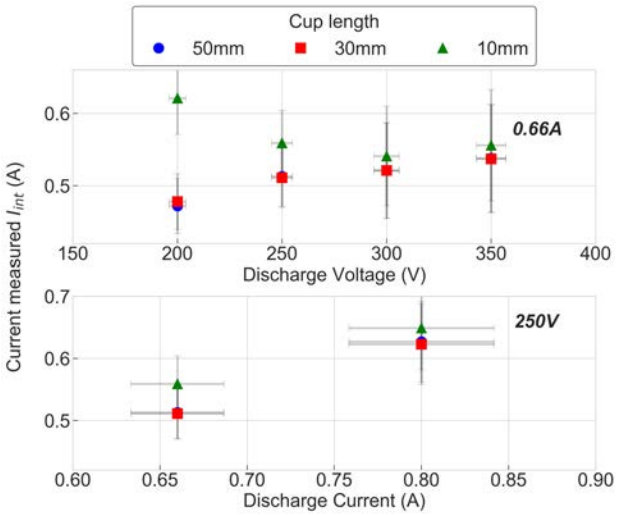

Figure 5.14: Ion current retrieved from beam profiles acquired with different cup length: 50 mm (blue circle), 30 mm (red square) and 10 mm (green triangle). HT2 fires at 0.66 A for different discharge voltages (top) or 250 V for different discharge currents (bottom). During acquisitions the repeller is floating and the cup is biased to -60 V. The coverage factor k equals 2.

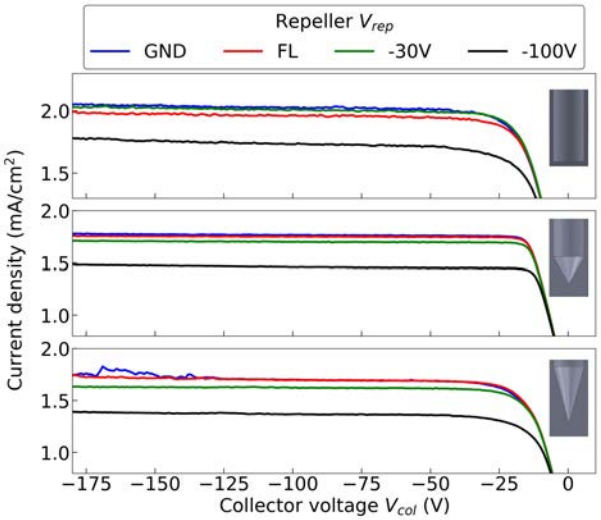

Figure 5.15: I-V curved acquired at 0° with different cup shape: flat (top), conical with 60° (middle) and conical with 30° (bottom). The repeller is set to grounded, floating, -30 V and -100 V. HT2 fires at 0.66 A and 300 V.

repeller voltage values. In the same manner than in the previous section, no sharp current drop are seen when V_{coll} overtakes V_{rep}. This indicates that perturbations from ion-induced electron escaping the cup are negligible here. Moreover, figure 5.16 shows the fraction of total ion current entering the FC being measured by the repeller from -90° to 0°. The collector voltage is always kept to -60 V. First, no differences are observed whatever the cup shape used. Moreover, when biased negatively the repeller always collect an ion current. In average 10% of the ion current entering the cup is collected by the repeller. However, this value can reach 30% near the beam edges for the lowest V_{rep}. In fact, it is noted two distinct behaviours over the angular distribution. In the thruster wings and when V_{rep} is the lowest, the repeller collects a larger ion current. Then below -40°, the trend changes and the repeller collects less ion current when biased with low voltages. Moreover, the ion current variations over the angular positions are flatter as the repeller voltage is larger. It was showed in section 5.1 that increasing negatively the voltage applied to the repeller tends to focus the ions inside the cup. This effect is accentuated when ions are less energetic. Therefore, in the thruster wings, where ions are the less energetic, increasing negatively V_{rep} pushes ions towards the cup rear part. This is experimentally proved in the next section (5.3.3).

Figure 5.17 plots beam profiles acquired from -90° to 90°. A linear (left) and

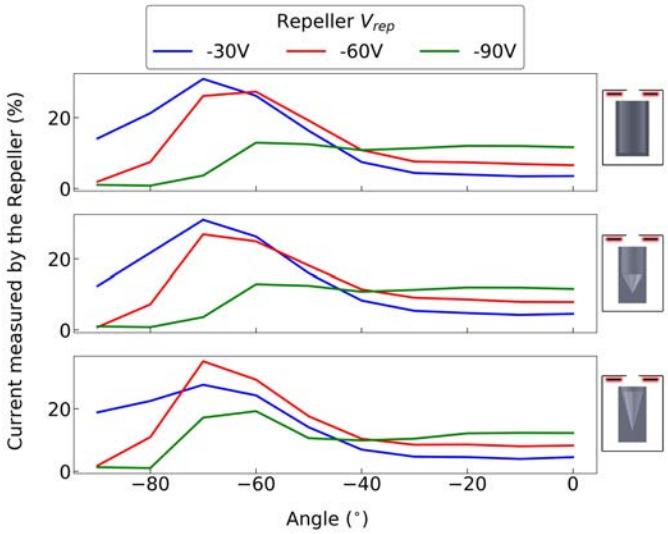

Figure 5.16: Fraction of current measured by the repeller. Measurements with a 30 mm long cup either flat (top), conical with 60° (middle) or conical with 30° (bottom). The repeller is either biased to -30 V (blue), -60 V (red) or -90 V (green) while the collector voltage is always set to -60 V. HT2 fires at 0.66 A and 250 V.

logarithmic (right) scale is given to properly monitor the current differences near the thruster centre line as well as inside its wings. Once again no specific trend can be seen from the beam profiles. Indeed, when profiles measured by H30.Al.3 are displaying lower values in the thruster centre axis region, they show larger signals in the wings, which can be interpreted as a higher rate of CEX collisions. Consequently, to get rid of this bias the ion current is computed from the beam profiles and plotted in figure 5.18. It is clear that no major differences are observed whatever the firing conditions set and the cup shape used.

5.3.3 Ion collection

Section 5.3.1 and 5.3.2 showed that dimensions and geometry of the cup barely impact the probe measurements outcomes. Therefore, an experiment was set to characterize the ion current distribution inside a Faraday cup. Figure 5.19 shows ion beam profiles acquired with FC 50.Al.3.P - F.Al.0 while HT2 fires at 0.66 A and 250 V. The repeller is floating and the collecting area is 7.06 mm^2. Here, the probe design follows the *B* configuration (see section 4.1) i.e, the side walls of the cup and the rear part (i.e. disk) are uncoupled with a PEEK insulator. The side

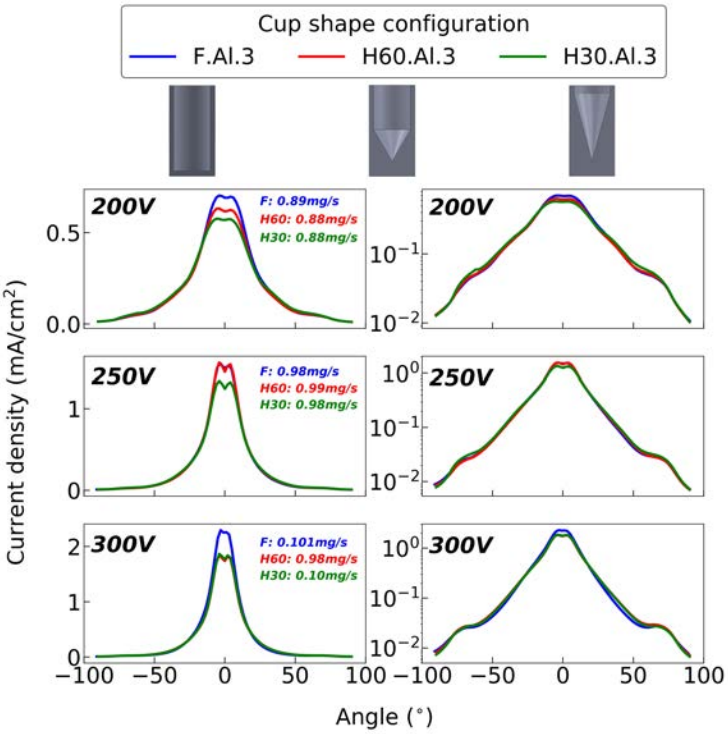

Figure 5.17: Ion current density angular distributions acquired with different cup shapes: flat (blue), conical with 60° (red) and conical with 30° (green). HT2 fires at 0.66 A for different discharge voltages. Profiles are given with a linear (left) and logarithmic (right) scale. During acquisition the repeller is floating and the cup is biased to -60 V.

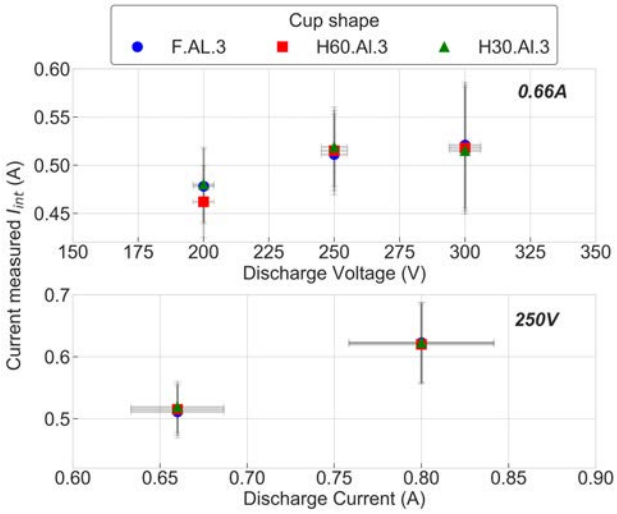

Figure 5.18: Ion current retrieved from beam profiles acquired with different cup shapes: flat (blue circle), conical with 60° (red square) and conical with 30° (green triangle). HT2 fires at 0.66 A for different discharge voltages (top) or 250 V for different discharge currents (bottom). The coverage factor k equals 2.

walls are termed "cup" and the rear disk is called "collector". Both are biased to -60V. The figure shows that most of the ion current is measured by the cup (green) and not by the collector (red). On a logarithmic scale one can see a sharp current drop once measuring outside the ±10° region. Then, the current density slightly decreases as the probe moves away from the centre axis until ±40°. Beyond this region, the slope is accentuated and the current decreases more rapidly. We note that the "bump" characteristic of CEX collisions inside the beam are clearly observed on the cup curve. Figure 5.20 presents the evolution of the fraction of ion current measured by the cup and collector relative to the total ion current measured by both. We observe that in the thruster wings (e.g. [-90:-50°] ∪ [50°:90°]), the ion current measured by the cup slightly decreases as the probe moves towards the thruster axis and the opposite occurs on the collector. In average between the negative and positive side the cup measures 75% of the ion current. Between ±50° and ±10°, the ion current measured by the collector sharply drops. Therefore, in the ±10° region the collector only measures 5% of the total ion current. Those results are counter intuitive. One would have expected to measure more signal on the collector (e.g. probe rear part) on the thruster axis as this is where ions are the most energetic and tend to have a velocity vector collinear to the probe axis.

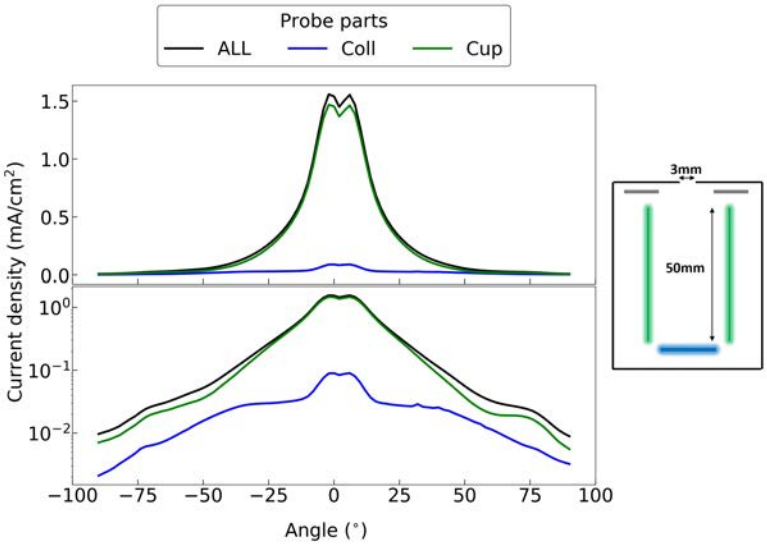

Figure 5.19: Current density measured inside the FC by the collector (blue), the cup (green) and both (black). Profiles are given with a linear (top) and logarithmic (bottom) scale. The probe 50.Al.3.P - F.Al.0 is used. HT2 fires at 0.66 A and 250 V.

We see two possibilities to explain this phenomenon. First, this is a direct effect of the beam divergence and of the complexity of the plume of a HT (divergence, different velocity vector, point source assumption not accurate). Measurements done with non-intrusive techniques (e.g. LIF) showed that ions VDF is large in the plume of Hall thrusters [43]. Moreover, the thruster has an annular geometry. Therefore, ions found a the thruster centre axis has rarely a velocity vector collinear to the axis. Second, the reduced area of the probe aperture enhance ion-ion or ion-neutral collision events with neutrals inside the probe pushing the ions to the cup walls directly at the probe entrance. A segmented FC is therefore used to better characterize the ion current distribution inside the probe. Figure 5.21 shows the fraction of current measured by several electrodes stacked one above each others and separated by a 10 mm PEEK insulator as represented in pictures on the right of the figure. Each electrodes is labelled from #1 to #4 with a colour code. Electrode n°2 and 4 are 10 mm long while n°3 is 30 mm and n°1 is a flat foam #3 disk. At the probe entrance a floating grid is placed to minimize the flux going through the probe since no repeller is used here. Moreover, the grid increases the possibilities to only have ions with velocity vector collinear to the

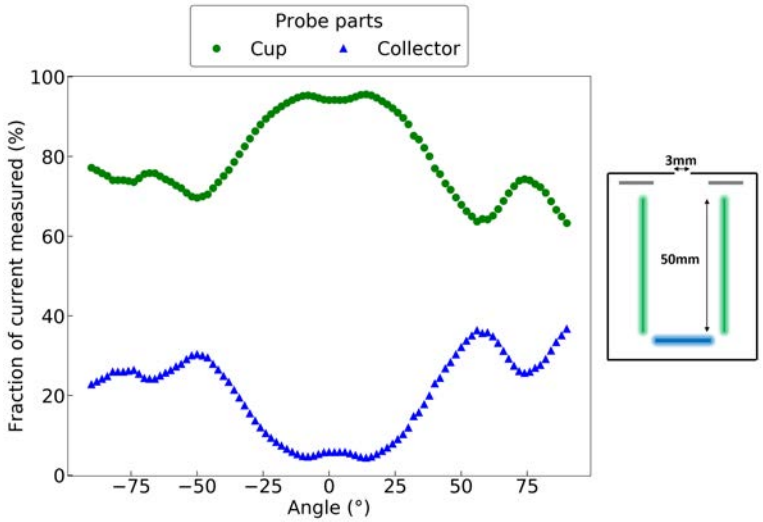

Figure 5.20: Fraction of current measured by the collector (blue) and cup (green). The values are relative to the total current measured by both electrodes. The probe 50.Al.3.P - F.Al.0 is used. HT2 fires at 0.66 A and 250 V.

probe axis to enter. In the first case (top) the grid mesh is 1 mm while in the second case (bottom) it is 0.5 mm. Overall, the total collecting area is 20.45 mm^2 and 15.21 mm^2, respectively. The plot located at the top of the figure confirms the presence of two distinct zones, one before -50° and another after. In the first one, electrode #4 located right at the probe entrance measures the most ion current, followed by #1 then #3 and finally #2. At most, 50% of the ion current is measured by #4 in this region. Between 30% and 40% is collected by #1 and 20% by #3. #2 does not measure more than 5% over the whole angular distribution except during the transition between zone 1 and 2. There, it collects close to 10%. In the second zone, #1 measures seven times less and #4 around twice less. On the opposite #3 increases by a factor four reaching close to 80% of the total ion current measured. When decreasing the diameter of the holes from 1 mm to 0.5 mm as showed in the second plot of figure 5.21, the ion current behaviour inside the probe changes. Now, we observe three different zones:

- Zone 1 is comprised between -90° and -50°. There, up to 60% of the ion current is measured by #3. The rest is equally shared between #1 and #4.
- Zone 2 delimits the region between -50° and -20°. Electrode #3 still collects close to 60% of the total ion current. However, #4 starts to collect more ion

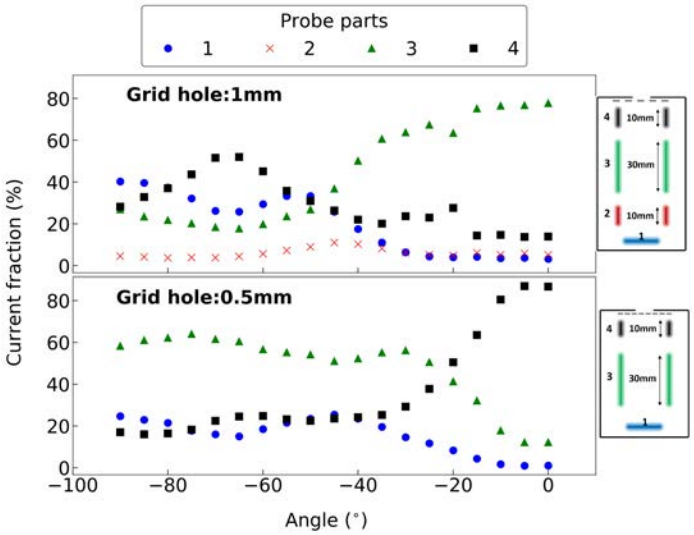

Figure 5.21: Fraction of current measured by electrode 1 (blue), 2 (red), 3 (green) and 4 (black). The probe is composed of staged electrodes as displayed by pictures on the right. Each electrode is spaced by a 10 mm long PEEK insulator. At the probe entrance an aluminium grid is inserted with hole size of 1 mm (top) and 0.5 mm (bottom). The collector is an aluminium foam n°3 while other electrodes are aluminium. The values are relative to the total current measured by all electrodes. HT2 fires at 0.66 A and 250 V.

current while #1 collects less.

- In the third zone, electrode #4 rises and stabilises to 87%. On the contrary both #3 and #1 curves decrease. In the end, on the thruster axis, #1 measures as low as 1% of the total ion current while a bit more than a tenth is captured by #3.

Figure 5.22 shows the influence of the voltages applied to each electrodes during signal acquisition. This time electrode #2 is 30 mm long and placed right after #1. #3 is 10 mm long and spaced by 10 mm from #2. #1 is made of molybdenum while #2 and #3 are of aluminium. #1 is always kept to -60 V and voltages applied to #2 and #3 are set to -60 V for both (top), -30 V (middle) or -100 V for #2 and -30 V for #3 (bottom). The grid mesh placed at the probe entrance is 0.5 mm. As the overall length of the collecting zone is shorter, we observe that between 50% and 60% of the ion current is measured by #1 in the region comprised between -90° and -70°. Close to a third is collected by #2 and only a few percent reach

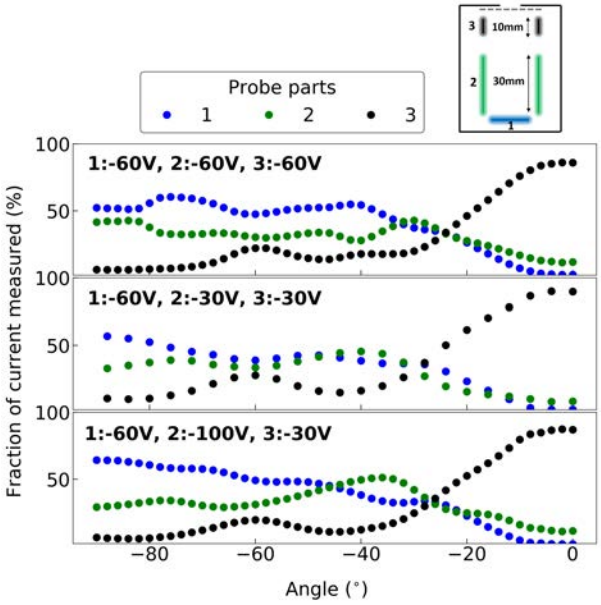

Figure 5.22: Fraction of current measured by electrode 1 (blue), 2 (green) and 3 (black). The probe is composed of staged electrodes as displayed by pictures on the right. At the probe entrance a floating grid is inserted with hole size of 0.5 mm. Electrode n° is either 30 mm (top) or 10 mm (bottom). The collector is made of molybdenum while other electrodes are aluminium. The values are relative to the total current measured by all electrodes. HT2 fires at 0.66 A and 250 V.

#3. Above -70° and below -40° both #1 and #2 curves slightly decrease while #3 increases up to 20% and then remain stable. Beyond -40°, #1 and #2 currents drop slowly to reach 2% and 12%, respectively on the thruster axis. The rest of the ion current is collected by #3. Overall, curves are barely influenced by the change of voltages on #2 and #3. The trend remains constant. Nonetheless, we note some differences in the thruster wings region where #1 collects more and #2 less ion current when the latter is biased to -100 V. As it was showed in section 5.1, increasing the voltage inside the probe tend to focus the ion beam especially when ions are not much energetic. This helps ions to reach #1 instead of splashing on #2. Also, electrode #1 collects more ions currents (close to 60%) at angular position <-50° compared to curves displayed in figure 5.20. We believe this is a direct effect of using a grid a the probe entrance where only ions with velocity vector close to the probe axis may enter. Finally, figure 5.23 show the ion current distribution fraction over three electrodes where electrode #2 is 30 mm

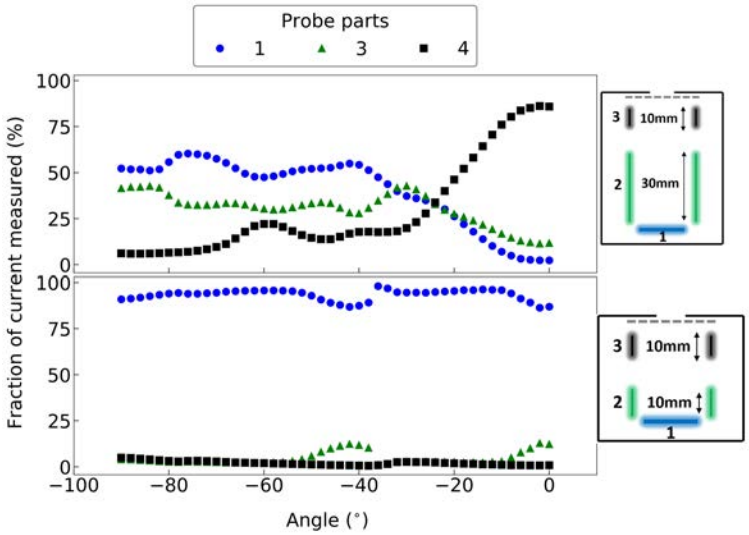

Figure 5.23: Fraction of current measured by electrode 1 (blue), 2 (red), 3 (green) and 4 (black). The probe is composed of staged electrodes as displayed by the picture on the right. Each electrode is spaced by a 10 mm long PEEK insulator. The values are relative to the total current measured by all electrodes. HT2 fires at 0.66 A and 250 V.

(top) or 10 mm (bottom). Here #1 is still made of molybdenum and the two other electrodes are in aluminium and the grid mesh placed at the probe entrance is 0.5 mm. When the overall length of the collection zone is 20 mm (bottom) close to 90% of the ion current is collected by #1. We note a slight oscillation on #1 and #2 between -60° and -40° where ions originating from CEX collisions are present. As the probe is shorter, the ion flight time is shorter, reducing the amount of time exposed to possible perturbation. Indeed, when the ions travel for a long distance in a closed system like in the case of a FC, two phenomena can occur: 1) CEX collisions are more likely to happen with neutrals inside the probe, shifting the ion energies to lower values and changing their direction; 2) The formation of virtual positive electrode in the probe caused by the accumulation of positive charged and low energetic ions bouncing between electrodes due to CEX and long flight time. The ion current distribution inside the probe explains why modifying the cup length and shape barely impacts the ion current. Also, it justifies as well why despite the material decency described in section 5.2 no major perturbations is monitored when modifying the material properties of the collector cup rear part. Indeed, most of the ion current is collected on the front of the cup.

5.3.4 Results Recap

In this section it was demonstrated that the length of the ion collector cup shall not be smaller than 30 mm. We observed that for lower values (i.e. 10 mm) the integrated ion current retrieved from ion current angular distribution measurements can be artificially increased. Indeed, the rise can be around 3% to 30% whether the thruster is operated at discharge voltages of 300 V and 200 V, respectively.

Experiments performed with different cup shape at its rear part showed no significant impact on the measured ion current.

Finally, we brought evidence that the ion trajectories once they penetrate the Faraday cup are not what we would have expected. Indeed, we measured that in the thruster wings 75% of the total amount of measured ion current are collected by the cup walls. When located close to the thruster centre vicinity this value rises above 95% and only a tiny fraction reach the probe rear side. Moreover, we observed that decreasing the total collection area of the probe tends to enhance ion collection at the front side of the ion collector cup. To increase the ion collection efficiency of the probe rear side one shall decrease the total length of the ion collector cup. We saw that passed a given length (e.g. 20 mm) close to the whole ion current going through the cup is properly collected by the rear side of the cup. This suggest that the walls of the ion collector cup are the parts to be optimized prior to the rear side.

5.4 Aperture of the FC

5.4.1 Material induced perturbations

As already broached in section 4 the front of the probe undergoes the highest level of stress during ion current measurements. In the case of Hall thrusters it has been showed by Grimaud et al. [52] that material used to build an electrostatic probe can induce perturbation on measurements outcomes. Their study recommended the use of materials like graphite, tungsten and molybdenum which present low IIE yields [63] and low thermal conductivity. Hall thrusters are operated at relatively high discharge current compared to other technologies, therefore surfaces are exposed to higher level of pulverization and heat which enhance IIE and neutral emission.

Figure 5.24 shows the beam profiles from HT1 firing at 200 V (left) and 250 V (right) at 0.66 A. Ion current densities are acquired with FC 50.**G**.10.E - F.Al.4 and 50.**Mo**.10.E - F.Al.4. Both probes are operated with the repeller exposed to the ion

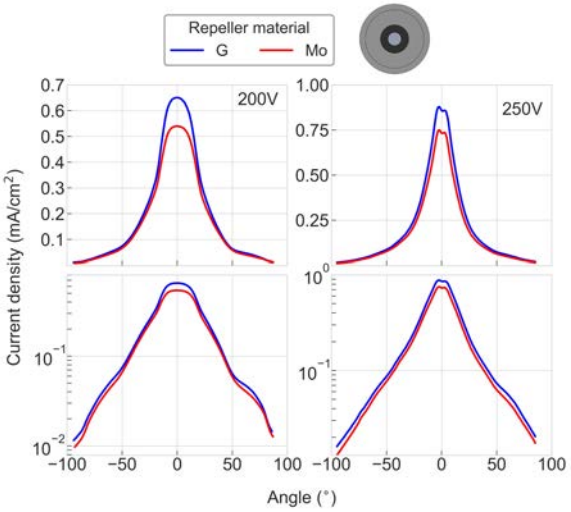

Figure 5.24: Ion current density angular distribution acquired with FC 50.**G**.10.E - F.Al.4 (blue) and 50.**Mo**.10.E - F.Al.4 (red). HT1 fires at 0.66 A, 200 V (left) and 250 V (right). Profiles are displayed with a linear (top) and logarithmic (bottom) scale.

beam and grounded while the collector is biased to -50 V. Note that for both current acquisition the thruster mass flow rate couldn't be kept constant and was set to 0.805 mg/s (G) and 0.82 mg/s (Mo) at 200 V and 0.8 mg/s (G) and 0.79 mg/s (Mo) at 250V. The probe equipped with a molybdenum repeller measures less ion current density over the whole beam profile. In average this FC reads 14%±5.4% and 17%±2.7% less ion at 200 V and 250 V, respectively. At most it measures 20% less near the thruster centre axis. The integrated ion current retrieved from the beam profiles are listed in table 5.2. The deduced current and propellant utilization is also given. The integrated ion current, and therefore the current and propellant utilization parameters are lower for the FC configured with a molybdenum repeller, for both thruster operations. η_b and α increases at 250 V because the thruster is more efficient as it is designed to operate at 200 W.

The software SRIM (Stopping and Range of Ions in Matter) is used to find the sputtering yield of Al, C (≡graphite) and Mo with xenon (Xe) ions as projectile (see section 2.1.5). Simulations including 10000 singly-charged xenon ions is run to compute the yield and heat losses. The latter corresponds to the energy transferred by projectiles to the target materials and subsequently converted into heat. Figures 5.25 and 5.26 show results for carbon (i.e. graphite) and molybdenum

Table 5.2: Ion current retrieved from HT1 beam profiles acquired with FC 50.**G**.05.E - F.Al.4 and 50.**Mo**.05.E - F.Al.4.The current and propellant utilization are also indicated.

Faraday cup	**Mass flow rate** mg/s	$I_{i_{int}}$ A	η_b	α
	0.66 A, 200 V			
50.**G**.05.E - F.Al.4	0.805	0.481 A	0.729	0.813
50.**Mo**.05.E - F.Al.4	0.82	0.433 A	0.656	0.718
	0.66 A, 250 V			
50.**G**.05.E - F.Al.4	0.8	0.499 A	0.756	0.849
50.**Mo**.05.E - F.Al.4	0.79	0.438 A	0.663	0.754

under Xe ion bombardment. The software computes the sputtering yield based on the binding surface energy (E_{surf}) specific to each target. When this value is not known the heat of sublimation is used instead [6]. Moreover, E_{surf} strongly depends on the material cleanliness and roughness. These properties will change over time as the target gets bombarded. It can lead to quick change of the sputtering yield. For instance, figure 5.25 shows the sputtering yield as a function of the target atom's energy which reach the surface of the material. Singly-charged xenon ions are used as projectile and targets are made of carbon (top) and molybdenum (bottom). The vertical blue line, which defines the average surface binding energy, gives 7.4 eV and 6.8 eV for the carbon and molybdenum targets respectively. The arrow, to the left of this line, with the legend "not sputtered" implies the number of atoms which reached the surface with more than 7.4 eV (C) or 6.8 eV (Mo) is 0.005 and 0.18, respectively. These values correspond to the sputtering yield and are listed in table 5.3. The vertical blue line will shift towards the left when the material surface gets damaged. The filled area shows how much effect small changes of the surface roughness ($\equiv E_{surf}$) will make on the final sputtering yield. It is seen that the two materials experience a fast degradation of the yield when the material surface is damaged. However, the maximum sputtering yield for carbon remains small (0.32 atoms/ion) compared to Mo yield that is 10 times higher. In the worst case molybdenum releases 3 sputtered atoms per incoming ion which is not negligible. In the case of carbon, shortly after the vertical blue line, the yield becomes very small and sputtered particle only have energies from 7.4 eV to 12 eV. Molybdenum sees its sputter energy distribution to be more important. The atoms can reach energies from 6.8 eV up to 20 eV. From these two

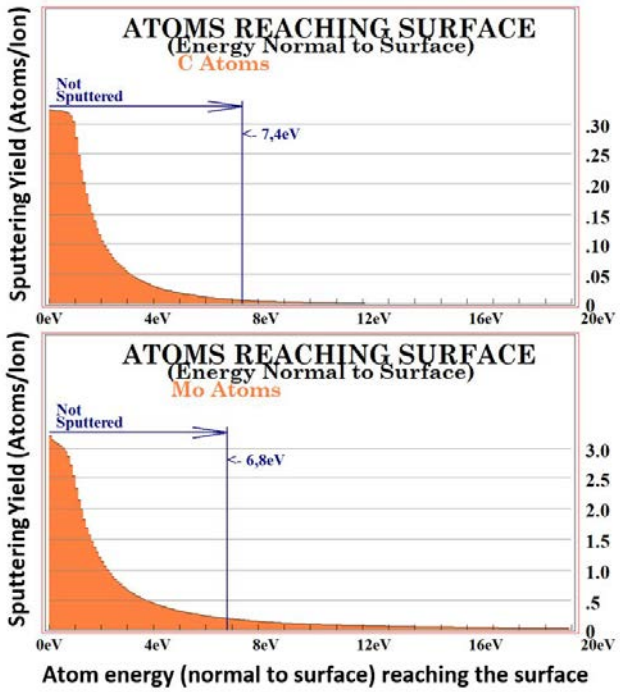

Figure 5.25: Carbon (top) and molybdenum (bottom) sputtering yields and threshold value for 250 eV Xe ions computed with the SRIM software.

Table 5.3: Sputtering yield coefficient computed for different discharge voltages with the software SRIM [6].

Material	**Sputtering yield (200V)** *Atoms/ions*	**Sputtering yield (250V)** *Atoms/ions*
Carbon (Graphite)	0.0018	0.0056
Molybdenum	0.13	0.18
Aluminium	0.11	0.16

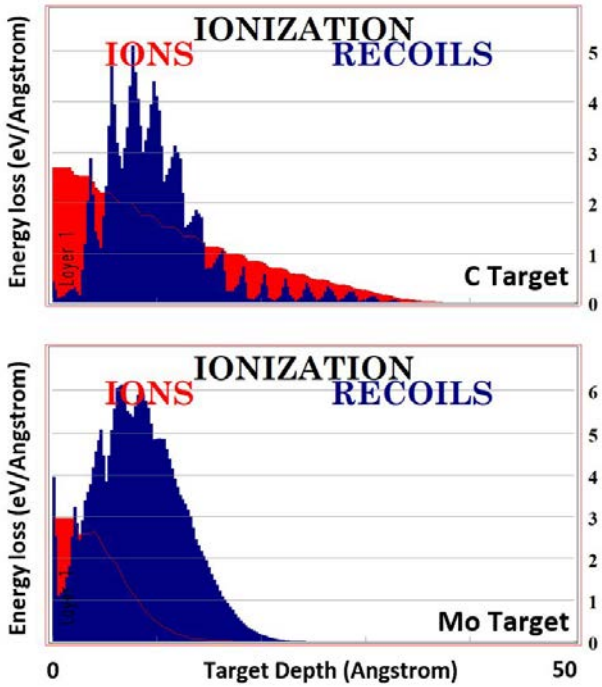

Figure 5.26: Xenon ions energy losses per angstroms to carbon (top) and molybdenum (bottom) targets computed with the SRIM software.

plots we understand that molybdenum will tend to sputter more atoms with an energy distribution broader than carbon. Any material subject to ion bombardment heats up. Its impact can be estimated with the software SRIM as pictured in figure 5.26. It shows the energy loss by the projectile for carbon and molybdenum. The red curve labelled "IONS" is the direct energy transferred from the ion to the target electrons. The blue curve, called "RECOILS", represents the energy transferred from recoiling target atoms to the target electrons. Both phenomena contribute to the heating process of materials. Figure 5.26 pictures ion energy per angstroms losses with targets made of carbon and molybdenum. Losses are smaller with C than with Mo. Additionally, the energy loss decreases as the projectile goes deeper into the target. The energy loss distribution in C is wider through the material thickness than molybdenum. Most energy losses from Xe ions into Mo occurs near the surface enhancing local heating on the material.

Experimental results and numerical simulations can only suggest conservative measures to limit plasma–probe perturbations. We know from section 5.3.3 that the main part of the ion current going through the probe is collected by the front

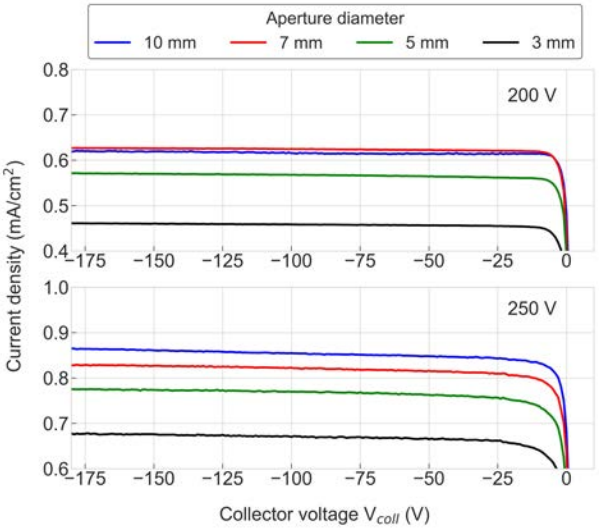

Figure 5.27: On-axis I-V curves obtained with HT1 firing at 0.66 A, 200 V and 250 V. The FC configuration is 50.G.**X**.E - F.Al.4. The aperture diameter is changed from 10 mm (blue) to 3 mm (black). The repeller is grounded while a voltage sweep is applied to the collector.

part of the cup. Therefore, the material chosen to be placed at the forefront of a Faraday cup must have a low sputtering yield. It is also preferable to have a wide energy absorption capacity to minimize material heating.

5.4.2 Aperture size induced perturbations

In this section the impact of the probe aperture diameter will be investigated. It was showed in section 4 that this parameter could decrease at most the ion current measured by 10% for a FEEP thruster. Here, the based design is 50.G.**X**.E - F.Al.4, with the repeller diameter changed from 10 mm to 3 mm. On-axis I-V curves are displayed in figure 5.27. We observe that the current density decreases when the aperture diameter d_a is reduced. For both thruster firing conditions the slope of each I-V curves is of the order of 10^{-5} mA . V^{-1} . cm^{-2}. The 3 mm configuration measured around 30$\pm$1% less than the 10 mm aperture design. Figure 5.28 shows the ion current density angular distribution acquired for each aperture diameter with HT1 firing at 0.66 A, 200 V and 250 V. The same current loss is observed over the whole beam profile as the aperture diameter decreases. This could be explained by the non-collection of thermal ions when the aperture is narrowed down.

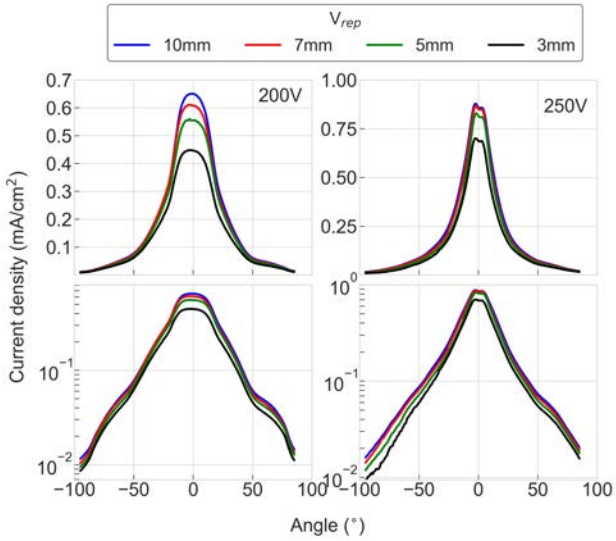

Figure 5.28: Current density angular distribution measured with different repeller diameters (10 mm, 7 mm, 5 mm, 3 mm). HT1 fires at 0.66 A, 200 V (left) and 250 V (right). Profiles are displayed with a linear (top) and logarithmic (bottom) scale.

However, Vaudolon et al. [123] showed that the ion thermal current is small in the ISCT200 plume. Figure 5.29 shows the evolution of the integrated ion current $I_{i_{int}}$ (top) and beam divergence angle θ_{div} (bottom) for different aperture diameters. HT1 fires at 0.66 A, 200 V and 250 V. θ_{div} seems to not be affected by the change of aperture size as the variations are comprise in our measurements uncertainties. On the opposite, $I_{i_{int}}$ decreases with the aperture diameter. In average from the ion current measured with the 10 mm configuration $I_{i_{int}}$ drops by $\sim$3% with 7 mm, $\sim$12% with 5 mm and $\sim$30% with 3 mm. So far, we could assume that the ion current measured is strongly influenced by the aperture dimension. One possible explanation is the invalidity of the point source assumption that is often found in the literature. Ions originate from an extended region of space that has an annular geometry. Moreover, the velocity vector dispersion is large in the case of HTs due to the overlap between the ionization and acceleration zones combined with many scattering and charge-exchange collision events.

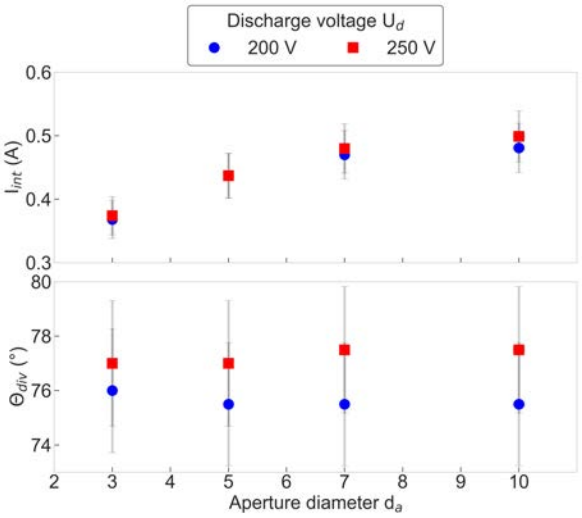

Figure 5.29: Evolution of integrated ion current $I_{i_{int}}$ (top) and divergence angle (bottom) computed from ion current density distributions obtained with different aperture diameters. HT1 is operated at 0.66 A, 200 V (blue), 250 V (red). The coverage factor k equals 2.

5.4.3 Perturbations mitigation

In the two previous sections, it was showed that materials and aperture dimensions chosen for a FC can have a non-negligible influence on the measured ion current, in the case of a HT. So far, we have been testing those parameters with the probe configuration X.X.X.**E**. Nevertheless, it was detailed in section 5.1 that this configuration would tend to worsen the probe-plasma interaction as the field-lines generated by the probe operation expand easily in the bulk plasma. In addition, coating formation is more likely on critical parts of the probe (e.g. insulators) as explained in section 4.3. Therefore, the X.X.X.**P** configuration is tested in this section. As a reminder, it uses the probe housing front to define the ion flux going through the cup while the repeller is placed behind with a diameter larger than d_a, just before the collector cup. Two different probe design are used: FC 50.Al.**05**.**P** - F.Al.4 and 50.Al.**03**.**P** - F.Al.4 as displayed in figure 5.30. Outcomes will be compared to profiles and currents measured in the two previous sub-sections.

Figure 5.31 show the ion current density angular distribution obtained with HT1 firing at 0.66 A 200 V (left) and 250 V (right). FC 50.**G**.**05**.**E** - F.Al.4 results are in blue FC 50.**Al**.**05**.**P** - F.Al.4results in red. Therefore, profiles in blue are

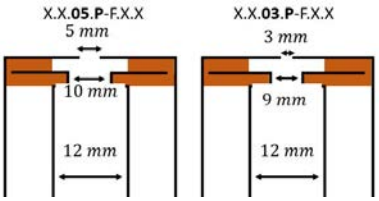

Figure 5.30: Schematic showing the probe configuration X.X.**05**.**P** - F.X.X and X.X.**03**.**P** - F.X.X. The repeller is 1 mm thick and is placed 1.5 mm behind the housing front and 3.5 mm before the cup.

acquired with a probe aperture of 5 mm diameter, with graphite as front material and the repeller exposed. In red, the probe aperture is 5 mm as well, made of aluminium with the repeller protected from direct exposure to the plasma. Aluminium has a thermal conductivity relatively high compared to graphite and molybdenum, its sputtering yield is of the same order than molybdenum and its γ_{EE} is the highest amongst them. It should therefore worsen the phenomenon observed with molybdenum in section 5.4.1.

For both thruster operation conditions, X.X.X.P measures the highest ion current density. On the thruster axis, the signal acquired by configuration X.X.X.P is 15 to 20% higher than X.X.X.E. The difference in current density is observed over the whole beam profile. The ion currents retrieved from the profiles are displayed in table 5.4. The value obtained with FC 50.**G**.**10**.**E** - F.Al.4 is given as well, as it is supposed to be the best design so far, based on the two previous sub-sections. For a constant aperture diameter of 5 mm the X.X.X.P configuration gives an ion current 8.2% and 10% higher than X.X.X.E at 200 V and 250 V, respectively. This rate of change is similar to observation done in section 5.4.2 between a 5 mm and 10 mm aperture diameter in a X.X.X.E configuration. Indeed, the table shows that the ion current values are now close, within experiment uncertainties, to figures computed with the 10 mm aperture X.X.X.E configuration. This seems to indicate current losses observed in section 5.2.1 and 5.4.2 are greatly mitigated when the probe is in X.X.X.P configuration.

Results display in figure 5.31 and table 5.4 shows that the X.X.X.P configuration mitigates or even suppresses perturbations induced by the front material and aperture size. To ensure that the study outcomes are not caused by experimental bias, the same measurements are done at a different time with a different thruster (e.g.HT2) but with the same procedure. Figure 5.32 shows J_i profiles with FC 50.G.03.**E** - F.Al.3 and 50.Al.03.**P** - F.Al.3. HT2 fires at 0.66 A and 250 V. Once

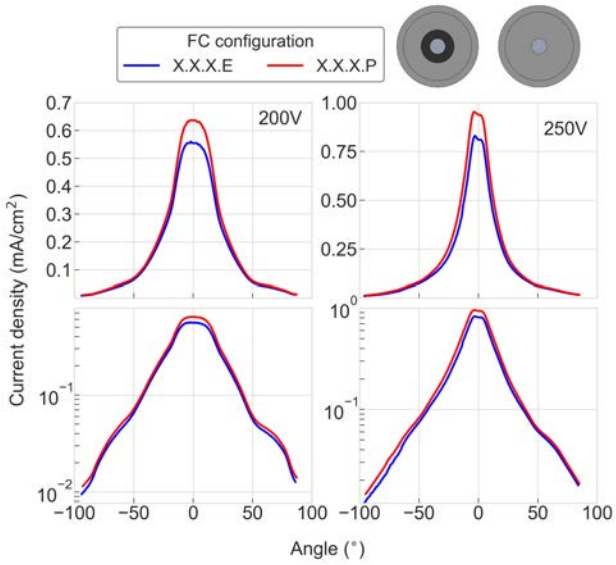

Figure 5.31: Current density angular profile acquired with FC 50.G.05.**E** - F.Al.4 (black) and 50.Al.05.**P** - F.Al.4 (blue). HT1 fires at 0.66 A, 200 V (left) and 250 V (right). Profiles are displayed with a linear (top) and logarithmic (bottom) scale.

Table 5.4: Impact of the X.X.X.P configuration on the integrated ion current i_{int}.

Faraday cup	**Mass flow rate** mg/s	$I_{i_{int}}$ A	Section
	0.66 A, 200 V		
50.G.**05**.**E** - F.Al.4	0.815	0.437	5.4.2
50.Al.**05**.**P** - F.Al.4	0.812	0.473	
50.G.**10**.**E** - F.Al.4	0.805	0.481	5.2.1 and 5.4.2
	0.66 A, 250 V		
50.G.**05**.**E** - F.Al.4	0.79	0.437	5.4.2
50.Al.**05**.**P** - F.Al.4	0.79	0.486	
50.G.**10**.**E** - F.Al.4	0.8	0.499	5.2.1 and 5.4.2

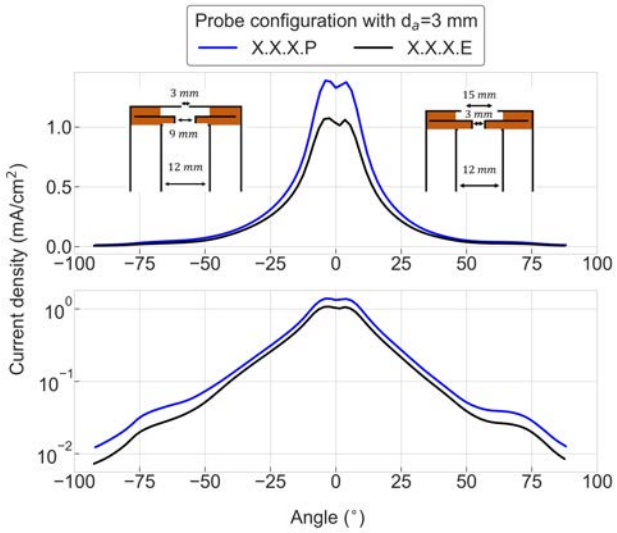

Figure 5.32: Ion current density angular distribution acquired with FC 50.Al.**03**.P - F.Al.3 (blue) and 50.Al.**07**.P - F.Al.3 (red). HT2 fires at 0.66 A and 250 V. Profiles are displayed with a linear (top) and logarithmic (bottom) scale.

again the X.X.X.P configuration measures more ion current. $I_{i_{int}}$ reads 30% more when X.X.X.P is used. Once more, the rates of change observed are similar to those measured in section 5.4.2 between a 3 mm and 10 mm wide aperture in a X.X.X.E configuration. Figure 5.33 display the beam profiles acquired with three different X.X.X.P configurations:

- $d_a = 3$ mm and $d_{rep} = 9$ mm (blue)
- $d_a = 7$ mm and $d_{rep} = 9$ mm (red)
- $d_a = 3$ mm and $d_{rep} = 5$ mm (green)

We observe no real changes near the thruster centre axis. The signal variation observed between $\pm 5°$ ($\sim$2%) is small enough to be attributed to measurement uncertainties. However, starting from $\pm 35°$ and until the end of the profile, the 3 mm configuration measures more ion current. Nonetheless, this current rise is different whether the gap between the aperture and repeller diameter is 2 mm (green) or 6 mm (blue). There, the mass flow rate was adjusted to allow identical discharge currents. The value was set to 0.96 mg/s when using $d_a = 3$ mm and $d_{rep} = 9$ mm (blue) and 0.97 mg/s for $d_a = 3$ mm and $d_{rep} = 5$ mm (green). The

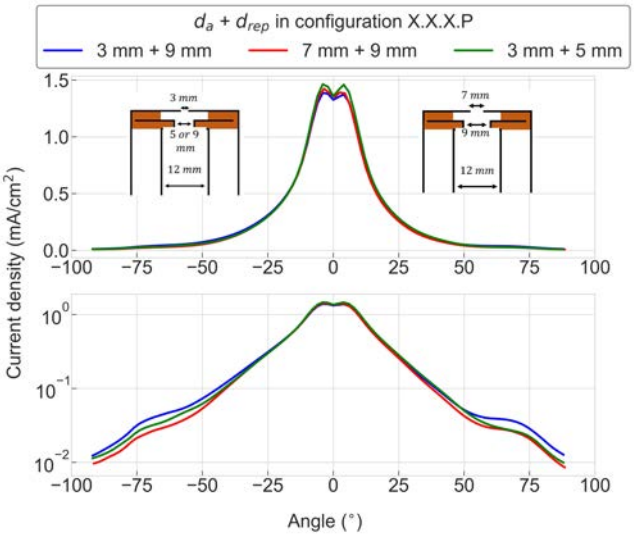

Figure 5.33: Ion current density angular distribution acquired with FC 50.G.03.**P** - F.Al.3 where $d_{rep} = d_a + 6$ mm (blue) or $d_{rep} = d_a + 2$ mm (green) and FC 50.Al.07.**P** - F.Al.3 where $d_{rep} = d_a + 2$ mm(red). HT2 fires at 0.66 A and 250 V. Profiles are displayed with a linear (top) and logarithmic (bottom) scale.

higher mass flow rate for the latter explains why there is more ion current measured on the thruster and less at large angles as the beam is more focus. In fact, when comparing the ion currents retrieved from profiles these two probe configurations only differ by 2.6% which lies in our uncertainties. However, compared to the ion current measured with the 7 mm aperture design (red), the value is 10% higher. Note that beam profiles presented in figure 5.33 were measured several times, at different day, after few vacuum and thruster thermal cycles and identical results were measured. The ion current increase observed with the $d_a = 3$ mm at medium and large angles is still not completely understood. Nonetheless, the thruster current utilization found with X.X.3.P is 81±5% while for X.X.7.P it is 73±5%. The latter seems more realistic for a 200 W class Hall thruster, implying that the X.X.7.P design is the optimal one.

Finally, figure 5.34 show ion beam profiles measured by two FC in configuration X.X.X.P with front material made of graphite (blue) and aluminium (red). No major differences are observed as variation are within our experiment uncertainties.

The observations made in this section tend to prove that the X.X.X.P configuration greatly help to mitigate material and aperture dimension induced perturba-

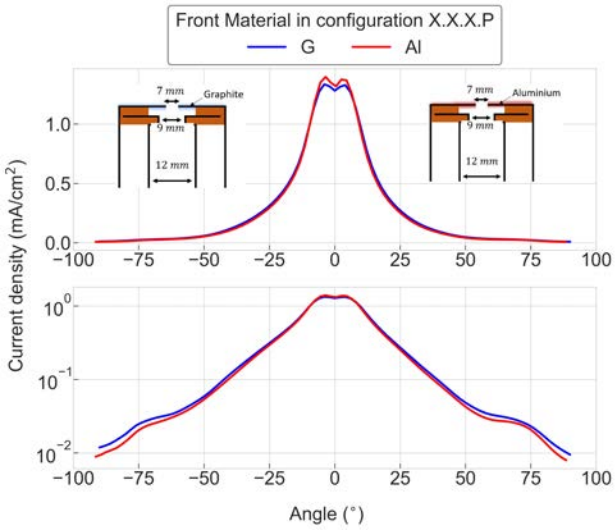

Figure 5.34: Ion current density angular distribution acquired with FC 50.**G**.07.P - F.Al.3 (blue) and 50.**Al**.07.P - F.Al.3 (red). HT2 fires at 0.66 A and 250 V. Profiles are displayed with a linear (top) and logarithmic (bottom) scale.

tions. There are two possible ways to artificially increase or decrease the measured ion current: non recollection of IIE and ion losses, respectively. It is more likely that IIE process are responsible for the lower currents measured when decreasing the aperture front. Same argument can be stated when using front materials which get hot and easily sputtered as both enhance the IIE effects. Section 5.3 showed that most of the ion current is measured on the front part of the cup near the probe entrance. Therefore, the distance between the probe inlet and the top of the collector cup seems to be a critical parameter. As already mentioned the probe front undergo a high level of stress including sheath expansion. Moreover, the cup is always biased negatively and therefore, it repels primary electrons and attract ions which creates a positive high voltage sheath. We know from [29] that the ion sheath is of the same order of magnitude than the electron sheath ($\sim s_{hv_i} = \frac{s_{hv_e}}{1.5}$). Moreover, the sheath is related to the Debye length which was given in section 3 for our thrusters. Therefore, $\sim s_{hv_i}$ range between 0.6 and 1.74 mm. Note that with the X.X.X.E configuration the distance between the cup and the probe aperture is of the same order. Moreover, the region between the probe entrance and the cup cannot be considered quasi-neutral as this is where electrons are being repelled towards outside. Consequently, ion-induced electrons emitted by the probe entrance in a X.X.X.E configuration will see a negative potential near the probe entrance

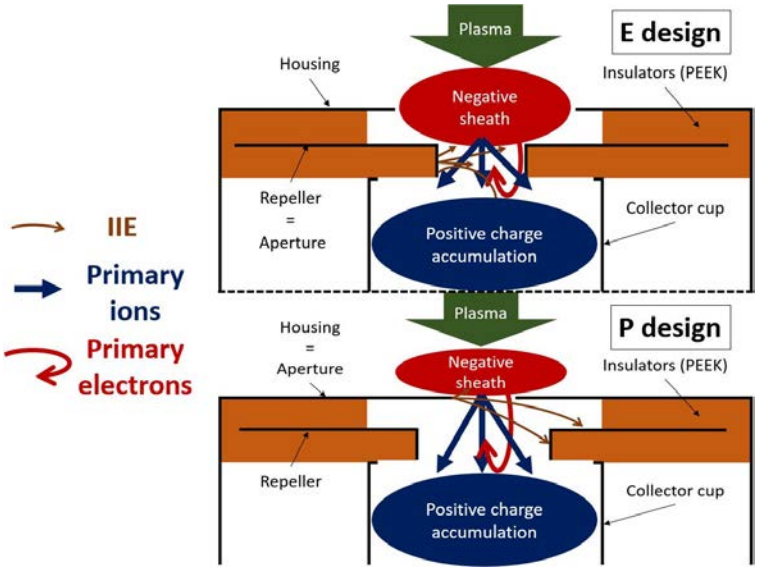

Figure 5.35: Drawing representing phenomenon leading to a current decrease when using X.X.X.E FC configuration.

(i.e. electrons being pushed back + negative sheath) and a positive potential inside the probe due to the positive sheath and flow of primary ions going through the cup. Therefore, IIE will tend to be accelerated and directed towards the cup, overtaking the negative potential of the probe on a short distance. Hence, the measured current decreases. Any process increasing the IIE population in this region would contribute to the ion current decrease measured by the cup, as described by figure 5.35. However, when increasing the distance between the probe entrance and the top of the cup, IIE emitted are less influenced by the positive sheath inside the probe, their velocity direction is less disturbed by the ion flux as well. They are still confined by the negative sheath expanding at the entrance and originate now in a region upstream the one where primary electrons are repelled. Consequently, they will either fly into the cup direction but will splashdown before reaching it or be pushed outside following the flow of repelled electrons.

This theory would explain the current behaviour observed with the X.X.X.E configuration. Further analysis shall be conducted to confirm or refute it.

Table 5.5: Material selection pros and cons.

Material	γ_{EE}	**Sputtering yield**	**Price (in 2022)** $/kg	**Material machining**
Aluminium	medium	high	∼3.4	easy
Graphite	low [99]	low	∼10	easy (but brittle)
Molybdenum	low	high	∼43	medium
Stainless Steel	medium	high	∼5	easy
Tungsten	low [63]	high	∼40	medium

5.4.4 Results Recap

In this section we shown that using a Faraday cup with a standard design (i.e. X.X.X.E configuration), as can be found in the literature, can lead to errors on the measured ion current. We, therefore, recommend to use at the probe front a material with low sputtering yield with a wide energy absorption capacity to minimise material heating. In addition, we spotlighted that the definition of the probe aperture diameter is of great importance. By decreasing the inlet from 10 mm down to 3 mm we observed a drop of 30% from the measure ion current density over the whole beam profile. Nevertheless, we demonstrated that perturbations induced by the choice of material and aperture dimension at the probe front can be mitigated or suppressed thanks to an alternative FC design. Indeed, the X.X.X.P configuration permits to better shield the ion collector cup from the mentioned perturbations. Therefore, we highly recommend to design a Faraday cup in X.X.X.P configuration.

Finally, table 5.5 summarizes the pros and cons when it comes to select the most appropriate material in a FC design.

Chapter 6

From ion current measurements to ion energy retrieval

Contents

6.1 Optimized Faraday cup architecture

Sections 4 and 5 provided the necessary information to obtain the optimal design of a Faraday cup to accurately measure the ion current from a FEEP and a low power HT at a distance larger than 24 cm from thruster exit plan. The two following sub-sections present beam profile acquisition and measured ion current with an optimized Faraday cup.

6.1.1 Field-emission electric propulsion thruster

In the case of FEEP thrusters, it was shown that the main source of perturbation is related to IIE. Moreover, the distance as well as the definition of the collection area can also be the cause of errors. The following list describes, in priority order, critical parameters to implement when designing a FC to measure the ion current 25 cm away from the thruster exit:

1. The cup should be longer than 30 mm. It is recommended to have a FC close to 50 mm to ensure very little disturbance induced by IIE in case of repeller failure.

2. The collector voltage shall be negative and < -30 V.

3. The repeller voltage should be set more negative than the collector to actively push all IIE back inside the probe. At least V_{rep}=V_{coll}-30 V. Based on our experimental results, we can recommend to have a repeller inner diameter 2 mm larger than the probe entrance.

4. The probe inlet should be large but also the smallest diameter of the probe system. Based on our experimental data we can recommend to have an inlet diameter > 7 mm.

5. The probe should be used in a X.X.X.P configuration. This imply that the distance between the probe entrance and the collector must be at least larger than 4.5 mm (based on experimental data).

6. Graphite should be preferred to equip the front of the probe. However, if previous recommendations were followed the material used for the probe front won't impact the outcomes. This allows the user to choose cheap and easy to manufacture materials like aluminum.

7. Based on our experimental analysis we can recommend to have a collector diameter 5 mm larger than the probe entrance and 3 mm than the repeller.

8. The optimal collector material shall have a low IIE yield. A foam type material with pore size >0.4 mm could further decrease γ_{EE}. However, if recommendations 1 and 2 were followed this parameter has little influence upon outcomes.

9. If recommendations 1 and 2 were followed the shape of the cup has little influence on outcomes. To ease drilling manufacturing, the rear part of the cup can have a conical shape. In this condition the normal of the sides of the cone shall be oriented towards inner part of the cup.

10. The bottom of the cup does not need to be uncoupled from the cup walls.

Therefore, a Faraday cup in configuration 50.Al.7.P - F.Al.3 is used to measure ion beam profiles for a range of thruster operation points. Figure 6.1 displays those profiles in a linear (left) and logarithmic (right) scale. The top of the figure presents ion current density angular distributions when the thruster LU-C fires at 2 mA and the emitter voltage goes from 3 kV to 8 kV. There, it is clearly shown that increasing the emitter voltage, and therefore decreasing the extractor one, enhance the ion beam focus, decreasing the beam divergence. In the bottom plot, the emitter current is increased from 1 mA to 4 mA while the emitter voltage is kept to 5 kV. Here, the ion current density bulks as the emitter current increases.

Despite non-negligible variations of the ion distribution intensity as we change the thruster settings we observe in figure 6.2 that ion current measurements are very little impacted. Indeed, the figure plots the ion current retrieved with the FC (blue) in comparison to the emitter current (i.e. ion current) input (red). For every operation point, from large current intensity to high discharge voltage, the FC is always able to provide the "true" ion current. Overall, the mean deviation of $I_{i_{int}}$ from I_{em} is $\pm 0.7\%$. The maximum deviation reaches -4.72% when the thruster fires at 2 mA and 6 kV. However, these deviations are still within or close to our experimental uncertainties.

Figure 6.1 and 6.2 show that our FC design enables to properly characterize the ion beam produce by the thruster LU-C with an accuracy of $\pm 4.5\%$ for a confidence level of 99%.

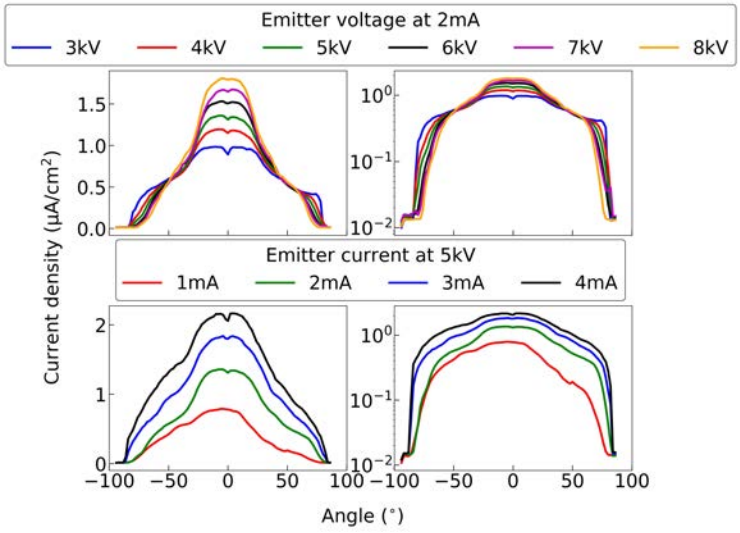

Figure 6.1: Ion beam profiles acquired with FC configuration 50.Al.7.P - F.Al.3 for different thruster (LU-C) operation points. Top: the emitter voltage varies for firing conditions of 2 mA. Bottom: the emitter voltage is fixed to 5 kV and I_{em} varies. The probe is operated with the collector set to -30 V and the repeller to -60 V.

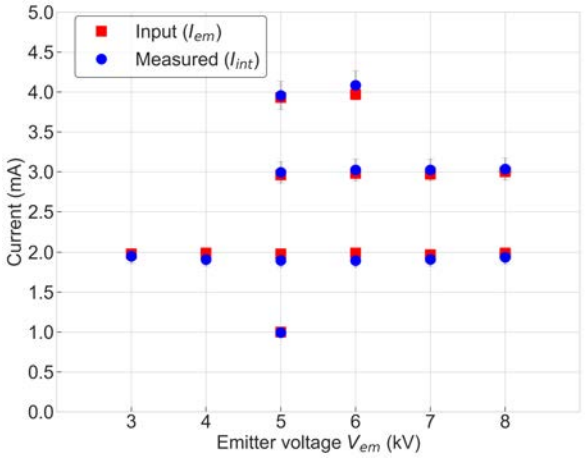

Figure 6.2: Ion current measured ($I_{i_{int}}$) with FC configuration 50.Al.7.P - F.Al.3 for different thruster (LU-C) operation points. The probe is operated with the collector set to -30 V and the repeller to -60 V. The input current (I_{em}) is plotted for reference.

6.1.2 Low power Hall thruster

Section 5 demonstrated that the design of the front of a Faraday cup is of great importance as it is enrolled in the main source of errors. The construction of a Faraday cup to measure the ion current within the plume of a low power Hall thruster should follow these recommendations:

1. We saw with typical I-V curves that when the collector is biased at voltages higher than -50 V the measured signal starts to be disturbed by primary electron coming from the thruster cathode, hence the ion saturation current cannot be accurately determined. Consequently, we recommend to have the collector voltage set to at least -50 V. However, this value greatly depends on the thruster power range and the fraction of electron current and their energy within the plume. In this case lower voltage are necessary.

2. We showed in section 5.3.1 that at length equals to and smaller than 10 mm the integrated total ion current obtained from current angular distribution measurements is higher than expected. Moreover, the artificial increase is at its worst ($\approx$30 %) when the thruster is operated at low discharge voltages and becomes smaller as the discharge voltage increases (i.e. $\approx$3 % at $U_d = 350$ V). Consequently, we recommend to keep the cup length larger than 10 mm. Also, to ease the probe implementation into small vacuum chamber it is preferable to not design a FC with a cup length larger than 50 mm.

3. We recommend using the X.X.X.P configuration since with this design the entrance of the probe is further away from the entrance of the cup, hence preventing ion-induced and secondary electrons coming from outside/entrance of the FC to reach the collector. With our experiments (see section 5.4.3) we observed that a distance of 4.5 mm between the point of collimation and the top of the collector cup is sufficient.

4. We recommend leaving the repeller floating to minimise perturbations with low energy ions inside the plume of a Hall thruster. Also, from our experiments we observed that when using the FC in X.X.X.P configuration a repeller inner diameter 2 mm wider than the probe aperture is sufficient to mitigate perturbations as described in section 5.4.3.

5. We proved in section 5.4.2 that decreasing the probe aperture leads to lower ion signal measurements over the whole plume profile if using a FC in

X.X.X.E configuration. However, section 5.4.3 brought evidence that when using the probe in X.X.X.P mode perturbations induced by the aperture dimension vanishes. Still, we would recommend to keep the aperture of the FC larger than 7 mm to maximise the collection solid angle of the probe. We would limit its upper value to 12 mm at most to minimise the overall size of the probe. Indeed, the rest of the parts diameter (i.e. repeller, collector) are driven by this dimension and shall be larger.

6. We discussed in section 5.4.1 that using a material with a low ion-induced electron emission yield, a low sputtering yield and a wide energy absorption capacity to minimize material heating is preferable to minimise perturbations induced by the plasma-probe interactions. In this regard, graphite seems to be a good candidate to equip the front of the probe due to the large current intensity at stake 25 cm away from a low power Hall Thruster exit plane.

7. On a pure dimensioning aspect for a FC we observed that having the collector diameter 5 mm larger than the probe entrance and 3 mm than the repeller is sufficient to obtain accurate results.

8. The choice of material as ion collector has little influence on the outcomes. However, if used as a simple disk (like in the case of planar probes) it is recommended to use bulk materials like tungsten, molybdenum and graphite since they have very low ion-induced electron emission yields.

9. The bottom of the cup can be uncouple from the cup walls. This would lead to a better visualization of current distribution inside the probe.

10. The shape of the cup influence is negligible.

Therefore, after several iterations the Faraday cup 50.G.7.P - F.Al.3 is used to scan the plume of HT2. Note that the design of the probe only differs from the one used on LU-C by the front which is made of graphite instead of aluminium. Figure 6.3 displays in a linear (left) and logarithmic (right) beam profiles acquired 26.5 cm away from the thruster exit plane. At the figure top profiles acquired when HT2 fires at 0.66 A from 200 V to 350 V are shown. We note a major change between 200 V and other profiles. At 200 V and 0.66 A the anode power (i.e. 132 W) is too low to properly operate the ISCT200, hence a lower thruster efficiency and a plume enlargement. Overall, beam profiles get more focus as U_d increases. Moreover, it is seen that the region characteristics of CEX collisions in the main

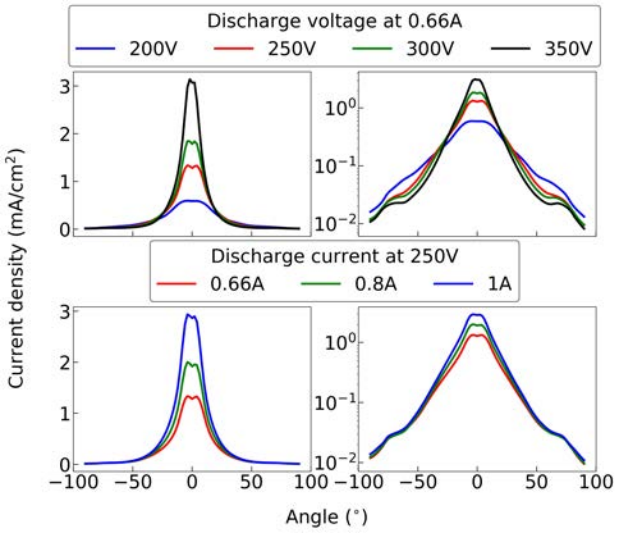

Figure 6.3: Ion current angular distribution acquired with FC configuration 50.G.7.P - F.Al.3 for different operation points. Top: the discharge voltage varies for firing conditions of 0.66 A. Bottom: the discharge voltage is fixed to 250 V and I_d varies. The probe is operated with the collector set to -60 V and the repeller is floating.

beam of the thruster is more visible with large discharge voltages. In the bottom figure, acquired profiles represent the thruster firing at 250 V, 0.66 A, 0.8 A and 1 A. The increase of ion current intensity is mainly observed in the region close to the thruster axis. At large angles the ion current density angular distribution is barely impacted by the thruster settings. Figure 6.4 gives the ion current retrieved from the above profiles. It is also showed the deduced current (η_b) and propellant (α) utilizations from known thruster parameters such as discharge current (I_d) and anode mass flow rate. These values are given to exemplify the usefulness of a FC properly designed. Thanks to the ion current measured we are able to characterize a few performance parameters of the thruster HT2. The current utilization, i.e. the thruster efficiency to ionize xenon, increases with the discharge voltage for a fixed input total current. It goes from 71% at 200 V to 81% at 350 V. These values are coherent with what is found in the literature for low power Hall Thrusters. However, the propellant utilization seems to be stable around 71%. The trend seems to imply that between 200 V and 250 V this parameter slightly improves before decreasing when the discharge voltage is higher. On the other hand, it is seen that increasing the discharge current while keeping U_d constant have the

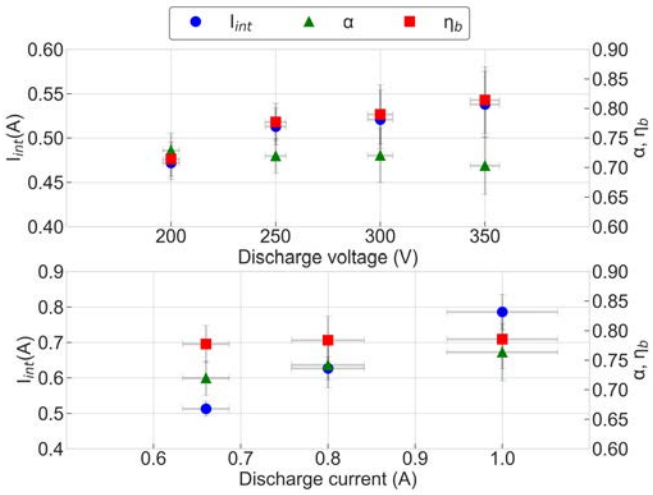

Figure 6.4: Ion current measured ($I_{i_{int}}$) with FC configuration 50.Al.7.P - F.Al.3 for different HT2 operation points. The probe is operated with the collector set to -60 V and the repeller is floating. The current and propellant utilization are also shown.

opposite behaviour. Indeed, α increases from 71% to 76% while η_b remains stable around 78%.

Figure 6.3 and 6.4 show that thanks to its reliability this FC design enables to start characterizing some performance parameters which strongly depend on the measured ion current.

6.2 Ion energy analyser

As described in section 2.2.2.2 and 3.2.3, two different RPA designs were used for the FEEP and HT. Since their plumes are different in terms of ion current density and ion energy specific designs had to be implemented for each of them to enable accurate determination of the ion energy.

6.2.1 Field-emission electric propulsion thruster

Figure 6.5 displays the first derivative of the RPA ion current as well as corresponding Gaussian fits, acquired at 0°, when LU-C fires at different operation

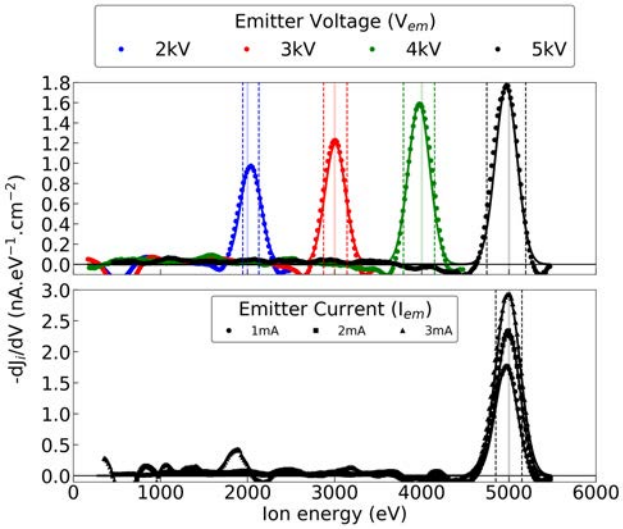

Figure 6.5: Current intensity as a function of the ion energy measured with an RPA. Top: LU-C fires at 1 mA and different emission voltage. Bottom: LU-C fires at 5 kV with different emission current. a Gaussian fit is applied to all profiles. Points represent raw data.

points. All traces are also smoothed by a Savitzky-Golay filter with a window size of 31 and polynomial order of 2. At the top, LU-C fires a 2 mA with emitter voltage varying from 2 kV to 5 kV. At the bottom, V_{em} is fixed to 5 kV and I_{em} is increased to 2 mA and 3 mA. The dashed lines represents the region including our experimental uncertainty. The filled vertical lines represent eV_{em}. We note that the peak of the curves, i.e. the most probable energy (E_{max}), is close to eV_{em}. In absolute value the mean deviation is as low as 0.4%. Also, we note that at 0° the energy dispersion (ΔE) increases by 16 eV between 2 kV and 5 kV. When the ion current is increased the energy distribution broadens by 10 eV. This can be caused by a potential drop at each hole centre of the grid mesh where ions with lower energy can go through. Values are listed in table 6.1 along with the Gaussian fit parameters. Note that the energy distribution measured in our study is of the same order than what is measured by Mühlich et al. [101] with a RPA placed 95 cm away from a laboratory unit firing with 27 needles.

Table 6.1: Most probable energy (E_{max}) and energy dispersion (ΔE) measured with a RPA 25 cm away from LU-C. Values are given for several operating points with the deviation of E_{max} from eV_{em}.

I_{em} mA	V_{em} kV	V_{ex} kV	E_{max} keV	**deviation from** eV_{em} %	ΔE eV
1	2	-8.6	2.038	1.88	117
1	3	-7.3	3.007	0.23	115
1	4	-6	3.969	-0.79	125
1	5	-4.7	4.969	-0.62	133
2	5	-7.1	4.994	-0.11	139
3	5	-8.8	5.010	0.19	143

6.2.2 Low power Hall thruster

A regular four-grids RPA as described in section 3.2.3 with a molybdenum flat disk collector is used to measure the ion energy distribution inside the plume of HT2. Figure 6.6 shows the normalized intensity as a function of the ion energy at 0° (blue), 20° (red), 40° (green), 60° (black) and 80° (magenta). To reduce the noise a Savitzky-Golay filter with a window size of 31 and polynomial order of 2 is used. H2 fires at 250 V and 0.66 A with an anode mass flow rate of 0.985 mg/s of xenon. The angular distribution of ion energy is characteristic of the plume of a HT. On the thruster axis, only the most energetic ions are observed. As the probe moves away from the thruster centre axis, the probe starts to detect ions with lower energies. Up to 40° energetic ions are still present. Beyond, only low energy ions are present in the beam. At 60° the maximum ion energy is near 100 V while it is 217 V at 0°. At 80° ions only carry at most 17% of the maximum energy measured on the thruster axis. These ions originate from CEX and scattering collisions inside the plume. Note that even at 0° E_{max} is 15% lower than the discharge voltage. This value needs to be adjusted with the CRP (Cathode Reference Potential) value which is -6.3 V in this case. This corresponds to the energy needed by the cathode to accelerate electrons and therefore, has to be removed from the available energy for ion acceleration. Even when including the energy losses induce by the cathode operation, E_{max} still read 12% less than eU_d. In the case of Hall thruster the potential energy is not entirely converted into kinetic energy as ionization, acceleration, electron transport and plasma-wall interactions induce losses. Moreover, the potential drop at the hole center of the grid leads to shift the ion energy towards higher values. One solution is to use two

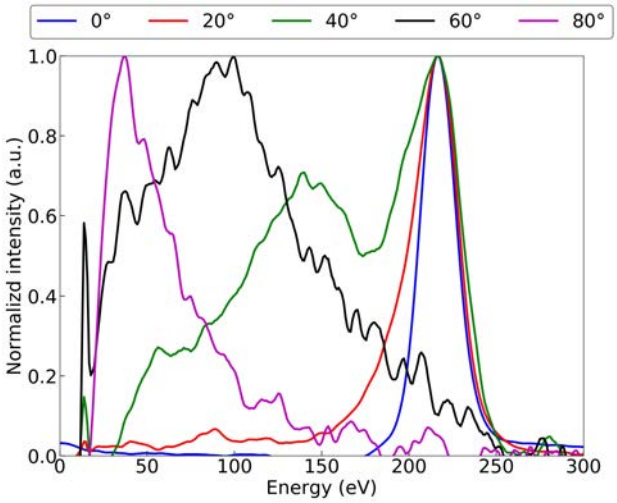

Figure 6.6: Energy distribution acquired 26.5 cm away from HT2 at different angular positions. HT2 fires at 0.66 A 250 V.

grids placed in row and biased to the same voltage. This method is used in section 6.3 when it comes to design a "gridless" RPA where the retarding electrode has a large diameter. Figure 6.7 shows the energy distribution acquired when HT2 fires at 0.66 A and 250 V, 300 V and 350 V. Profiles are acquired at 0° (top-left), 20° (top-right), 40° (bottom-left) and 50° (bottom-right). On the thruster axis E_{max} reads 12%, 10.7% and 10.2% less than U_d from 250 V to 350 V, respectively. For 0° and 20° the most energetic ions are obtained with the highest discharge voltage. At 40° when the thruster fires with 350 V, the ion energy intensity is equally split between 122 V and 320 V. Beyond that point, the highest ion energy is now found with the lowest discharge voltage. This does correlate with ion current angular distributions plotted in section 6.1.2 showing a shift of the current bump towards the plume edge as the discharge voltage increases. With higher discharge voltage, the ionization efficiency of the thruster improves, decreasing the probability of CEX collisions to occur. Moreover, ions with energies lower than E_{max} and larger than E_{atom} are produced by other mechanism: 1) CEX collisions between singly and multiply charged particles. Diffusion of slow ions, produced close to the thruster exit, to large angles due to Xe-XE^+ collisions without charge exchange.

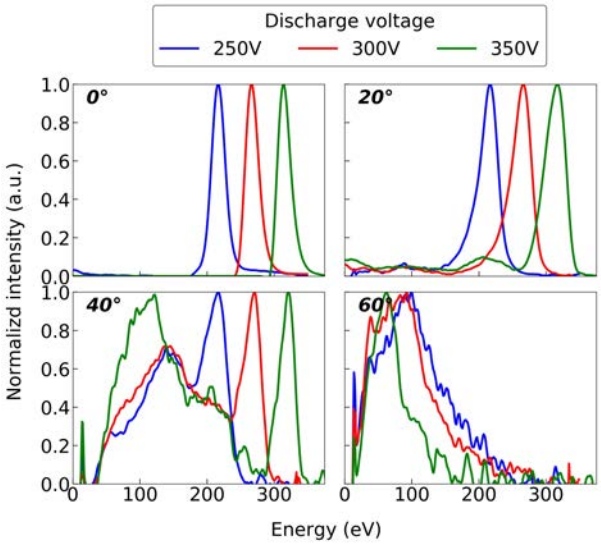

Figure 6.7: Energy distribution acquired 26.5 cm away from HT2 at different angular positions. HT2 fires at 0.66 A 250 V, 300 V and 350 V.

6.3 Ion energy and current density measurement: Dual mode instrument

6.3.1 Concept

The purpose of the dual-mode probe (DMP) development is fourfold: 1) to ease probe implementation into small vacuum chambers 2) to decrease probe design complexity 3) to measure ion current density and energy for similar plasma conditions and 4) to enable better plume characterization for electric propulsion system mass production. The following list describes design and technical requirements:

- To minimize plasma perturbations and overall dimensions.
- To make the probe design as simple as possible.
- To enable measurement accuracy better than 10%.
- Electrodes shall be spaced so no shorting can happen when used to measure keV-range ion energies.
- To minimize IIE perturbations.

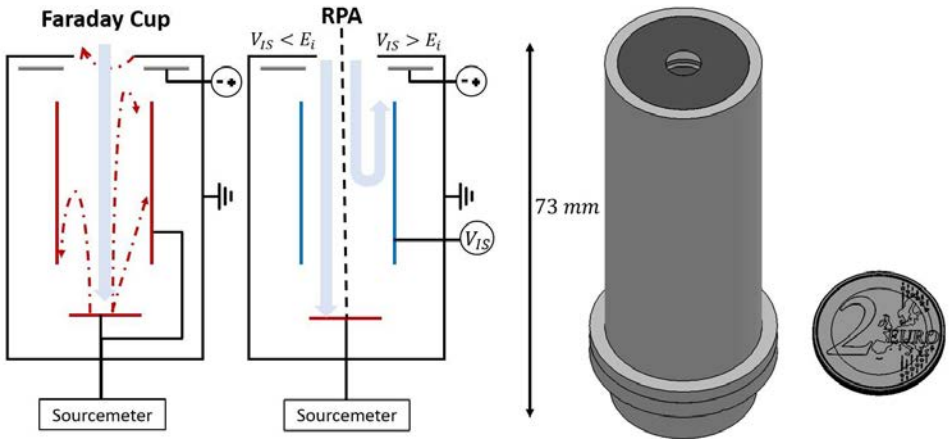

Figure 6.8: Left: Schematic showing the concept of a dual-mode probe when being operated as a ion current acquisition system or ion energy analyser. Right: Size estimation of a dual-mode probe.

- The potential drop at the centre of the retarding electrode shall be as small as possible to well filter ion energies.

Figure 6.8 shows the design chosen for the DMP based on our requirements. The probe is composed of three electrodes electrically uncoupled from each others. The first one, called RE, is used to screen any charged particles susceptible to deteriorate the ion signal going through the cup. The second is either used as ion collector or ion screener depending if the DMP is operated as a Faraday cup or grid-less RPA. Finally, at the rear of the probe a disk is used as ion collector. Due to the absence of a IIE recollection electrode the material used must present low IIE emission (e.g. tungsten). Left, the DMP is set to be operated as a FC. There the middle electrode is electrically connected from the air side to the disk. Right, the DMP operates as an energy analyser. The middle electrode is used as ion screener (IS), it acts as retarding electrode for ions. In the next sections different aspect of the DMP design are investigated.

6.3.2 Results and limits: kV-range energy analyser configuration

Ion-induced electrons mitigation

In the case of a FEEP thruster only three electrodes are used: the electron screener (RE), the retarding electrode (IS) and the collector (C). The first aspect to analyse is the IIE effect on the outcomes when the DMP is used as a RPA. Figure 6.9 show the ion current densities against the retarding electrode voltage acquired for several thruster operating points. Electrodes are spaced by 10 mm PEEK insulators. RE and IS are 9 mm wide, 10 mm and 30 mm long, respectively. The two plots display the DMP design baseline (top) and the DMP upgraded with a fourth electrode (bottom) placed between IS and C, called SE and biased to -60 V. In the top plot, ion current densities are adjusted with γ_{EE} for tungsten found in section 4.1. Both design display the same range of measured ion current. We note that the signal acquired before the ion acceleration voltage slowly increases with V_{IS}. The same behaviour was noticed by Bohm and Perrin and Nina et al. during their experiments [73, 77]. We attribute this current rise to ion induced electrons and secondary electron due to neutrals. Due to the available space inside the DMP and the probe orifice dimension we assume that more neutrals will form inside the probe during measurements. Moreover, as long as all ions are not entirely repelled by IS some induced electrons will not be collected back as $E_i \gg V_{SE}$ leading to a current increase. The main difference between these plots occurs when the retarding potential is larger than the maximum ion energy. With our baseline design, we note a positive ion current off-set while all ions are supposed screened. This is due to IIE from remaining neutrals inside the probe [73]. This issue is solved with the upgraded design as can be seen at the bottom. There, when IIE are recollected as $V_{SE} < V_C$, no more ion current is seen on the collector once all ions are filtered. This is clearly seen in figure 6.10 displaying IIE (green) emission simulation with the software SIMION inside the DMP when V_{SE} is larger or smaller than V_C. RE is set to -40 V, IS is set to +7 kV and C is -10 V. To the left, SE is grounded while to the right SE is set to -60 V. The field lines induced by IS voltage are plotted in colour according to the legend. First, even when SE is grounded it shields the collector from field lines induced by IS. When V_{SE} is lower than V_C, all IIE are properly recollected, hence no artificial ion current is measured by C. The main advantage of using a fourth electrode is to have a clean signal once all IIE are recollected. This part is not of interest to retrieve the most probable ion energy as the current drop, linked to the retarding electrode potential, has already occurred.

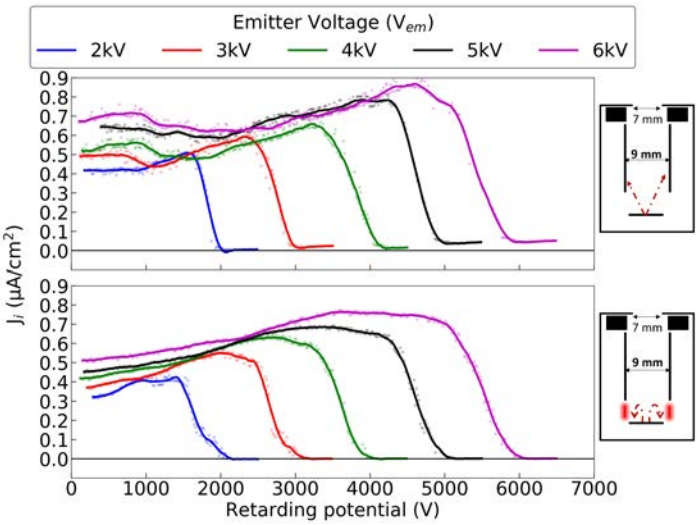

Figure 6.9: Ion current density against potential plots measured with the DMP in ion energy analyser mode. LU-C fires at 1 mA from 2 kV to 6 kV. Top: the effect of IIE is not mitigated. Bottom: IIE are actively recollected by the collector with V_{SE}=-60 V.

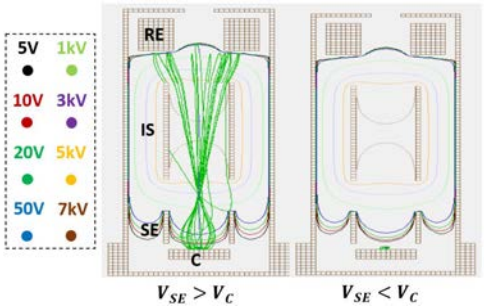

Figure 6.10: Collector ion-induced electron (green) trajectories computed with the software SIMION. Coloured lines represent field lines induced by the IS biased to 7 kV. Left: the voltage of SE higher than C. Right: the voltage of SE is lower than C.

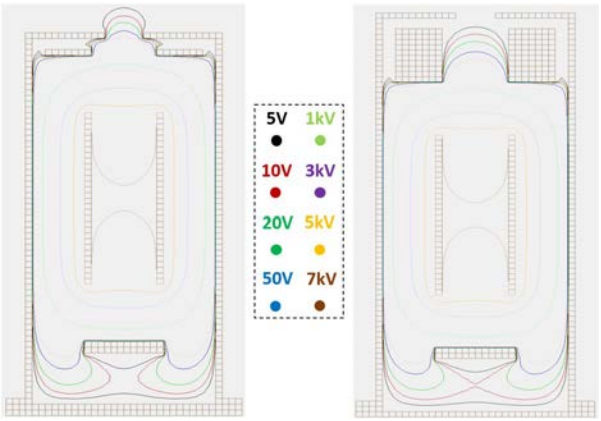

Figure 6.11: Field lines distribution inside the probe computed with the software SIMION when RE is 1 mm (left) or 10 mm (right). IS is 9 mm wide and set to 7 kV.

However, this can lead to errors if a group of ions with energies larger than the main peak is present. Nevertheless, implementing SE imply that we shall increase the overall dimension of the probe, add more connection which can lead to shorts between electrodes. In general it is better to have an additional electrode but if the design is limited (e.g. dimensions, cost) we can remove it and use γ_{EE} instead.

Dimensioning of RE

Figure 6.11 shows the simulation of positive filed lines distribution induced by the high voltage applied to IS. To the right RE is 10 mm thick and to the left RE is 1 mm. $V_{em} \times 1.001$ is IS voltage is set to repel ions with energy eV_{em} and V_{em} is set to 7 kV. In both configurations RE is left grounded. IS is 9 mm wide and 30 mm long. All electrodes are spaced by 10 mm insulators. Based on the simulations the 10 mm thick RE seems to better confine the field lines inside the cup. Note that field lines inferior to 50 V reach the probe exit in the case of the 1 mm thick RE. Considering the energies at stake in terms of primary ion (kV-range) perturbations induced by this voltage disturbance can be negligible. Figure 6.12 plots the current intensity against the ion energy when LU-C fires at 1 mA from 2 kV to 5 kV. The curves are obtain with a Savitzky-Golay filter with a window size of 31 and polynomial order of 2. We see that with a thicker RE the profiles get asymmetric and distorted as the energy increases. Profiles are more stable with a thin RE but they broaden and the intensity decreases as well when

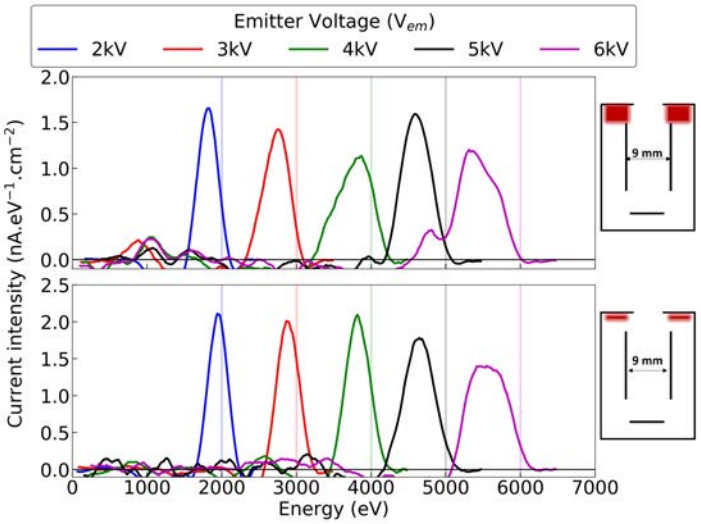

Figure 6.12: Impact of the thickness of RE when measuring the ion energy 25 cm away from the thruster exit plane. LU-C fires at 1 mA from 2 kV to 6 kV.

the energy increases. In both cases E_{max} is always shifted to lower energy. This is worsen as the ion energy increases. Therefore, a thinner RE is preferable while the dimensioning of IS must be improved.

Dimensioning of the retarding electrode

The retarding electrode IS is limited in length and width. In our baseline design we decided to have IS 30 mm long. This parameter won't be changed in our study. This value was chosen as a trade-off to minimize the overall probe length. The optimal width corresponds to the size where the potential drop in the centre of IS is minimized. In our case a 9 mm wide retarding electrode is sufficient to have $V_{IS_{applied}} \approx V_{IS_{centre}}$ as showed by figure 6.13. There, the field line distribution inside the probe when IS equals V_{em} is displayed to the left for a 9 mm and 13 mm wide IS. We see that the potential drop in the centre prevents to properly push back ions with $E_i = eV_{em}$. Nevertheless, to the right of the figure we can see that applying a potential either 0.1% or 0.5% higher than V_{em} works to screen all ions. For instance, in figure 6.13 V_{em} is set to 7 kV. The applied voltage to the 9 mm IS is 7.007 kV and the 13 mm one is 7.035 kV. This potential shift will not be visible in our experiment as our uncertainties range within $\pm 4.5\%$. Experimental results are given in figure 6.14. There, the current intensity is given as a function

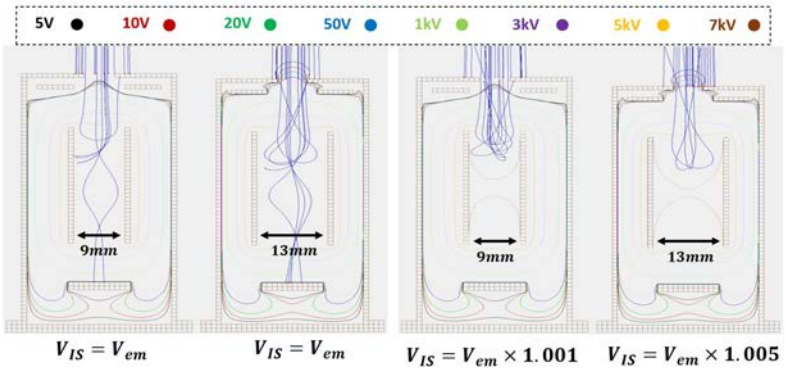

Figure 6.13: Ion trajectory simulation with the software SIMION. IS is either 9 mm or 13 mm wide. To the left $V_{IS} = V_{em}$ while to the right V_{IS} is set so ions are screened.

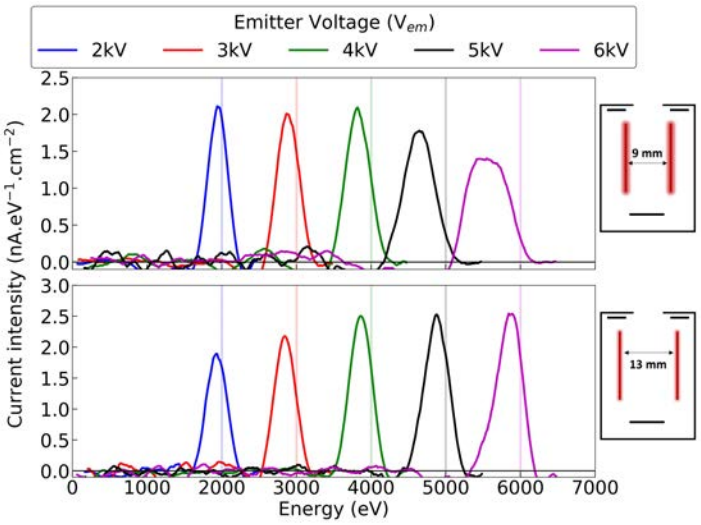

Figure 6.14: Impact of the width of IS when measuring the ion energy 25 cm away from the thruster exit plane. LU-C fires at 1 mA from 2 kV to 6 kV.

of the energy measured. LU-C fires at 1 mA from 2 kV to 6 kV. Both DMP are equipped with a thin RE spaced by 10 mm from IS. The latter is 30 mm long and either 9 mm wide (top) or 13 mm (bottom). The collector is made of tungsten and is located 10 mm downstream IS. First, we note that in both cases the curves are smooth. However, the 13 mm wide DMP displays better results in terms of current intensity and profile shape. Indeed, the current intensity does increase with the emitter voltage applied as it was seen in section 6.2.1. Moreover, contrary to the 9 mm wide IS, the shape of the profiles acquired with the 13 mm are almost Gaussian for any thruster operating points. Still, an energy shift is noticed in both cases between measured E_{max} and eV_{em}. This phenomenon is induced by the probe (i.e. IS) length and was already observed in previous studied [76, 101]. The ions going through he probe cannot be decelerated by a finite retarding potential over a long distance. In our case, IS is long enough to allow the creation of virtual electrodes by charged particles induced by particle collisions. In fact, due to the length of the retarding electrode ions are pushed back at different locations with random directions which enhance this phenomenon. Ions with enough energy to pass the retarding electrode potential barrier would instead be defected by an axial field created by these virtual electrodes. Hence, the energy distribution is shifted towards lower energy. The observed energy shift worsen for the 9 mm configuration when the ion energy increase. It goes from -3% up to -8%. In the case of the 13 mm one, the shift is in average constant around -3.5%$\pm$1% for all operation points.

Influence of probe settings

The influence of the voltage setting on RE and C are display in figure 6.15. The top plot shows current densities and intensities when RE is left floating and different voltages are applied to C. To the bottom, C is kept to -10 V while RE voltage settings are modified. LU-C fires at 1 mA and 5 kV. The DMP is equipped with 9 mm wide retarding electrode, hence the energy shift noticed. We note that the voltage settings barely impact the DMP outcomes. However, intensities measured are lower when C is positive, therefore a negative voltage should be applied. RE voltage settings has no importance when studying an ion beam. Therefore, it can be either negative or floating. With the latter configuration, RE could be placed closer to IS, as chances of shorting are decreased, which reduces the overall length of the DMP.

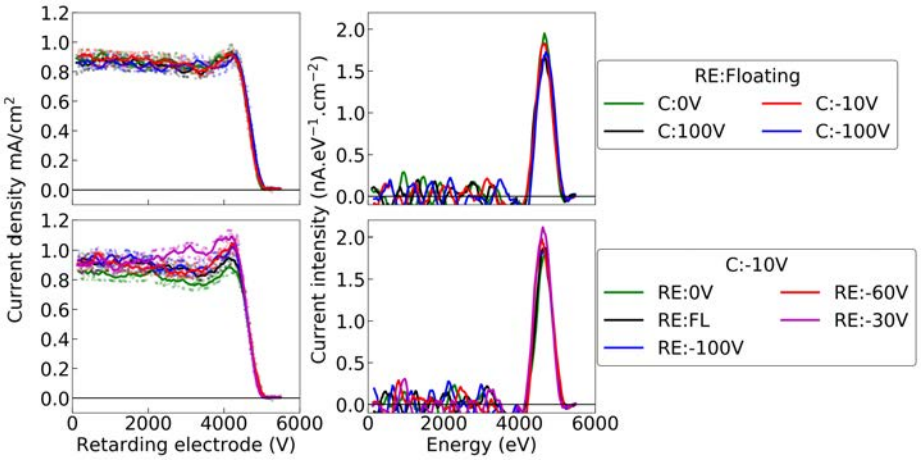

Figure 6.15: Influence of the voltage settings on RE and C when measuring the ion energy 25 cm away from the thruster exit plane. LU-C fires at 1 mA and 5 kV.

Primary electrons impact

Finally, we tried to operate the DMP when the ion beam is neutralized by an electron source. Due to confidential purpose it is not possible to provide details on the electron source. Nonetheless, we can say that they are thermo-emitted before being accelerated towards the ion beam. The DMP was equipped with one 1 mm thick RE, one 30 mm long and 13 mm wide IS and one 12 mm diameter tungsten disk as C. The probe is located 30° off the thruster axis. LU-C is operated at 1 mA and 5 kV. First step was to find the right voltage to apply on RE to make sure that all primary electrons are screened. Figure 6.16 shows I-V curves acquired in ion current measurement mode with the collector (C+IS) when RE voltage is set to -100 V (red), -300 V (black) and -400 V (blue) and the electron source (NTR) is ON. As a reference one I-V curve measured when NTR is OFF (green) and RE is biased to -100 V is plotted. When NTR is ON and V_{RE} is the highest, the collector measures an electron current, whatever the voltage applied. When V_{RE} = -300 V and V_C < -80 V an ion current is measured. However, this current is heavily disturbed by electrons hence the slope is large. For V_{RE} = -400 V, the I-V curve measured is now identical to the one with NTR OFF. Electrons produced by the NTR have an energy E_e larger than 100 eV. Therefore, V_{RE} must be, in absolute value larger than E_e. We note that once electrons are screened no ion losses are observed. In this case, V_{RE} accounts for 8% of the measured ion energy, which is negligible to induce perturbations on ions.

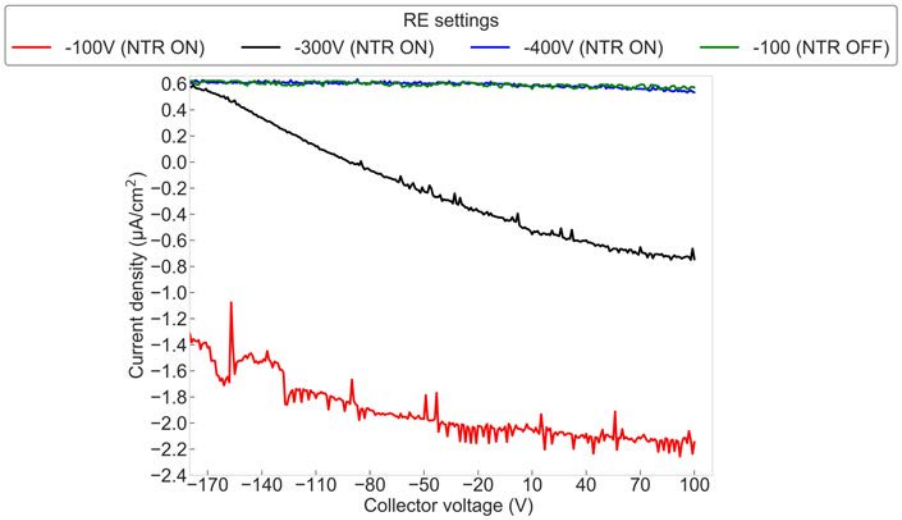

Figure 6.16: Influence of primary electrons on the DMP outcomes when operated to measure an ion current. The probe is placed at 30° and 25 cm away from the thruster exit plane. In red, black, blue the DMP is used with RE set to -100 V, -300 V and -400 V, respectively with the NTR ON. In green RE is set to -100 V and the NTR is turned off. LU-C fires at 1 mA and 5 kV

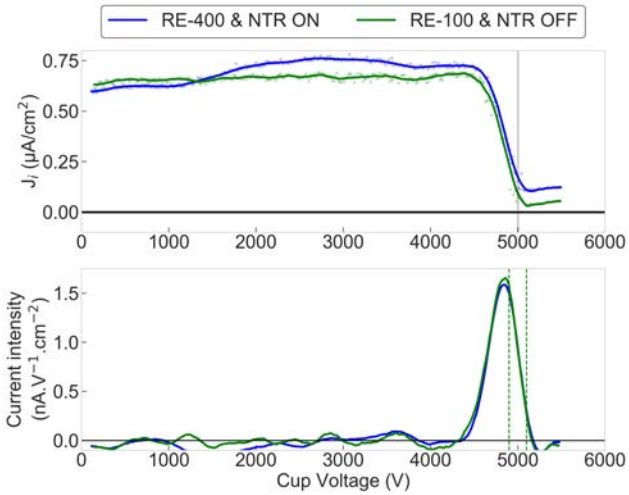

Figure 6.17: Influence primary electrons on the DMP outcomes when used as an energy analyzer. The probe is placed at 30° and 25 cm away from the thruster exit plane. In blue the DMP is used with RE set to -400 V and the NTR firing (blue). In green RE is set to -100 V and the NTR is turned off. LU-C fires at 1 mA and 5 kV

In a second step, the DMP is set in ion analyser mode with V_{RE} = -400 V. Measurement outcomes are displayed in figure 6.17. At the top the current density measured when LU-C is operated with and without NTR is shown. At the bottom is plotted the current density against the energy measured with and without NTR. We observe that the current density is less stable when the NTR is ON even though electrons are screened. As both probes do not recollect IIE they show a current off-set when $V_{IS} > V_{em}$. However, the current intensity and energy distribution are close whether or not electrons are flown along side ions in the thruster plume. E_{max} measured when NTR is ON is 3.2% lower than eV_{em} while without NTR it is 2.74%. This variation is included in our experiment uncertainties and therefore can be considered negligible.

Confirmed operation

After several design iterations it was possible to find an architecture to measure the ion energy from a FEEP thruster:

- A tungsten ion collector disk,

Table 6.2: Most probable energy (E_{max}) and energy dispersion (ΔE) measured with the DMP and a RPA 25 cm away from LU-C. Values are given for several operating points with the deviation of E_{max} from eV_{em}.

I_{em} mA	V_{em} kV	V_{ex} kV	E_{max} keV	**deviation from** eV_{em} %	ΔE eV
RPA					
1	2	-8.6	2.038	1.88	117
1	3	-7.3	3.007	0.23	115
1	4	-6	3.969	-0.79	125
1	5	-4.7	4.969	-0.62	133
DMP					
1	2	-8.6	1.938	-3.1	131
1	3	-7.3	2.843	-5.2	133
1	4	-6	3.862	-3.44	141
1	5	-4.7	4.877	-2.45	157
1	6	-7.1	5.842	-2.63	163

- A 30 mm long and 13 mm wide retarding electrode,
- A thin, floating, electrode placed between the entrance and the retarding electrode,
- A distance C-IS of 10 mm and IS-RE of 2 mm.

Table 6.2 shows the Gaussian fit parameters obtain with the aforementioned DMP compared to those from a regular RPA design as detailed in section 6.2.1. We observe that the measured ion energy is in average 3.5% lower with the DMP than the RPA. Moreover, ΔE is 14 eV to 24 eV larger with the DMP. These variations are small compared to the studied energy range studied.

Consequently, we can use the DMP as an ion analyser knowing that the probe provide the ion energy with -3.5% off-set. Figure 6.18 display the current intensity and the ion energy distribution from 0° to -90° by 5° step acquired with our DMP. LU-C fires at 4 mA and 6 kV. Unlike Hall thrusters, measurements show that ion energy does not depend upon the angle for a FEEP. This aligns with measurements published by Mühlich et al. [77] with a 4-grid RPA placed 95 cm away from a FEEP thruster. In our case, the intensity is the highest up to -15°, then decreases from -20° to -30° before going further down from -35 to -70°. At angles larger than -70° the DMP was not able to measure any signal.

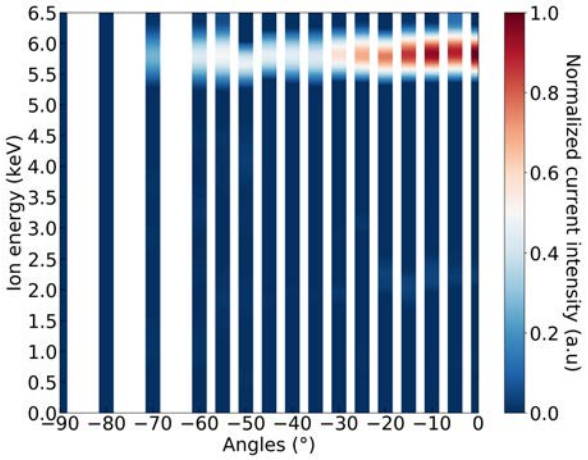

Figure 6.18: Energy angular distribution and the corresponding current intensity of LU-C firing at 4 mA and 6 kV. The DMP is configured as an ion energy analyser and placed 25 cm away from the thruster exit plane. RE is left floating.

6.3.3 Results and limits: ion current measurement

Now that the design of the DMP is operational when configured as an ion energy analyser, we shall try out whether it can accurately capture the ion beam profile and retrieve the ion current. Figure 6.19 displays ion current density angular distribution acquired with the DMP (green) and the optimized Faraday cup (section 6.1.1) when LU-C fires at 2 mA and 5 kV. The beam profile acquired with the DMP is adjusted with γ_{LEE} measured in section 4.2.2. Both measured profiles look similar. The variations can be attributed to experimental bias as they were not acquired simultaneously (different days, slight extractor voltage differences). When computing $I_{i_{int}}$ DMP reads 3.8% lower ion current than the real emitter current input. In this case the optimized FC reads 4.2% less. This experimental study proves the feasibility of a dual-mode probe to be used to measure the ion current and energy within the beam of a FEEP thruster for similar plasma conditions and acquired 25 cm away from its exit plan.

6.3.4 Dual-mode configurations applied to Hall thrusters

Low energy analyser configuration

In the case of a Hall thruster, the DMP was designed as follow:

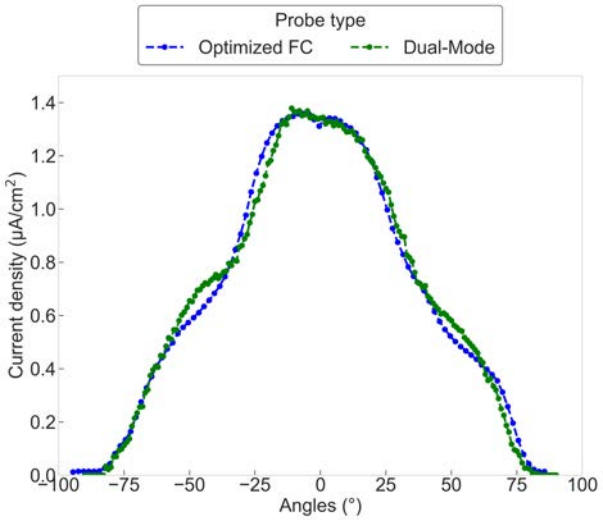

Figure 6.19: Ion current densities acquired with an optimized FC (blue) and the DMP configured in ion current acquisition mode. The FC is parametrised as follow: V_{col}=-30 V and V_{rep}=-60 V. The DMP collector is set to -80 V and the RE is left floating. Therefore, γ_{LEE} for a 50 mm long cup (see section 4.2.2) is applied. LU-C fires at 2 mA and 5 kV.

- C is 12 mm in diameter and made of molybdenum
- IS is directly placed after C since energies meant to be measured are low enough to prevent shorts between electrodes. It is 30 mm long and 13 mm wide.
- RE is 10 mm long and 13 mm wide. It is spaced by a 10 mm PEEK insulator from IS.

Due to the important fraction of electrons in the plume of a Hall thruster (20% to 30%) and the small Debye length we have to use a grid with small mesh dimension to prevent field lines induced by voltage applied to electrodes to perturb the plasma. Here the mesh holes are 0.5 mm in diameter which gives a collection area of 15.21 mm^2. HT2 fires at 0.66 A with a discharge voltage of 250 V. The collector is biased to -10 V, RE to -60 V and a positive voltage sweep from 0 V to 350 V is applied to IS. I-V traces (top) as well as energy distributions (bottom) obtain for different angular positions are given in figure 6.20. To ease visualization all traces are normalized. We note that I-V traces are perturbed. When all ions are repelled a positive ion current is still measured. In the same way than with the FEEP this is due to remaining neutrals provoking electron emission from the molybdenum collector. This effect is strong due to the actual pressure during our measurements (10^{-5}mbar) but also to the gaseous propellant used to operate the thruster (i.e. xenon). Nevertheless, when looking at the energy distribution on the bottom plot we still identify energy peak seen with the a real RPA in section 6.2.2. On the thruster axis E_{max} reads 227 eV, 9% less than the discharge voltage. We note the presence of very low energy ($\sim$50 eV) ions on the thruster axis which was not measured with a RPA. Same behaviour is seen at 20°and 40° where the main energy peak is at the maximum energy while lower ion energies are identified. At 60° the energy distribution is a lot broader. It covers a bit more than 100 eV with a maximum around 150 eV. Compared to results obtained in section 6.2.2, there are more energetic ions identified at this location. At 80° E_{max} is measured around 30 eV, similarly than what was obtained with a regular RPA. Overall, the energy peak are similar between the DMP and a regular RPA outcomes. However, the DMP outcomes show as well lower energy peak for all angular positions. Based on measurements done with classical RPA (see 6.2.2) this large energy distribution is considered artificial as it is induced the probe itself. These energy shifts induced by collisions inside the probe would explain the large fraction of ion current measured on the front and side of the cup as observed in section 5.3.3. The electrostatic length effects induced by the potential applied

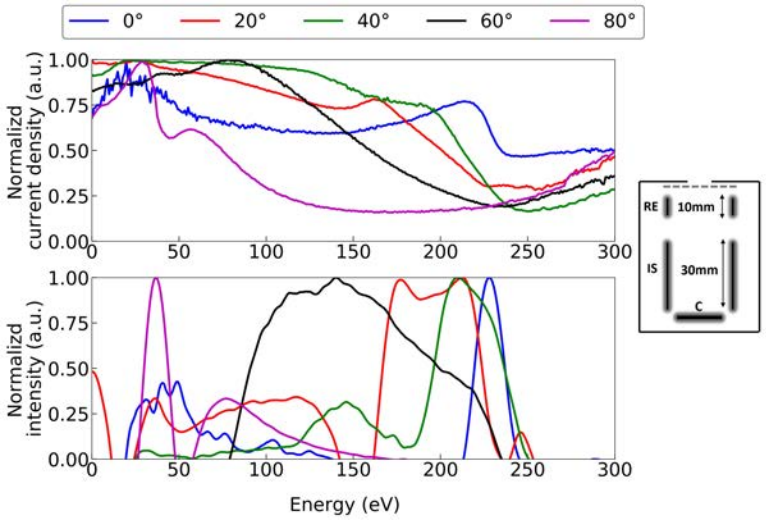

Figure 6.20: Ion current density and normalized energy distribution acquired with the DMP configured as an energy analyser. RE is 10 mm, IS is 30 mm and C is made of molybdenum. HT2 fires at 0.66 A and 250 V. The probe scan the ion energy at different angular positions from 0° to 80°.

to electrodes (see section 5.1) as well as the presence of neutrals inside the probe due to its large dimension would enhance ion-ion and CEX collisions. Hence, the energy transition and broadening observed would be purely induced by the probe itself. Consequently we can suggest that a DMP is not properly working as we do not meet technical requirements set in section 6.3.1.

Current density measurement configuration

Even though our DMP concept is not properly working to measure the ion energy inside the plume of a low power Hall thruster, we investigated its capability to measure the ion current. Profile acquired with the same probe design and thruster operation described in the previous section is displayed in figure 6.21. Traces are displayed in linear (top) and logarithmic (bottom) scales. We note that on the thruster axis a large current drop occurs and was also noticed in section 5.3.3 when highlighting the current distribution inside our Faraday cup. This effect can also be worsen by the presence of a grid at the probe entrance. The ion current retrieved from the profile give a thruster current utilization of 30%, a value 1.5 times less than actual thruster performances. We can conclude that our DMP is

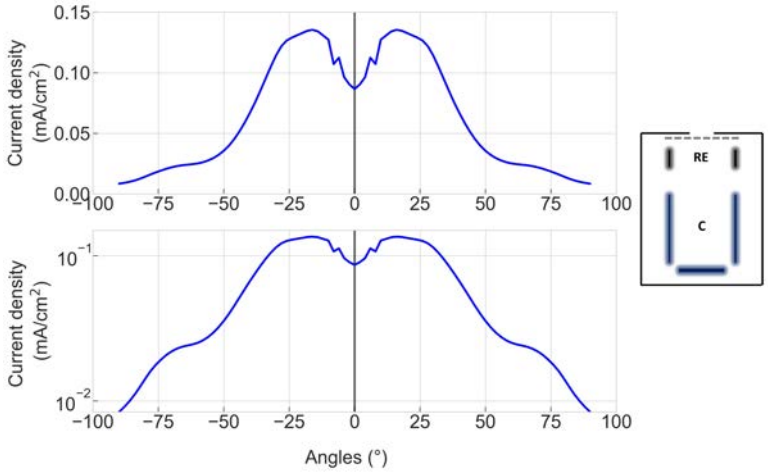

Figure 6.21: Ion current densities angular distributions acquired with the DMP configured as a Faraday cup. RE is 10 mm, the cup is 30 mm long and biased to -60 V. HT2 fires at 0;66 A and 250 V.

not properly working to meet technical requirements set in section 6.3.1.

Indeed, as it was showed in section 5 and 6.2.2 ions behaviours in the plume of a Hall thruster cannot be assimilate to a simple beam. Section 5 clearly showed that the probe outcomes is heavily impacted if perturbations are not properly mitigated, hence the DMP is not providing reliable data in the case of a Hall thruster.

6.3.5 Summary: Design directions

DMP applied to the ENPULSION NANO laboratory unit

It was shown in section 6.3.2 and 6.3.3 that the concept of a DMP works in the case of the ENPULSION NANO thruster. We, therefore, propose the following guidelines to meet technical requirements mentioned in section 6.3.1:

- The collector disk shall be made of a material with a low ion-induced electron yield such as tungsten, molybdenum, stainless steel as showed in section 4.1.2.
- The ion retarding electrode should not be too long neither too short. On one hand, if the electrode is too long, ions reaching the collector might experience an energy shift due to positive particle accumulation giving birth to virtual electrode. On the other hand, an electrode not long enough will

decrease the accuracy of the DMP. Indeed, a potential drop will appear at the centre of the cylindrical electrode potential barrier. As a consequence ions with energy equal or slightly lower than the eV_{IS} will still manage to go through. We experimental found that a 30 mm long ion screener is enough to measure the ion energy as specified by our requirements. Due to the order of magnitude of the ion energies we must prevent any possible sparks or shorts between electrodes during the DMP operation. We, therefore, recommend to leave at least 10 mm between the IS electrode and the collector. When the probe is operated in the current measurement mode IS is electrically connected to the collector from outside the vacuum chamber to form one cup-like electrode

- RE must be thin enough (1 to 3 mm) to not disturb measurements. Also, its inner diameter shall be larger than the probe aperture to 1) repeal electrons coming from outside the probe (primary electrons, thermal electrons) and 2) to push away ion-induced electrons originating from the probe front entrance. This way the electrode is barely exposed to direct ion bombardment, hence minimising its own ion-induced electrons emission. RE can be left floating when operating the DMP in energy analyser mode. Therefore, it can be placed very close to the IS electrode which minimises the overall length of the probe. In ion current measurement mode RE voltage shall be set lower than the collector.

- If we define the probe entrance to be 7 mm wide then one should set the inner diameter of RE to 9 mm and 13 mm for IS.

DMP applied to the ISCT200

We saw in section 6.3.4 that the tested design of our DMP is not properly working when studying the plume of a Hall thruster. Nevertheless, when we compare our results at 0°, on the thruster axis with results published by Hey et al. [124] when they developed a "gridless" RPA to study the plume of a HEMPT thruster, we observe some similarities. This lead to think that our design can be improved. First, we would discard an important perturbation factor by removing the grid at the probe entrance. Therefore, we shall reduce the probe entrance so the flux of primary electrons from the thruster cathode going through the probe is not too high. We would try to test the probe with an aperture of 3 mm diameter. We showed in section 5.4.3 that if the ion collector is far enough from the probe entrance when trying to measure the ion current the inlet diameter has less significant impact on

the acquired signal. Secondly, RE should be as thin as possible with an inner diameter close, but larger, than the probe entrance. The maximum thickness of RE will be driven by the shape of the potential barrier when applying a given voltage. We shall avoid to have a potential drop at electrode centre as mentioned in previous sections. To prevent to use thick electrode one could use two 1 mm thick RE placed right after the probe entrance. Both would be spaced 1 mm from each other and be biased to the same potential to facilitate the potential homogeneity at their centre. Then, the ion screener would be placed 4 mm from RE, as explained in sections 2.2.2 and 3.2.3. We know from section 5.3.3 that most of the ions entering the measurement device are collected at the front of the probe. Moreover, the ion energy to be measured with the electric thruster technology are low (1 to 400 eV). Therefore, we propose to use the IS electrode and collector disk as one cup electrode like in regular Faraday cup design, hence it would collect and screen ions simultaneously. This way the probe should be more efficient to screen ions at the probe entrance and with low energy (better field lines distribution due to the cup shape). Such probe design should also enable better ion current collection efficiency when operated in current collection mode. Indeed, the absence of grid at the probe front will ease ion collection. To meet decent accuracy the overall collector cup (IS + collector disk) shall be larger than 10 mm as explained in section 5.3.1. Figure 30 presents a drawing of the DMP architecture to make it work to measure the ion energy and current density at any angular position from the plume of a Hall thruster.

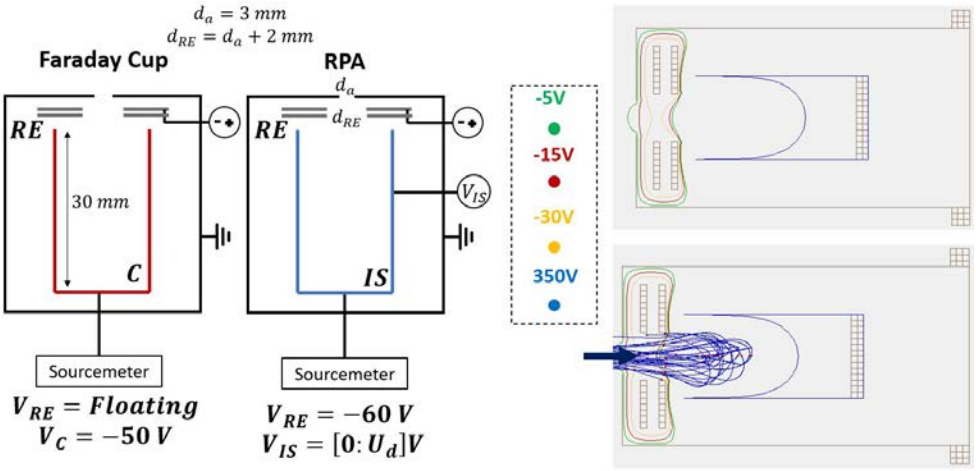

Figure 6.22: Schematic of the DMP alternative design to be tested to have a working concept with Hall thrusters. To the left, the probe is operated in ion current measurement mode (i.e. like a Faraday cup) and to the right the probe is configured as an energy analyser (i.e. like a RPA).

Conclusion

Summary

This dissertation focuses on the optimization and the design standardization of electrostatic probes to measure ion current and energy within the plume of different low-power electric thruster technologies: a Field-emission electric propulsion thruster, a Hall thruster and a Radio frequency ion thruster. The work relies on experimental methods to iterate several architectures of Faraday cup to converge towards a common design to be used for these three thruster categories.

A large fraction of the work was dedicated to the development of a Faraday cup to accurately measure the ion current of a FEEP thruster. The advantage of these electric propulsion devices is that they can be operated with controlled and stabilized emission parameters (e.g. current and voltage). Hence, these reference values can be used for comparison with the ion current or energy measured with a Faraday Cup ($I_{i_{int}}$) or a RPA (E_i). We showed that the firing needles distribution from a crown can lead to a decrease in the FC accuracy. This is mainly due to the mathematical method used to integrate the current density profiles to retrieve the ion current. There, we make the assumption that the ion beam has a symmetry around the thruster axis. This becomes false when the ion beam largely deviates from the thruster firing axis as ion signal measured by the probe is off-set from the beam centre. In one case study (see section 3) we showed that a crown firing with only 32% (i.e. LU-A) of its capacity without homogeneous distribution can lead to an error of -20% upon $I_{i_{int}}$. Errors are maximized when the extractor voltage magnitude is further increased because it leads to increased beam deviation from the thruster centre axis. Nonetheless, our integration method works for firing crowns with 60% or more of its capacity and with homogeneous needle distribution (i.e. LU-B, LU-C and LU-D). It was also shown that the distance between the thruster and the probe impact the determination of the ion beam divergence angle. Indeed, we could measure the beam spreading (θ_{div}) of two laboratory units with

more than 85% of needles firing (LU-C and LU-D) from 25 cm and 84 cm. We observed that from close distances to the crown θ_{div} is in average 16% larger no matter the thruster operation settings. It is believed that it is caused by the extractor geometry and the probe location within its sphere of influence. Nevertheless, the value of $I_{i_{int}}$ is not influenced by the probe distance from the thruster. Indeed, with the right architecture we are able to retrieve the real ion current which leaves the thruster.

Several parameters involved in the design of a FC were assessed in this dissertation. We observed that the most important source of errors, in the case of a FEEP and RIT thruster, is the ion-induced electron (IIE) emission effects from energetic (kV-range) indium ions. Ways to mitigate this effect on the FC outcomes are twofold: 1) passive and 2) active. Method 1) is qualified as passive because there is no modification of the electric field lines inside the probe to suppress the current increase induced by IIE. One solution is to increase the length of the ion collector cup. This way only a small fraction of IIE manage to leave the cup as they mostly originate from its bottom with divergence angles between 33° and 43° when d_a equals 7 mm. In fact with a 50 mm long cup the ion current measured by the cup can be 3% to 6% higher, depending on the energy of incoming ions. This value can be of 30% for 30 mm long cups and goes from 125% to 180% for cups of 10 mm. A second solution to passively suppress the ion current rise caused by IIE is to choose a material with a low IIE yield ion bombardment. We saw that stainless-steel, molybdenum and tungsten have small yields compared to aluminium. In the case of the FEEP thruster they go from values lower than 0.05 for $E_i = 3$ keV up to 0.25 for 8 keV energetic ions. Moreover, for a given material it was showed that a foam structure with pore size larger or equal to 0.4 mm can reduce γ_{EE} by 60%. The same decrease effect on the yield was observed for the RIT thruster. Note that it is difficult to find foam structures for materials like molybdenum and tungsten essentially due to manufacturing challenges. The shape of the cup rear part can also minimize the IIE effects. We showed that the most efficient way is to have a conical shape with the normal of the cone side directed towards inner parts of the cup. As a conical shape changes the incidence angle where ions hit the surface. This leads to increase the amount of induced electrons being emitted. However, they are less likely to reach the cup top hence they are properly recollected and no artificial additional ion current is observed. Nonetheless, compared to the two previous methods the latter is less efficient and should only be considered as last. The use of method 1) (i.e. active) is of interest in the case of a FEEP and RIT thruster because it permits to shorten the overall length of the probe by decreasing the dimension of the cup. This technique re-

quires the use of a second electrode placed at the probe entrance before the cup. The voltage applied to this electrode, termed repeller, shall be lower than the cup so all IIE are pushed back towards the ion collector, hence no extra ion current is measured. However, this method has to be used carefully because it can induce ion losses. Since V_{rep} is more negative than V_{coll} some ions can be collected by the repeller instead of the collector. This effect is negligible in the case of the study of a single FEEP or RIT thruster. However, it can be critical for the analysis of the plume from thruster clusters where beams can interact leading to beams with a wider energy distribution and velocity vector not collinear to the probe centre axis.

On the contrary, when studying the plume of a low power Hall thruster IIE effect can only increase the ion current by 3% for materials like molybdenum, tungsten or steel and 10% for aluminium. This is mainly due to the fact that the energy of ions present in the plume of a HT is relatively low. Moreover, we saw that using a foam structure has no positive effects on the emission rate of ion-induced electrons. This is mainly due to the random ion velocity vector at stake in the plume of a Hall thruster. However, a foam ion collector can still provide reliable results if a cup shape like is used. More importantly, due to the complex ion behaviour in the plume of HTs and their energy range no active method shall be used to push IIE back to the collector. Indeed, a non-negligible fraction of ion current is lost to the repeller when the later is biased more negatively than the collector, especially on the thruster axis. We highlighted that once inside the probe ions are collected at different locations. In the thruster wings (i.e. [$\pm$50:$\pm$90]), 20% of the ion signal is collected by the probe rear part. Near the thruster centre axis this value drops to 2% at most for a 50 mm long cup. The major fraction of the ions signal is collected by the cup side walls. Despite that the length and the shape of the cup have no influence on the measured ion current, modifying these parameters changes the ion behaviours inside the probe. Indeed, the shorter the cup the more ion signal measured by the cup rear part. This is certainly an effect of the complexity of the plume of a HT. The phenomenon has a lot to do with the annular geometry of the Hall thruster core. Ions present at the thruster centre axis do not have a velocity vector collinear to the axis due to the divergence of the beam. The velocity vector dispersion is large in the case of HTs due to the overlap between the ionization and acceleration zones combined with many scattering and charge-exchange collision events.

The probe entrance has been studied in terms of material and diameter. In the case of a FEEP and RIT thruster, we observed that the material has little impact on the ion current measured even though graphite tends to provide more accurate

results. However, our experiments showed that the distance between the probe entrance and the start of the ion collector cup can lead to a decrease in the ion current signal. Based on our experimental data we found that a minimum distance of 4.5 mm is required between the probe inlet and the cup to suppress this effect. It is preferable to use the front of the probe housing to define the collection area and placed the repeller downstream, shielded from direct exposure to the ion beam. We called this configuration X.X.X.**P**. It has the advantage to prevent particles deposition on insulators which reduces probability to have a short cut between electrodes after several hours of operation. Moreover, it was seen that decreasing the probe inlet diameter leads to decrease the measured ion current. A 7 mm wide entrance is the minimum dimension that we would recommend when the cup diameter is 12 mm. Note that the entrance diameter shall be the smallest.

The exact same behaviour was observed in the case of a Hall thruster. However, errors induced by the material front or inlet dimension are worsen for this thruster. Indeed, the measured ion current can be 10% to 30% lower depending on the front material used and the inlet diameter. However, these effects are mitigated if the configuration X.X.X**P** is used.

Finally, we looked into the development of probe termed dual-mode to enable the measurement of the ion current and energy for similar plasma conditions with reduced plasma-probe interactions. The complex behaviour of ions inside a Faraday cup and the wide energy distribution found with an optimized RPA characteristics of a Hall thruster prevented us to succeed. Indeed, we saw that with the tested design it was not possible to clearly distinguish the values of ion energies. In the region of the thruster wings, it is known that there should be the presence of medium to low energy ions but those are not visible with the DMP. It is believed that this is due to the shape of the IS used in the DMP design to screen ions. When being operated in ion current mode, the shape of the measured beam profiles measured is wrong and the signal intensity is too low. This is the consequence of the use of a grid at the probe entrance and also ion losses to the insulators between each electrodes. Still, it is believed that the DMP could work with a Hall thruster if several design parameters are modified. We would recommend, as pictured in figure 6.22 in section 6.3.5, to change the shape of the ion collector and ion screener electrode to 1) reduce the ion losses to insulators, 2) to make the ion repulsion region as close as possible to the probe entrance and 3) to concentrate the point of repulsion as much as possible on the probe centre axis to mitigate the possibility to have ions flying with a transversal velocity component. In addition, we would discard the grid at the probe entrance and decrease the aperture diameter of the probe instead to reduce the flux of electrons which

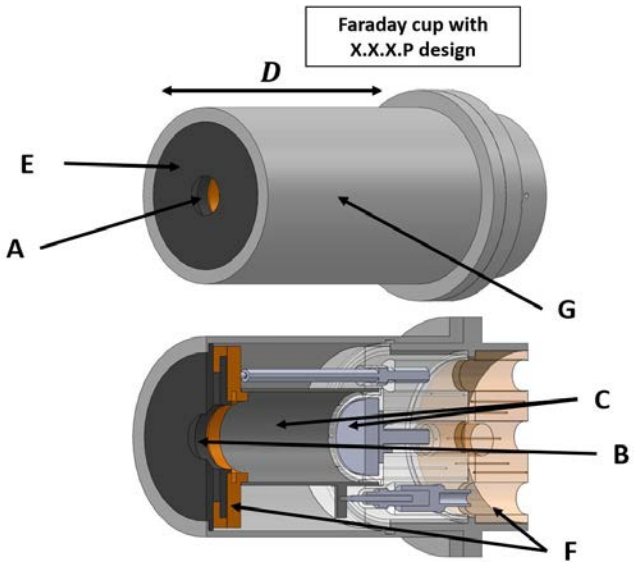

Figure 6.23: Drawing of a Faraday cup design suitable to study the plume of a FEEP, low power RIT and low power Hall thruster. A = Probe aperture, B = Repeller aperture, C = Collector, D = Collector cup length, E = Front material, F = Insulators, G = Housing

goes through the probe. In the case of a FEEP we were able to develop a probe allowing accurate measurements. We used the design of an optimized Faraday cup. The collector is a disk made of tungsten, the retarding electrode is 30 mm$\times$13 mm and the repeller is 1 mm$\times$9 mm. We observed that when the probe is operated as an energy analyser the outcomes is off-set by -3.5% in average and seems to not much increase with the ion energy. Likewise, when configured as a Faraday cup, the probe reads ion current with 3% off-set and accuracy of $\pm$4.5%.

Design guidelines

This experimental work has shown that it is indeed possible to find a probe design that can be used to study the ion beam of a FEEP (Chapter 4), a RIT (Appendix B) and a Hall thruster (Chapter 5). Table 6 provides guidelines to build the most suitable architecture to study the plume of one of these thrusters. We propose two designs one for FEEP and low power RIT thrusters while a different one for low power Hall thrusters. First, for all of them it is recommended to have a **P** design as

introduced in previous chapters. This way particle deposition will be mitigated at the probe front. Also, in the case of a FEEP and RIT thruster the use of a **P** design is necessary to confine the field lines created by the repeller placed at the front to "actively" recollect IIE. Regarding Hall thrusters, this configuration is needed as well to properly shield the ion collector since ions are being captured by the cup front. Secondly, the aperture diameter d_a is set to 7 mm for both designs. We saw that we could decrease the probe aperture with the **P** configuration however we would risk to increase the inaccuracy of the probe pointing to the thruster centre. Therefore, a good trade-off is found to be 7 mm as this parameter will drive the diameter of other parts of the probe, hence its overall width. The front of the probe is recommended to be in graphite for both designs as this material is affordable, has a low sputtering yield, a good resistance to heat and a low IIE yield. The repeller aperture d_{rep} is recommended to be at least 2 mm wider than d_a, hence 9 mm. Here, the repeller shall be left floating when studying the plume of a Hall thruster to not interact with low ion energies at stake. On the contrary, for a FEEP and RIT the voltage applied to the repeller V_{rep} as to follow $V_{rep} < V_{coll} < 0$. Then, the collector diameter d_c must be larger than d_{rep}. The electrode shall also be negatively biased, at least -40 V for Hall thrusters design while -30 V is sufficient for the other. For a FEEP and RIT, the cup can be one single electrode as most of the ion signal reaches the probe rear side. On the opposite, we would recommend to have a segmented cup to study the plume of a Hall thruster to 1) have a better visualization of where ion are collected and 2) to have more freedom in the applied voltage to both electrodes to enhance ion collection to the probe rear side by modifying the field lines distribution inside the probe. The overall length of the collector cup shall be > 10 mm for both design. A small cup length is important to operate the probe in a small chamber and minimize plasma-probe interactions. Therefore, a 30 mm long cup would suits both architecture while being little intrusive. However, we would recommend to use a 50 mm long cup when studying the plume of a FEEP and RIT to add another safety measure to mitigate IIE emission effects on the acquired ion current. If the repeller is damaged or electrically short after a long operation time, the probe would still be able to recollect most of IIE thanks to its length. The collector material should presents a low IIE emission yield. For the three thrusters, materials like Molybdenum or tungsten would fit perfectly. However, for FEEPs and RITs, those materials could be used in a form of a foam of velvet to decrease further IIE emission yield and enhance ion collection. Finally, the probe housing can be aluminium as it is cheap and easy to manufacture. However, to study the plume of a FEEP thruster a stainless steel casing would be better since it has a lower IIE emission yield as experimentally

Table 6.3: Design recommendations for the construction of an optimized Faraday cup in **P** configuration to be used to study the ion beam of a FEEP, a low power RIT and low power Hall thruster.

Parameter	**FEEP&RIT**	**Hall thruster**
Configuration	P	P
A	$d_a = 7$ mm	$d_a = 7$ mm
B	$d_{rep} = 9$ mm, graphite, $V_{rep} < V_{coll} < 0$	$d_{rep} = 9$ mm, graphite, V_{rep} floating
C	1 cup, $d_c > d_{rep}$, low γ_{EE}, foam	Segmented, $d_c > d_{rep}$, low γ_{EE}, low sputtering yield
D	$L_{cup} = 50$ mm	$L_{cup} = 30$ mm
E	Graphite	Graphite
F	PEEK	PEEK
G	Stainless steel	Aluminium

Table 6.4: Design recommendations for the construction of a universal Faraday cup in **P** configuration to be used to study the ion beam of a FEEP, a low power RIT and low power Hall thruster.

Parameter	**Universal**
Configuration	P
A	$d_a = 7$ mm
B	d_{rep} 9 mm, graphite, $V_{rep} < V_{coll} < 0$ (FEEP&RIT) or V_{rep} floating (HT)
C	Segmented, $d_c > d_{rep}$, low γ_{EE}, low sputtering yield
D	$L_{cup} = 50$ mm
E	Graphite
F	PEEK
G	Stainless steel

measured in chapter 4.

It is possible to use the above mentioned guidelines to build a single, universal, probe architecture working with all three thrusters. Indeed, some parameters are identical between the two proposed designs. It is then necessary to pay attention to parameter "**B**", "**C**", "**D**" and "**G**" as showed in table 7. In "**B**", the design does not change whereas the way to operate the probe does. This parameter can be adjusted from outside the vacuum chamber. Regarding parameter "C" a segmented collector would not affect results obtained with a FEEP and RIT if the insulation is properly done (high particle deposition shielding capacity). The overall length of the probe is preferred to be 50 mm. In this case, the probe front shall be properly designed when using the probe for a Hall thruster. Finally, stainless steel should be preferred as material for the probe housing.

Perspectives

First, further studies should be conducted in the case of Hall thrusters to better understand the ion behaviour once inside a Faraday cup. We saw that modifying the probe aperture or length influence the location where ions are collected. A probe with several segments could be used to better localized the region collecting the most ions and monitor how it changes when some design parameters (aperture diameter, probe length) are modified.

In the case of the FEEP, the beam profiles presented in this dissertation can be compared to plume model already available. This way numerical simulations could be improved to better characterize the plume of the ENPULSION NANO and by extend products based on the same technology.

This work provided information upon the feasibility of a universal Faraday cup design to be used to measure the ion current from electrostatic thrusters like FEEP (4) Hall thrusters (5) and RIT (B). It would be of interest to extend the study to other type of electric thrusters with more complex plumes (ECR) or pulsed operations (VAT, PPT) to converge with a design enabling the characterization of as much EP systems as possible. Method to operate the probe will definitely be different than those presented in this dissertation.

The design requirements detailed in the conclusion were elaborated to assess the plume of low power EP systems. Despite the vivid interest of the industry into small and nano satellites, the market shares of medium size and mass class satellites remain important. Hence, our design requirements should be extended to EP systems which can be operated at higher input power (> 500 W). At this power range materials composing the probe shall be much more sputter resistant and have a better heat dissipation capacity. For instance, voltage settings to operate kW-class hall thrusters remains relatively low while the discharge current can be as high as several amps. The most exposed parts of the probe will therefore reach very high temperature which can eventually lead to failure.

In this study we only assessed the capacity of a Faraday cup to measure positive ions. Some electric propulsion systems are operated with negative ions instead. This makes more difficult their collection and to screen electrons flying along. In this case, the collector should be biased positively to attract the negatively charged ions. Moreover, the use of a magnetic field would be of interest to see how well it could help to screen electrons. Of course, this would add complexity to the measurement system and might require the use of an adjustable magnetic field (i.e. coils) and not a permanent one (i.e. magnets).

In our study most measurements were done at a constant distance from the

thruster. In the case of the FEEP thruster it was possible to try a probe design for two distances (25 cm and 84 cm) but in different vacuum chambers. Therefore, these experiments should be redo but this time in the same facility. Moreover, to measure the ion current closer to the thruster exit plane one shall update the probe design. The reasons are twofold: 1) the probe will induce much more perturbations, so it should be as small as possible 2) near the thruster exit plane the probe enters the near field region and several assumptions used in this dissertation do not hold any more (point source, plume symmetry), hence the aperture shall be large. Moreover, the current density rises as the probe get closer to the thruster. Hence, probe materials shall be adapted to sustain higher stress level. Also to minimise perturbations induced by plasma-probe interactions time exposure to the ion beam shall be minimized, hence shorter measurement times. Last but not least reducing the overall probe dimension decrease the efficiency of passive techniques (e.g. Length) to reduce IIE effects. Hence, they must be compensated by improving IIE and ion trapping. We showed that in the case of a GIE or a FEEP, collector made of complex surfaces do increase the overall ion collection efficiency of the probe. However, aluminium based materials are not recommended when the probe is exposed to larger current intensities or densities. Many studies claimed that carbon velvet is a very good candidate as carbon is sputtered and heat resistant, whilst decreasing having a low γ_{EE}. Unfortunately, it is a very difficult material to buy. Nonetheless, technological progress in the field of 3-D printing could help to build a porous or at least complex structure vacuum compatible and exploitable.

Appendices

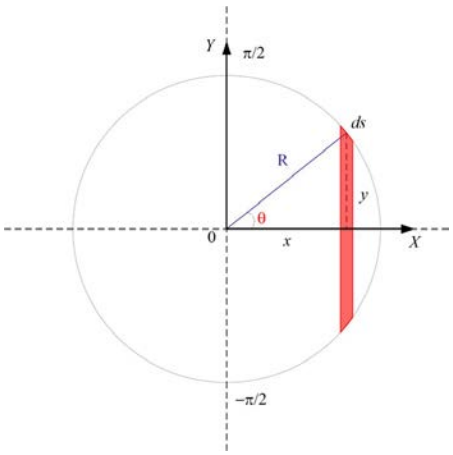

Figure 24: Schematic of the cylindrical coordinate system used to compute the experimental ion current $I_{i_{int}}$ from the current density angular distribution profile.

A Ion current retrieval demonstration

The ion current $I_{i_{int}}$ corresponds to a flux of positive charges going through a surface per unit of time. It reads:

$$I_{i_{int}} = \int\int j_i \times \boldsymbol{n} dS. \tag{1}$$

The ion current density $\boldsymbol{j_i}$ (A/m^2) is assumed to be collinear to the outward pointed unit normal vector to the surface. We obtain:

$$I_{i_{int}} = \int\int j_i dS. \tag{2}$$

A spherical coordinate system is often used to determine dS and compute $I_{i_{int}}$. The probe is usually fixed at a distance R and the thruster is supposed to be a point source at the centre of a sphere. To compute $I_{i_{int}}$ it is needed to know $j_i(\theta, \phi)$, where θ is the latitude and ϕ the longitude. When the current density is solely recorded in a plane that contains the thruster axis, e.g. following the angle θ from $-\pi/2$ to $\pi/2$, one can assume a cylindrical symmetry of the ion beam around the thruster axis to determine $j_i(\theta, \phi)$ and compute $I_{i_{int}}$. It is in fact easier to use a cylindrical coordinate system to solve equation 2. The coordinate system is depicted in figure 24 along with the elementary arc ds. The thruster exit plan points toward the x axis. Measurements are performed at a fixed distance R and

defined by the angle θ. Cylindrical symmetry implies a constant j_i inside the element with radius y and thickness ds. The sum of these elements, each weighted with $j_i(\theta)$, gives the ion current:

$$I_{i_{int}} = \int_0^R j(x,y)2\pi y ds, \tag{3}$$

with $j_i(x,y) = j_i(\theta)$. From figure 24, we have:

$$cos(\theta) = \frac{x}{R}, sin(\theta) = \frac{y}{R}. \tag{4}$$

The circular arc ds can be found with:

$$ds = \sqrt{1 + (\frac{dy}{dx})^2}. \tag{5}$$

The circle, of the sphere, of radius R is centred on the thruster exit plane:

$$R^2 = x^2 + y^2 \longrightarrow y = \sqrt{R^2 - x^2}, \tag{6}$$

and:

$$\frac{dy}{dx} = \frac{-x^2}{\sqrt{R^2 - x^2}}. \tag{7}$$

Combining equations 5 and 7 the elementary arc therefore reads:

$$ds = \sqrt{\frac{R^2}{R^2 - x^2}} dx, \tag{8}$$

equation 3 finally becomes:

$$I_{i_{int}} = \int_0^R j_i(x,y)2\pi\sqrt{R^2 - x^2}dx \longrightarrow 2\pi R \int_0^R j_i(x,y)dx. \tag{9}$$

In the case $j_i(x,y)$ equals 1, the equation gives the area of an hemisphere. With a planar measurement configuration, the current density is defined by θ. Figure 24 gives the relation between x and θ:

$$\cos(\theta) = \frac{x}{R} \longrightarrow x = R\cos(\theta), \tag{10}$$

$$dx = -R\sin(\theta)d\theta. \tag{11}$$

Finally, changing the boundaries, the final form of the current density is:

$$I_{i_{int}} = 2\pi R^2 \int_0^{\frac{\pi}{2}} j_i(\theta)\sin(\theta)d\theta. \tag{12}$$

This form is also used by [63] in his recommended guidelines for use of Faraday probes. In the case of perfect symmetry around the x axis we can use the form proposed in equation 12. If the ion beam is not symmetric, one must use an integral from $-\pi/2$ to $\pi/2$. There are two possibles:

- One calculates the mean current density from $j_{i(\theta)}$ and $j_{i(-\theta)}$ and then equation 12 can be used
- Equation 12 is split into the sum of two terms that represents positive and negative angles:

$$I_{i_{int}} = \pi R^2 \left[\int_0^{\frac{\pi}{2}} j_i(\theta)\sin(\theta)d\theta + \int_0^{\frac{-\pi}{2}} j_i(\theta')\sin(\theta')d\theta' \right]. \tag{13}$$

  This comes down to take the absolute of the sine inside the integral as followed:

$$I_{i_{int}} = \pi R^2 \int_{\frac{-\pi}{2}}^{\frac{\pi}{2}} j_i(\theta) \mid \sin(\theta) \mid d\theta. \tag{14}$$

B Ion beam study: Low power Radio-frequency Ion Thruster (RIT)

B.1 Experimental apparatus

At the end of the PhD thesis it was possible to test a few designs of our Faraday cup with a low-power GIE owned by ESA. The thruster is operated with xenon for our case study and the total ion acceleration is 2 kV with an ion current of 14.5 mA. For confidential reason no further details of the GIE source will be given. Since this thruster can be operated with xenon, in direct ion current control with ion energies lying between typical values found for Hall thruster and FEEP, it makes the link with our previous studies (section 4 and 5). Tests were performed in the Netherlands at the ESTEC electric propulsion laboratory [125]. The test campaign was conducting in the GIGANT vacuum chamber. It is 1.6 m wide and 2.5 m long. Its pump capacity allows to reach a residual background pressure of 10^{-7} mbar during the thruster operation. A mechanical arm is installed 95 cm away from the thruster exit plane. Due to short allocated time dedicated to this test campaign we optimized the number of design parameters to be tested. We conducted two vacuum cycles where design parameters were changed in between. Also, for each cycles three probes were installed on the boom as indicated in figure 25. We labelled the probe locations 1 (left), 2 (right) and 3 (middle). Each slot was used to assess one design parameter, so three in total. In slot #1 we examined the effect of a foam #1 (50 Al 7 P - F Al **1**) and flat aluminium (50 Al 7 P - F Al **0**) collector material. In location #2 we examined the impact of the probe inlet diameter when it is either 3 mm (50 G **3** E - F Al 6) or 7 mm (50 G **7** E - F Al 6). Finally, in slot #3 we characterized the influence of the cup length on the integrated ion current. Probes are either 50 mm (**50** G 7 P - F Al 3) or 30 mm (**30** G 7 P - F Al 3) in length. Currents were measured with the Keithley 2450 used for other test campaigns. Due to mechanical complications we were only able to measure one half of the thruster plume (lower part). Moreover, we had to manually move the arm allowing ion current acquisition every 5°. Finally, the probes located in #1 and #2 are $\pm 7.2°$ off-centre from the thruster axis.

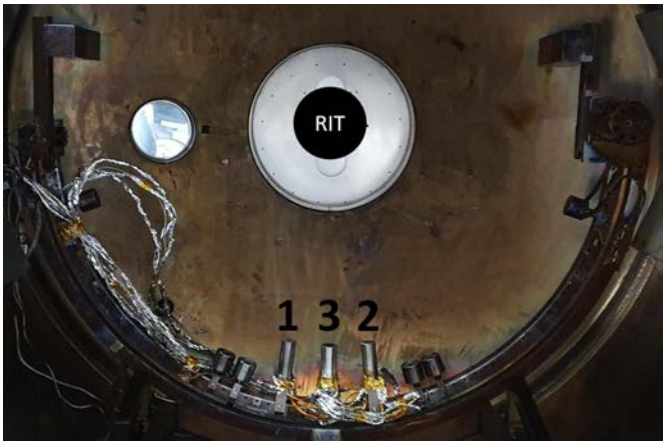

Figure 25: Experimental apparatus used at ESTEC in the GIGANT chamber. Location 1 and 2 are $\pm 7.2°$ off-centre. Probe are located 63 cm from the rotation axis of the arm. The latter is 30 cm upwards the thruster exit plane.

B.2 Ion-induced electrons

Ion collector material

We measured the capacity to reduce the yield of emitted ion-induced electrons of an aluminium foam material compared to an aluminium disk. The methods used to compute γ_{EE} and $\gamma_{L_{EE}}$ are detailed in section 4.1.1 and 4.2.1. Figure 26 shows I-V traces obtained with ion collector made of foam #1 when the probe is operated in configuration *A* and *B*. The repeller and cup are set to -60 V for *A* and *B*. Hence the current drops when V_{coll} overtakes this value. Overall, the signal is stable but we notice a current drift. This is why we interpolate both sections of each traces to measure the yield. Note that close to 8% of the ion signal is lost to the cup when using configuration *B* and $V_{coll} > V_{cup}$. This was also noticed in the case of the FEEP thruster (section 4). Results are displayed in table 5 for aluminium and foam. This time, contrary to observations made with the low power Hall thruster the foam does help to mitigate the induced electrons effect on the measured ion current. The plume of a RIT is similar to the one of a FEEP as it is an ion beam where ions are likely to have velocity vector collinear to the thruster axis. We observe that using a foam can reduce by 10% the emission rate and by 45% the fraction of IIE leaving the cup.

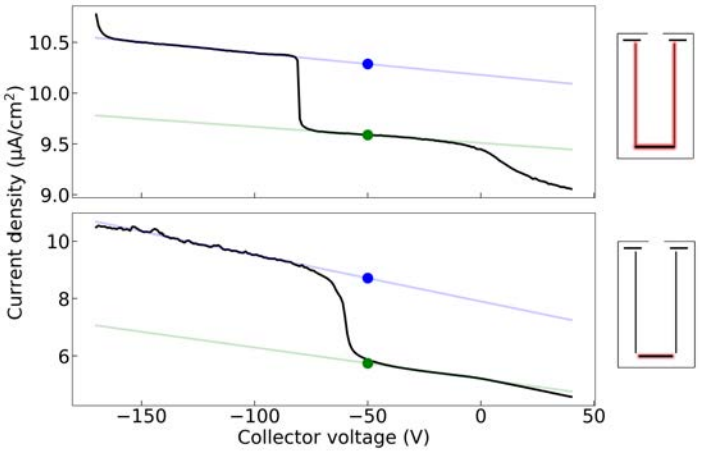

Figure 26: I-V traces obtained with a FC in configuration *A* (top) and *B* (bottom). The thruster fires at 14.5 mA and 2 kV. The repeller and cup voltage are set to -60 V for *A* and *B*. In blue the current increases by IIE ($I_{i\&EE}$) and in green the ion current I_i.

Table 5: γ_{EE} and $\gamma_{L_{EE}}$ measured for a foam#1 and an aluminium disk when bombarded by 2 kV xenon ions. $\gamma_{L_{EE}}$ is given for a 50 mm long cup.

Material	$\gamma_{L_{EE}}$	γ_{EE}
Aluminium	0.105	0.448
Foam #1	0.072	0.404

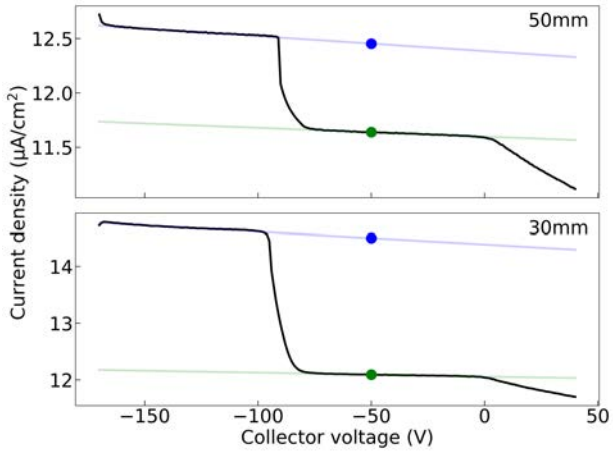

Figure 27: I-V traces obtained with a FC in configuration *A* with a 50 mm (top) and 30 mm (bottom) long cup. The thruster fires at 14.5 mA and 2 kV. The repeller voltage is set to -60 V. In blue the current increases by IIE ($I_{i\&EE}$) ans in green the ion current I_i.

Ion collector length

Since IIE effects are non-negligible in the case of a RIT, we studied how the length of the cup can lead to current acquisition errors. We measured $\gamma_{L_{EE}}$ for a 50 mm and 30 mm long cup. The probe was placed on the thruster axis (i.e. location #3). The collector is made of foam #3. Figure 27 displays I-V traces acquired with both probes in configurations *A*. The computed $\gamma_{L_{EE}}$ are 0.198 and 0.0699 for a 30 mm and 50 mm long cup, receptively. Note that the value for the 50 mm cup is almost identical to the one obtained in section B.2 where the probe collector was a foams #1. The yield of induced electrons leaving the cup is 2.83 larger for a 30 mm long cup. We remark that for both lengths values are similar to those obtained in the case of a FEEP thruster (see section 4.2.2). Similarly to the FEEP, most of the ion current is collected by the cup rear section as we can see in figure 28, which gives the current on different parts of a FC in configuration *A* (top) and *B* (bottom) as a function of the collector voltage at the position #1. To the top the repeller voltage is set to 20 V (red dashed line) and to the bottom the cup voltage is -30 V (green dashed line). In both cases we observed the effect of IIE as explained in previous section. All current fractions for each plot were acquired simultaneously. We see from the first plot that only 3% of the ion current going through the cup at most is collected by the repeller, the rest is shared between

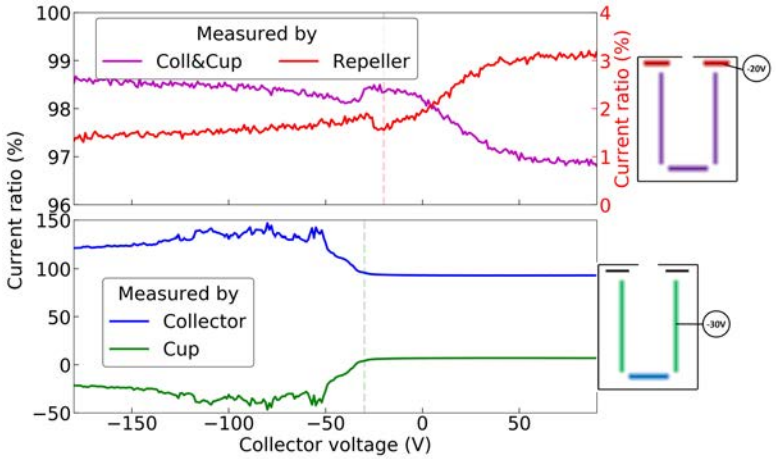

Figure 28: Current share between different FC parts in configuration *A* (top) and *B* (bottom) against the voltage on the collector. The thruster fires at 14.5 mA and 2 kV. The probe located in position #1.

the collector and cup. When looking in details how the ion current is distributed we see that once all IIE are recollected (i.e. $V_{coll} > V_{cup}$) only 8% is measured by the cup while the rest is properly collected by the probe rear section. The same behaviour is observed with the FEEP thruster.

Therefore, with this type of thruster we can, like with a FEEP, use the repeller to actively push IIE back into the cup if one wants to reduce the overall length of the probe.

B.3 Probe Inlet diameter

Finally, we measured the impact of the probe inlet diameter. Two configurations with 7 mm and 3 mm wide aperture are tested in locations #2. The ion current densities obtained with each probe when the collector is biased to -30 V and the repeller to -60 V are displayed in figure 29. The thruster fires at 14.5 mA and 2 kV. As explained in previous sections only half of the angular profile (the "negative" part) is actually measured. The other half is extrapolated assuming the profile is perfectly symmetrical. We observe that when d_a is 7 mm there is more ion current measured in the $\pm 10°$ region. The difference seen on the logarithmic scale at large angles between the two configurations is negligible since the signal magnitude is very low. RIT thrusters have the characteristic to be highly efficient in term of beam divergence, hence signal measured at large angles can be attributed to

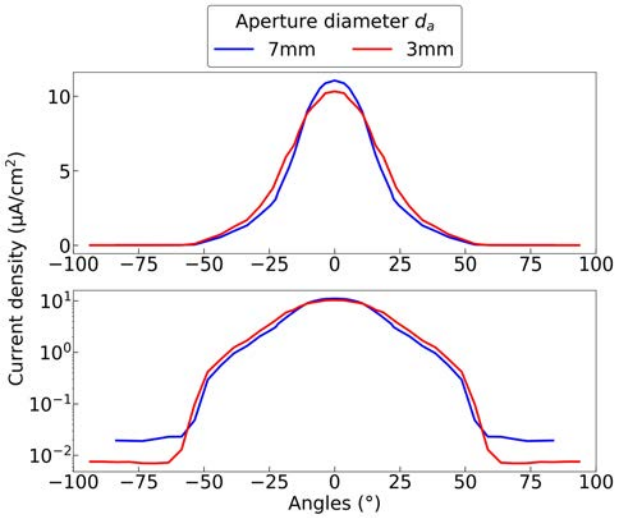

Figure 29: Ion current density angular distribution acquired with a FC aperture of 7 mm (blue) and 3 mm (red). The thruster fires at 14.5 mA and 2 kV. Only half of the profiles is measured, the other half is extrapolated.

facilities effects. The value of $I_{i_{int}}$ computed for the 3 mm wide aperture is near 19% lower than what is measured by the 7 mm. Nonetheless, this figure must be handled carefully since we had to apply several corrections in terms of collecting area and effective angle due to the position of the probe and the axis of rotation from the arm. Moreover, due to mechanical issues and time constraint only a small fraction of angular position could be tested, increasing the uncertainties on our measurements. However, results are in line with our findings in the case of a FEEP and Hall thruster regarding the dimension of d_a, the larger the better.

B.4 Conclusion

The study conducted on a low power GIE shows similar behaviour on the impact of different design parameters for a FC. In fact, we saw that a foam material could be efficient to reduce the rate of IIE emitted by the ion collector. Moreover, we showed that increasing the length of the cup help to prevent IIE to escape the cup, hence minimizing the artificial current rise. The current distribution inside the probe is very similar to a FEEP thruster where most of the ion signal is collected by the cup rear part. In fact at worst, up to 3% can be measured by the repeller. In addition, An ion current decrease is noticed when reducing the diameter of the

probe entrance. Finally, we could not effectively compared the effect of X.X.X**E** and X.X.X.**P** configurations. However, based on the other results it seems that a X.X.X.**P** architecture is better to minimize perturbation. Overall, the response of the FC while studying the ion beam of RIT is quite similar to a FEEP thruster even though propellants are different. Hence, we would recommend the same guidelines for the RIT than what was suggested for the FEEP in section 6.1.1 and in the conclusion.

C Version Française

C.1 Résumé

La propulsion électrique est aujourd'hui une technologie incontournable dans le secteur spatial grâce aux avantages qu'elle procure en termes de masse, de volume et d'impulsion totale. Elle est désormais couramment utilisée pour le transfert d'orbite, le contrôle d'attitude et le maintien à poste des satellites géostationnaires de télécommunication. Les propulseurs électriques deviennent également incontournables pour améliorer les performances et les capacités des CubeSats et des microsatellites dont le nombre de mises en orbite croit de façon exponentielle. De plus ce type de propulsion apparaît avantageux pour les nouvelles générations de satellites GPS, les systèmes d'extension de vie des satellites, les véhicules cargo et les sondes interplanétaires. Il existe une grande variété de technologies de propulseurs électriques spatiaux, ou propulseurs ioniques. Certains types sont déjà à disposition, e.g. les propulseurs de Hall et les moteurs ioniques à grilles, alors que d'autres sont en cours de qualification ou de développement, tels que les propulseurs miniatures destinés aux petits satellites. Quelle que soit la technologie et son degré de maturité, il est primordial de valider l'ensemble des caractéristiques ainsi que les performances du propulseur, afin de fournir des données et informations pertinentes et fiables aux constructeurs de satellites ainsi qu'aux utilisateurs et clients. Pour répondre à la problématique, il est nécessaire de réaliser deux types de mesures : i) des mesures de la poussée d'une part et ii) des mesures des propriétés du faisceau d'ions d'autre part. Les travaux de recherche qui ont été conduits dans cette thèse traitent en particulier les mesures de type ii. Le faisceau d'un propulseur est composé principalement d'ions et d'électrons ; les premiers sont à l'origine de la poussée et les seconds garantissent la neutralité électrique du système. Les données à collecter sur les ions sont le flux, l'énergie et la charge en fonction de la position et de l'angle. Elles permettent de déterminer le courant total d'ions, l'efficacité d'ionisation et l'angle de divergence du faisceau. Ces grandeurs sont importantes pour évaluer les performances du système propulsif ainsi que les possibles interactions entre le plasma et le satellite qui peuvent conduire à des anomalies, voire à l'échec de la mission. La thèse a deux objectifs majeurs : 1) optimiser les instruments qui permettent la mesure de la densité de courant ionique (coupe de Faraday) et de l'énergie des ions (analyseur à champ retardateur) et 2) fournir des données sur le dimensionnement d'une sonde « universelle » pour l'étude de faisceaux provenant de différents propulseurs électriques. Il s'agit en fait de fiabiliser la mesure des

grandeurs ioniques et de standardiser les essais pour garantir les valeurs et permettre une comparaison tangible et pertinente entre différents propulseurs, entre différentes chambres d'essais au sol et entre les données sol/vol. Les études expérimentales conduites pour atteindre les objectifs ont pu être réalisées avec trois types de propulseurs :un propulseur de Hall, un moteur ionique à grilles de type radio fréquence et un propulseur à effet de champ. Les caractéristiques et les performances cumulées de ces trois propulseurs couvrent un très vaste domaine, ce qui permet de valider la majorité des cas rencontrés. Ces moteurs ont été fournis par le CNRS, l'ESA et la start-up ENPULSION, respectivement. Il a aussi été possible d'accéder à différents moyens d'essais pour l'étude des effets induits par les bancs de tests sur un moteur à effet de champs. Les résultats obtenus montrent qu'il est possible d'utiliser une architecture commune pour l'étude de ces trois moteurs. Cependant, les parties de la sonde les plus exposées aux perturbations induites par l'interaction avec le faisceau étudié dépendent des propriétés de ce dernier. Cela implique que la sonde fonctionne d'une manière différente pour chaque moteur. Il a aussi été possible de comprendre le comportement des ions une fois dans la sonde. Enfin, le développement d'une sonde dite à mode double a été étudié. Le but est de pouvoir mesurer, à conditions plasma identiques, l'énergie et le courant d'ions au sein du faisceau. Ces deux informations permettent de déduire de façon indirecte la poussée produite par un moteur.

C.2 Propulsion spatiale

De nos jours la propulsion spatiale est un acteur majeur de l'industrie du New Space. La capacité des fabricants de lanceurs et satellites à réduire les coûts d'accès à l'espace notamment grâce à la miniaturisation des composants électroniques à fait exploser le marché des petits satellites et constellations. Ces nouveaux engins spatiaux ont besoin de system pour se mouvoir une fois en opération pour rectifier leur attitude, changer d'orbite ou pour des procédures de fin de vie une le satellite hors d'usage. La réponse de la communauté de la propulsion électrique a été vive et permet dorénavant d'avoir accès à une large gamme hétérogène de moteur spatiaux électriques. Ces moteurs ont des principes de fonctionnement ainsi que des carburant différent. Il est alors pour le moment difficile de sonder le faisceau d'ion, aussi appelé plume, avec des outils optimiser et conçu pour être opérationnel pour chacun d'entre eux. Le but de cette thèse est de lettre au point une sonde dite de Faraday capable de mesurer de manière fiable le courant d'ion au sein de la plume d'un moteur à effet de Hall, à effet de champs et à grille. Ces trois moteurs couvrent à eux seule une large gamme de densité de courant d'ion

et d'énergie ionique. Plusieurs architectures de sonde sont testées pour essayer de trouver une architecture commune et exploitable pour l'étude de chacun de ces moteurs. Dans un deuxième temps, nous allons étudier la possibilité d'utiliser une sonde en mode double capable de mesurer un courant d'ion et d'avaliser les énergies ioniques au sein d'une plume pour des conditions plasma identique.

C.3 La physique des plasmas appliquée à l'étude des moteurs électriques

La physique des plasmas nous permet d'étudier la composition ionique et électrique au sein de la plume d'un moteur électrique. Plusieurs technique existe mais notre étude se concentre sur les méthodes de mesure par sonde électrostatique. Elles permettent de mesurer des paramètre plasma important comme la densité et la température des ions et électrons ainsi que le potentiel plasma ou flottant. Pour l'étude par sonde il est capital convenablement définir le plasma étudier par sa longueur de Debye ou les possibles collisions de charges. Une fois immergé dans la plume d'un moteur électrique une coupe de Faraday peut mesurer le courant d'ions en son sein. Cela permet par la suite de retrouver des paramètres de performance moteur capitaux tels que la divergence de la plume, l'efficacité d'ionisation du carburant, la déviation du faisceau et la poussée. Pour cela il faut minimiser les jauges d'incertitudes induite par les mesures et les interactions entre la sonde et la plume. Une sonde convenablement conçue permet la mesure de ces paramètres pour une fiabilité inférieure à 5

C.4 Installation expérimentale et études préliminaires

Trois types de moteurs ont été utilisés dans cette études : un moteur de Hall basse puissance, un moteur à effet de champ (FEEP) et une source d'ion à grille.

Le premier (voir le chapitre 5) appartient au laboratoire ICARE du CNRS et fût développer par l'équipe propulsion électrique qui l'a nommé ISCT200 car il est conçu pour fonctionner à 200W de puissance anode. L'étude de la plume de ce moteur a pu être faite sur deux versions : HT1 et HT2. Les campagnes de tests sur ces moteurs se sont déroulées au sein du caisson NExET dont le system de pompage permet une pression résiduelle de $10-5$ mbar avec le moteur allumé. La sonde est située à une distance supérieure à 25 cm du plan de sortie moteur pour l'intégralité de l'étude.

Le moteur à effet de champs (voir le chapitre 4) a été fourni par la compagnie

privée ENPULSION qui commercialise une version de vol. Quatre différentes unités de laboratoire ont été mises à notre disposition pour analyser la dépendance des résultats mesurés avec la coupe de Faraday avec la distribution sur la couronne du nombre d'aiguille en tir. De plus il a été possible de tester ce moteur dans deux caissons différents. L'un de taille similaire à NExET, mais la pression pendant les expériences atteints $10-6$ mbar. L'autre d'une taille bien plus grande ($2.2\,\mathrm{m}\times 3\,\mathrm{m}$) nous a permis de voir les effets des caissons sur les meures de densité de courant ionique.

Le dernier moteur fut utilisé à l'Agence Spatiale Européenne sur son site de l'ESTEC aux Pays-Bas au sein du laboratoire de propulsion électrique (voir le chapitre B). Dans ce chapitre il est fait des études préliminaires nous permettant de caractériser des paramètres plasma comme la longueur de Debye, la densité électronique et ionique, la température électronique ou le potentiel plasma au sein de la plume des différents moteurs.

Enfin les différents designs de coupe de Faraday sont énumérés ainsi que le nomenclature qui sera utilisé tout au long de la dissertation. De même, il est présenté les architectures des sondes permettant d'analyser les énergies ioniques au sein de la plume d'un moteur à effet Hall et à effet de champs.

C.5 Etude d'un faisceau d'ion: Le moteur à effet de champs ENPULSION Nano

Dans ce chapitre la plume de l'ENPULSION NANO est étudiée. Dans un premier temps, l'étude se porte sur la détermination du taux d'émission des électrons induit par les ions γ_{EE}. La méthode de mesure est tout d'abord détaillée. Ensuite γ_{EE} est mesuré pour de l'aluminium, de l'inox, du molybdène et du tungstène pour des énergies ioniques allant de 3 keV à 8 keV. Ces matériaux sont très utilisés dans le domaine de la propulsion électrique. Les résultats montrent que l'aluminium est le matériau avec le plus haut γ_{EE} (>0.4) tandis que les autres taux sont du même ordre (<0.4). Pour tous, le taux augmente avec l'énergie des ions. Afin de minimiser γ_{EE} nous étudions un matériau avec une structure en forme de mousse en aluminium. Différents types de mousse sont utilisé avec des pores de différentes tailles. Les résultats montrent que plus la tailles de pores est grande plus γ_{EE} diminue. Pour exemple, une mousse d'aluminium #6 permet de réduire γ_{EE} de 60% par rapport à un disque d'aluminium. L'impact de l'angle d'incidence entre les ions et le disque sur γ_{EE} est aussi évalué. On voit que plus l'angle est grand plus le taux d'électrons induit sera élevé. Enfin, nous montrons que dans le cas

d'un moteur FEEP, le matériau utilisé pour collecter les ions dans une FC n'a que peu d'importance. En appliquant les bonnes tensions au collector et au repeller il est possible de recollecter l'ensemble des électrons induit. Ainsi, les mesures de profiles et de courant sont identiques pour n'importe quels matériaux.

Dans un second temps, nous évaluons la taille de la sonde (50 mm, 30 mm et 10 mm). Les résultats montrent que plus la sonde est grande plus celle-ci recollecte facilement les électrons induit émis par la coupe. En effet, si aucune tension n'est appliquée au repeller le courant mesuré n'est que 1.6 fois supérieur au vrai courant pour une sonde de 50 mm. Dans le cas d'une sonde de 30 mm le courant mesuré est entre 1.19 et 1.32 et pour une longueur de 10 mm il est de 1.82 à 2.26. Dans le cas d'une sonde de 50 mm cette augmentation de courant est la même peut import l'énergie des ions étudiés. À l'inverse, plus la sonde est petite et plus le courant mesuré augmentera avec l'énergie ionique. De plus, pour une sonde de 10 mm il semble qu'une partie du signal ionique est perdue une fois que les perturbations induites par les électrons induits sont supprimées. Nous pensons que les ions non collectés sont réémis hors de la coupe. Avec une sonde de 10 mm les ions réémis on moins de chance d'être recapturé par les côtés de la coupe. En combinant nos mesures expérimentales avec les résultats d'un logiciel de simulation de trajectoire de particules chargées (SIMION) il nous est possible de déterminer l'angle de divergence de l'émission des électrons induits. On trouve une valeur comprise entre 33° et 43°.

Dans un second temps, on étudie l'influence du matériau utilisé sur le devant de la sonde. On voit que pour certain matériau (molybdène, aluminium) l'efficacité de collection des ions de la sonde diminue. Cependant, les variations sont très faibles. De plus, on observe que quand la sonde est configurée en X.X.X.**P** (i.e. le devant du capot de la sonde défini le flux d'ions qui entre), l'efficacité de collection des ions n'est plus affectée quel que soit le matériau.

Enfin, nous avons étudié la taille du trou d'entrée de la sonde et son effet sur le courant d'ion mesuré. On s'aperçoit que le plus le diamètre d'entrée est petit moins plus le courant d'ion mesuré s'éloigne de la valeur réelle du courant (i.e. I_{em}). Cependant, une série d'expérience nous a permis de voir que si le trou d'entré est éloigné (>4.5 mm) du collecteur en forme de coupe, le courant d'ions mesuré redevient proche I_{em}. Pour finir, nous avons pu étudier l'effet de la distance de mesure sonde-moteur dans deux chambres différentes. Les résultats montrent qu'avec la bonne architecture de sonde peu importe cette distance le courant d'ion mesuré est très proche de I_{em}. Cependant, l'angle de divergence mesuré change entre des mesures faites à 25 cm et 84 cm du plan de sortie du moteur. En effet, au plus proche du moteur cette valeur 16% plus grande. Cela

peut être induit par la sonde elle-même, par la forme des lignes de champs créer par l'extracteur ou bien par des espaces de charge proche de l'émetteur due aux nombreuses zones d'émission induite par la forme circulaire de la couronne. Pour clarifier ce phénomène il faudrait réitérer cette étude dans des chambres identiques.

C.6 Etude d'un faisceau d'ion: Le moteur à effet de Hall ISCT200

Dans ce chapitre nous étudions la plume d'un moteur à effet Hall basse puissance. Dans un premier temps nous donnons γ_{EE} pour du molybdène, de l'inox et de l'aluminium pour des ions de xénon. L'aluminium est le matériau avec le plus haut taux d'émission mais n'augmente le courant mesuré que de 10% tout au plus pour des tensions de décharge de 250 V et 300 V. Les autres contribue seulement à une augmentation de $\sim$4 à 5%. De plus, l'utilisation de mousse métallique semble augmenter γ_{EE} dans le cas d'un moteur à effet Hall. On observe que plus la tailles des pores est grande plus le taux d'émission augmente. Cela peut être due à la présence de particules neutres dans les pores. Aussi, dans la plume d'un moteur de Hall les ions ont des vecteurs vitesses différentes ce qui engendrerait des angles d'incidences aléatoire et qui augmenterais γ_{EE}. À l'opposé d'un moteur à effet de champs, la taille et la forme de la coupe d'une sonde de Faraday n'a que peu d'influence sur la mesure du courant ionique. En effet, notre étude a permis de mettre en évidence que seulement une petite fraction (5% à 0°) du flux d'ion atteint le fond de la coupe. En réalité, il semblerait qu'aux grands angles 80% du flux d'ion est capturé par les côtés de la coupe et entre 95 et 98% quand la sonde est proche de l'axe du moteur. On observe aussi que selon la taille d'entrée de la sonde plus ou moins de courant est mesuré sur le devant de la coupe. Plus on réduit la taille d'entrée plus on augmente les probabilités de collision ion-ion ou ion-neutre qui induisent des changements de directions des ions, et donc qui les empêche d'atteindre le fond de la coupe. À l'inverse pour une sonde de petite taille ($\sim$20 mm), proche de 100% du signal est mesuré par le fond de la coupe. Cela indique que pour une sonde longue, les ions sont repoussés ou bloqués.

De la même manière que pour le moteur à effet de champs, nous avons étudier l'effet du matériau utilisé sur le devant de la sonde. Les mêmes observations ont été faites mais pour des impacts plus importants. En effet, dans le cas d'un moteur de Hall le courant d'ion mesuré est environ 14% plus petit quand le devant de la sonde est équipé avec du molybdène qu'avec du graphite. Cela peut être explique par le fait que le molybdène est plus sensible à la pulvérisation, l'émission de neutre et tend à chauffer plus facilement que le graphite. Le diamètre d'entrée

de la sonde a aussi été étudié. Une nouvelle fois nous faisons des observations similaires à celles faites avec le moteur à effet de champs. Cette fois-ci en diminuant le diamètre d'entrée de 10 mm à 3 mm on observe une diminution du courant d'ions de 30%. Cependant, une fois que la sonde est en configuration X.X.X.**P**, les effets induits par le matériau ou le diamètre d'entrée sur la mesure du courant d'ion disparaissent. Il semblerait qu'avoir une distance de plus de 4.5 mm entre l'entrée est le collecteur en forme de coupe permettent de protéger ce dernier des perturbations. Cela s'aligne sur les observations faites précédemment par rapport à la répartition du flux d'ions à l'intérieur de la sonde où l'intensité du courant d'ions est la plus grande sur le devant de la coupe.

C.7 Mesure du courant et des energies ionique: Sonde à mode double

Dans ce dernier chapitre nous montrons la fiabilité d'une architecture optimisée d'une sonde pour un moteur à effet Hall et de champs. Des recommandations sur l'architecture de la sonde pour l'étude des deux moteurs sont données. Par la suite, nous mesurons à l'aide d'une sonde à analyseur de champs (RPA) la distribution des énergies ioniques dans la plume des deux moteurs. On note que pour l'ENPULSION NANO les énergies sont identiques à la valeur de la tension d'émission du moteur. À l'inverse, dans le cas d'un moteur de Hall la distribution des énergies ioniques est beaucoup plus dispersée mais aussi soumis à des pertes. En effet, à 0° l'énergie maximum mesuré est 15% inférieur à la tension de décharge appliquée. Aux grands angles les énergies ioniques mesurées sont de plus en plus petites et atteignent à 80° seulement 17% de l'énergie maximum mesuré sur l'axe du moteur. Pour les moteurs à effet Hall l'énergie potentiel n'est pas complètement convertie en énergie cinétique car il y a des pertes induites par l'ionisation, l'accélération des ions, le transport des électrons et l'interaction entre le plasma et les parois du moteur. Après avoir convenablement mesuré le courant d'ion ainsi que les énergies ioniques pour chaque moteur, nous avons développé un instrument, appelé sonde en mode double (DMP) qui nous permet de mesurer ces deux valeurs pour des conditions plasmas identiques. Cet instrument peut être configurer en mode FC ou bien RPA selon les paramètres à mesurer. La sonde est composée de trois électrodes. La première (RE) permet de repousser les électrons primaires, la deuxième (IS) qui fait 30 mm de longueur permet de sélectionner les ions selon leur énergie. La troisième (C) mesure les ions qui ont une énergie supérieure à eV_{IS}. Dans le cas d'un moteur à effet de champs plusieurs architec-

Table 6: Directives pour la construction d'une sonde de Faraday optimisée en configuration **P** pour l'étude du faisceau d'ion d'un moteur à effet de champs, d'un moteur radio fréquence basse puissance et d'un moteur à effet Hall basse puissance.

Paramètre	**Moteur à effet de champs&radio fréquence**	**Moteur à effet Hall**
Configuration	P	P
A	$d_a = 7$ mm	$d_a = 7$ mm
B	$d_{rep} = 9$ mm, graphite, $V_{rep} < V_{coll} < 0$	$d_{rep} = 9$ mm, graphite, V_{rep} flottant
C	1 coupe, $d_c > d_{rep}$, faible γ_{EE}, mousse	Segmenté, $d_c > d_{rep}$, faible γ_{EE}, faible taux de pulvérisation
D	$L_{cup} = 50$ mm	$L_{cup} = 30$ mm
E	Graphite	Graphite
F	PEEK	PEEK
G	Inox	Aluminium

ture de la sonde ont été étudié afin de trouver la configuration la plus optimale. La version optimisée permet de mesurer le courant d'ion avec la même fiabilité qu'une FC fonctionnelle. Elle permet aussi de mesurer les énergies ioniques mais avec une déviation d'environ -3% par rapport à un RPA. Pour un moteur de Hall les résultats montrent que ce type de sonde ne peut pas mesurer de manière fiables le courant et l'énergie ionique. Cela est principalement dû à la large distribution des énergies ioniques et à la longueur de la sonde DMP. En effet, avec ce type de sonde nous mesurons la présence d'ions de faible énergie proche de l'axe moteur. Cela est purement induit par la sonde elle-même et fausse donc l'analyse de la distribution énergétique ioniques. Pour ce type de moteur, l'architecture de la sonde à mode double doit être améliorer. Aux vues de la fable énergie des ions dans la plume de ces moteurs on peut alors penser à utiliser la coupe pour mesurer le courant d'ions et simultanément repousser les ions avec de faibles énergies. Il faudra cependant bien écraser les électrons à l'entrée de la sonde pour éviter que ces derniers soit collectés par le collecteur.

C.8 Conclusion

Notre étude a montré qu'il était possible de construire une sonde qui peut être utilisée pour étudier le faisceau d'ion d'un moteru à effet de champs (Chapitre 4) , d'un moteur radio fréquence (Annexe B) et d'un moteur à effet Hall (Chapitre 5). Le tableau 6 donne les directives à suivre pour construire une sonde de Faraday pour l'étude de ces trois moteurs. Nous proposons deux architectures différentes. L'une pour l'étude du faisceau d'un moteru à effet de champs et radio fréquence basse puissance et une autre pour un moteur à effet Hall basse puissance.

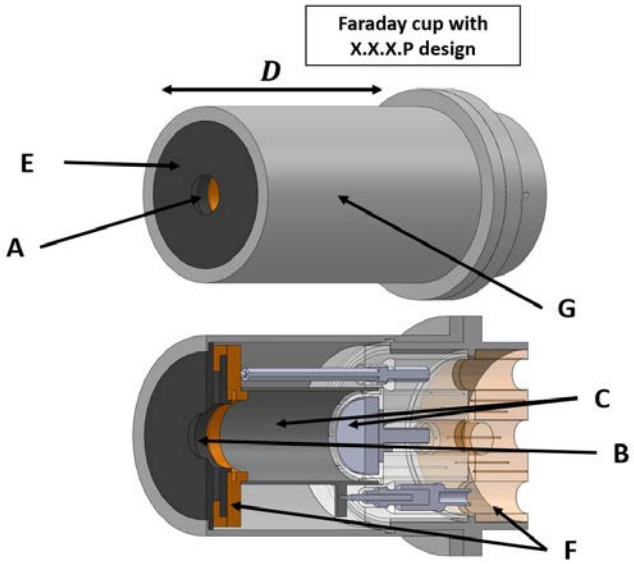

Figure 30: Visualisation d'une sonde de Faraday utilisable pour l'étude de la plume d'un moteur FEEP, basse puissance RIT et basse puissance HT. A = Sonde diamètre d'entrée, B = Diamètre du repeller, C = Collecteur, D = longueur de la coupe du collecteur, E = matériau de la face avant, F = Isolants, G = Capot

Table 7: Directives pour la construction d'une sonde de Faraday universelle en configuration **P** pour l'étude du faisceau d'ion d'un moteur à effet de champs, d'un moteur radio fréquence basse puissance et d'un moteur à effet Hall basse puissance.

Paramètre	**Universelle**
Configuration	P
A	$d_a = 7$ mm
B	d_{rep} 9 mm, graphite, $V_{rep} < V_{coll} < 0$ (FEEP&RIT) or V_{rep} flottant (HT)
C	Segmenté, $d_c > d_{rep}$, faible γ_{EE}, faible taux de pulvérisation
D	$L_{cup} = 50$ mm
E	Graphite
F	PEEK
G	Inox

Il est aussi possible d'utiliser ces directives pour construire une sonde dite universelle qui peut être utilisée pour l'étude du faisceau d'ion de ces trois moteurs. En effet, certains paramètres sont identiques tandis que d'autres peuvent être ajustés comme il est montré dans le tableau 7.

D Doctoral contributions

D.1 Journal articles (published)

- V.Hugonnaud and S.Mazouffre. Optimization of a Faraday Cup Collimator for Electric Propulsion Device Beam Study: Case of a Hall Thruster. *Appl. Sci.* 2021, *11,* 2419. *https://doi.org/10.3390/app11052419*

  In this article we broach the effects of a Faraday cup design upon the measurement of the ion current densities in the far-field region of a low power Hall thruster, the ISCT200. We demonstrate that measurements accuracy are sensitive to the material used at the front of the probe. Likewise, ion current densities measured in the plume of a Hall thruster are heavily impacted by the Faraday cup inlet aperture diameter. Findings described in this article are included in Chapter 5 of this thesis work.

- V.Hugonnaud, S.Mazouffre, and D.Krejci. Faraday cup sizing for electric propulsion ion beam study: Case of a field-emission-electric propulsion thruster. Rev. Sci. Instrum. **92**, 084502 (2021); doi: 10.1063/5.0060931.

  In this article we discuss about the effects of a Faraday cup design upon the measurement of the ion current densities in the far-field region of a field-emission-electric propulsion (FEEP) thruster, the ENPULSION NANO laboratory units. Here, it is showed that measurement outcomes are weakly dependant on the design of the probe front. However, the main error factor in the case of FEEPs is caused by ion-induce electron (IIE) emission from kV-range indium ions. Indeed, we observe an important ion current increase if no active or passive actions are implemented to counter act the effect of IIE. We proposed two solutions to minimize or completely suppress this effect. One consist of redirecting the IIE back to where they were emitted by modifying the electric field lines inside the Faraday cup. The second one tries to passively mitigate the current bulk by increasing the probe length, hence preventing IIE to escape the probe as they are recollected by the cup walls. Findings described in this article are included in Chapter 4 of this thesis work.

D.2 Journal articles (to be submitted)

- V.Hugonnaud, S.Mazouffre, and D.Krejci. Ion-induced electron emission by kV-range energy indium ions: Impact of material and geometry. J. Appl.

Phys. (2022). *In this article we give the ion-induced electron (IIE) yields from kV-range indium ions experimentally measured with a modified Faraday cup for a flat disks made of aluminium, stainless steel, molybdenum, tungsten and aluminium foam with different pores size. The ion source here is the ENPULSION NANO laboratory units. In addition we show that modifying the shape of the ion collector disk for a Faraday cup may contribute to increase the rate of IIE emitted. However, if the orientation of surface emitting IIE is well oriented such as the normal to the surface points towards inner wall of the collector cup, then the additional emission of IIE is properly mitigated. Findings described in this article are included in Chapter 4 of this thesis work.*

- V.Hugonnaud, S.Mazouffre, and D.Krejci. Ion current and ion energy measurement: Dual-mode electrostatic probe development. Rev. Sci. Instrum. (2022).

  In this article we present the development of an electrostatic probe capable of measuring the ion current density and the ion energy in the plume of a field-emission-electric propulsion thruster, the ENPULSION NANO laboratory units. The advantage of such device is threefold: 1) it allows to minimize the number of probes inside a vacuum chamber during measurements, 2) it enable to measure two important quantities included in the formula to compute the thrust of an electric thruster with only one probe, hence reducing experiment induced errors, and 3) it permits to measure two different plume properties at the same location and plasma conditions. Findings described in this article are included in Chapter 6 of this thesis work.

- V.Hugonnaud, S.Mazouffre. Effects of probe dimensions upon xenon ions trajectories generated by a low power Hall thruster inside a Faraday cup. Vacuum Journal (2022).

  This article provide a new insight on how ions generated by a low power Hall thruster (the ISCT200) are distributed once they penetrate a Faraday cup. We show here that in the case of low power Hall thrusters ions rarely reach the bottom of the cup and on the contrary are collected by the top of the probe inner wall. This brings new evidence, and confirms findings reported in previous publications (see D.1), that one should carefully the front of a Faraday cup when studying the plume of a Hall thruster. Findings described in this article are included in Chapter 5 of this thesis work.

D.3 Conference proceedings

- V.Hugonnaud, S.Mazouffre, D.Krejci, B.Seifert, and C.Scharlemann. Faraday cup design for low power electric thrusters. In Space Propulsion 2020+1, March 2021.

  During this conference we showed ion current densities measurements acquired with similar Faraday cup designs from the plume of two deeply different electric propulsion systems: a low power Hall thruster (the ISCT200) and a field-emission-electric propulsion thruster (the ENPULSION NANO laboratory units). We showed that in both cases the design of the Faraday cup has a non negligible impact on the signal measured. However, the effects cause and magnitude are different from one thruster to another. Findings are detailed in Chapter 4 and 5 of this thesis work.

D.4 Conference proceedings (abstract submitted)

- V.Hugonnaud, S.Mazouffre, D.Krejci, B.Seifert, S.Zoehrer, E.Bosch Borràs, and N.Wallace. Study of Faraday cup designs suiting multiple electric propulsion systems. In 37th International Electric propulsion Conference, June 19-23 2022.

  In this conference we will show how to build a Faraday cup which is accurately measuring the ion current density for three different electric thrusters: a low power Hall thruster (the ISCT200), a field-emission-electric propulsion thruster (the ENPULSION NANO laboratory units) and a low power gridded ion thruster. The paper will cover the impact of the probe dimension and material used for its construction. Moreover, it will show the similarities as well as the differences observed when using an identical design on these three electric propulsion systems.

References

[1] D.Krejci and P.Lozano. Micro-machined ionic liquid electrospray thrusters for cubesat applications. In *35th International Electric Propulsion Conference*, October 2017.

[2] J-M.Rax. *Physique des plasmas*. Dunod, 2005.

[3] R.Joussot, L.Grimaud, and S.Mazouffre. Examination of a 5 A-class cathode with a LaB_6 flat disk emitter in the 2 A - 20 A current range. 146:10, 2017.

[4] D.Krejci and P.Lozano. Space Propulsion Technology for Small Spacecraft. In *Proceedings of the IEEE*, volume 106. IEEE, 2018.

[5] Exxentis. Exxentis Website Homepage. `https://www.exxentis.co.uk/porous-aluminium/porous-aluminium-technology/aluminium-foam-overview-types-production-applications/`.

[6] J.F.Ziegler, J.P.Biersack, and M.D.Ziegler. *SRIM-The Stopping and Range of Ions in Matter*. SRIM Co., 7 edition, 2008.

[7] I.Levchenko, M.Keidar, J.Cantrell, Y-L.Wu, H.Kuninaka, K.Bazaka, and S.Xu. Explore space using swarms of tiny satellites. *Nature*, 562(185), October 2018.

[8] G.M. Sandonato, J.A.N. Gonçalves, and R.T. Irita. Preliminary Performance Results of a 5-cm Kaufman-Type Ion Thruster. In *32nd International Electric Propulsion Conference*, September 2011.

[9] J.S.Snyder, D.M.Goebel, and R.Hofer. Performance Evaluation of the T6 Ion Engine. *Journal of Propulsion and Power*, 28(2), 2012.

[10] E.A.Bering, F.Chang-Diaz, and J.Squire. The Use of RF Waves in Space Propulsion Systems. *The Radio Science Bulletin*, 2004(310), September 2004.

[11] H.Bassner, R.Killinger, H.Leiter, and J.Müller. Development Steps of the RF-Ion Thrusters RIT. In *27th International Electric Propulsion Conference*, October 2001.

[12] H.W.Loeb, D.Feili, G.A.Popov, V.A.Obukhov, V.V.Balashov, A.I.Mogulkin, V.M.Murashko, A.N.Nesterenko, and S.Khartov. Design of High-Power High-Specific Impulse RF-Ion Thruster. In *32nd International Electric Propulsion Conference*, September 2011.

[13] H.Kuninaka and K.Kajiwara. Overview of JAXA's Activities on Electric Propulsion. In *32nd International Electric Propulsion Conference*, September 2011.

[14] Y.Yamashita, Y.Tani, R.Tsukizarda, K.Daiki, K.Nishiyama, and H.Kuninaka. Numerical study of microwave discharge ion thruster μ10. In *36th International Electric Propulsion Conference*, September 2019.

[15] H.W.Loeb. Plasma-based ion beam sources. *Plasma Physics and Controlled Fusion*, 37(26), 2005.

[16] M.Sangregorio, K.Wie, N.Wang, N.Guo, and Z.Zhang. Ion engine grids: Function, main parameters, issues, configurations, geometries, materials and fabrication methods. *Chinese Journal of Aeronautics*, 31(8), 2018.

[17] J.P.Boeuf. Tutorial: Physics and modeling of Hall thrusters. *Journal of Applied Physics*, 121(011101), January 2017.

[18] L.Grimaud. Magnetic shielding topology applied to low power Hall Thrusters, October 2018.

[19] G.I.Taylor. Desintegration of water drops in an electric field. *Royal Society*, 280, 1964.

[20] M.Tajmar, C.Scharlemann, A.Genovese, N.Buldrini, W.Steiger, and I.Vasiljevich. Liquid-metal-ion source development for space propulsion at ARC. *Ultramicroscopy*, 109, 2009.

[21] D.Selva and D.Krejci. A survey and assessment of the capabilities of Cubesats for Earth observation. *Acta Astronautica*, 74, 2012.

[22] K.Lemmer. Propulsion for CubeSats. *Acta Astronautica*, 134, 2017.

[23] D.Lev, R.M.Myers, K.M.Lemmer, J.Kolbeck, H.Koizumi, and K.Polzin. The technological and commercial expansion of electric propulsion. 159, June 2019.

[24] M.Yu.Bernikova and V.V.Gopanchuk. Parametric family of the PlaS-type thrusters: development status and future activities. In *35th International Electric Propulsion Conference*, 2017.

[25] T.Misuri, C.Ducci, S.Gregucci, D.Pedrini, F.Cannelli, U.Cesari, F.Nania, A.Vicini, G.Pace, F.Magistro, J.Cenni, D.Dignani, C.Farauanu, V.Quaranta, B.Tiseo, M.Orefice, and G.Bruno. SITAEL HT100 Thruster

Unit, Full Ground Qualification. In *35th International Electric Propulsion Conference*, September 2019.

[26] S.Mazouffre. Electric propulsion for satellites and spacecraft: established technologies and novel approaches. *Plasma Sources Science and Technology*, 25(3), April 2016.

[27] I.Levchenko, S.Xu, S.Mazouffre, D.Lev, D.Pedrini, D.Goebel, L.Garrigues, F.Taccogna, and K.Bazaka. Perspectives, frontiers, and new horizons for plasma-based space electric propulsion. *Physics of Plasmas*, 27(2), February 2020.

[28] E.Dale, B.Jorns, and A.Gallimore. Future Directions for Electric Propulsion Research. *Aerospace*, 7(120), August 2020.

[29] S.Mazouffre. Mesure de la densité de courant ionique dans le jet plasma d'un propulseur de Hall, Théorie et instrumentation, 2016.

[30] S.Mazouffre. Mesure de la densité de courant ionique dans le jet plasma d'un propulseur de Hall, Expériences dans la plume du PPS1350ML.

[31] S.Mazouffre, G.Largeau, L.Garrigues, C.Boniface, and K.Dannenmayer. Evaluation of various probe designs for measuring the ion current density in a Hall thruster plume. In *35th International Electric Propulsion Conference*, October 2017.

[32] D.Krejci and A.Reissner and T.Schoenherr and B.Seifert and Z.Saleem and R.Alejos. Recent flight data from IFM Nano Thrusters in a low earth orbit. In *36th International Electric Propulsion Conference*, September 2019.

[33] T.Schoenherr and B.Little and D.Krejci and A.Reissner and B.Seifert. Development, Production, and Testing of the IFM Nano FEEP Thruster. In *36th International Electric Propulsion Conference*, September 2019.

[34] L.Grimaud, J.Vaudolon, and S.Mazouffre. Design and characterization of a 200W Hall thruster in magnetic shielding configuration. In *52nd AIAA/SAE/ASEE Joint Propulsion Conference*, 2016.

[35] F.F.Chen. *Mini course on Plasma Diagnostics (Langmuir probes)*. Electrical Engineering Department University of California, Los Angeles, 2003.

[36] D.Rapp and P.Englander-Golden. Total Cross Sections for Ionization and Attachement in Gases by Electron Impact. I.Positive Ionization. *The Journal of chemical physics*, 43, 1965.

[37] D.L.Brown and A.D.Gallimore. Evaluation of facility effects on ion migration in a Hall thruster plume. *J. Propul. Power*, 27:573–585, 2011.

[38] S.Mazouffre. Plasma diagnostic tools for ion current density and ion energy measurment. Report H2020 CHEOPS ID66 ICARE, February 2019.

[39] J.S.Miller, S.H.Pullins, D.J.Levandier, Y.Chiu, and R.A.Dressler. Xenon charge exchange cross sections for electrostatic thruster models. *J. Appl. Phys*, 91(3), February 2002.

[40] R.A.Baragiola and P.Riccardi. Critical potentials in secondary electorn emission from Iron, Nickel and Molybdenum. *Reactive Sputter Deposition*, 109, 1965.

[41] E.V.Alonso, M.A.Alurralde, and R.A.Baragiola. Kinetic electron emission from solids induced by slow heavy ions. *Surface science*, 166:155–160, February 1986.

[42] H.Eder, W.Messerschmidt, HP.Winter, and F.Aumayr. Electron emission from clean gold bombarded by slow Au^{q+} (q=1–3) ions. *Journal of Applied Physics*, 87(11), June 2000.

[43] S.Mazouffre. Laser-induced fluorescence diagnostics of the cross-field discharge of Hall thrusters. *Plasma Sources Science and Technologies*, 22, November 2012.

[44] S.Mazouffre and G.Bourgeois. Spatio-temporal characteristics of ion velocity in a Hall thruster discharge. *Plasma Sources Science and Technology*, 19, 2010.

[45] J.Vaudolon, B.Khiar, and S.Mazouffre. Time evolution of the electric field in a Hall Thruster. *Plasma Sources Science and Technology*, 23(022002), February 2014.

[46] J.Vaudolon. Electric field determination and magnetic topology optimization in Hall thrusters, October 2015.

[47] R.Pasqualotto, P.Nielsen, C.Gowers, M.Beurskens ans M.Kempenaars, T.Carlstrom, and D.Johnson. High resolution Thomson scattering for Joint European Torus (JET). *Review of Scientific Instruments*, 75, October 2004.

[48] M.Y.Kantor, A.J.H.Donne, R.J.E.Jaspers, and H.J.van der Meiden. Thomson scattering system on the TEXTOR tokamak using a multi-pass laser beam configuration. *Plasma Physics and Controlled Fusion*, February 2009.

[49] B.Vincent, S.Tsikata, S.Mazouffre, T.Minea, and J.Fils. A compact new incoherent Thompson scattering diagnostic for low-temperature plasma studies. *Plasma Sources Sci. Technol.*, 27, May 2018.

[50] B.Vincent. Incoherent Thomason scattering investigations in Hall thruster, planar magnetron and ECR ion source plasmas, December 2019.

[51] B.Vincent, S.Tsikata, G-C.Potrivitu, and S.Mazouffre. Incoherent Thomson scattering diagnostic development for plasma propulsion investigations. In *35th International Electric Propulsion Conference*, October 2017.

[52] L.Grimaud, A.Pétin, J.Vaudolon, and S.Mazouffre. Perturbations induced by electrostatic probe in the discharge of Hall thrusters. *Review of Scientific instruments*, 87, April 2016.

[53] C.M.Marerese, N.Majumdar, J.M.haas, G.Williams, L.B.King, and A.D.Gallimore. Development of a single-orifice Retarding Potential Analyser for Hall Thruster Plume Characterization. In *25th International Electric Propulsion Conference*, August 1997.

[54] T.E.Sheridan. How big is a small Langmuir probe. *Physics of Plasmas*, 7(7), July 2000.

[55] V.I.Demidov, S.V.Ratynskaia, and K.Rypdal. Electric probes for plasmas, the link between theory and instrument. *Review of scientific instruments*, 73(10), October 2002.

[56] F.F.Chen. Langmuir probe analysis for high density plasmas. *Physics of Plasmas*, 8(6), June 2001.

[57] R.L.Merlino. Understanding Langmuir probe current-voltage characteristics. *American Journal of Physics*, 75(12), July 2007.

[58] K.J.Terhune and L.B.King. Ion and Mass Measurement of an ELectrospray Emitter using ExB filter. In *32nd International Electric Propulsion Conference*, September 2011.

[59] J.P.Sheehan and N.Hershkovitz. Emissive probes. *Plasma Sources Science and Technology*, 20(6), 2011.

[60] N.Teshigahara, S.Shinohara, Y.Yamagata, D.Kuwahara, and M.Watanabe. Development of 2D Laser-Induced Fluorescence (LIF) System in High-Density Helicon Plasma. *Plasma and Fusion Research*, 9, March 2014.

[61] D. Renaud, D. Gerst, S. Mazouffre, and A. Aanesland. E×B probe measurements in molecular and electronegative plasmas. *Research of Scientifique Instrument*, 86(123507), December 2015.

[62] B.S.Rawat, S.Vala, M.Abhangi, R.Kumar, and S.Chauhan. Design and simulation of 10kW Faraday cup for ion beam current. In *25th International Conference on Nuclear Engineering ICONE25*, July 2017.

[63] D.L.Brown, M.L.R.Walker, J.Szabo, W.Huang, and J.E.Foster. Recommended Practice for Use of Faraday Probes in Electric Propulsion Testing. *Journal of Propulsion and Power*, 33(3), May - June 2017.

[64] D.Krejci, F.Mier-Hicks, R.Thomas, T.Haag, and P.Lozano. Emission Characteristics of Passively Fed Electrospray Microthruster with Propellant Reservoirs. *Journal of Spacecraft and Rockets*, 54(2), March 2017.

[65] L.Habl, D.Rafalskyi, and T.Lafleur. Secondary electron emission due to multi-species iodine ion bombardment of different target materials. *Journal of Applied Physics*, 129(15), 2021.

[66] K.Dannenmayer, P.Kudrna, M.Tichý, and S.Mazouffre. Measurement of plasma parameters in the far-field plume of a Hall effect thruster. *Plasma Sources Science and Technology*, 20(6):9, November 2011.

[67] H.M.Mott-Smith and I.Langmuir. The theory of collectors in gaseous discharges. *Physical Review*, 28, 1926.

[68] I.B.bernstein and I.N.Rabinowitz. Theory of Electrostatic Probes in a Low-Density Plasma. *Physics of Fluids*, 2(2), 1959.

[69] J.G.Laframboise. Theory of spherical and cylindrical Langmuir probes in a collisionless, maxwellian plasma at rest, 1966.

[70] L.Talbot. Theory of the Stagnation-Point Langmuir Probe. *Physics of Fluids*, 3(2), 1960.

[71] F.F.Chen, C.Etievant, and D.Mosher. Measurement of Low Plasma Densities in a Magnetic Field. *Physics of Fluids*, 11(4), 1968.

[72] D.L.Brown and A.D.Gallimore. Evaluation of ion collection area in Faraday probes. *Rev. Sci. Instrum.*, 81:063504, 2010.

[73] C.Bohm and J.Perrin. Retarding field analyzer for measurements of ion energy distributions and secondary electron emission coefficients in low pressure radio frequency discharges. *Review of Scientific Instruments*, 64, September 1992.

[74] M.Ya-li, T.Fu-jun, X.Yu-xiong, C.Yi-feng, G.Xin, W.Yi, T.Kai, and Y.Zedong. Retarding Potential Analyzer Design and Result Analysis for Ion Energy Distribution Measurement of the Thruster Plume in the Laboratory. *International Journal of Aerospace and Mechanical Engineering*, 6, 2012.

[75] Z.Zhang, H.Tang, Z.Zhang, J.Wang, and S.Cao. A retarding potential analyzer design for keV-level ion thruster beams. *Review of Scientific Instruments*, 87, December 2016.

[76] Y.Sakai and I.Katsumata. An energy resolution formula of a three plane grids retarding field energy analyzer. *Japanese Journal of Applied Physics*, 24, March 1985.

[77] N.Mühlich, S.Keerl, W.Engel, E.Ceribas, and R-J.Koopmans. Retarding Potential Analyser Development for Low Density FEEP Thruster Beam Diagnostics. In *36th International Electric Propulsion Conference*, September 2019.

[78] V.Hugonnaud, S.Mazouffre, D.Krejci, B.Seifert, and C.Scharlemann. Faraday cup design for low power electric thrusters. In *Space Propulsion 2020+1*, March 2021.

[79] R.Blott, D.Robinson, and S.Gabriel. *Space electric propulsion verification by test*. Esa edition, 2016.

[80] T.Hallouin and S.Mazouffre. Far-Field Plume Characterization of a 100-W Class Hall Thruster. *Aerospace*, May 2020.

[81] R.R.Hofer and A.D.Gallimore. High-Specific Impulse Hall Thrusters, Part 2: Efficiency Analysis. volume 22.

[82] K.Dannenmayer and S.Mazouffre. Elementary scaling relations for hall effect thrusters. In *J.Propulsion Power*, number 27, page 236:245.

[83] R.R.Hoffer and R.S.Jankovsky. A Hall thruster performance model incorporating the effects of a multiply-charged plasma. In AIAA, editor, *AIAA*, number AIAA-2001-3322, 2001.

[84] J.M.Ekholm and W.A.Hargus. ExB Measurements of a 200 W Xenon Hall Thruster. In AIAA, editor, *41st Joint Propulsion Conference and Exhibit*, number AIAA-2005-4405, July 2005.

[85] D.L.Brown, A.W.Larson, and B.E.Beal. Methodology and Historical Perspective of a Hall Thruster Efficiency Analysis. *Journal of Propulsion and Power*, 25, 2009.

[86] L.Habl, D.Rafalskyi, and T.Lafleur. Ion beam diagnostic for the assessment of miniaturized electric propulsion systems. *Review of Scientific Instruments*, (91), 2020.

[87] A.Genovese, W.Steiger, and M.Tajmar. Indium FEEP microthruster: Experimental characterization in the 1-100μN range. In *37th AIAA/ASME/SAE/ASEE Joint Propulsion Conference and Exhibit*, July 2001.

[88] M.Tajmar, W.Steiger, and A.Genovese. Indium FEEP Thruster Beam Diagnostics, Analysis and Simulation. In *37th AIAA/ASME/SAE/ASEE Joint Propulsion Conference and Exhibit*, July 2001.

[89] D.M.Goebel and I.Katz. *Fundamentals of Electric Propulsion: Ion and Hall Thrusters*. Jet propulsion laboratory, california institute of technology edition, 2008.

[90] D.Brown. Investigation of low discharge voltage Hall Thruster characteristics and evaluation of loss mechanisms, May 2009.

[91] D.Krejci, V.Hugonnaud, T.Schönherr, B.Little, A.Reissner, B.Seifert, Q.Koch, E.Bosch Borràs, and J.González Del Amo. Full Performance Mapping of the IFM Nano Thruster including Direct Thrust Measurements. *Journal of Small Satellites*, 8(2):881–893, 2019.

[92] F.G.Rüdenauer, H.M.Fehringer, A.Sieber, and W.Stieger. Behaviour of Backsputterred Contaminations on Liquid Metal Indium Ion Emitters.

[93] S.Keerl, W.Engel, N.S.Mühlich, J.Fries, and B.Seifert. Two-dimensional plasma plume density characterisation of the IFM Nano Thruster. In *36th International Electric Propulsion Conference*, September 2019.

[94] Heinzinger. Heinzinger Website Homepage. `https://www.heinzinger.com/en/power-supplies/high-voltage/universal-high-voltage-power-supplies/`.

[95] Impedans. Impedance plasma measurements. `https://www.impedans.com/semion-single-sensor/`.

[96] M.Ye, Y.He, S.Hu, R.Wang, and T.Hu et al. Suppression of secondary electron yield by micro-porous array structure. *Journal of Applied Physics*, 113(074904), February 2013.

[97] C.Swanson and I.Kaganovich. Modeling of reduced secondary electron emission yield from a foam or fuzz surface. *Journal of Applied Physics*, 123(023302), January 2018.

[98] C.Huerta, M.I.Patino, and R.E.Wirz. Secondary electron emission from textured surfaces. *Journal Physics D:Applied Physics*, 151(145202), March 2018.

[99] E.Huerta and E.Wirz. Ion-induced electron emission reduction via complex surface trapping. *AIP advances*, 9(125009), December 2019.

[100] A.Ottaviano, S.Banerjee, and Y.Raitses. A rapid technique for the determination of secondary electron emission yield from complex surfaces. *Journal of Applied Physics*, 126(223301), December 2019.

[101] N.S.Mühlich, B.Seifert, and F.Aumayr. IFM Nano Thruster performance studied by experiments and numerical simulations. *Journal of Physics D: Applied Physics*, 54(9), 2020.

[102] S.Humphries. Intense ion-beam neutralization in free space. *Applied Physics Letters*, 32(12), 1978.

[103] V.V.Zhurin, H.R.Kaufman, and R.S.Robinson. Physics of closed drift thrusters. *Plasma Sources Sci. Technol*, 8, 1999.

[104] S.Mazouffre, G.Bourgeois, K.Dannenmayer, and A.Lejeune. Ionization and acceleration processes in a small, variable channel width, permanent-magnet Hall thruster. *Journal of Physics D: Applied Physics*, 45(185203), April 2012.

[105] J.M.Sankovic, J.A.Hamley, and T.W.Haag. Performance Evaluation of the SPT-100 Thruster at NASA LeRC. In *23rd International Electric Propulsion Conference*, September 1993.

[106] M.R.Nakles, W.A.Hargus Jr, J.J.Delgado, and R.L.Corey. A Performance Comparison of Xenon and Krypton. In *32nd International Electric Propulsion Conference*, September 2011.

[107] G-C.Potrivitu, R.Joussot, and S.Mazouffre. Anode position influence on discharge modes of a LaB_6 cathode in diode configuration. *Vacuum*, 151:122–132, February 2018.

[108] I.Vasiljevich, M.Tajmar, W.Grienauer, F.Plesescu, N.Buldrini, J.Gonzalez Del Amo, B.Carnicero-Dominguez, and M.Betto. Development of an Indium mN-FEEP Thruster. In *44th AIAA/ASME/SAE/ASEE Joint Propulsion Conference and Exhibit*, July 2008.

[109] D.Jelem, B.Seifert, R.Sypniewski, N.Buldrini, and A.Reissner. Performance mapping and qualification of the IFM Nano thruster EM for in orbit demonstration. In *53rd AIAA/SAE/ASEE Joint Propulsion Conference*, October 2017.

[110] D.Jelem, A.Reissner, B.Seifert, N.Buldrini, L.Wilding, and D.Krejci. Direct thrust and plume divergence measurements of the IFM Nano Thruster. *Advances in Space Research*, 62(12):3398–3404, 2018.

[111] A.Reissner, N.Buldrini, B.Seifert, T.Hörbe, and F.Plesescu. Testing and Modelling of the mN-FEEP Start-Up Performance. In *34th International Electric Propulsion Conference*, July 2015.

[112] S.Marcuccio, A.Genovese, and M.Andrenucci. Experimental Performance of Field Emission Microthrusters. *Journal of Propulsion and Power*, 14(5), 1998.

[113] M.Tajmar, A.Genovese, and W.Steiger. Experimental Performance of Field Emission Microthrusters. *Journal of Propulsion and Power*, 20(2), 2004.

[114] A.Genovese, N.Buldrini, M.Tajmar, E.Tamas, I.Vasiljevich, and K.Marhold. Development of an Indium mN-FEEP Thruster. In *41st AIAA/ASME/SAE/ASEE Joint Propulsion Conference and Exhibit*, July 2005.

[115] I.Vasiljevich, N.Buldrini, F.Plesescu, M.Tajmar, M.Betto, and J.Gonzalez Del Amo. Porous Tungsten Crown Multiemitter Testing Programmes Using Three Different Grain Sizes and Sintering Procedures. In *The 32nd International Electric Propulsion Conference*, September 2011.

[116] R.G.Forbes. Understanding how the liquid-metal ion source works. *Vacuum*, 48(1), 1996.

[117] H.Niedrig. Ion and electron emission from liquid metal sources. *Scanning Microscopy*, 10(4), 1996.

[118] W.Czarczynski. Secondary electrons in liquid metal ion sources. *Journal of Vacuum Science & Technology A*, 13, 1094.

[119] G.L.R.Mair and A.von Engel. Gallium-field-ion emission from liquid point anodes. *Journal of Applied Physics*, 50, 1979.

[120] C.Corbella, A.Marcak, T.de los Arcos, and A.von Keudell. Revising secondary electron yields of ion-sputerred metal oxides. *Journal of Physics D: Applied Physics*, 49, 2016.

[121] M.L.R.Walker, A.L.Victor, R.R.Hofer, and A.D.Gallimore. Effect of Backpressure on Ion current density Measurements in Hall Thruster Plumes. In *Journal of Propulsion and Power*, volume 21, May-June 2005.

[122] D.A.Dahl. SIMION for the personal computer in reflection. In *International Journal of Mass Spectrometry*, volume 200, August 2000.

[123] J.Vaudolon and S.Mazouffre. Impact of the magnetic barrier extent on the performance of a krypton-fuelled Hall thruster. In *51st AIAA/SAE/ASEE Joint Propulsion Conference*, July 2015.

[124] F.G.Hey, M.Vaupel, C.Groll andC.Braxmaier, M.Tajmar, A.Sell, K.Eckert, D.Weise, and U.Johann. Development of a Gridless Retarding Potential Analyser. In *35th International Electric Propulsion Conference*, October 2017.

[125] J. Gonzales del Amo. Electric Propulsion at the European Space Agency. In *36th International Electric Propulsion Conference*, September 2019.